Modeling of Bio-inspired Jellyfish Vehicle for Energy Efficient Propulsion

Keyur B Joshi

Dissertation submitted to the faculty of the Virginia Polytechnic Institute and State University in partial fulfillment of the requirements for the degree of

Doctor of Philosophy
In
Mechanical Engineering

Shashank Priya, Chair
John Henry Costello
Walter F O'Brien
Danesh K Tafti
Robert L West

11/30/2012
Blacksburg, VA

Keywords: Bio-inspiration, Energy efficiency, Jellyfish, Buoyancy engine, Solar energy harvesting, Thermo-magnetic energy harvester, Finite element model, autonomous vehicle, artificial muscle, actuator, shape memory alloy, ionic polymer metal composite

Modeling of Bio-inspired Jellyfish Vehicle for Energy Efficient Propulsion

Keyur B Joshi

Abstract

Jellyfish have inhabited this planet for millions of years and are the oldest known metazoans that swim using muscles. They are found in freshwater sources and in oceans all over the world. Over millions of years of evolution, they have adapted to survive in a given environment. They are considered as one of the most energy efficient swimmers. Owing to these characteristics, jellyfish has attracted a lot of attention for developing energy efficient unmanned undersea vehicles (UUVs).

The goal of this thesis is to provide understanding of the different physical mechanisms that jellyfish employs to achieve efficient swimming by using analytical and computational models. The models were validated by using the experimental data from literature. Based upon these models refinements and changes to engineering vehicles was proposed that could lead to significant enhancement in propulsion efficiency. In addition to the propulsion, the thesis addresses the practical aspects of deploying a jellyfish-inspired robotic vehicle by providing insights into buoyancy control and energy generation. The thesis is structured in a manner such that propulsive and structural models inspired from the natural animal were systematically combined with the practical aspects related to ionic diffusion driven buoyancy control system and thermal – magnetic energy harvesting system. Jellyfish morphology, swimming mechanism and muscle architecture were critically reviewed to accurately describe the natural behavior and material properties. We provide full understanding of mesoglea, which plays most significant

role towards swimming performance, in terms of composition, mechanical properties and nonlinear dynamics. Different jellyfish species exhibit different microstructure of mesoglea and thus there is a wide variety of soft materials. Mechanical properties of collagen fibers that form the main constituent toward imparting elasticity to mesoglea were reviewed and analyzed. The thesis discusses the theoretical models describing the role of structure of mesoglea towards its mechanical properties and explains the variation occurring in stiffness under given experimental environment. Muscle architecture found in jellyfish, nerve nets and its interconnection with the muscles were investigated to develop comprehensive understanding of jellyfish propulsion and its reaction to external stimuli.

Different muscle arrangements were studied including radial, coronal muscle, and coronal-muscles-with-breaks in-between them as observed in *Cyanea capillata*. We modeled these muscle arrangements through finite element modeling (FEM) to determine their deformation and stroke characteristics and their overall role in bell contraction. We found that location and arrangement of coronal muscle rings plays an important role in determining their efficient utilization.

Once the understanding of natural jellyfish was achieved, we translated the findings onto artificial jellyfish vehicle designed using Bio-inspired Shape Memory Alloy Composite (BISMAC) actuators. Detailed structural modeling was conducted to demonstrate deformation similar to that of jellyfish bell. FEM model incorporated hyperelastic behavior of artificial mesoglea (Ecoflex-0010 RTV, room temperature vulcanizing silicone with shore hardness (0010)), experimentally measured SMA temperature transformation, gravity and buoyancy forces. The model uses the actual control cycle that was optimized for driving the artificial

jellyfish vehicle “robojelly”. Using a comparative analysis approach, fundamental understanding of the jellyfish bell deformation, thrust generation, and mechanical efficiency were provided.

Meeting energy needs of artificial vehicle is of prime importance for the UUVs. Some jellyfish species are known to use photosynthesis process indirectly by growing algae on their exumbrella and thereby utilizing the sunlight to generate energy. Inspired by this concept, an extensive model was developed for harvesting solar energy in underwater environment from the jellyfish bell structure. Three different species were modeled for solar energy harvesting, namely *A.aurita, C.capillata* and *Mastigia sp.,* using the amorphous silicon solar cell and taking into account effect of fineness ratio, bell diameter, turbidity, depth in water and incidence angle. The models shows that in shallow water with low turbidity a large diameter vehicle may actually generate enough energy as required for meeting the demand of low duty cycle propulsion. In future, when the solar energy harvesting technology based upon artificial photosynthesis, referred to as “dye-sensitized solar cells”, matures the model presented here can be easily extended to determine its performance in underwater conditions.

In order to supplement the energy demand, a novel concept of thermal – magnetic energy harvesting was developed and extensively modeled. The proposed harvester design allows capturing of even small temperature differences which are difficult for the thermoelectrics. A systematic step-by-step model of thermo-magnetic energy harvester was presented and validated against the experimental data available in literature. The multi-physics model incorporates heat transfer, magnetostatic forces, mechanical vibrations, interface contact behavior, and piezoelectric based energy converter. We estimated natural frequency of the harvester, operating temperature regimes, and electromechanical efficiency as a function of dimensional and physical

variables. The model provided limit cycle operation regimes which can be tuned using physical variables to meet the specific environment.

Buoyancy control is used in aquatic animals in order to maintain their vertical trajectory and travel in water column with minimum energy expense. Some crustaceans employ selective ion replacement of heavy or lighter ions in their dorsal carapace. A model of a buoyancy chamber was developed to achieve similar buoyancy control using electro-osmosis. The model captures all the essential ionic transport and electrochemistry to provide practical operating cycle for the buoyancy engine in the ocean environment.

Dedication

I would like to dedicate this work to all my teachers, including my parents and other elders who influenced me right from my childhood. Teachers who have taught me well not because they were paid to do so, but because they believed in sacred profession of knowledge; teachers who inspired me and ignited my passion about science; teachers who helped me whenever I needed it smilingly; teachers who formed not only my knowledge base but my passion for science, my value system, my moral character. After all, “Vidya Vinayen Shobhate” (Sanskrit quote: Meaning, Knowledge shines only through humbleness).

I would like to mention just a few names with utmost respect, Shamimbanu Hakim/Patel, D H Tiwari, C R Patel, Jasbhai Patel, Dr P Prabhakaran, Dr P B Desai, Dr V K Mahyavanshi, Dr P S Gandhi, Dr C Amarnath, Dr Danesh Tafti, Dr Andrew Kurdila and Dr Shashank Priya; you have influenced my life and I am grateful to god to bestow me the honor of your guidance and your company. May this and future generations keep getting to be inspired by you.

Acknowledgement

God's blessings is first to be acknowledged. Next, I would like to acknowledge my mother who stood by me always and went through a very challenging time to provide me good education and a good life. I acknowledge discussions with Dr Kurdila, Dr Tafti and Dr Blottman as greatly helpful. Dr Priya has shown me a brave new world of research; always giving tough assignments and every time dealing with new physics; initially I resisted because I felt "that's not my field", but finally I understood that a researcher is just a curious learner of nature and shouldn't be bound by boundaries of disciplines. It helped me break my cocoon and now I am filled with a new confidence that I can do research successfully in any given field if sufficient time is available. I would like to thank all my committee members, Dr John Henry Costello, Dr Walter F O'Brien, Dr Danesh K Tafti, and Dr Robert L West, for their time and guidance during the course of this thesis. They have been most approachable. I enjoyed discussing fluid dynamics topics with Dr Tafti and got wonderful insight into jellyfish biology from Dr Costello.

My friend Kapil did help me lighten up when things got too tense for my liking. And of course support of my dedicated wife Karuna who sportingly took on hardships of graduate studies with me and has been my strength.

I acknowledge all my coworkers and especially jellyfish team – Alex Villanueva, Colin Smith, Colin Stewart and Dr Shantanu Mitra. It has been pleasure working with you.

I also acknowledge support of ONR (Office of Naval Research) for sponsoring me through contract number N00014-08-1-0654.

Table of contents

List of figures

List of tables

Chapter 1. Introduction

Tethered buoys (or stationary) are widely used for data collection and surveillance. The problem with tethering is that it limits the mobility and thus the area covered by the buoy. Untethered passive buoys drift with the ocean waves and offer very little in terms of retracing their original position. This makes the tasks such as intrusion monitoring and chemical hazard monitoring difficult. It is thus desirable to develop alternative sensory vehicle platform that can maintain its allocated area in the ocean by using a combination of active and passive locomotion. The useful life of such underwater swimming vehicle is inarguably dependent on its battery life. In order to extend the vehicle's lifetime, it should not only conserve energy while swimming but also recharge its batteries through environmental energy sources such as sunlight, temperature gradient and microbes.

Jellyfish have been in existence for millions of years and is earliest known metazoans using muscles for swimming (Valentine,2004). It has adapted and perfected its motion to yield the best swimming efficiency over millions of years of evolution. They are found at various ocean depths and possess ability to survive under hostile ocean environment. Jellyfish have relatively simple biological form and muscle architecture lacking advanced sensors and complex neural network possessed by many oceanic creatures (Gladfelter,1972, Gladfelter,1973, Chapman,1974) but they are still able to survive and adapt in hostile environments. They maintain territorial existence by swimming on minimal energy intake. These abilities have created tremendous interest in the scientific community to discover their structure-property-performance relationships and apply the learning towards creating a jellyfish inspired swimming vehicle to perform various surveillance and monitoring tasks.

Jellyfish exhibit colonial behavior and have the ability to maintain specific depth and distance from the ocean shore (Albert,2009). They maintain their position near coast by sinking down during receding wave and swimming up during rising wave. Jellyfish can be divided into two classes of swimmers – jetters and rowers. Rowers form starting and stopping counter-rotating vortices for thrust production that is known to provide higher Froude efficiency as compared to jetters. Interaction of these starting and stopping vortices helps in recovering some of the energy lost in the wake. Rower jellyfish, particularly *Aurelia aurita*, have substantially low cost of transportation (COT) defined by energy used per distance travelled per body mass/weight. COT is a popular way of comparing the energy used by biological species for locomotion and is calculated from measurement of the biological oxygen demand (BOD) - amount of oxygen consumption - during transport and knowing the chemical reaction, the amount of biological fuel used is calculated; the amount of the fuel used multiplied by calorific value of the fuel gives energy of transportation; dividing it by distance and body mass/weight gives us COT. As illustrated in Figure 1-1, swimmers in general have less cost of transportation compared to runner and fliers. Moreover data suggests that Scyphomedusa (Rower class Jellyfish), particularly *Aurelia aurita* is comparatively much more economical in the swimmer class. The data shown in Figure 1-1 makes Jellyfish a suitable inspiration for designing future surveillance and monitoring vehicles.

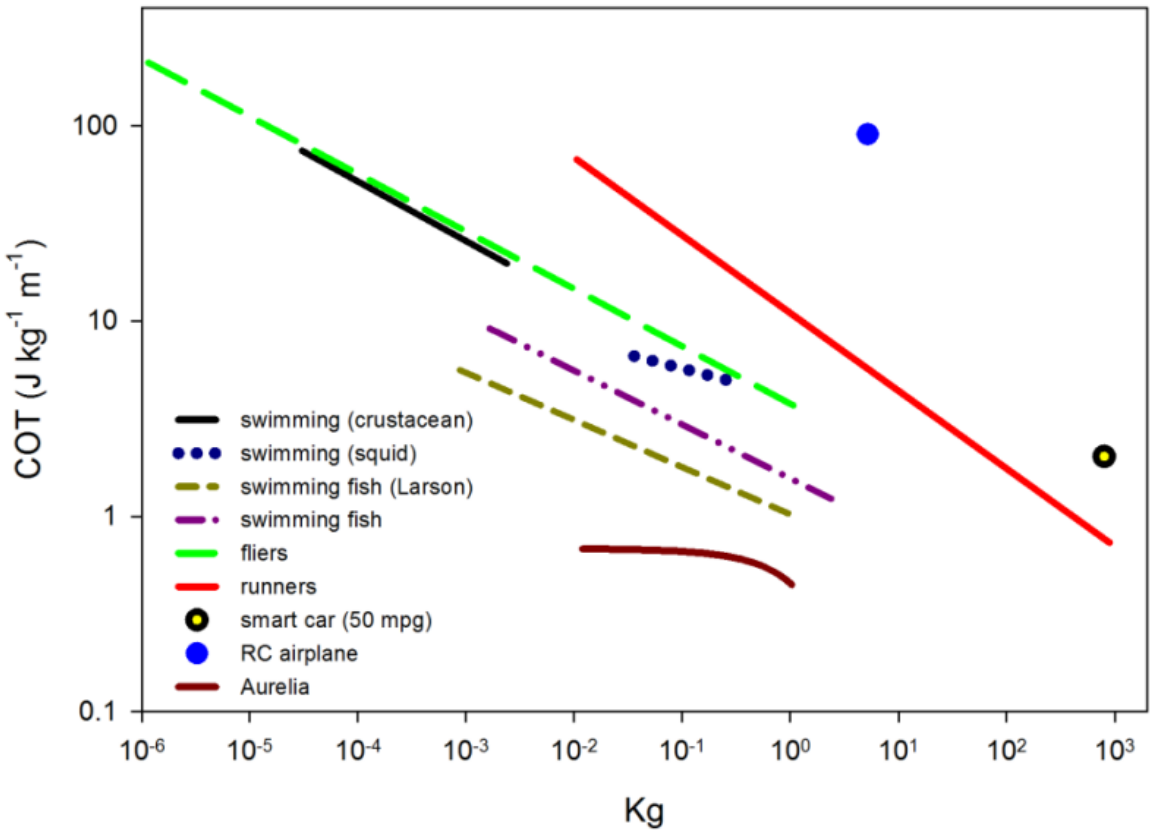

Figure 1-1. Comparative cost of transport for living organisms and some representative vehicle. Biological data from (Tucker,1975, Larson,1987) and unpublished work of Gemmel

The prime objective of this thesis is to identify and understand the propulsion mechanism of rower jellyfish with respect to their structural dynamics, muscle arrangement and kinematics parameters. In order to transition the learning achieved related to efficient swimming of natural species on to the artificial vehicle platform termed “robojelly”, various numerical models were developed to provide simulation environment for quantifying the role of relevant parameters. It is believed that the theoretical understanding provided by this thesis will significantly reduce the time towards development of jellyfish-inspired underwater surveillance vehicle (JUSV).

Nature has provided optimum solutions tailored for a given environment. Modern aircraft designers utilize diversity in bird flight as the learning tool and for continuous innovation. Modern aircraft wings are representative of bird's wing through an airfoil cross-section. Fuselage is made streamlined like a bird's body. Similar aspect of bio-inspired engineering solutions can be found in almost every aspect of our life. Thus, in developing underwater vehicles we naturally took inspiration from the aquatic creatures that have evolved over millions of years in the relevant surrounding.

1.1 Background and historical information

Taxonomically jellyfish belong to phylum "cnidaria" named after their venomous stinging glands nematocyst also called "cnidae". The phylum is also called "coelenterate" by its characteristic blind bodysac like gastrovascular cavity (coelenteron) (Oxforddictionaries.com). Jellyfish comprise of more than 350 species found in scyphozoan, hydrozoan and cubozoan class. They are also called medusa due to the fact that their sting causes its prey disable to move, like "stone". Detailed Jellyfish terminology is given in the Appendix. Figure 1-2 illustrates basic anatomy of typical scyphozoan medusa.

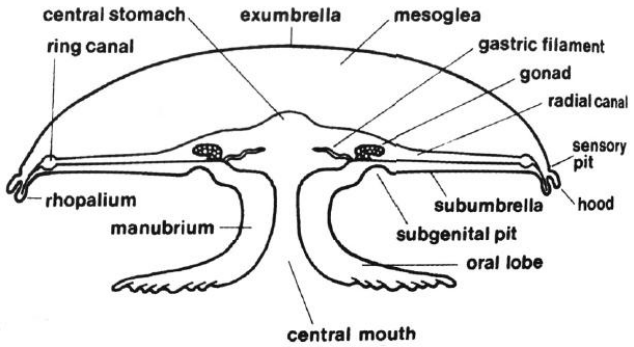

Figure 1-2. Schematic description of typical scyphozoan jellyfish (Stachowitsch,1992)

1.2 Ocean environment

The typical ocean has 35 ppt (part per thousand) salinity and temperature ranges from 5-25°C. Turbidity is of the order of 1-7 where average ocean turbidity can be taken to 3 (Williams,1970). Sunlight reaches only up to a few hundred meters, while the rest of the ocean is cold and dark with almost zero visibility. Temperature varies with season in upper layer of the ocean, and has thermal gradients (thermocline) upto a certain depth, while deep ocean is at a uniformly low temperatures as shown in Figure 1-3. Pressure increases with depth. Pressure and temperature changes cause solubility of various salts and gases to change. This results in halocline (change of salinity/concentration of halogen group with depth). Both halocline and thermocline cause change in density of ocean water with depth (pycnocline), which is very useful for aquatic creatures in maintaining their position in water column.

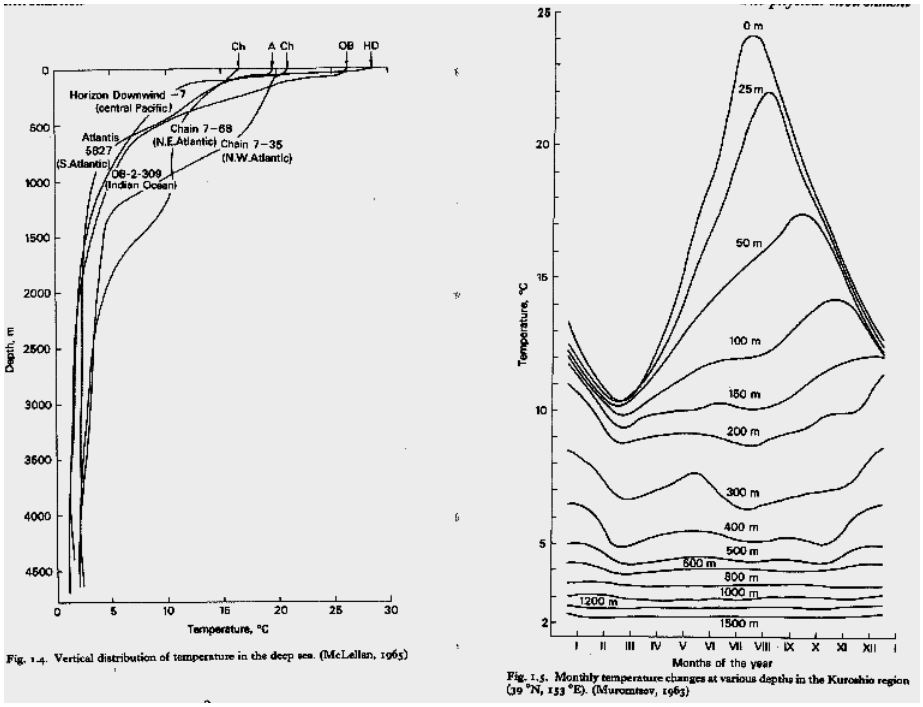

Figure 1-3. Temperature variations in ocean (Macdonald,1975)

Jellyfish are found in ocean as well as in freshwater. They are believed to exist at few hundred meters depth in the ocean but some species like red giant *Tiburonia granrojo* are found

at depths more than 1500 m (Wikipedia). Jellyfish have to survive in violent storm turbulence and use their sensory organs to escape from the predators.

In ocean environment energy availability is very less. Solar radiation reaches only a few hundred meters and attenuates fast with depth. Wave energy is available at shallow depths and is most pronounced near the coast. Wind energy is unavailable under water surface. Thermal gradients exist in the thermocline that may be used to run a thermodynamic engine. A successful use of thermal gradient in upper ocean layer where thermocline is present was demonstrated by SLOCUM glider (named after Joshua Slocum, first man to sail around the world) developed by webb et.al.(Webb,2001) using solid-gaseous transformation of the working medium. However for monitoring purpose, where station keeping is main requirement, and diving to hundreds of meters is not possible to take advantage of ocean thermal gradients, one needs to explore other energy sources to meet vehicle's need.

1.3 Adaptations

Jellyfish body mainly constitutes of water. They maintain salinity levels in their body very close to their environment. They are neutrally buoyant and thus spend no energy in order to maintain the depth in the ocean. Its rhopalium has statocyst that gives it sense of gravity and ocellus that contains photosensitive cells (Stachowitsch,1992). They can sense shadow of their predator and swim away from it. Many jellyfish have transparent body to reduce their shadow signature, a camouflage that allows protection against predators and helps them capture their prey (Chapman,1976). It usually has extended tentacles and in some species extensive oral structures whose surface is covered with touch sensitive and possibly chemical sensitive sensors, cnidocils, that are paired with tightly wound coil like stinging filament (nematocyst) capsule. On contact with prey, nematocyst triggers and penetrates prey with harpoon like needle,

simultaneously injecting prey with rapid acting venom that paralyses it. The oral arm or manubrium moves in the direction of prey capture site and grabs it, slowly transferring it to the gastric cavity for digestion by ciliated motion. Waste after digestion is also excreted from the same tract. In this energy efficient hunting, it doesn't have to fight with its prey trying to escape. It stores energy in form of polysaccharides and collagen fibers in mesoglea that can be used on demand. Its respiration is through diffusion of oxygen through permeable epidermis (van Bergen,2005). Some deep sea species also exhibit bio-luminescence that helps them scare off the predators, provide visibility and help in mating (Hirano,1996).

1.4 Swimming behavior

Jellyfish can be divided into two classes of swimmers – Jetters and Rowers. Rowers form starting and stopping counter-rotating vortex for thrust production that is known to provide higher Froude efficiency as compared to Jetters. Interaction of these starting and stopping vortices helps it recover some of the energy lost in the wake. Jellyfish tend to swim towards light. They turn by pivoting, keeping one side contracted while the other side swims to form asymmetrical thrust creating needed turning moment. With temperature rise, their swimming frequency generally increases but reduces sharply as temperature reaches close to the level where it dissolves collagen (Rigby,1972). Some researchers believe that jellyfish pulsate at resonance frequency of its bell structure for most effective swimming (Demont,1988a).

Chapter 2. Research objectives

Research community has been recently focusing on developing bio-inspired underwater swimming robots (Akle,2011, Guo,2003, Liwei,2010, Najem,2011, Shuxiang,2007, Tadesse,2012, Xiu Fen,2008, Yang,2007, Yeom,2009, Villanueva,2009, Villanueva,2010a). Several of these robots took inspiration from Jellyfish and utilized smart materials to mimic the actuation muscles and structural components. Chu et al. (Chu,2012) have provided the comparative analysis of these bio-mimetic and bio-inspired robots in their review and suggested that smart actuators have lower proficiency than electrical motor. SMA based actuators offer highest proficiency amongst smart actuators, followed by IPMC and PZT.

Prior researchers have made an early attempt towards incorporating the jellyfish bell kinematics in their robot design. However, most of the jellyfish robotic structure proposed in literature is still far from incorporating the fundamental swimming behavior of the rowers. One of the reasons for this limited development is the lack of understanding of the biology and fluid-structure interaction driving the locomotion. The second reason limiting the robot development has been the lack of theoretical models describing the structural dynamics and bell kinematics in terms of currently available artificial hyperelastic materials and smart actuator materials. The third reason has been the lack of methodology for implementing the adaptive control system on artificial muscles that can drive the robot through the similar contraction – relaxation cycles as used by natural species. During the course of this thesis, several of these limitations had been overcome which made possible to develop robots that mimic the natural species in many important aspects. The work described in this thesis concentrated on investigating the role of morphology, muscle architecture and kinematics towards achieving superior swimming performance. A due consideration to energy efficiency was given while developing the

numerical models for robotic vehicle utilizing bio-inspired shape memory alloy composite (BISMAC) actuator that serve as artificial muscles. In developing the analytical / numerical model, serious consideration was given to the energy needs of the underwater vehicle. Figure 2-1 pictorially describes the questions that were addressed in this thesis. In addition to answering these questions, detailed analytical models related to the solar and thermal energy harvesting were developed to provide a possible solution for the autonomous operation of the robotic vehicle. Lastly, a parametric model for the buoyancy control system was provided to improve the efficiency of the vehicle during vertical motion.

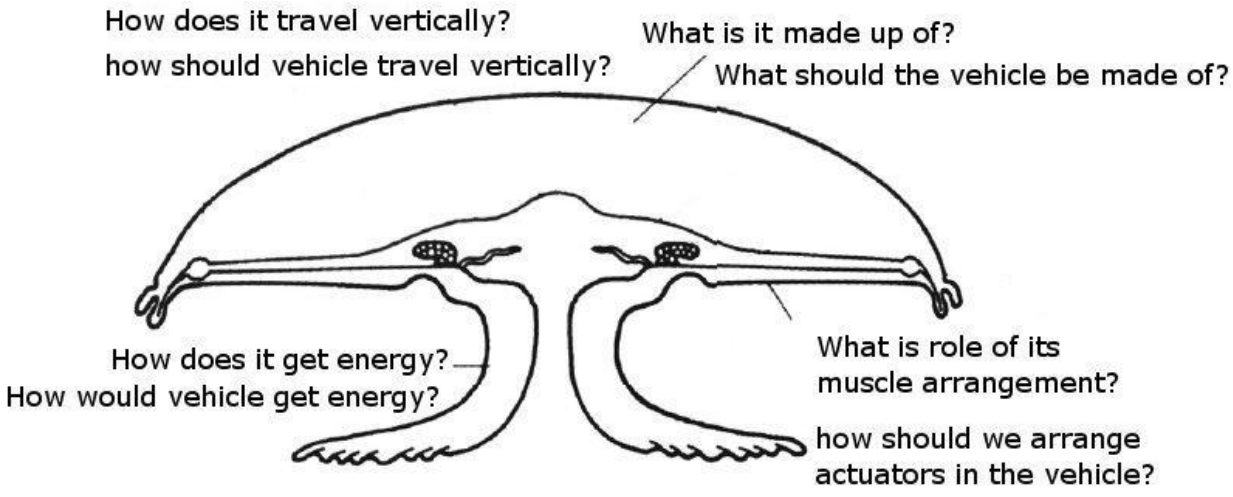

Figure 2-1. Pictorial representation of the questions addressed in this thesis [modified from (Stachowitsch,1992)].

2.1 Research objective statement

The prime objective of this thesis is to investigate the rowing swimming mechanism for artificial vehicles in terms of muscle arrangement, structural dynamics (artificial mesoglea and bell deformation), kinematic variables (proficiency, fineness ratio, thrust) and energy efficiency (ratio of output mechanical energy to input electrical energy) by developing numerical and analytical models that provide realistic guidance for improving the system performance. In doing

this analysis, initial efforts were made towards modeling the energy available from sunlight and thermal gradients in the ocean environments. In order to improve the efficiency of the vehicle a novel buoyancy control system was designed and modeled. Combining all these aspects, this thesis makes major contributions in the area of bio-mimetic rowing propulsion and energy efficiency.

The inspiration for this thesis comes from the natural jellyfish that exist in wide variety of shape and sizes. Throughout the course of this work, extensive collaboration with biologist was maintained to learn and adopt the natural mechanisms. It is very impressive that Jellyfish while possessing such as simple structure with no advanced sensing or predating capability has survived the hostile ocean environment for hundreds of millions of years. Several functionalities of Jellyfish are directly applicable for the design of autonomous sensor nodes and surveillance vehicles platform and these were considered in architecture of "robojelly". Jellyfish are efficient swimmers given their metabolic energy intake and the amount of work performed. The efficiency factor was paid attention while considering the material and actuator design.

2.2 Thesis objective and chapter overview:

The organization of the chapters in this thesis is as following:

Chapter 3 provides the discussion on morphology and composition of the jellyfish, their muscle arrangement, and actuation principles. It intends to provide the scientific foundation for the role of mesoglea illustrating the form and function of collagen fibers network, interconnectivity of muscles and nerve nets and decomposition of the decision-making processes.

Chapter 4 provides the understanding of the relationship between the macroscopic deformation and microscopic muscle arrangement. We develop and implement a high fidelity finite element model of artificial jellyfish vehicle consisting of three different muscle structures –

circular muscles, segmented circular muscles and radial muscles. Artificial muscles were modeled based upon the shape memory alloy (SMA) wires, BISMAC (Bio-inspired shape memory alloy composite) arranged circumferentially, and BISMAC arranged radially. The mesoglea for the artificial vehicle was approximated my RTV silicone. Since experimenting on live jellyfish muscle in an isolated condition is complex and prone to errors, the effect of the muscle architecture was simulated by varying the SMA based muscle architecture. Optimization of location of different muscle types and relative contributions to jellyfish bell deformation were investigated through Finite element model, including simulation of a full *Cyanea capillata* model incorporating all three type of muscle architecture. The prototype "robojelly" vehicle was modeled through finite elements including actual power cycle used to drive the actual prototype. Full transient analysis of heat transfer and structural deformations was conducted, incorporating hyperelastic material properties of silicone, temperature dependent phase transformation of SMA wires, large bell deformation, application of gravity and buoyancy force. Bell deformations of natural animal and robojelly were compared in terms of curvature analysis and average displacement error.

Chapter 5 forms the core of energy balance scenarios in ocean environment. We first provide the background towards understanding of the energy flow in natural jellyfish and then carve out various possibilities that could drive the artificial jellyfish. The focus in this chapter was on underpinning the environmental resources that will always be available to the vehicle. We conducted in-depth analysis of the solar energy harvesting in underwater environment with respect to common jellyfish species. Parametric study comprising of variables such as bell diameter, turbidity depth, incidence angle of sun, and orientation of jellyfish was conducted resulting in optimization of the combined metrics.

As a supplement to the solar energy, we also considered the scavenging of thermal energy. Detailed physics-based analytical and numerical models were developed to analyze the performance of a novel thermal harvester that has the ability to capture even low temperature gradients. This analysis is described in later parts of Chapter 5. The multiphysics model included modeling of thermal contact conductance, heat transfer model, magneto-static force, mechanical vibration and surface contact.

Chapter 6 investigates the biological principle for regulating buoyancy. Many underwater animals use osmotic regulation to maintain their vertical position in water column and efficiently travel vertically. We developed a novel concept for the buoyancy engine inspired by biology of swim bladder. This engine achieves buoyancy control through selective ion transfers occurring via electro-osmosis. Our computational fluid flow model takes into account osmotic pressure, interaction forces between ions and water, rate of chemical reactions, generation and destruction of densities of components, electrical pull on ions, modification of electrical field by redistribution of ion concentration, and diffusion in addition to viscous and pressure forces.

Chapter 7 focuses on providing the understanding of deformation of artificial jellyfish vehicle and compares it with the experimental prototype “robojelly”. The finite element model developed in this chapter incorporates hyperelastic silicone properties. The model simulates the temperature transformation of SMA wires taking into account very high aspect ratios and incorporates the gravity and buoyancy force. Transient thermal as well mechanical behavior was studied as part of the analysis. The model is robust enough to serve as a design tool for evaluating the performance of artificial vehicles.

Chapter 3. Natural mesoglea, collagen and jellyfish muscle

In this chapter, the objective was to understand what jellyfish is made up of; understand the properties of its building blocks; identify how it actuates its muscles, and explain its swimming mechanism.

Recently there has been growing interest amongst researchers on answering the question "how does the jellyfish swim?" In spite of being made up of 95 to 98% water, jellyfish is known to survive and swim in oceans throughout the world. They swim with only one cell layer thick sheet of muscles and these muscles do not have antagonistic pair. They lack complex sensor network and their nervous system is believed to be quite preliminary; yet, they are considered to be one of the most efficient swimmers. This chapter reviews basic building blocks of the jellyfish swimming mechanism. It discusses the role and properties of mesoglea and collagen reported in literature, explains why it is difficult to measure their mechanical properties and presents a hypothesis that explains why different researchers report orders of magnitude different value for the elastic coefficients. A comprehensive survey on the muscle structure and the nervous system of jellyfish was conducted with respect to jellyfish swimming mechanism.

3.1 Jellyfish

In order to understand the jellyfish swimming the first and foremost requirement is the understanding of what components make up its structure; what are the physical properties of the bell material; how are the muscles activated, and what is the role of each component present in the bell towards propulsion. This chapter discusses the literature with respect to these questions. The chapter is divided in three main parts: (i) mesoglea properties (ii) collagen properties, and (iii) muscle and neural activation.

3.2 Mesoglea properties

The main body mass of jellyfish – from which jellyfish derives its name – is “jelly” or jelly-like material called mesoglea. Mesoglea is also the structural component of many other coelenterate species. Epidermis or outer skin of the animal covering the entire body is classified into subumbrella and exumbrella – concave and convex surfaces of the jellyfish body respectively. Just below the epidermis on the subumbrellar side a single cell layer thick sheet of muscles and spanning over it nervous system and some sensory glands, such as rhopalia statocycsts, exist. Around the characteristic gastric pouch (coelenteron) is another skin layer called gastrodermis. Between the epidermis and gastrodermis, the entire body is made up of usually non-cellular mesoglea (some species have cells in mesoglea too)(Chapman,1953a). Thus, the understanding of mesoglea is critical in the understanding of jellyfish swimming.

3.2.1 Mesoglea constituents

Mesoglea constitutes of 95-98% of water content by volume. Depending upon whether the species is from the freshwater or the sea water, the volume percent of water content varies. Freshwater *Aurelia* mesoglea may have up to 95.56% of water as compared to the mesoglea of *Aurelia* found in ocean that may have up to 98% of water content. The reason for ocean species having higher water content is that their mesoglea also contains salt for osmotic regulation. Mesoglea maintains same level of acidity (pH level) and same amount of cation and anion concentrations on the whole, but maintains slightly different concentrations of individual ions as shown in Table 3-1. This fact may have some physiological implications that are not yet understood.

Table 3-1. Jellyfish mesoglea ioninc concentration (Krogh,1965)

	Cl- (mM/l)	SO4-- (mM/l)	Ca++ (mM/l)	Mg++ (mM/l)	K+ (mM/l)	Na+ (mM/l)	Total Acid mE	Total base mE	Total salt g/litre
Sea water	465	23.6	8.78	45.6	8.56	400	512	517	29.8
Cyanea	474	14.1	8.68	41.95	17.62	391	502	508	29.3
Aurelia	485	15.2	9.58	45.2	12.3	404	515	526	30

The water content however is not completely in free flowing form. It is mainly in bound form of mucopolysaccharide hydrogel that makes up the mesogleal matrix. Ions present in the mesoglea create an electric field around them that attracts opposite polarity end of water molecules. Water molecules lose their regular form and form covalent bonds amongst themselves to neutralize the effect of electric field and form special molecular structures around the ion several radius larger than the ion that created it, called the hydration shell. The hydration shell acts as a big bonded football-type molecule with ion at its core. There could be more than just one primary hydration shell and its structure depends on the radius and valency of the ion. Effect of electric charge of ion can reach much beyond the hydration shell that makes the flow of water molecule sluggish around the hydration shell. This phenomenon is the basis of formation of colloidal matters and hydrogels. Mesoglea also has fibrous network in it, mainly made up of proteins consisting of aminoacids that form the collagen, also found in vertebrate animals and some mucoprotien. Collagen is one of the most influential elements in mesoglea and thus will be discussed later in detail. Some researchers believe that these fibers also act as fibrilin.

3.2.2 Role and function of mesoglea

Mesoglea other than forming the main body volume provides the basis for muscles. Mesoglea also is a functionally graded material and provides different levels of stiffness at different location. Due to its viscoelastic nature, it also resists the sudden deformations caused by

the external forces and maintains the jellyfish shape. This feature is essential adaptation for efficient swimming and reduces loss of energy in rapid deformations(Chapman,1953b). Collagen fibers are elastic and store elastic energy during contraction stroke that is released slowly to restore its relaxed state. This is very essential function as the jellyfish do not have antagonistic muscle to relax the bell. Mucoprotien is believed to help in digestion of the food particles. Maintenance of similar salt concentration is essential for maintaining the osmotic equilibrium with its surroundings (Chapman,1953a). Permeable nature of mesoglea helps respiration by assisting the diffusion of oxygen (van Bergen,2005) through it and further the proteins made by digestion of food may be readily absorbed through it. Mesoglea also stores food buffer for later use when it starves. Starving jellyfish have thinner less stiff bell, sparser network of collagen fibers and it is believed that it first consumes the mucopolysaccharides and later partially collagen fibers to meet its metabolic needs.

3.2.3 Mechanical properties of mesoglea

Mesoglea is viscoelastic in nature. It exhibits rapid initial strain under the applied load followed by the slow and gradual strain increment (creep) with time as the load is maintained. Alexander (McN. Alexander,1964) has investigated this viscoelastic characteristics of mesoglea in some detail. On release of load, it showed some rapid elastic recovery followed by the slow time dependent recovery as shown in Figure 3-1. If deformation is too large, viscous dissipation dominates and complete recovery may not be possible. His results however had quite different time scale of testing and thus need to be interpreted carefully.

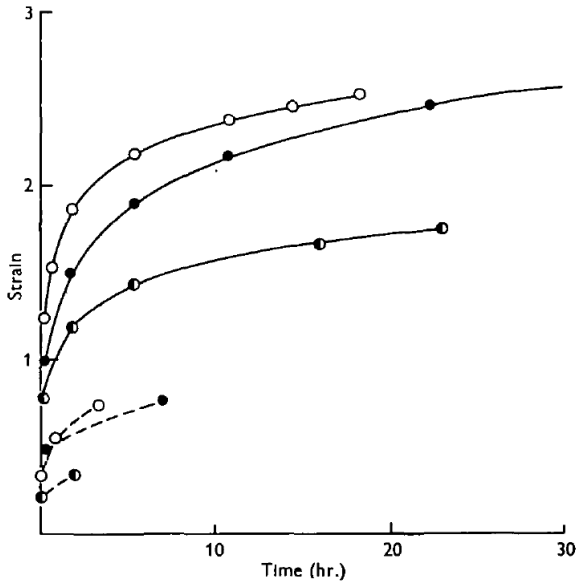

Figure 3-1. Viscoelastic properties of *Cyanea* mesoglea (solid line= loading, dashed lines=recovery)(McN. Alexander,1964)

Determining the mesoglea properties is daunting task. Mesoglea testing is made difficult by the fact that it is too compliant, viscoelastic and contains 95-98% water. Several researchers have thus reported fresh mesoglea weight (wet weight) and specimen weight (dry weight) that is usually a lot less (up to ~40%) due to the loss of water. Mesoglea has different collagen fiber densities in different section of the bell. Megill et.al. (Megill,2005) reports that near exumbrella and gastrodermis, collagen fiber densities are higher and in mid-bell section it is much less dense. Collagen is responsible for elastic stiffness which gives varying stiffness values in different directions and at different location of the bell. How the sample is cut is crucial for testing; if many collagen fibers are severed then the sample would exhibit much lower stiffness. Collagen fiber properties and network structure also varies from species to species and their densities from individual animal to another. The preparation method and time of the testing is quite important (Chapman,1953b) as shown in Figure 3-2(a). We get different behavior if the test is carried out too soon or too late. If the sample is tested too soon (Figure 3-2(a) upper trace), it

may still have some spontaneous contraction from live muscle tissues. If tested too late (Figure 3-2(a) lower trace), much of its water gets evaporated and its properties change irreversibly (Chapman,1953b). Figure 3-2(b) shows the muscle contraction as ripples occur in test data in lower trace in comparison with the regular test. Figure 3-2(c) and Figure 3-2(d) compare the test result of mesoglea sample tested with and without muscle layer, suggesting that the mesoglea with muscle layer is softer and hence muscles must be of much lower stiffness than the mesoglea. Chapman (Chapman,1953b) reported mesoglea properties of the *Calliactis* as listed in Table 3-2. *Calliactis* mesoglea however is too stiff, has almost cartilage like properties that is much different than the jellyfish mesoglea.

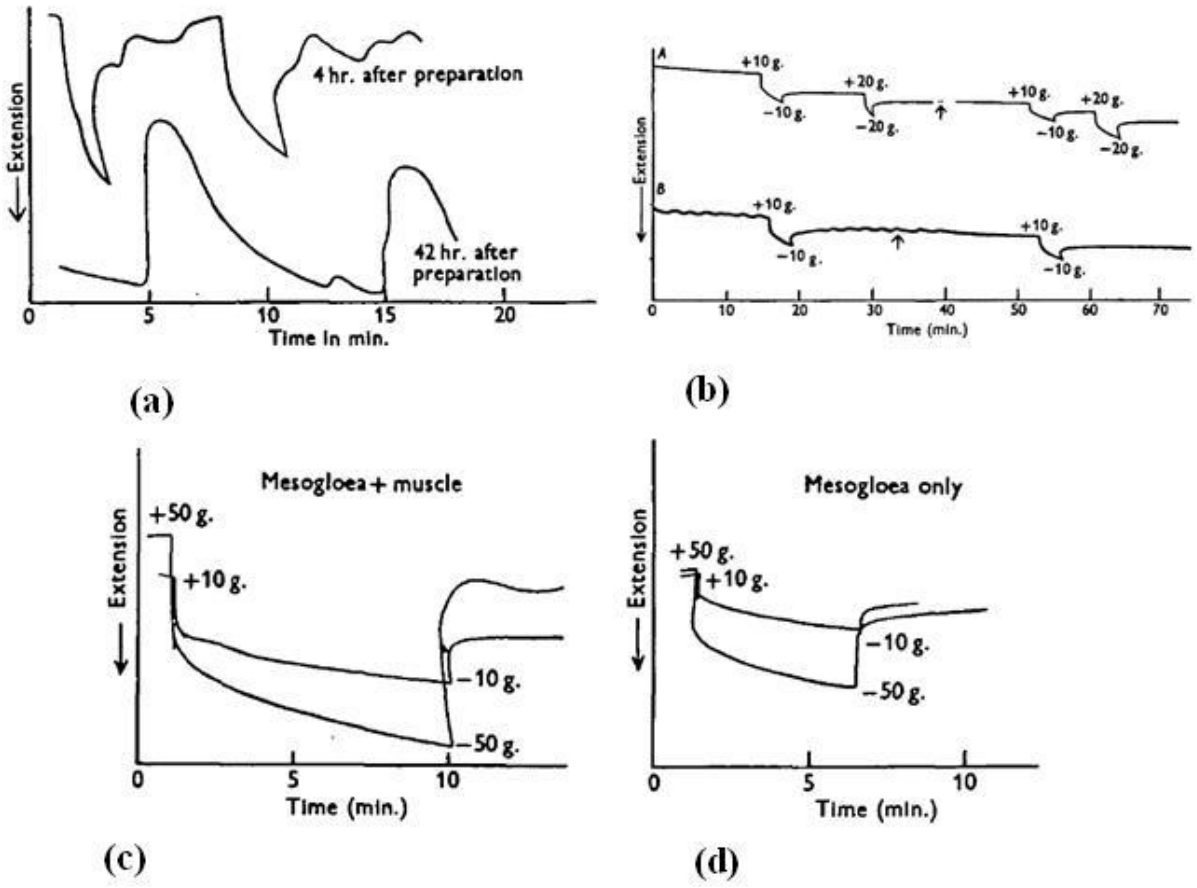

Figure 3-2. Tension test (a) showing dependence on preparation time (b) of live tissue (c) of mesoglea with muscle layer (d) of only mesoglea (Chapman,1953b)

Table 3-2. Extension test on *Calliactis* mesoglea sample (Chapman,1953b)

(Dimensions of test piece, 1·5 × 1·0 × 12 mm.)

Load in g.	% immediate extension	Load in g.	% immediate extension
10	1·7	200	13·3
20	4·2	300	18·3
30	5·0	400	25·0
50	7·5	500	28·3
70	6·7	600	30·0
100	8·3	700	35·0
150	11·7	900	Breakage

Chapman(Chapman,1953a) also observed different collagen structures in mesoglea of different species. As shown in Figure 3-3, *Aurelia* mesoglea has cells of about 10μ diameter embedded in the collagen fiber network. Cells occupy 0.3% of total mesoglea volume(Chapman,1953a). Collagen fiber network consists of regions with thick straight fibers having regular orientation with some randomly oriented serpentine and spiral fibers interspersed in between them. *Cyanea* mesgoglea doesn't possess any cell in it; collagen fibers are random and sparse. *Chrysoara* mesoglea has very well oriented collagen fibers in an oriented branched network.

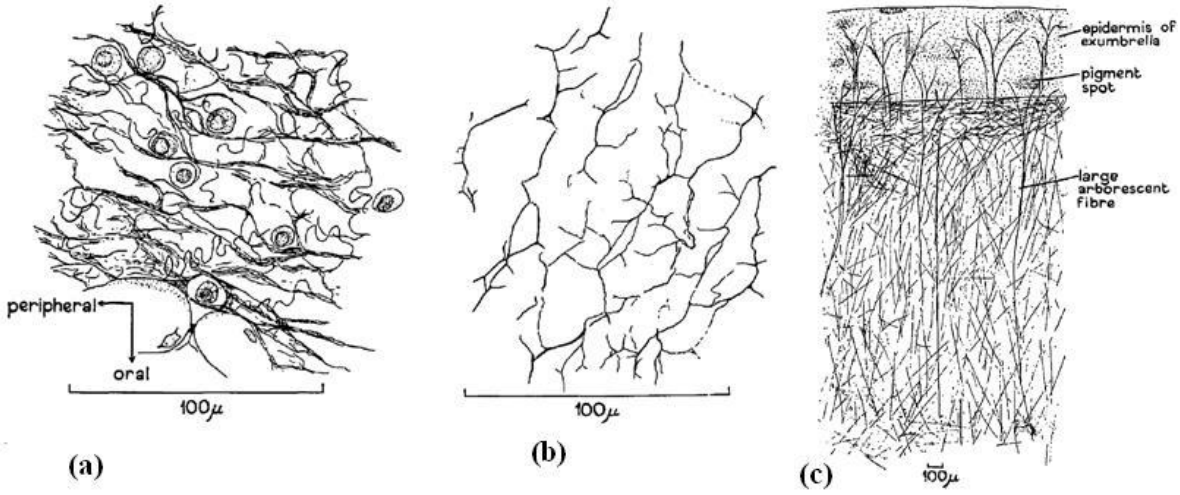

Figure 3-3. Histological observation of mesoglea of (a*) Aurelia* (b) *Cyanea* (c) *Chrysoara*(Chapman,1953a)

These motley arrangements of collagen fiber networks give rise to varying stiffness both in magnitude and in orthogonality. This makes attaching any accurate quantitative value to jellyfish mesoglea quite difficult. Megill et. al. (Megill,2005) reports the mesoglea elastic modulus to be higher in tension than in compression. For hydromedusa, *Polyorchis Pennicilatus,* average mesoglea elastic modulus was found to be $E_m = 344 \pm 52Pa$. In tension, the mesoglea is stiffer $E_T = 974 \pm 162Pa$ and in compression it is more compliant $E_C = 130 \pm 11Pa$.

3.3 Collagen properties

Collagen fibers are mainly responsible for providing structure and stiffness to the mesoglea. Knowing elastic properties of the collagen is vital towards knowing the elastic properties of mesoglea. Inside mesoglea, collagen fibers are usually found to be oriented from exumbrella towards gastrodermis direction. They are oriented radially near the exumbrella and gastrodermis. Their density is low in mid-bell section but quite high near the exumbrella and gastrodermis. The density also varies along the circumference; higher along the adradii and interradii, but lower near the perradii. The mesoglea between the gastrodermis and subumbrella, called joint mesoglea, has much sparser and randomly oriented collagen fibers. This distribution causes the bell mesoglea to deform in polygonal shape as observed from the subumbrellar side and eases the bell deformation. Collagen density is also found to be approximately linear function of bell height (Megill,2005). They are of thicker diameter in the mesoglea, but towards exumbrella and gastrodermis they branch out into many finer fibers that intertwine with the epidermis and gastrodermis tissues to provide structural connection between the two surfaces.

Collagen fibers are made up of three long helical chains (α chains) of protein strands. They are quite capable of extension as helical chains and in mesoglea they are usually in their pre-tension state. Thus, in tension they store more strain energy and become stiffer giving

mesoglea higher stiffness due to its nonlinear stiffness function. During compression, they relax offering much less resistance. This non-linear stiffness is important because during the contraction bell thickens extending the fibers and thus storing the strain energy. Here initial lower stiffness is important to expel the water out of the bell with least effort by the muscles. Towards the end of contraction, stiffness increases and enough energy is stored in the fibers to relax the bell using this stored strain energy. Demont and Gosline (Demont,1988b) have experimented on the live animal while trying to maintain conditions as close to free swimming as possible. He studied the energy budget of jellyfish swimming by measuring pressure and bell volume variations precisely and calculated the total energy spent in contraction. The estimated energy stored in the collagen fiber strain was based on Gladfelter's work (Gladfelter,1972) and results showed that it is possible to store entire bell deformation energy in stretching of collagen fiber. In another work Demont and Gosline (Demont,1988a) also claimed that jellyfish swims at resonance frequency of the mesoglea (based on collagen fiber stiffness). Jellyfish swimming is adversely affected if temperatures are close to dissolution temperature of collagen (Rigby,1972). Rigby's conclusions contradict with Demont and Gosline's belief of jellyfish swimming at resonance based on collagen fiber stiffness. As temperature increases, collagen fiber stiffness decreases and thus swim frequency should decrease if jellyfish were to swim at resonance frequency. Figure 3-4 clearly suggests that collagen affects jellyfish swimming greatly.

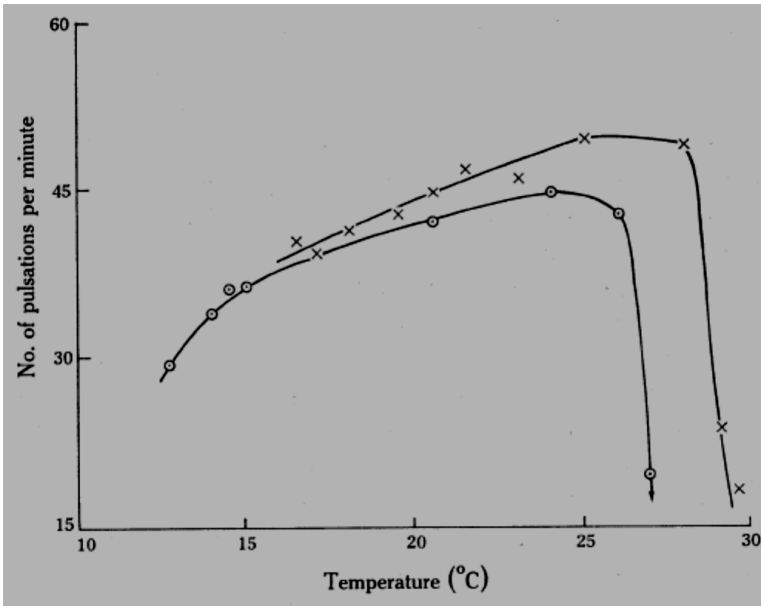

Figure 3-4. Pulsation frequency of jellyfish against temperature (x=first experiment, o=second experiment after overnight rest at 20C)(Rigby,1972)

Table 3-3. Aminoacids found in composition of collagen of different species(Chapman,1953a)

Amino-acid composition of coelenterate collagens						
	Calliactis	***Aurelia***	***Cyanea***	***Chrysaora***	***Rat tendon***	***Blood albumen***
Alanine	++++	+++	++++	+++	+++	+++
Glutamic Acid	++++	++	++	+++	++	++++
Glycine	++++	+++	+++	++++	++++	++++
Histidine	++	+	? +	? +	?	+++
Leucine	+++	+++	+++	+++	+++	+++
Lycine	++	++	+	++	++	++
Proline and hydroxy-proline	++	++	++	+++	+++	?
Serine	+	+	? +	+	?	++
Valine	++	+++	+++	++	++++	++
						3 additional-aminoacids

Collagen stiffness also depends on the types of amino-acids present in the structure and fiber diameter. Jellyfish mesoglea is reported to have collagen type IV fibers. Table 3-3 shows different aminoacids that form collagen of different species. Collagen is a basic protein found in all animal and Zhang et. al. (Zhang,2007) claim that evolution of species can be traced out by studying their collagen composition.

3.3.1 Mechanical properties of collagen fibers

Nagai et al. (Nagai,1999) have reported that the elastic modulus of partially digested jellyfish collagen is on the order of 100Pa. Roeder et al. (Roeder,2002) have reported that the extracellular matrix of collagen type I has elastic modulus of 5-25KPa. Megill et.al. (Megill,2005) estimate the elastic modulus of jellyfish fiber to be ~0.9MPa. Wenger et. al. (Wenger,2007) in their very careful experiment using nano-indentation technique reported that collagen from rat tail has elastic modulus of 5-11.5GPa. Modulus of collagen fiber is thus reported to vary by 10 orders of magnitude. This obviously raises question even if we consider collagen to be made up of different amino-acids. Nagai et al.'s results were obviously affected by partial digestion and should not be regarded to represent true value. Roeder et al. measured property of extra-celluar matrix (mesoglea) without isolating the collagen fibers from it, thus his values are more or less in tune with mesoglea elastic modulus. Megill et.al. based on Demont and Gosline's (Demont,1988b) estimation of strain energy reported more representative value for the modulus (Note that this estimate is still of collagen in the form of helical spring). Wenger et. al. however with their precise experiment seem to be measuring the elastic modulus of collagen material itself and thus reports much higher value. If we use analogy, Megill et. al. report spring stiffness while Wenger et. al. report stiffness of spring material (e.g., iron stiffness).

3.4 Muscle and nerve nets

Jellyfish possess only a single layer of muscle sheet just below the subumbrellar epithelial layer. However, in some species, this muscle layers develop folds to increase the surface area (Gladfelter,1973). These muscles are striated in the direction parallel to the circumference. In general, it has two kinds of muscles: circular/ coronal muscles that are usually associated with the rhythmic swimming contraction, and the radial muscles usually found in subumbrellar margin and around manubrium. A third kind of muscles – a variation of coronal muscles – that pass over radially oriented fold of joint mesoglea also can be observed in some species. These segmented coronal muscles, due to folding over very compliant joint mesoglea, act as if sections separated by the fold were hinged together. In circular muscles, contraction wave travel symmetrically throughout the bell. While radial muscles are believed to impart asymmetric contractions; they affect the turning behavior and prey capture. Their contraction is not rhythmic but event based and is triggered by usually prey touching the tentacles. A series of articles on "The nerves and muscles of medusa" by Horridge (Horridge,1954, Horridge,1955a, Horridge,1955b, Horridge,1955c, Horridge,1956, Horridge,1959) forms major portion of discussion in this section. Results are also included from the pioneering studies of Satterlie (Satterlie,2008, Satterlie,2011) and Gladfelter (Gladfelter,1972, Gladfelter,1973). The literature covers wide variety of jellyfish speices, thus to avoid confusion, only summary of general swimming system is presented.

The contraction behavior is initiated at a certain location in the form of excitation through a conduction system called nervenets. Nerve fibers are intertwined with muscle layer and excite mechanical contraction as excitation impulse pass through them. Corresponding to these two separated contraction behaviors that happen simultaneously, there are two separate nerve nets

that can be identified because unlike nerve nets of vertebrate and higher order animal, jellyfish nerve nets also cannot carry information of two separate excitations in same system simultaneously.

3.4.1 Swimming contraction: giant fiber nerve net and circular muscles

The nerve net responsible for main swimming contraction is called giant fiber nerve net (GFNN) and is mainly composed of bipolar neurons (Passano,1973). Conduction of excitation impulses in this nerve net is reported to travel at about 50cm/s rate (Horridge,1954). Contraction wave in the circular muscle follows the travel of impulse with some delay. The contraction in muscle travels at same speed in all direction simultaneously and irrespective of muscle orientation. The contraction also travels through areas not having muscles but at much slower rate. The contraction of circular muscles is not maintained though, and it doesn't have antagonistic counterpart to relax it. GFNN is spread uniformly throughout the bell, excitation of any part of the bell causes contraction wave to spread throughout the bell. Excitation would spread everywhere with equal speed as long as a single nerve fiber is present in the specimen. Each single excitation causes one swimming beat if sufficiently apart in time.

3.4.2 Manubrium and tentacle contraction: diffused nerve net and radial muscles

The other nerve net responsible for tentacle contraction and motion of manubrium is called diffused nerve net (DNN)(Horridge,1956). It is made up of a complex network of multipolar axons(Horridge,1959). It is radially oriented, that is, if radial cut severs the nerve connections, excitation cannot find another path across it. Excitation in this nerve net travels at about half the speed than that of GFNN. This nerve net is responsible for contraction of radial muscles found in margin of the bell, tentacles and in manubrium. On even gentle touching of bell

edges near tentacle causes excitation to travel across the bell and manubrium mouth to move and touch at the point of origin of excitation at the bell edge. This motion is very precise and rapid and it is believed that jellyfish uses this motion for prey capture. This may purely be reflex response. Excitation on two locations on bell edge simultaneously causes manubrium to touch exactly in between the two places(Horridge,1955a). Excitation in any tentacle causes it to contract and move inwards towards the center of the bell. This excitation also travels across the bell periphery through the ring nerves and induces contraction in all other tentacles simultaneously (Horridge,1956). Radial muscles do have antagonistic pairs; their contraction is rapid that can be sustained for longer time. The contraction of tentacle or manubrium motion is not affected by travel of contraction wave. However, excitation of tentacle as it travels through the ring nerve affects rhopalia and causes acceleration of swimming contraction. Thus radial conduction system can affect circular conduction system unilaterally(Horridge,1956).

3.4.3 Refractory period

Once excitation travels through the nerve system, it takes some time before it can respond to another excitation. This latency period is called “refractory period”. Muscles also have similar refractory period although muscle refractory period is larger than nerve system refractory period. Due to this, when on a rectangular specimen of muscle sheet one end A is excited, the contraction wave reaches the opposite end B, and another excitation is applied at B after waiting for refractory period of nerves but less than refractory period of muscle contraction, we may see one contraction wave at B but two contraction wave at A (Horridge,1955c). The reason being nerve system capable of carrying excitation travels over to the side A where muscles have had enough time to come out of refractory period and on seeing another excitation they contract again.

3.5 Swimming mechanism

Swimming beat is initiated by any one of the eight rhopalia located in the margin of the bell near the end of perradius and interradius. Each rhopalium is perfectly capable of inducing contraction wave, but the one that fires first spreads the excitation around nerve ring and resets all other rhopalia (Satterlie,2002). The contraction wave is induced in circular muscles and they contract symmetrically. Due to contraction, bell is stretched in thickness direction, this causes tension in collagen fibers and stores strain energy. At the end of contraction stroke, collagen fiber works against contraction and relaxes the bell to bring it to its relaxed state. Tentacles fire nematocyst on encountering prey, injecting it with venom to cause temporary disability. Tentacles contract and move towards center of the bell radially after which manubrium moves and grabs the prey. All this happens without getting disturbed by swimming contractions. Swim contractions gets accelerated as tentacle contracts.

For turning, tentacle contraction occurs on the side jellyfish is turning. It is believed that marginal radial muscles contract and in the section of the bell wedge in which the tentacle contraction is initiated, bell stiffens (Horridge,1955b). The contraction is sustained longer and the section doesn't open completely on relaxation with each swimming beat. The other section of the bell maintains its regular contraction, causing imbalance of force and generates turning moment. It may be noted that contraction wave of circular muscle is still symmetric. Turning behavior is still not very well understood and there are different opinions amongst researchers.

3.6 Summary

To develop basic understanding of jellyfish swimming, its building blocks – mesoglea, collagen, muscles and nerve nets, were reviewed. Mesoglea is highly viscoelastic material, with stiffness in range of a few hundreds of pascals to few kilopascals depending upon the jellyfish

species. Mesoglea is made up of mucopolysaccharide hydrogel matrix with collagen fibers forming network to provide structure to jellyfish. Collagen fibers are made up of 3 helical α chains of aminoacids. Helical spring structure is responsible for providing mesoglea its elasticity. It stores strain energy during contraction stroke and releases gradually to bring the bell back to its relaxed state.

Rhythmic contraction of circular muscles is responsible for regular swimming. These striated muscles are just one cell layer thick located just below the subumbrellar epithelium. Contraction is initiated by one of the eight rhopalia located at the edge of the bell in perradii and interradii direction. First rhopalium fired inhibits other rhopalia's for some "refractory" time. The excitation travels through giant fiber nerve net covering entire muscle layer. On excitation, circular muscle contract; contraction wave travels symmetrically at 50cm/s speed, causing mesoglea at the center of the bell to thicken stretching collagen fibers that store strain energy. After contraction stroke, stored energy in collagen fibers is used to bring the bell back to its relaxed state.

Knowing jellyfish component and how they work together, provides a strong basis for mimicking some of the material and mechanism of jellyfish swimming, while sprouting many other ideas on how to make bio-inspired jellyfish vehicles swim.

Chapter 4. Understanding the muscle architecture of jellyfish for artificial jellyfish vehicle

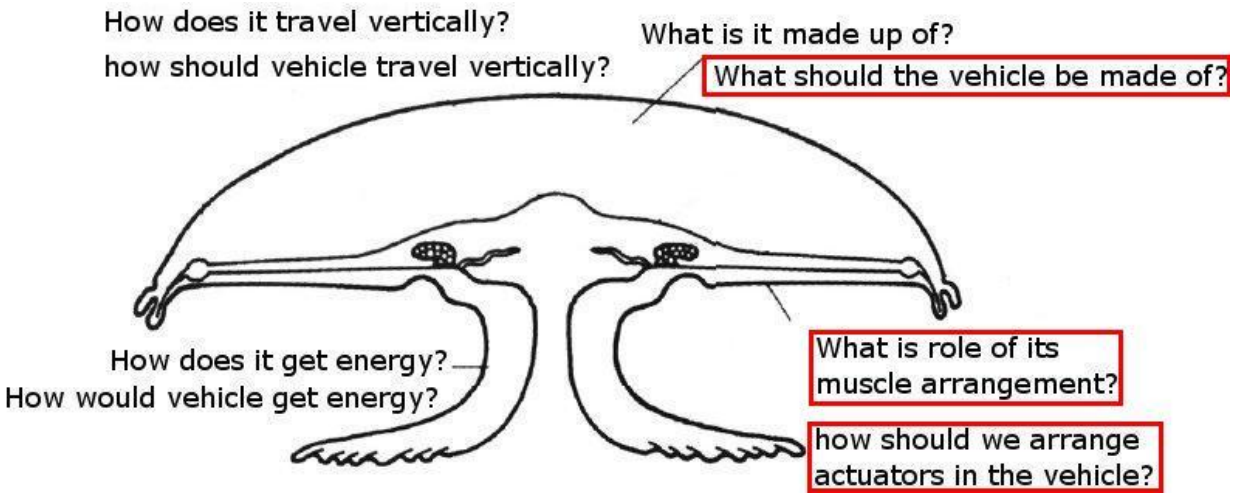

Figure 4-1. Research objective of chapter 4

In this chapter, the goal is to understand how one can approximate jellyfish architecture: its body (mesoglea) and its actuation mechanisms (muscle arrangements) to create an artificial jellyfish vehicle. Since artificial vehicle may be larger than the natural animal to accommodate different sensors and transmission equipment, a large jellyfish *Cyanea capillata* that can grow up to 2 meters in diameter was chosen as a model system. Three different muscle architectures are found in *C. capillata* : circular/coronal muscles, coronal muscles with folds and radial muscles. These muscle arrangements were approximated by shape memory alloy (SMA) wires, BISMAC arranged circumferentially with gap in metallic strip and BISMAC arranged radially respectively. A finite element model was built for comparing deformations achieved by each of the three kinds of muscle architecture and also to study the effectiveness of the circular muscles based on their location.

4.1 Inspiration

In general, jellyfish usually have dimensions ranging from a few millimeters to a few tens of centimeters. However, any practical underwater surveillance vehicle with all the necessary

sensory and communication equipment's would tend to be larger. *Cyanea capillata* growing up to 2 meters in diameter forms an ideal model system for developing artificial vehicle. To understand its swimming mechanism, it is necessary to understand its muscle arrangement. In this animal, however, the muscle arrangement is a little different. Compared to regular scyphozoan species where radial muscles mostly impart asymmetric contraction and do not take part in regular swimming contractions, in *Cyanea*, they do take part in regular swimming (Gladfelter,1973) and do not have antagonistic pair to relax them. Since, no specific details about its nervous system arrangement is available, it was left out of the discussion in the previous chapter. Modeling actual jellyfish is still very difficult due to highly complex nature of mesoglea, its functionally graded properties, viscoelastic nature, being too compliant and dimensions on the order of a single cell layer of muscle sheet. Thus to understand the relative performance of different muscle architecture and to understand their possible role in swimming, it was desirable to model it in terms of more approachable engineering approximations that can be implemented through finite element method.

4.2 Muscle architecture in *Cyanea* jellyfish

Gladfelter (Gladfelter,1973) has described the locomotary system of *Cyanea*. Figure 4-2 shows the bottom view of the animal. Here three distinct zones can be easily identified. Around the central disk, just centrifugal to the coronal joint, circular muscle rings are arranged concentric with the center of the bell and are parallel to each other.

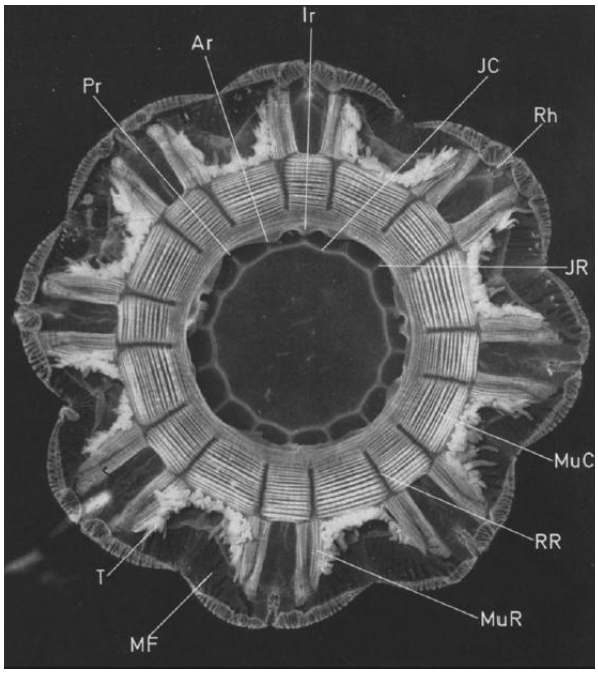

Figure 4-2. ***Cyanea capillata*** **bottom view showing its muscle arrangement (Pr-perradius, Ir-interradius, Ar-adradius, JC-coronal joint, Rh-Rhopalium, JR-radial joint, MuC-coronal muscle, MuR-raidal muscle, RR-radial ridge (septum), MF-marginal flap, T-tentacle)(Gladfelter,1973)**

Around them, there are other set of circular (coronal) muscles that seem segmented radially by the 16 folds in mesoglea. These are termed as segmented circular (coronal) muscles to distinguish them from the previous zone. Note that Gladfelter did not distinguish between these two muscles, but due to folds, which are filled with highly compliant joint mesoglea, they are functionally different from the circular muscles due to fold in between that acts as a hinge. The third sets of muscles are radial muscles that are arranged in 8 pairs along perradii and interradii. Radial muscle fibers are longer towards the perradius/interradius side and gradually shorten as we move towards adradius. All fibers begin at the base where segmented circular muscle zone ends and extends radially outwards, thus this muscle zone makes a triangular shaped pattern. Beyond radial muscle zone there is marginal flap that is devoid of muscles and is considered as passive portion of mesoglea.

4.3 Engineering approximation to the muscle architecture

Due to the difficulties mentioned in prior section, these three muscle architectures were modeled by including engineering approximations as shown in Figure 4-3. Circular muscles are approximated by shape memory alloy (SMA) wires arranged radially. SMA wire undergoes ~4-6% contraction upon heating as it changes its phase from martensite to austenite. In the process, they decrease the circumference of the bell at that location, thus creating effect similar to circular muscle contraction.

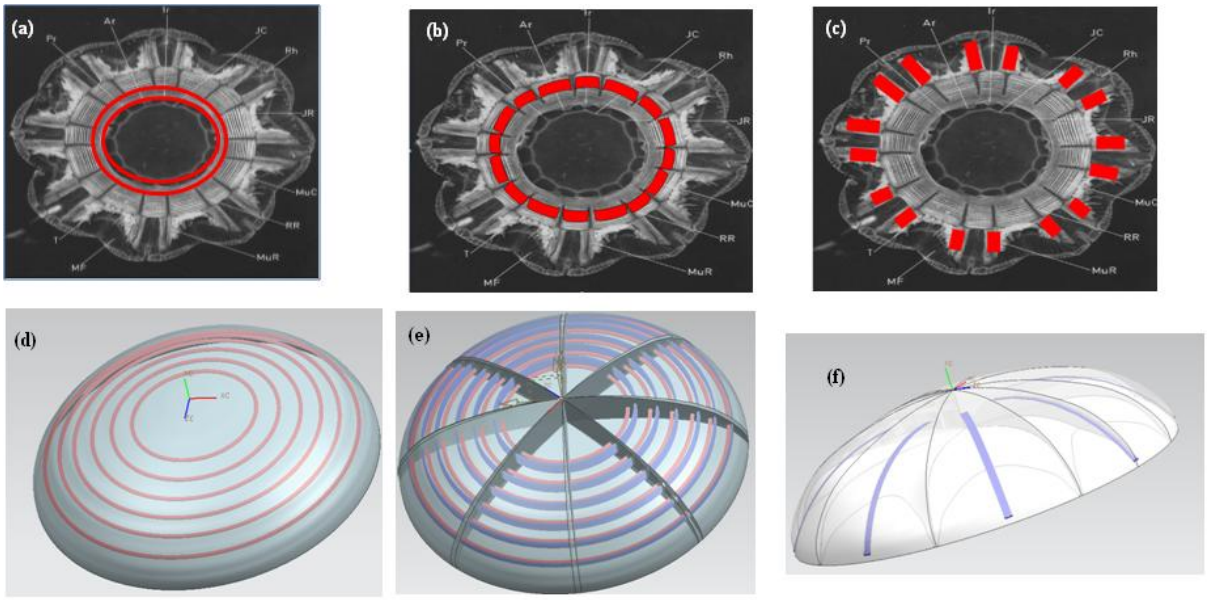

Figure 4-3. Engineering approximation to *Cyanea* muscle architecture (a-c) circular muscles, segmented circular muscles, radial muscles respectively (d-f) circular rings of SMA wires, ciecumferentially arranged BISMAC and radially arranged BISMAC respectively

Segmented circular muscles are approximated by circumferentially arranged BISMAC (Bio-inspired shape memory alloy composite) that were invented by Villanueva et. al. (Villanueva,2010b). BISMAC converts small axial deformation of SMA wires into large flexural deformation with help of a special structural arrangement of SMA wires and a flexible metal strip embedded into a highly compliant silicone matrix. To simulate the continuity of circular muscles across the fold with hinge effect due to highly compliant joint mesoglea, we kept the

active element SMA wires in continuous rings, but provided breaks in metal strip running parallel to it a little outward in circumferentially arranged BISMAC.

Radial muscles were approximated by radially arranged BISMAC capable of providing large flexion comparable to that of *Cyanea* radial muscles. They were arranged in 8 bell segments similar to *Cyanea* and modeled by a single BISMAC located at perradii and interradii location instead of a pair of triangular regions of radial muscle fibers of varying length (Figure 4-2).

4.4 Finite element modeling

4.4.1 Circular muscles modeling

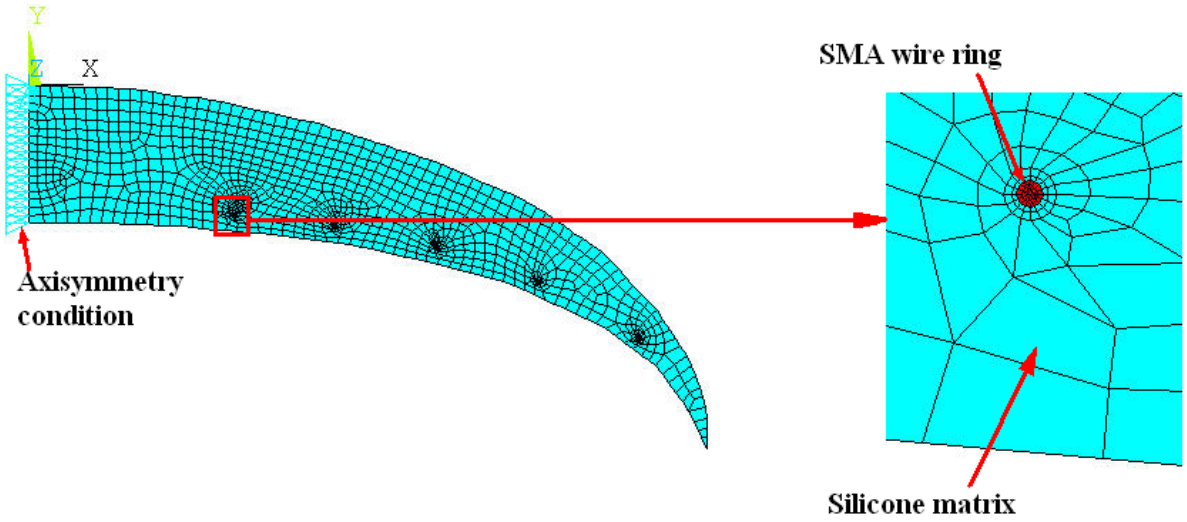

Figure 4-4. Circular muscle mesh and boundary condition

As shown in Figure 4-4, the model for jellyfish bell with circular muscles is essentially an axi-symmetric model. The SMA wire ring was modeled as a circle of area equal to gross area of four 100 micron diameter SMA wires located at 30% location radially, which is nominal location of circular muscles in *Cyanea*. The rest of the bell was made up of artificial mesoglea (silicone) matrix. The axi-symmetric boundary condition was applied at the bell axis. One point at the top of the bell was fixed in y-direction to provide proper fixity of vertical displacements. The elements used were PLANE42 element with axi-symmetric option. The loading in the model was applied temperature $140°C$ (beyond SMA transformation temperature) as body load to SMA

nodes. For properties of SMA and silicone matrix, please refer to Chapter 7 (also (Joshi,2011a)). SMA wire and a couple of elements around it were meshed with fine elements. Rest of the bell was meshed with coarse free area mesh. The profile was taken from *Aurelia aurita* bell scaled to diameter of 82.25mm.

4.4.2 Segmented circular muscles modeling

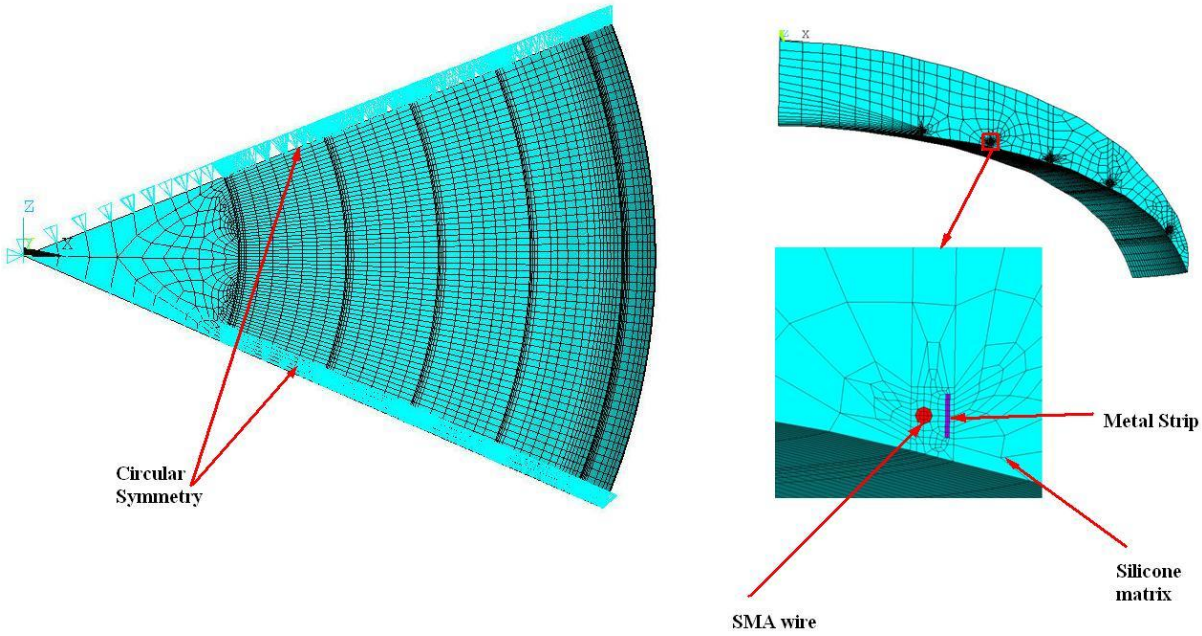

Figure 4-5. Segmented circular muscle mesh and boundary condition

As shown in Figure 4-5, the jellyfish bell with segmented circular muscles was circular symmetric, but not axi-symmetric. The axi-symmetry is broken by the radial folds that act as hinge between the adjacent segments of the muscle ring. The SMA wire ring was modeled as a circle of area corresponding to gross cross sectional area of four 100 micron diameter SMA wires, just as in circular muscles. In addition, thin flexible metal strip ring was also placed parallel to the SMA wire at a small distance. The metal strip has 1° break at both the ends, spanning a total 43° angle. The bell section modeled was $1/8^{th}$ of the bell or 45°. The rest of the bell was made up of artificial mesoglea (silicone) matrix. The elements used were SOLID 185 elements. The circular symmetry was applied on the sides of bell section and one point at the top

of the bell was fixed to obtain necessary fixity on displacements in axial and tangential directions. The loading in the model was temperature applied $140°C$ (beyond SMA transformation temperature) as body load to SMA nodes. The mesh for SMA wire, metal strip and section around them were meshed with fine elements. The rest of the bell was meshed such that overall model size was manageable. Also, as there are a number of segmented circular muscles in the *Cyanea*, five similar segmented circumferential muscle rings were included to understand the effect of location of the segmented circular muscle. The profile was taken from *Aurelia aurita* bell scaled to diameter of 82.25mm.

4.4.3 Radial muscles modeling

Radial muscles have been discussed at length in Chapter 7. Hence to avoid repetition it is not presented here.

4.5 Results

4.5.1 Bell deformation due to circular muscles

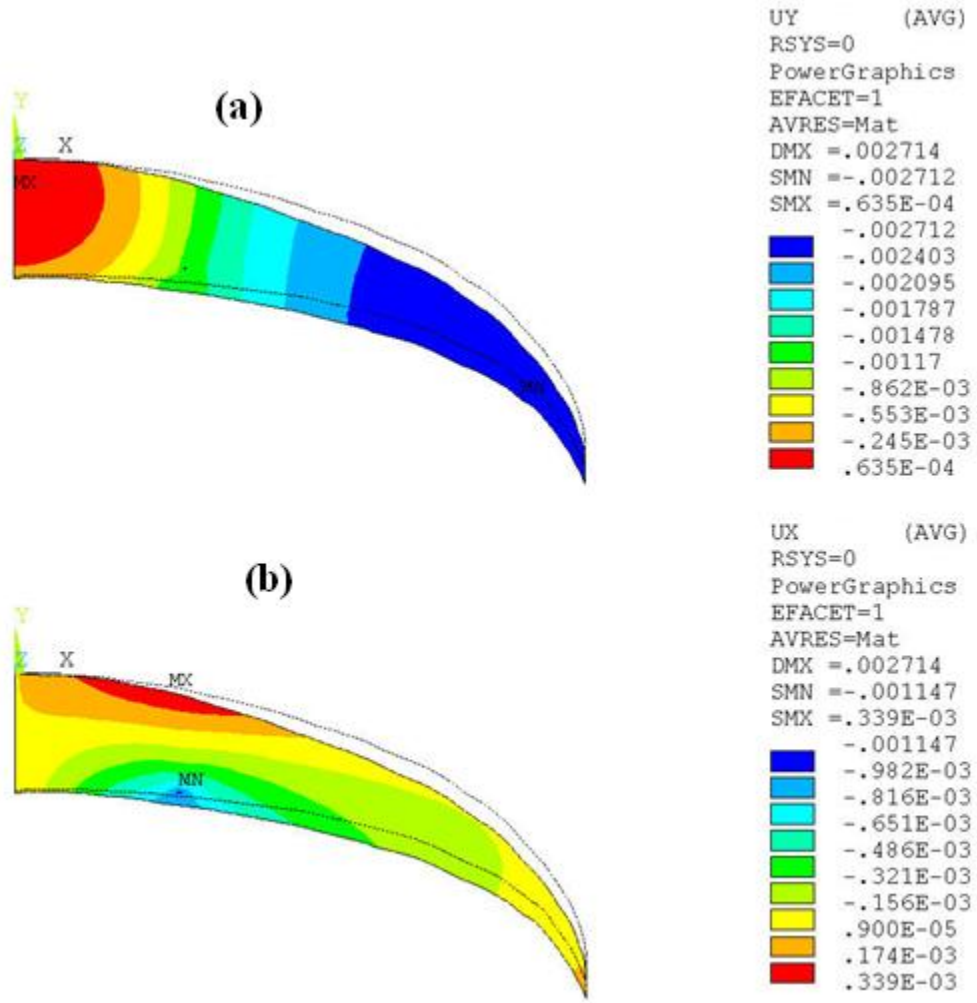

Figure 4-6. Deformation due to circular muscle ring (a) in axial direction and (b) in radial direction

The result of the simulation of circular muscle ring contraction is displayed in Figure 4-6. The edge of the bell moves axially downward (UY=2.71mm) by a small amount and moves even lesser radially (UX=1.11mm) inwards. But it induces a great compression in the central bell.

4.5.2 Bell deformation due to segmented circular muscles

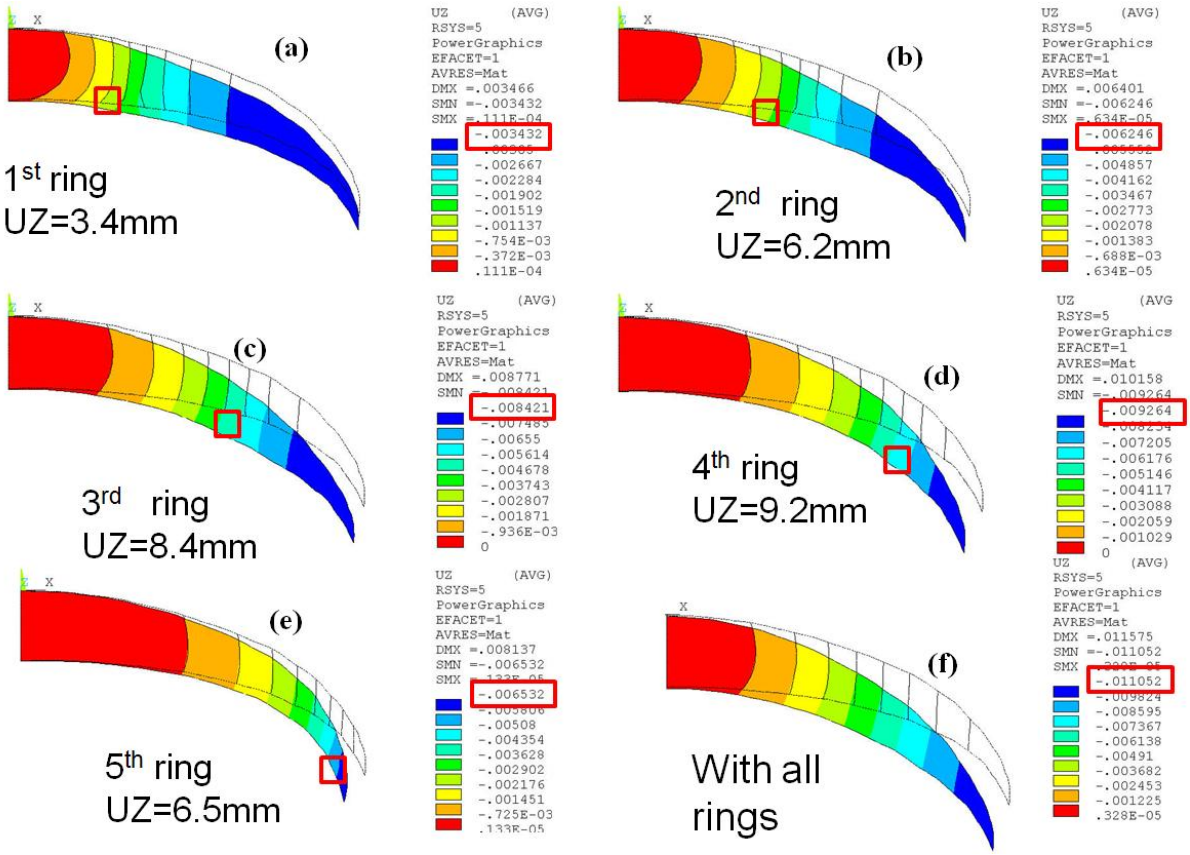

Figure 4-7. Bell deformation with segmented circular muscles

Segmented circular muscles are mainly responsible for axial deformation of the bell as seen in the cross-sectional view through the middle of the muscle segment in Figure 4-7. However, we can make another interesting observation that the deformation of the bell does depend greatly on the location of the muscle ring. Figure 4-8(a) shows deformation by actuation of each individual ring located at radial location normalized by the bell radius. Fourth ring achieved 83.80% of the total axial deformation UY obtained by actuation of all five rings simultaneously. If one further normalizes the displacement by the length of SMA wire used, then as shown in Figure 4-8(b), the most effective muscle ring location is 3rd ring. Same information can also be obtained from Figure 4-8(c) that shows measure of effectiveness,

$$Effectiveness\ (r) = \frac{UY\ by\ a\ ring\ at\ \ r}{UY\ by\ all\ muscle\ 5\ ring} * \frac{SMA\ length\ used\ at\ location\ r}{SMA\ length\ used\ by\ all\ 5\ rings}$$

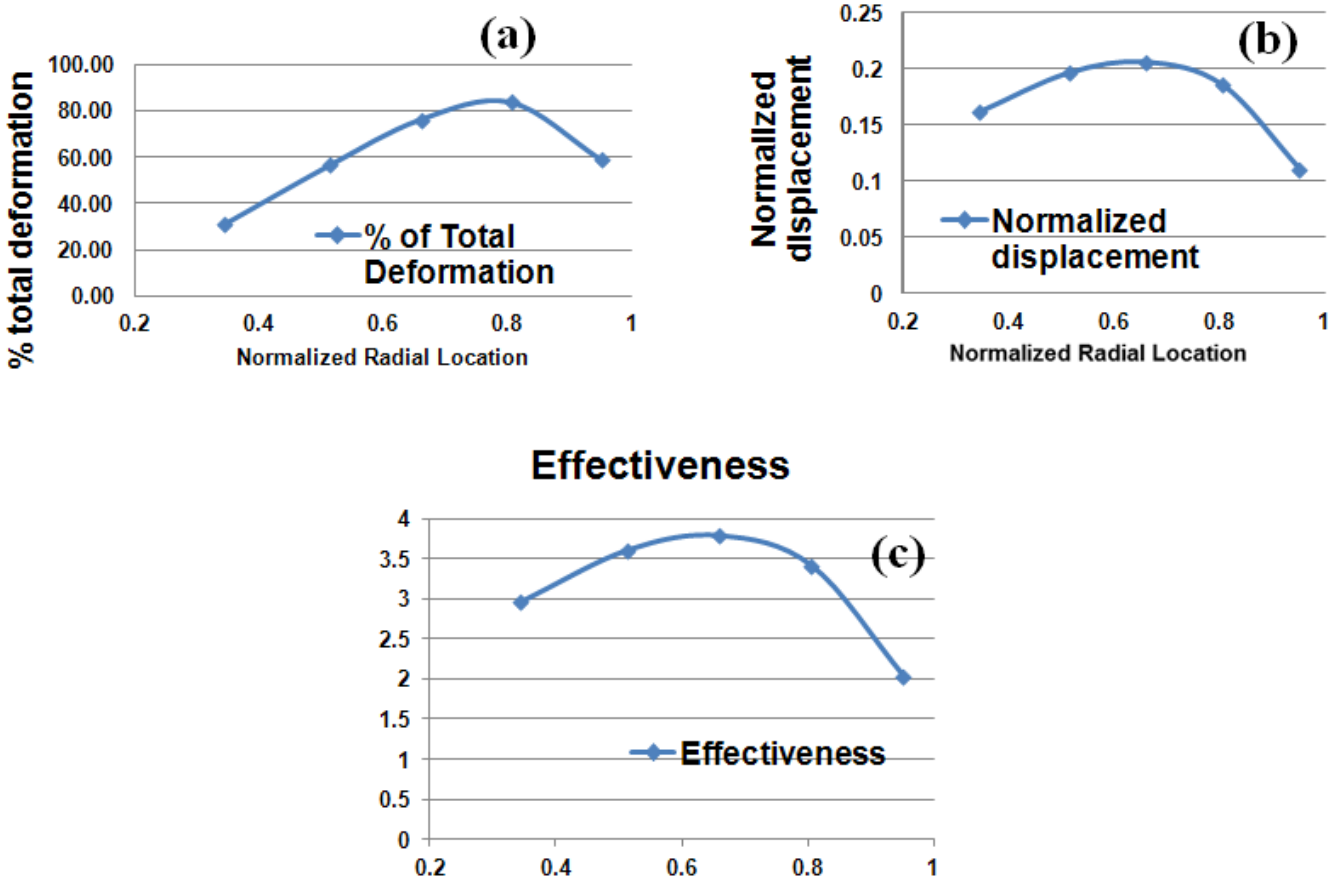

Figure 4-8. Tip axial displacement with segmented circumferential muscle ring (a) total deformation as % of total deformation obtained by all 5 rings (b) displacement normalized by total displacement by all 5 rings and (c) effectiveness.

We can conclude that there is a certain radial location where segmented circumferential muscles are most effective in creating axial deformation. It can be interpreted that for *Cyanea* bell geometry segmented circumferential muscles are located such that they would be most effective. From this study, the optimum radial location was found to at 66%. In *Cyanea* we observe that segmented circumferential muscles are located between 35-60% of bell radius.

4.5.3 Bell deformation due to radial muscles

Radial muscles are responsible for majority of the bell deformation. They impart axial as well as radial deformation as seen in Figure 4-9. In radial direction the deformation was found to be $UX = 13.95mm$ and in axial direction the displacement was $UZ = 7.7mm$.

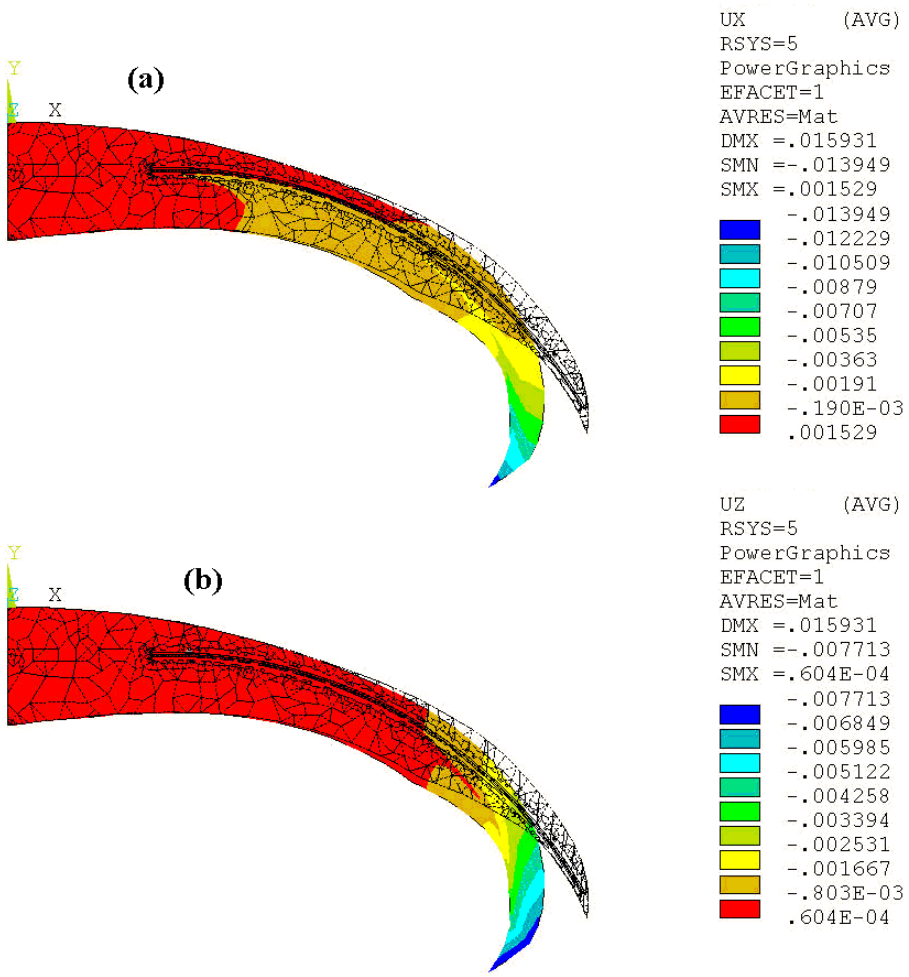

Figure 4-9. Bell deformation due to radial muscles (a) in radial direction and (b) in axial direction

4.6 Summary

Through finite element study, it was shown that the muscle architectures found in *Cyanea* play very different roles in creating bell deformation. Circular muscles closest to the bell center do not contribute much to the overall bell deformation. But, they compress the center of the bell and bring the bell in strained state - ready to deform. Segmented circumferential muscles deform the bell more axially than radially; also there is an optimum location where these muscles are most effective. It is hypothesized that *Cyanea* has its segmented circumferential muscles placed at ideal location where it can be most effective in imparting bell deformation. Radial muscles

perform majority of bell deformation, they contribute in both axial as well as radial deformation. But radial deformation is mostly due to contribution of radial muscles.

Chapter 5. Modeling of energy system for the artificial jellyfish vehicle

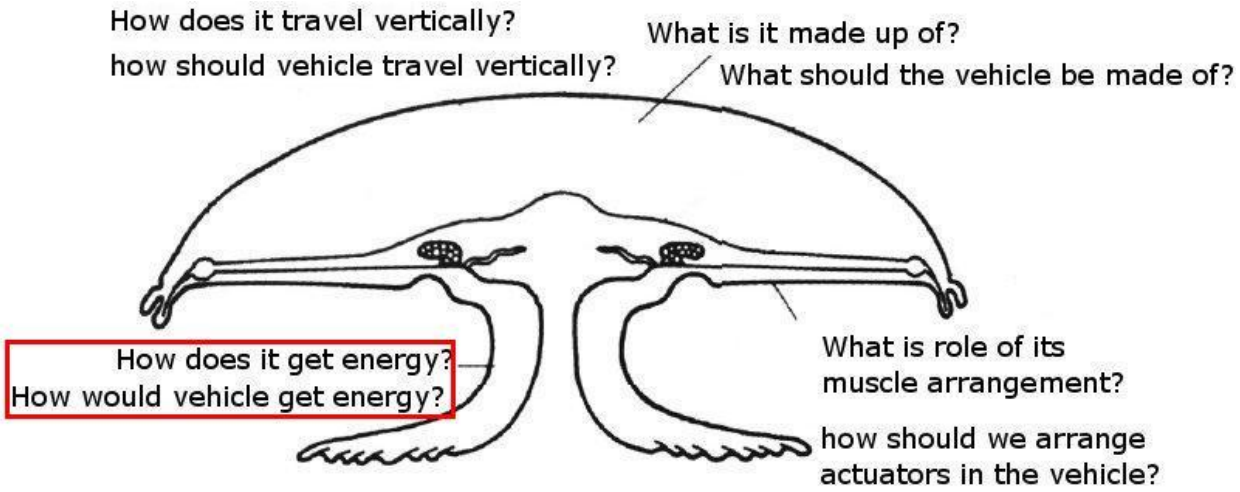

Figure 5-1. Research objective of chapter 5

This chapter is dedicated to understanding how jellyfish meets its energy needs and more importantly how bio-inspired jellyfish vehicle can meet its energy needs.

Natural jellyfish consumes organic food, and its energy consumption can be measured in Biological Oxygen Demand (BOD) and knowing the calorific value of the organic source of energy, in case of jellyfish polysaccharides, we can calculate energy consumption of the animal. While attempting to mimic organic food capture and its digestion for meeting energy need of the jellyfish vehicle may be very interesting, the technology to do so are still in very primitive states. Filtering food particles from the flow efficiently could be difficult task. And digesting the food to store energy in chemical form may be another challenge. Sundaresan (Sundaresan,2007) has developed a protein pump using ATP-power. But the efficiency numbers are far from being practical. Microbial fuel cell technology also generates power several order less compared to vehicle needs. Other sources of energy in ocean environment are very limited. Wave energy is a surface phenomenon and most efficient devices that can harvest wave energy require some kind of tethering to the floor or sea-shore, which is not very practical for a swimming vehicle. Wind energy is not accessible to underwater vehicle.

Solar energy is available in ocean at least for a few hundreds of meters; about the depths most jellyfish are found. Thus it was desired to explore prospective of underwater solar energy harvesting. The first part of the chapter deals with model for harvesting of solar energy for underwater jellyfish vehicles.

The next part of the chapter intends to increase utilization factor of available energy by converting part of the thermal energy discarded into the ocean by actuators and on-board electronics. A multi-physics model for a thermo-magnetic beam vibration is provided. The model currently just estimates vibration frequencies, transient and steady state behavior and heat transfer. It also tries to explore effect of various parameters on the physics of vibration. Nonlinear behavior such as stable spiral, limit cycle and limit cycle bifurcation are observed. Electrical energy harvesting through piezoelectric spring elements may be explored later.

Estimation of solar energy harvested for autonomous jellyfish vehicles (AJVs)[1]

There is significant interest in harvesting ocean energy for powering the autonomous vehicles that can conduct surveillance for long durations. In this study we analyze the applicability of solar cells as a power source for medusa-inspired biomimetic vehicles. Since these vehicles will be operating under ocean waters and may need to dive at various depths, a systematic investigation was conducted to determine the variation of output power as a function of depth and salinity levels. We modeled solar energy harvested by flexible amorphous solar cell coated jellyfish vehicles by considering the variables bell diameter, turbidity, depth and fineness ratio. Low fineness ratio shapes were found to be better for solar energy powered vehicles. Study of three representative species, *Aurelia aurita (AA), Mastigias* sp. and *Cyanea capillata* indicates that power harvested was proportional to bell diameter. Optimum power can be harvested by tilting the vehicle axis to face refracted sunrays. Depending on swimming pattern, power harvested in charging mode and in propulsion mode could vary significantly. The model indicates that, under some circumstances, amorphous silicon solar cell may be cost effective way to power AUVs operating in shallow water conditions with large lateral travel distances.

TERMS USED

I_0 Incidence radiation intensity

I_t transmitted radiation intensity

d depth from air-water interface

[1] © IEEE.Reprinted, with permission, from Joshi, K.B.; Costello, J.H.; Priya, S., "Estimation of Solar Energy Harvested for Autonomous Jellyfish Vehicles (AJVs), Oceanic Engineering, IEEE Journal of, October, 2011.

T	turbidity level (in ntu)
c_0, c_1, c_2	model coefficients
I_λ	radiation intensity of wavelength λ
$f(\lambda)$	Spectral distribution
I_a	radiation absorbed by photovoltaic cell material
u	extinction co-efficient of water
α	absorption co-efficient of cell material
r	reflection co-efficient of cell material
I_p	harvested power intensity
λ_g	Absorption edge
θ_{water}	Apparent zenith angle of the sun in water
θ_{air}	Actual zenith angle of the sun in air
n_{water}	Refractive index of water
n_{air}	Refractive index of air
I_{p0}	harvested power intensity at normal incident
$I_{p\theta}$	harvested power intensity at θ angle
A	Lateral area of frustum of cone
D	Bell diameter
P	Power harvested

5.1 Background

Unmanned Undersea Vehicles (UUVs) have been gaining importance for variety of civilian and defense applications such as sea exploration, surveillance, and remote monitoring of national borders. However, conventional on-board energy available for such vehicles restricts the size, tasks, lifetime and range of the vehicles. These vehicles tend to use more energy than the onboard batteries can supply. Thus, research has focused on enhancing the energy efficiency of these vehicles by combining more than one source of energy to satisfy the total power requirement. Solar, wave and thermal sources of ambient energy may be available for UUVs. Rudnick et al. (Rudnick,2004) have reviewed development and trends in powering underwater gliders. Some of the initial designs, like SOFAR(SOund Fixing And Ranging) (Webb,1977) in 1978, were just buoyancy controlled floats to accomplish vertical profiling at desired location in ocean. Several different glider designs have been developed in past decades before the development of ALACE (the Autonomous LAgrangian Circulation Explorer) and BOBBER (a generic type of floats made of cork like material) (Davis,1992) which introduced the concept of energy harvesting from thermoclines for propulsion. This concept was fully developed and employed in the SLOCUM (named after Joshua Slocum, first man to sail around the world) design by Webb et al. (Webb,2001). The SLOCUM gliders harvest propulsive energy from heat flow between vehicle engines and surrounding fluids using thermal gradient existing in temperate and tropical ocean waters. The heat is used to achieve solid-liquid transformation of the working fluid resulting in buoyancy control. Additionally, a clever design of wing converts roll motion into translation. Other popular form of propulsion uses fuel cell for their efficiency and compact size, making good use of abundant cooling water. Wang et al. (Wang,2007) proposed enhancing the Proton Exchange Membrane Fuel Cell (PEMFC) efficiency by using thermal engine of SLOCUM gliders. It was however noted that for thermal engine to work, a

minimum of 10°C temperature difference is required across ocean depths which is not available for a jellyfish vehicle. PEMFC may be an option but it suffers from poor efficiency if the heat generated in the process is not quickly removed and there are challenges in its implementation on the biomimetic vehicle.

An alternative means of energy acquisition that we explore here is the use of photovoltaic cells for conversion of the sunlight to the useful energy. A variety of cnidarian symbioses, notably corals, may meet large portions of their metabolic requirements via photosynthetic symbionts (Muscatine,1981). The ability of jellyfish to move to high-light environments can allow light energy to make important contributions to the jellyfish energetic demands. A variety of jellyfish species have evolved these capabilities ((Kremer,1990) and (Welch,2009)) and these animals provide a useful model for meeting the energetic demands of an autonomous vehicle.

5.2 Introduction

Villanueva et al. (Villanueva,2009) have recently developed JETSUM (name of the prototype) UUV inspired by jet-propelled type of jellyfish. At larger bell diameters, it is well-known now that the rowers exhibit better swimming efficiencies by taking advantage from interaction between counter rotating starting and stopping vortices (Colin,2002). The breakthrough in the Bio-Inspired Shape Memory Alloy Composite (BISMAC) (Villanueva,2010b) actuators opened the possibility of mimicking the rower jellyfish propulsion which relies on vortex generation. The BISMAC requires large electrical power to operate in the underwater conditions. To enhance the useful life of jellyfish node based on BISMAC actuators, it is desirable to explore energy harvesting from ambient underwater environment. Non-universal existence of thermal gradients in shallow water makes it difficult for use of thermal engines. Solar energy is available at shallow depths in the ocean and can be used to aid the battery life and to operate low power

sensor nodes. This is the motivation behind this study and we present results on evaluation of the solar cell in ocean environment quantifying the change in its performance with ocean depth and salinity level.

Dave (Dave,1978) modeled the effect of atmospheric condition on solar cell performance and numerically predicted the performance of $Ga_{1-x}Al_xAs$-GaAs solar cell. The model was based on terrestrial solar radiation at five different altitudes on average, cloud-free, mid-latitude summer conditions and incorporates absorption by CO_2, O_2, Ozone, water vapor and aerosols. Gonzalez and Carrol (Gonzalez,1994) studied solar cell efficiency variation with atmospheric conditions, especially turbidity and humidity, using SPCTRAL2 model for both mono-crystalline as well as amorphous silicon solar cell and reported increase in conversion efficiency with increase in humidity (especially in amorphous silicon) and decrease in turbidity level.

Stoddard and Incropera (Stoddard,1982) studied distribution of solar radiation in natural waters experimentally and reported that collimated beam of solar radiation, refracted from the air-water interface redistributes and strongly influences vertical distribution of available solar radiation. This phenomenon causes maximum irradiance to occur below air-water interface and is pronounced at 22.1° angle. Muaddi and Jamal (Muaddi,1992) presented a model for variation in solar radiation spectrum under water surface and predicted solar cell efficiency variation under water surface. They noted reduction in spectral width with depth and reported that relative efficiency of silicon solar cell increases with depth until specific point after which it reduces and becomes equal to surface efficiencies at depths of about 3.5 m. The increase in conversion efficiency was attributed to rapid reduction of long wavelength radiation and correspondingly the total available radiation energy with depth. The short wavelength radiation, including visible ranges that contribute to the cell current does not change as rapidly with depth. Wang and Seyed-

Yagoobi (Wang,1994) studied the effect of turbidity and salinity on penetration of solar radiation under water and concluded that salinity has no significant effect on transmittance of solar radiation in water, but turbidity tends to reduce the solar radiation available and has more pronounced effect with increase in depth. Gottschalg et. al. (Gottschalg,2003) studied the effect of variation in solar spectrum experimentally for thin film solar cells by taking large number of measurements over a period of 30 months covering seasonal changes and reported that amorphous silicon solar cell are most susceptible to the changes in the spectral distribution with useful fraction of light varying between +6% to -9% with maximum occurring in the summer.

Research has also been done in enhancing solar cell efficiency. Chen and Sun (Chen,2010) showed use of anti-reflective layer of PMMA(poly (methylmetacrylate)) on the poly-silicon solar cell improves the efficiency from 10.4% to 13.5%. Strümpel et. al. (Strümpel,2007) has presented overview of techniques to modify solar spectrum to achieve high efficiency solar cell by down-conversion (cutting one high energy photon into two low energy photons), photoluminescence (shifting photons into wavelength regions better accepted by the solar cell) and up-conversion (combining low energy photons to one high energy photon) and better materials to achieve these effects. Custodio et. al. (Custodio,2001) has reported improvement in conversion efficiency achieved by reducing operating temperature of the cell by employing infrared filters. In recent development, Yun et. al. (Yun,2009) achieved increased solar cell efficiency by using full solar spectrum with a new conjugated polymer-ZnSe-PbSe nanocrystal hybrid photovoltaic cell. All these developments indicate the promise of solar cell for powering autonomous jellyfish vehicles (AJVs).

5.3 Experimental setup

The experimental setup, as shown in Figure 5-2(a) consisted of an acrylic water tank with 200 mm nominal diameter and 1.676 m height. The solar cell and light sensor were mounted together on a flat platform as shown in Figure 5-2(b). The mounting was raised and lowered with a 20 mm nominal diameter aluminum elevator pipe attached to it along with the metal halide lamp. The light source, 400W metal halide lamp with a concentrating reflector, was placed directly above the water tank. The water used in these experiments was tap water available in the lab. CORALIFE® scientific grade marine salt was added manually to achieve different salinity levels and salinity measurements were done using an Instant Ocean hydrometer. The cables from light sensor and the solar cell were routed through the aluminum pipe to the Data Acquisition (DAQ) system attached to a laptop. NI-6211 DAQ card from National Instruments (NI) with 16bit Analog to Digital Converter (ADC) channels was used to obtain high resolution. The load resistor used across the cell terminal was fixed at 1kΩ. Figure 5-3(a) shows the electrical wiring diagram and Figure 5-3(b) displays the LabView sample program used for the automated measurements.

(a)

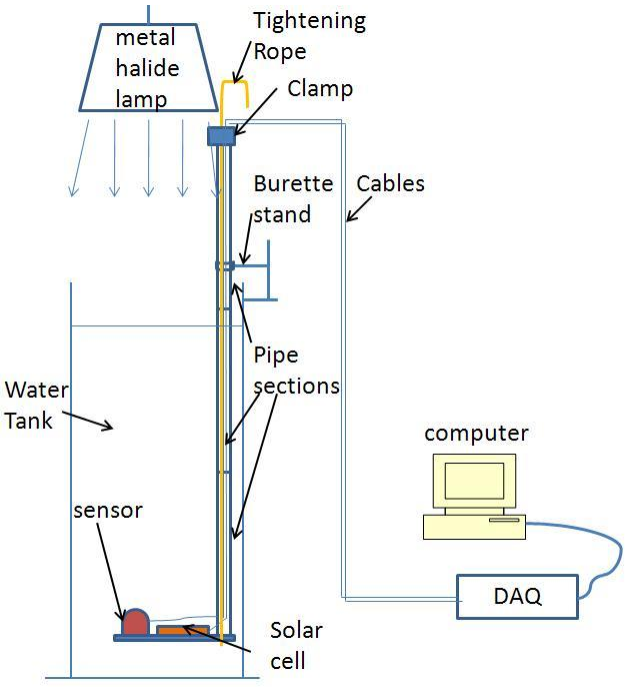

(b)

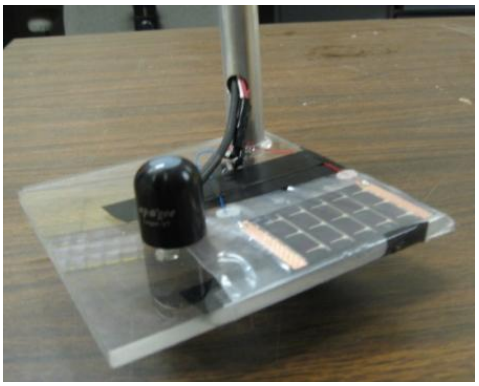

Figure 5-2. (a) Schematic of the experimental set-up, (b) quantum sensor and solar cell mounted on submersible platform.

(a)

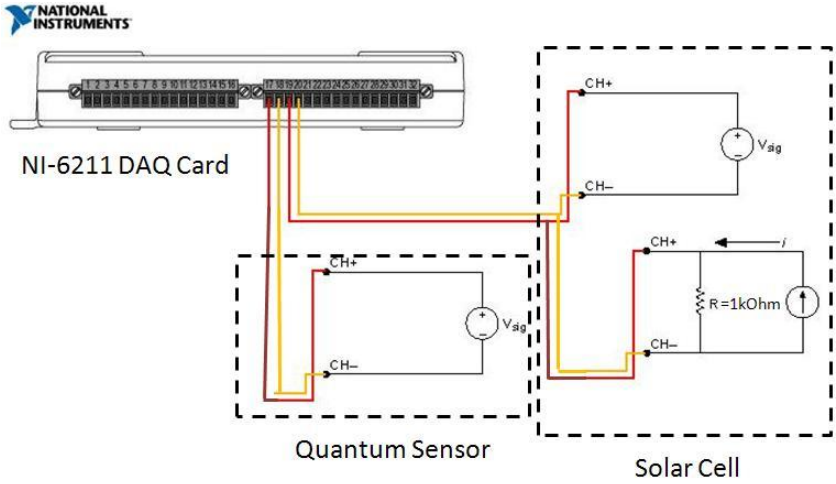

(b)

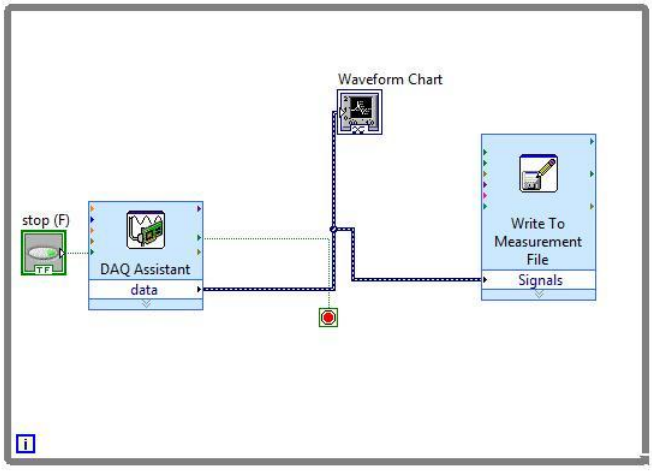

Figure 5-3. (a) Wire connection to the DAQ card, (b) VI file used for the experiment.

5.3.1 Choice of system components

The elevator pipe was made in segmented construction (resembling to blind man's cane), to add length as required without interfering with the metal halide lamp on top of the tank. The tension rope required to maintain platform level was routed from inside the pipe along with the electrical cables from the light sensor and the solar cell.

The solar cell was sealed water-proof with a polyethylene sheet and adhesive tapes. In the field, the solar cell will be placed just below the exumbrella (the external convex surface of the jellyfish body) of the jellyfish with a thin, transparent layer of silicone on top for waterproofing. Flexible amorphous silicon solar cell films, commercially available as PowerFilm®(http://www.powerfilmsolar.com), was chosen to meet the flexibility requirement imposed by continuous flexing of exumbrella during propulsion of the jellyfish. It also lends itself to being coated with a thin layer of Room Temperature Vulcanizing (RTV) silicone rubber for weather protection in underwater environment without significant drop in performance. The particular cell used for the test, SP3-37 (5x3.5cm2), is rated to provide 22mA output current at 3V.

SQ-110 quantum sensor from apogee instruments (http://www.apogeeinstruments.com) has the ability to measure the radiation intensities in the active spectral range of amorphous silicon and is suitable for use in underwater environment. Figure 5-4(a) shows the spectral response of the sensor in active range which also encompasses full spectrum of the metal halide lamp shown in Figure 5-4(b). The sensor measurement was calibrated for Photosynthetic Photon Flux (PPF) measurement, which can be converted into corresponding radiation intensity by multiplying the value with energy required to generate a photon at average wavelength and dividing by active sensor area. The light source, Cayman Sun 400W HQI System with a metal halide bulb has

capability of simulating 14K temperature. Thus, this system was chosen for its capability of simulating full sun spectrum up to 6m depth in water (http://www.hamiltontechnology.com).

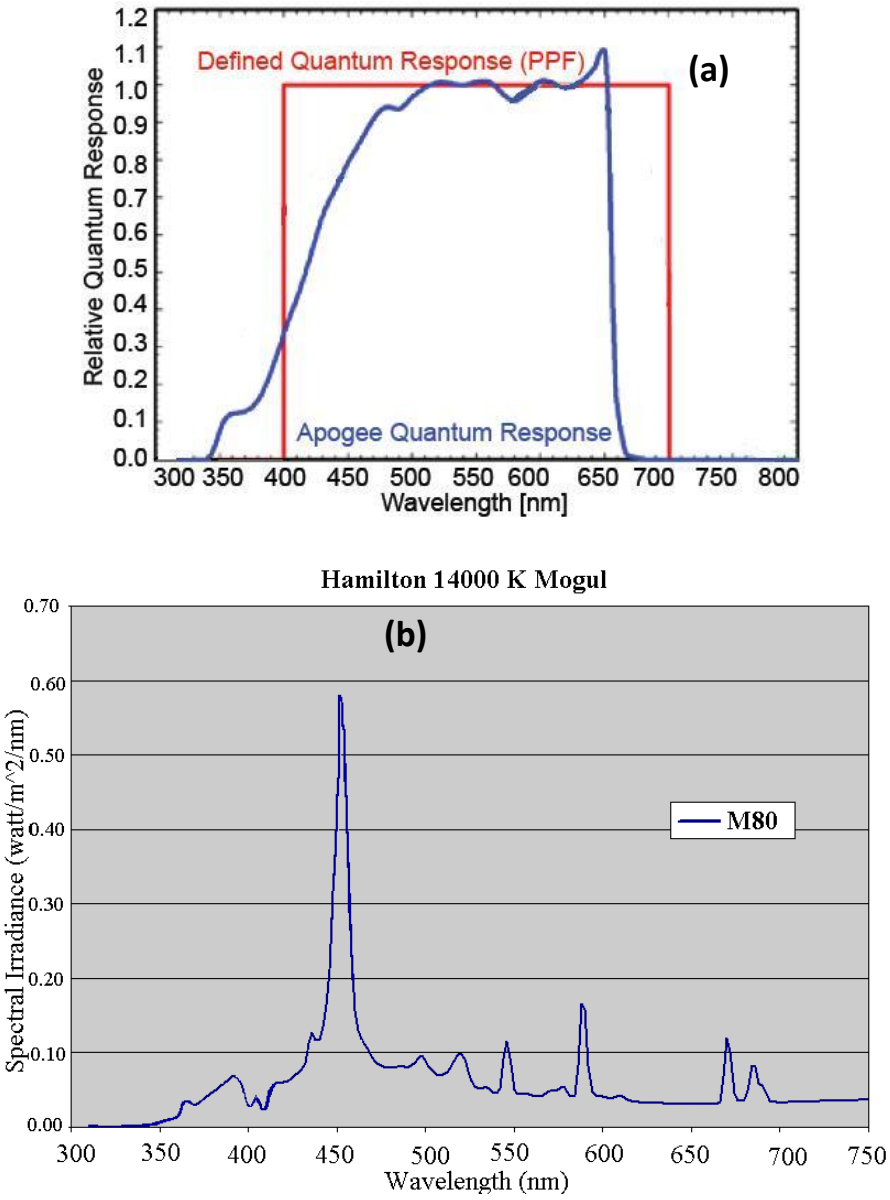

Figure 5-4. (a) Spectral response of the quantum sensor SQ-110 (http://www.apogeeinstruments.com), and (b) spectral plot of the metal halide lamp used with electronic ballast M80 (http://www.advancedaquarist.com/issues/july2004/review.htm).

5.3.2 Experimental results

Figure 5-5 (a) – (e) illustrates the experimental results on variation of voltage, current, available radiation intensity, harvested power intensity, and efficiency with depth. Interestingly, the efficiency peaks at depth of ~40cm to about 28%. This observation agrees with the prior result reported by Muaddi and Jamal (Muaddi,1992). The reason for apparent increase in efficiency is related to faster rate of decrease in available radiation density with depth due to absorption of longer wavelength radiation compared to reduction in shortwave radiation. Since amorphous silicon solar cell utilizes only shortwave radiation for conversion into electrical energy, the conversion efficiency increases. After a certain depth, reduction in shortwave radiation becomes more significant and efficiency begins to drop. The voltage and current plots exhibit maximum at certain depth from the air-water interface and then show a continuing decreasing trend. The variation with salinity did not show any conclusive trend and is within the error bar of the experiment. Wang and Seyed-Yagoobi (Wang,1994) has conducted experiment with salt concentration as high as 25% and showed that salt concentration does not have any noticeable effect on radiation energy transmission. Our experiments are in agreement with his results. The error bar was determined based on three sets of experiments with seven different salinity levels at each depth (0, 6, 15, 21, 31, 33 and 37 PPT, part per thousand) of marine grade salt.

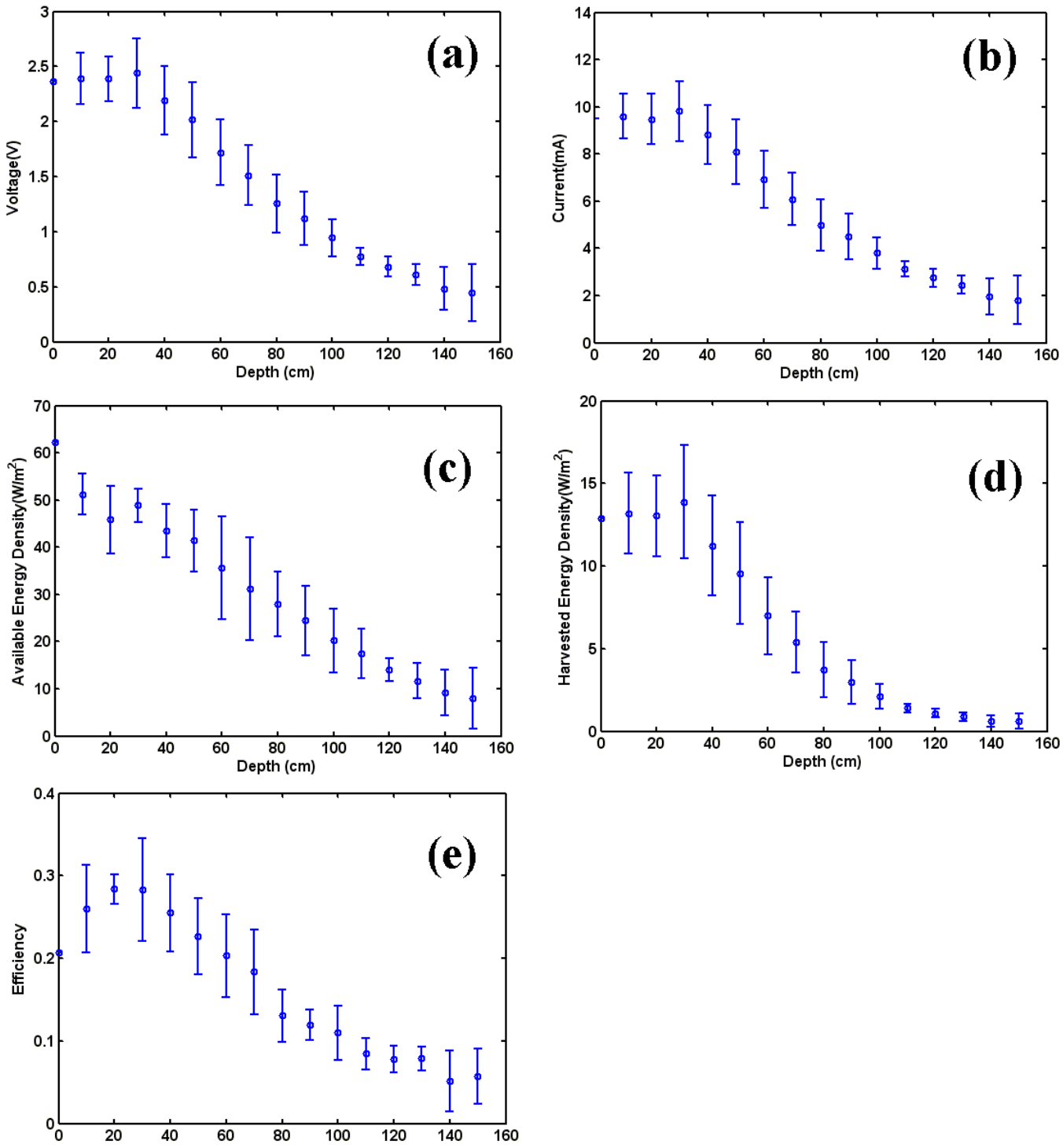

Figure 5-5. Variation with depth in (a) voltage, (b) current, (c) available power density, (d) harvested energy density, and (e) conversion efficiency of the solar cell. The error bar was determined from 21 data points for each depth level.

5.4 Model for underwater energy harvesting using solar cell

5.4.1 Effect of turbidity on transmission of solar radiation

Ocean turbidity is measure of haziness of the ocean waters and is computed in one of the popular units, ntu (neophelometric turbidity unit). Ocean turbidity changes with atmospheric conditions such as hurricane, storm, rain, depth of the ocean floor, distance from shore, mouth of a river, suspended organic matters etc. Typical ocean turbidity is found to be in the range of 1-7 ntu. Wang and Seyed-Yagoobi (Wang,1994) studied the effect of turbidity on transmission of solar radiation in underwater environment and presented experimental data for transmission coefficient in the turbidity range of 1 - 4.5 ntu at depths up to 1.34 m. We developed a mathematical model to fit his experimental data. Individual curve at a particular depth follow a quadratic function, for which, coefficients $\mathbf{c_0}, \mathbf{c_1}$ and $\mathbf{c_2}$ were found to obtain least square fit. These coefficients varied linearly with depth. The transmission coefficient is given by Eq. (1) as:

$$\frac{I_t}{I_0} = c_0(d) - c_1(d)T + c_2(d)T^2 \quad (1)$$

where I_t is the transmitted radiation intensity, I_0 is the incidence radiation intensity, d is the depth from the air-water interface, T is the turbidity level, and c_0, c_1, c_2 are coefficients that vary with depth. The variation laws for these coefficients are given by Eq. (2-4) as:

$$c_0(d) = 1.00041 + 0.060862\, d \quad (2)$$

$$c_1(d) = 0.000159442 + 0.202067d \quad (3)$$

$$c_2(d) = 0.00025378 + 0.013629d \quad (4)$$

Figure 5-6 illustrates the mathematical model fitted to the experimental data presented by Wang and Seyed-Yagoobi (Wang,1994). This mathematical modeling extends the transmission

estimation to turbidity and depth levels not covered by the experimental data and allows us to predict the behavior over a wider range.

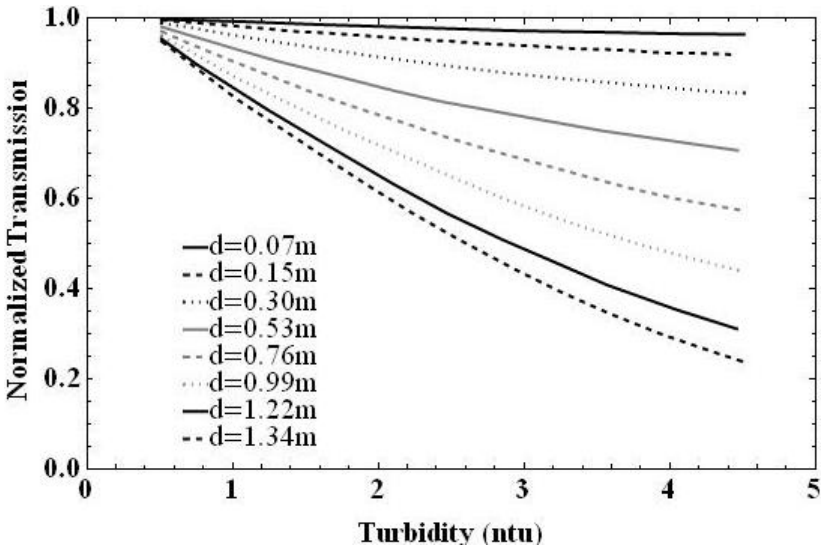

Figure 5-6. Mathematical model for variation of normalized transmission with turbidity and depth using data from Wang [15] [2].

5.4.2 Variation of solar spectrum and solar cell response with underwater depth

Our experiment confirmed the trends predicted by numerical model of Muaddi and Jamal (Muaddi,1992). Hence we take advantage of their numerical data to predict the spectrum variation and solar cell spectral response at depths as much as 100m. The solar spectrum gets modified with depth from air-water interface. Muaddi and Jamal numerical model (Muaddi,1992) predicts underwater solar spectrum with variation in depth. This model was built by considering atmospheric absorption bands from spectrum as received at the top of the

[2] Based on data from Solar Energy, Vol. 52/5, J. Wang, Seyed-Yagoobi, "Effects of turbidity and salt concentration levels on penetration of solar radiation under water", 429-438 ,1994, printed with permission from Elsevier.

atmosphere and reduces the radiation intensities to 70% in order to arrive at incident radiation spectrum on water surface. The radiation energy available is given by Eq. (5) as:

$$I_\lambda(x) = \int_{\lambda_0} I_t e^{-u(\lambda)x} f(\lambda) d\lambda \quad (5)$$

where x is depth from water surface, λ is wavelength of the radiation, I_λ is transmitted intensity at x m from water surface, I_t is transmitted intensity at water surface, $u(\lambda)$ is extinction co-efficient of water, and $f(\lambda)$ is spectral distribution function.

This model does not include the effect of water turbidity. To include effect of turbidity, we use the model developed here in Eq. (1)-(4) for calculation of transmitted radiation energy with respect to depth and turbidity. The transmitted energy upon incidence on solar cell is reflected and absorbed which is described by Eq. (6) as:

$$I_a(\lambda) = \int_0^\infty I_\lambda(x)[1 - r(\lambda)][1 - e^{-\alpha(\lambda)x}] d\lambda \quad (6)$$

where, $I_\lambda(x)$ is incident energy intensity at x m depth, $r(\lambda)$ is reflection co-efficient of solar cell material, and $\alpha(\lambda)$ is absorption coefficient of solar cell material. From this absorbed energy, I_a, solar cell converts a fraction of energy into useful electrical energy according to Eq. (7) as:

$$I_p = \int_0^{\lambda_g} I_a(\lambda) d_\lambda \quad (7)$$

where $\lambda_g = hc/E_g$ is absorption edge, h is Planck's constant, c is velocity of light, and E_g is band gap energy for solar cell material.

The solar spectral variation with depth is depicted in

Figure 5-7(a) and the corresponding spectral response of single crystal silicon solar cell is shown in

Figure 5-7(b). The data in this figure was generated from single crystal solar cell and can't readily be extended to amorphous silicon solar cell. We used the spectral response of single crystal silicon and amorphous silicon solar cells from Gonzalez and Carrol (Gonzalez,1994) as shown in Figure 5-8(a) to scale the single crystal spectral response given by

Figure 5-7(b). The scaling factor is shown in, Figure 5-8(b). It should be noted from

Figure 5-7(a) that the solar spectrum shrinks down with increase in depth to 400-600 nm range. For most part of this range (350-550 nm), the scaling factor is greater than 1. This result shows that amorphous silicon solar cell may be better for harvesting solar energy in underwater environment in comparison to its single crystal counterpart. This result also provides a relative cost advantage due to low cost manufacturing of amorphous silicon cell. After scaling, the spectral response for amorphous silicon cell is as shown in Figure 5-8 (c).

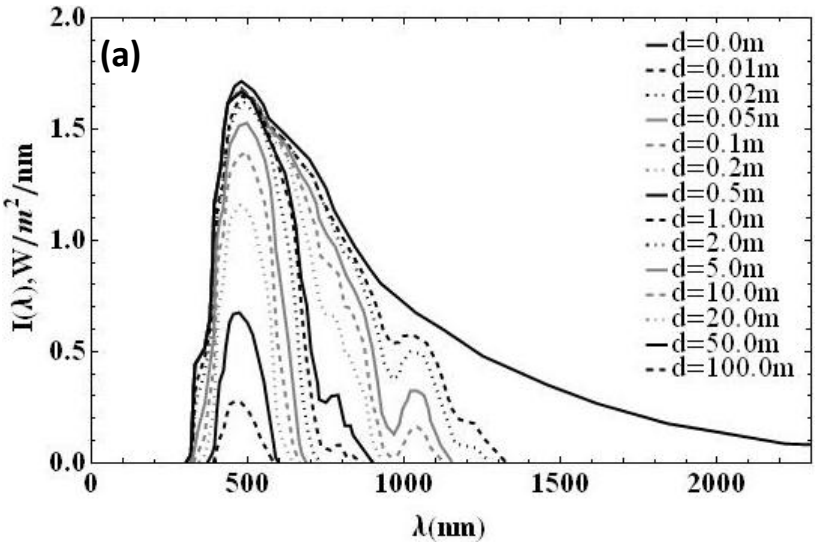

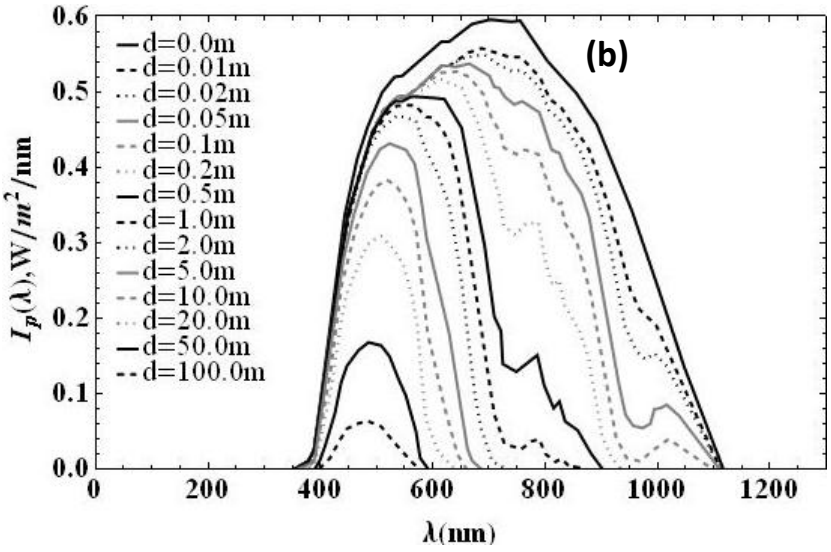

Figure 5-7. (a) Solar spectral variation with depth in water [7] [3], (b) single crystal silicon cell spectral response with depth in water [7][3.]

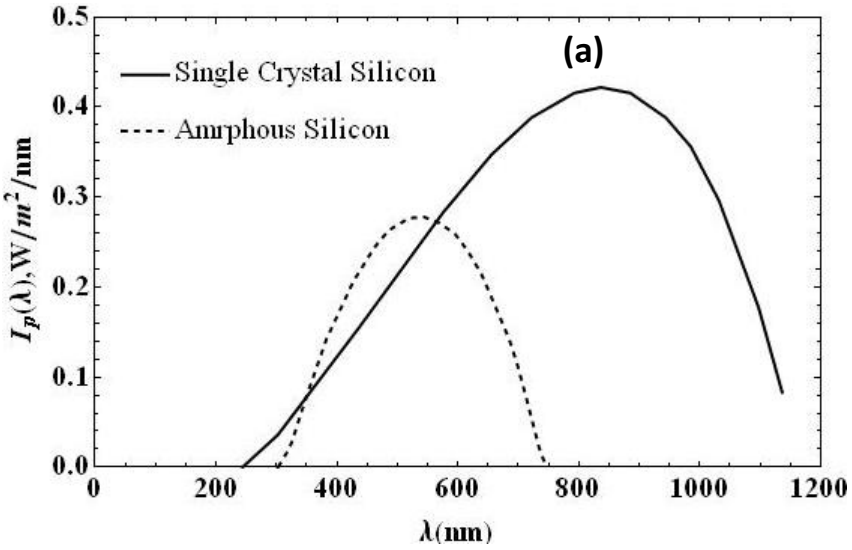

[3] Reprinted from Solar Energy, Vol. 49/1, J. A. Muaddi, M. A. Jamal, "Spectral response and efficiency of a silicon solar cell below water surface", 29-33,1992, with permission from Elsevier.

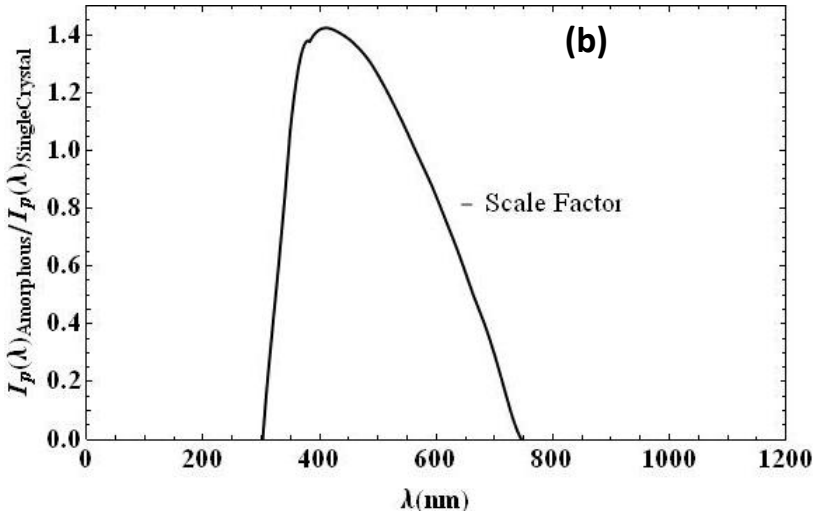

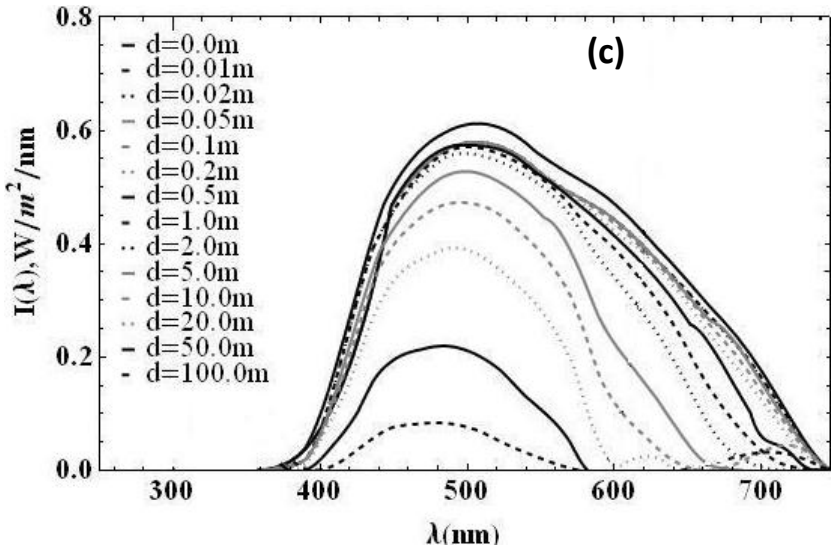

Figure 5-8. (a) Comparison of spectral response of single crystal silicon with amorphous silicon (Gonzalez,1994)[4], (b) Factor applied to scale single crystal silicon spectral response with that of amorphous silicon, and (c) spectral response of amorphous silicon cell obtained after scaling.

[4] Reprinted from Solar Energy, Vol. 53/5, M. C. Gonzalez, J. J. Carol, "Solar cells efficiency variations with varying atmospheric conditions",395-402,1994, with permission from Elsevier

5.4.3 Effect of incidence angle

For estimation of solar power harvested by covering exumbrella of jellyfish vehicle with solar cell, we need to take into account the effect of incidence angle as solar radiation is received by the animal at different incidence angle along the length of its bell. Stoddard and Incropera (Stoddard,1982) has studied the response of incidence angle in underwater environment in actual sun. We modified their result to calculate the response of solar cell with respect to the angle made with the incidence beam instead of air-water interface by subtracting the apparent zenith angle of the sun from the data. We used 3rd order interpolation function to obtain a continuous response function of normalized radiation intensity as a function of incidence angle as shown in Figure 5-9. The model extrapolates incidence angles beyond the range of available experimental data.

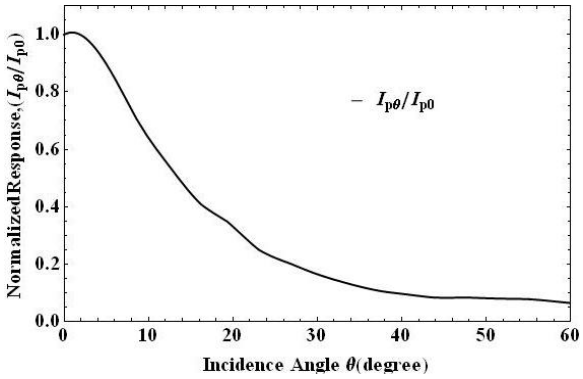

Figure 5-9. Effect of incidence angle on harvested solar energy.

Due to refraction of the solar beam, the actual incidence angle onto underwater surface parallel to air-water interface is less than actual zenith angle of the sun above the interface, which is advantageous for harvesting in underwater environment. Using Snell's law:

$$\frac{\sin(\theta_{water})}{\sin(\theta_{air})} = \frac{n_{air}}{n_{water}} = \frac{3}{4} \quad (8)$$

Where θ_{water} is apparent zenith angle in water, θ_{air} is actual zenith angle of the sun, n_{air} is refractive index of air, and n_{water} is refractive index of water.

This is advantageous as apparent zenith in water can be only 48.6° (critical angle for total internal reflection). As an illustration, Figure 5-10(a) plots the actual sun zenith in air and apparent zenith in water near a possible deployment location in Florida (34°26'N, 84°17'W) on 21st May, 2010. However, this advantage does not overcome the sharp reduction in radiation intensity with incident angle in water compared to that in air as illustrated by Figure 5-10(b)

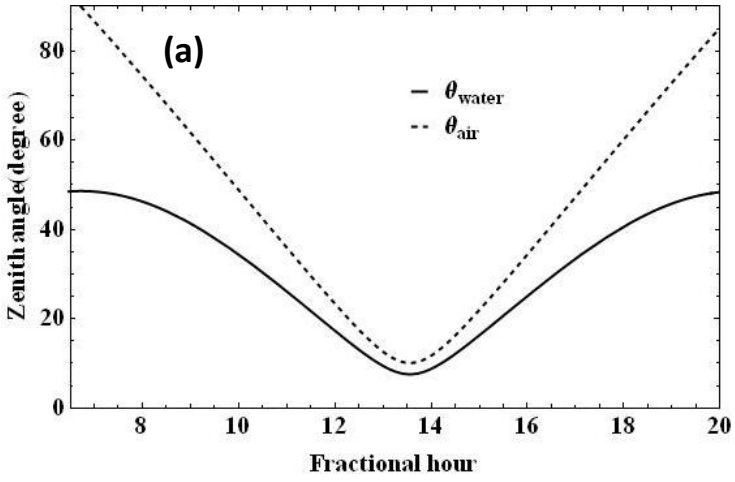

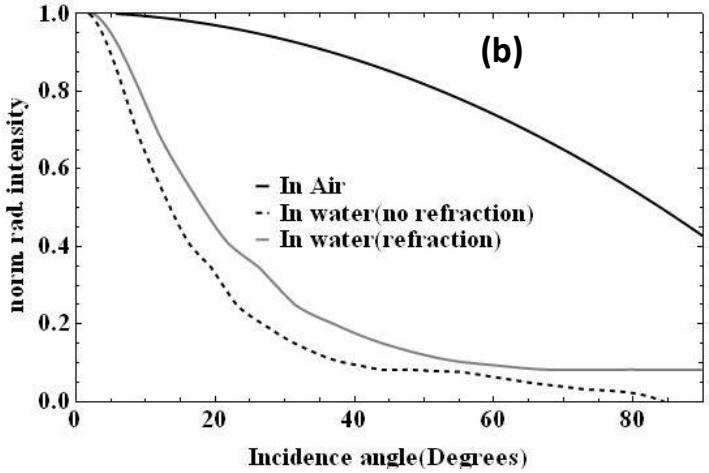

Figure 5-10. (a) Apparent zenith angle of sun in water, and (b) effect of incidence angle in presence of refraction.

5.5 Estimation of power harvested for jellyfish node

We combine all the above mentioned effects to estimate the power that can be harvested from the jellyfish node if its entire top surface is covered with the flexible amorphous silicon solar cell. We used the jellyfish profile of *Aurelia aurita* as shown in Figure 5-11 (Dabiri et al.(Dabiri,2005a)) and scaled it parametrically using the bell diameter (D) in relaxed condition.

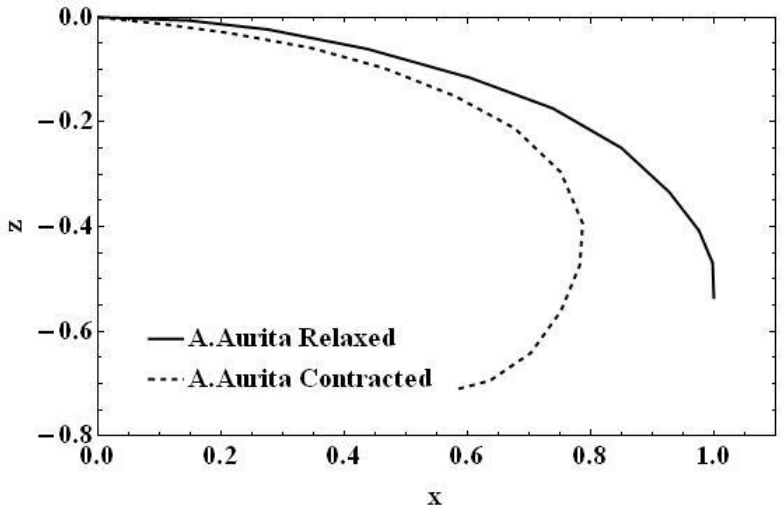

Figure 5-11. Normalized *Aurelia aurita* exumbrella profile(Dabiri,2005a).

The parameters considered in the calculation are depth d (distance of jellyfish top from the water surface), jellyfish bell diameter D, and turbidity level T. Consider a small strip of frustum of cone at x as shown in Figure 5-12:

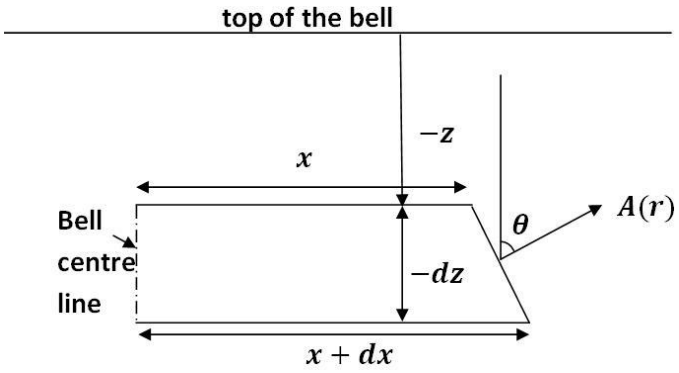

Figure 5-12. Small frustum of cone of height $\boldsymbol{dz}$ at position $\boldsymbol{x}$.

It's lateral area can be given by Eq. (9) as:

$$A(D,x) = \pi D^2\big(x + (x+dx)\big)\sqrt{dx^2 + dz^2(x,dx)} \tag{9}$$

Assuming that jellyfish is facing directly up, and sun is at zenith directly above the jellyfish, the incidence angle is given by Eq. (10) as:

$$\theta = \tan^{-1}\left(\frac{dz}{dx}\right) \tag{10}$$

The power harvested from this frustum of cone can be calculated by multiplying the integrated scaled spectral response of amorphous silicon cell with lateral area, transmission coefficient, and relative intensity at the incidence angle of the area. This is represented by Eq. (11) as:

$$P(d,T,D,x) = A(D,x)\left[c_0\left(d - \mathrm{z} - \frac{dz}{2}\right) - c_1\left(d - \mathrm{z} - \frac{dz}{2}\right)T + c_2\left(d - \mathrm{z} - \frac{dz}{2}\right)T^2\right]\left[\int_\lambda I_{p\lambda(sc)}\left(d - \mathrm{z} + \frac{dz}{2}\right)\left(\frac{I_{p\lambda(as)}}{I_{p\lambda(sc)}}\right)d\lambda\right]\left(\frac{I_{p\theta}}{I_{p0}}\right) \tag{11}$$

The total power harvested by the vehicle is calculated by integrating Eq. (11) over radius as shown below:

$$P(d,T,D) = \int_0^{\frac{D}{2}} P(d,T,D,x)dx \tag{12}$$

5.6 Parametric study of power estimation

5.6.1 Effect of fineness ratio

Jellyfish shape can be approximated by semi-ellipsoid. Fineness ratio(h/D), defined as ratio of jellyfish height to the bell diameter, is an important parameter for describing jellyfish shape. It governs the swimming pattern preferred by jellyfish. High fineness ratio jellyfish are jetters whereas low fineness ratio oblate jellyfishes select rowing mode of swimming. Besides this, fineness ratio also affects solar energy harvested by the model presented here. Increase in this parameter has two effects: increase in the area of the exumbrellar surface (tends to increase the harvested energy) and increase in the inclination angle of the area at any radial location x other than center ($x = 0$) according to Eq. (16) (tends to decrease the harvested energy). For constant bell diameter, equation of ellipse with major axis of 1 unit can be written as:

$$x^2 + \left(\frac{h}{2D}\right)^2 y^2 = 1 \tag{13}$$

Thus,

$$y = \frac{h}{2D}\sqrt{1 - x^2} \tag{14}$$

$$\frac{dy}{dx} = -\frac{\left(0.5\frac{h}{d}\right)x}{\sqrt{(1-x^2)}} \tag{15}$$

The inclination angle at any location on the semi-ellipsoid is given as:

$$\theta(x) = \tan^{-1}\left(-\frac{\left(0.5\frac{h}{d}\right)x}{\sqrt{(1-x^2)}}\right) \tag{16}$$

where 0.5h/d is semi-minor axis of the ellipsoid and x is normalized radial location.

Increased incidence angle reduces harvested energy density as shown in Figure 5-13(a). Figure **5-13**(b) illustrates reduction in total energy harvested considering both the effects of increasing area by increased fineness ratio and incident angle.

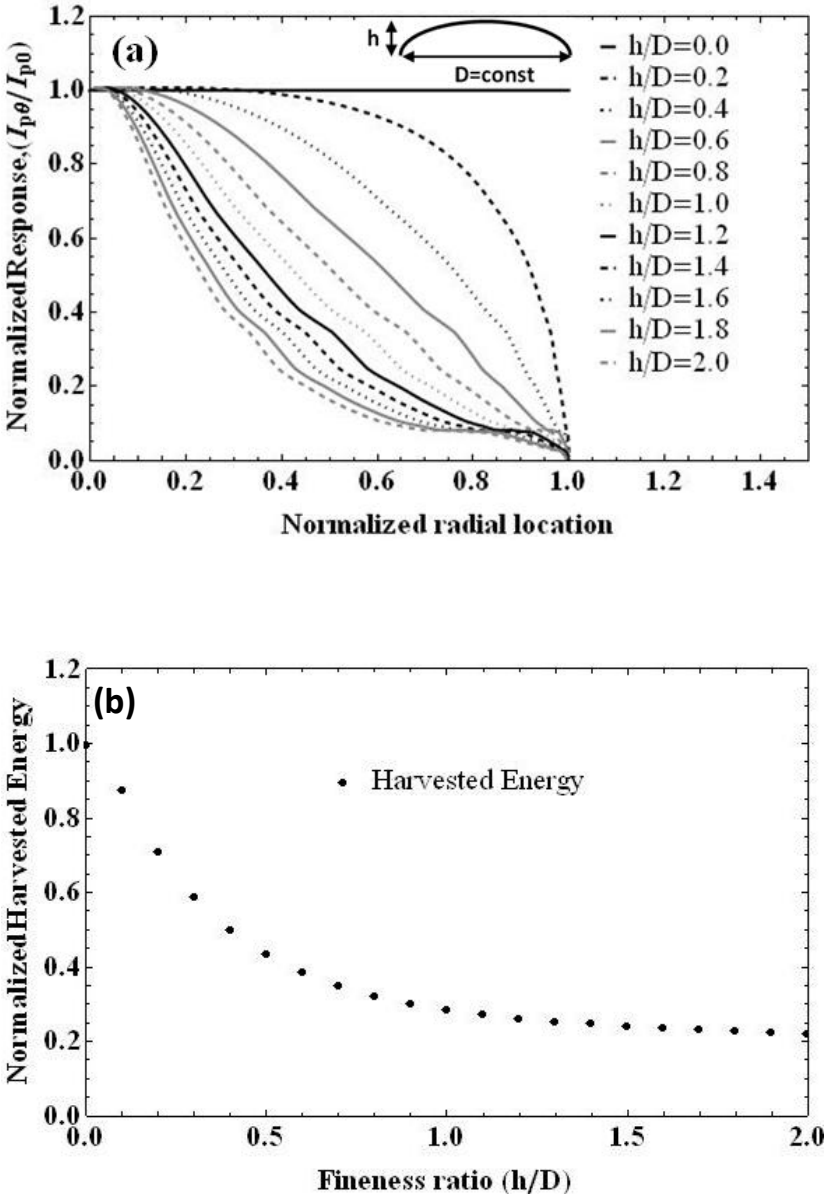

Figure 5-13. (a) Effect of only incidence angle on harvested energy, and (b) effect of increased area and incidence angle on total harvested energy as result of increasing fineness ratio.

5.6.2 Effect of exumbrella profile, depth, bell diameter and turbidity

This model is very useful in studying parametric variation in power harvested with change in depth, turbidity and bell diameter. We present here comparison between three representative jellyfish species namely, *Aurelia aurita* (Figure **5-11**), *Mastigias* sp. (Figure 5-14 (a)) and *Cyanea capillata* (Figure 5-14 (b)). *A. aurita* and *C. capillata* are semaeostome medusae and *Mastigias* sp. is representative of the diverse rhizostome scyphozoan lineage. The selection of these three species is based on their spread in the common waters of interest.

For illustrative case of d=1 m, T= 1 ntu and D=0.164 m the power generated by these 3 species in relaxed and contracted conditions are tabulated in
Table 5-1 and are also compared in Figure 5-14 (c).

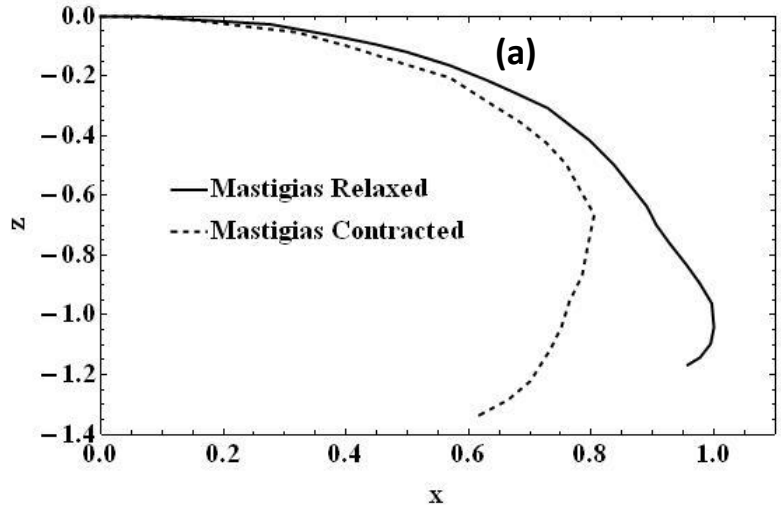

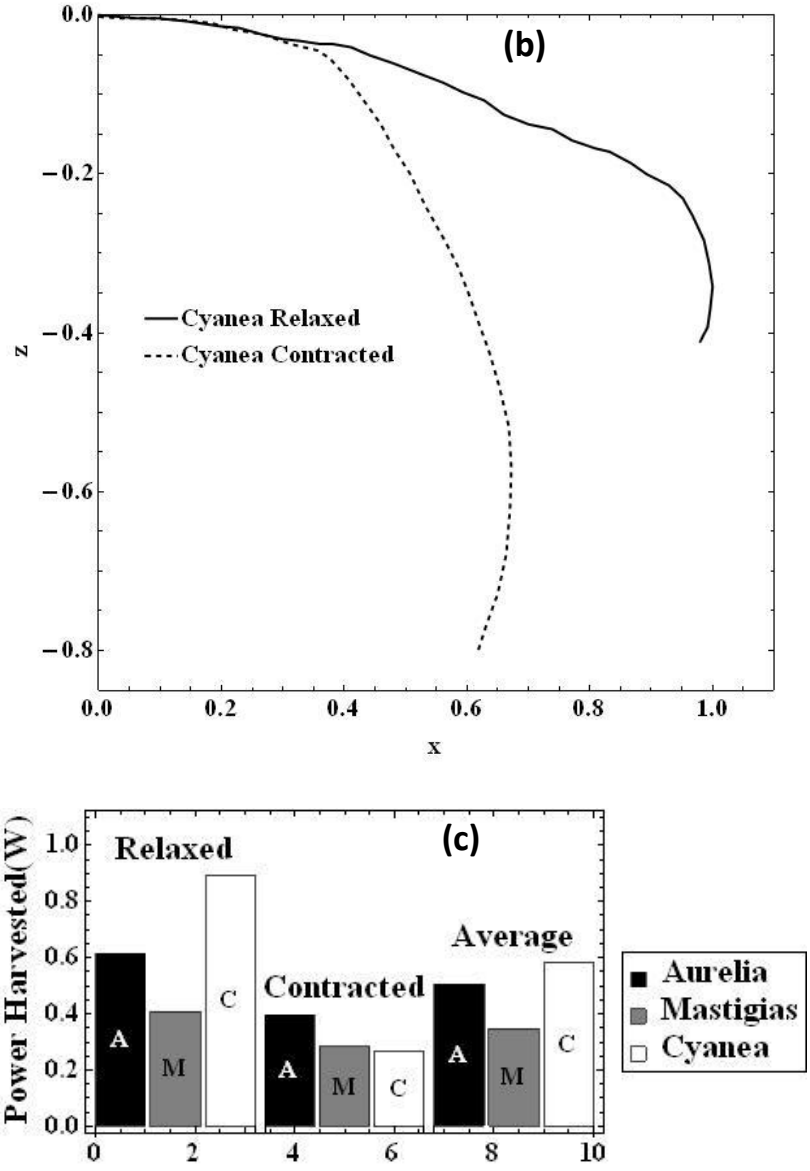

Figure 5-14. (a) *Mastigias* sp. exumbrella profile (courtesy:Dr. John H. Costello), (b) *Cyanea capillata* exumbrella profile(Gladfelter,1973), and (c) comparison of power harvested by jellyfish species, *A. aurita*, *Mastigias* sp. and *C. capillata* in relaxed condition, contracted condition and average power over the cycle.

TABLE 5-1: COMPARISON OF POWER HARVESTED BY DIFFERENT SPECIES

Species	Power Harvested (W)

	Relaxed condition	Contracted condition	Average
A.aurita	0.613	0.395	0.504
Mastigias sp.	0.409	0.283	0.346
C. capillata	0.892	0.269	0.581

Figure 5-15 (a) – (f) illustrate the variation in estimated power with bell diameter, ocean turbidity and depth in the water respectively for the three jellyfish species under relaxed and contracted conditions.

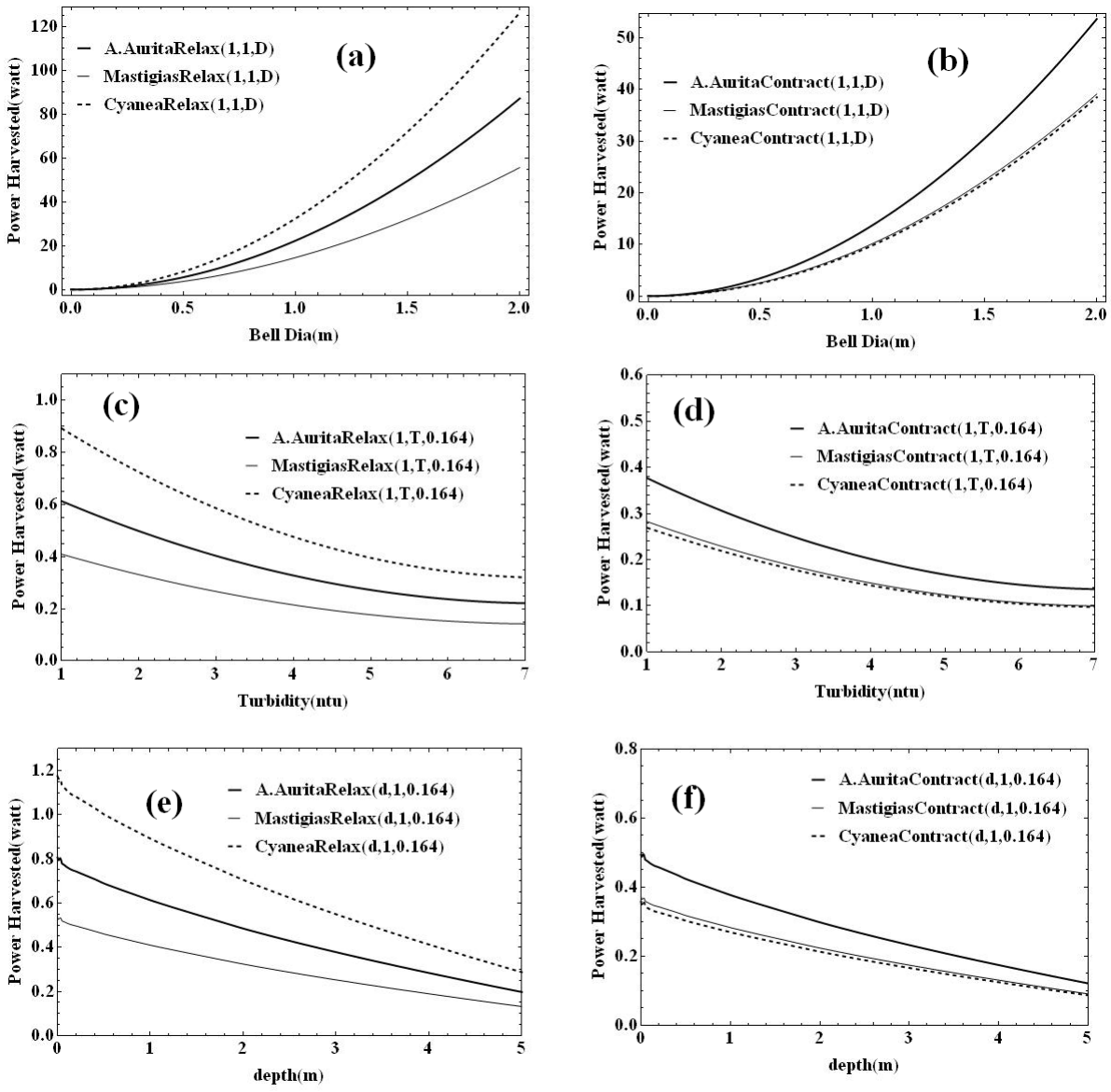

Figure 5-15. Harvested power variation with jellyfish bell diameter in (a) relaxed (b) contracted condition; harvested power variation with turbidity of ocean water in (c) relaxed (d) contracted condition; harvested power variation with depth from the ocean surface in (e) relaxed, and (f) contracted condition

5.7 Generalized model

The simplified model presented in earlier section is useful for studying effect of various parameters but in real field application we need to account for power harvesting capability with general orientation of AJV with respect to sun.

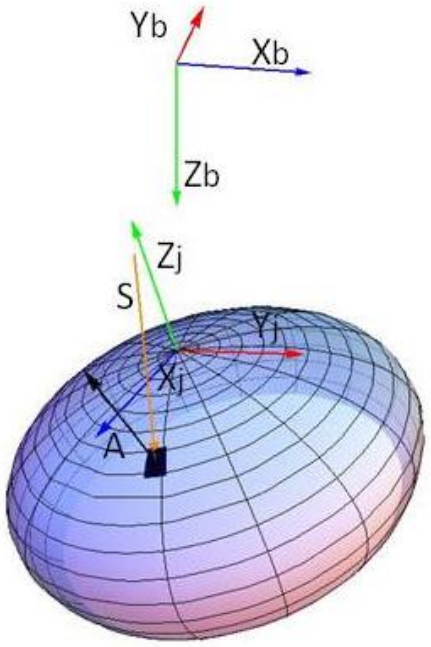

Figure 5-16. Generalization of solar energy harvesting model considering general orientation of AJV and sun.

Consider the geometric setup as depicted in Figure 5-16. The base co-ordinate system(B) was assumed to be located directly above the AJV top-center. The $\overrightarrow{Z_b}$ axis was in depth direction, $\overrightarrow{X_b}$ and $\overrightarrow{Y_b}$ axes were taken to be parallel to longitude and latitude. AJV co-ordinate system (J) was fixed such that $\overrightarrow{Z_J}$ becomes AJV central axis pointing upward. $\overrightarrow{X_J}$and $\overrightarrow{Y_J}$ axis can be placed arbitrarily following right hand rule. At point p on the AJV surface, normal area vector $\vec{A}$ is shown by black arrow and the incremental area is shown by black patch. The refracted sunray direction is shown by vector $\vec{S} = (l_s, m_s, n_s)$. Direction cosines of $\overrightarrow{X_J}$, $\overrightarrow{Y_J}$ and $\overrightarrow{Z_J}$ in system B are $(l1, m1, n1)$, $(l2, m2, n2)$ and $(l3, m3, n3)$. We can define a rotational transform by Eq.(17) as:

$$R = Transpose \begin{bmatrix} l1 & l2 & l3 \\ m1 & m2 & m3 \\ n1 & n2 & n3 \end{bmatrix} = \begin{bmatrix} l1 & m1 & n1 \\ l2 & m2 & n2 \\ l3 & m3 & n3 \end{bmatrix} \quad (17)$$

Multiplying the AJV geometry by the transform R would map the points and vectors from coordinate system J to that in the coordinate system B. The available 2D profiles shown in Figure 5-11 and Figure 5-14 (a)-(b) can be used to define any point in system J as:

$$\overrightarrow{p_J} = (X(s)\cos\Gamma, X(s)\sin\Gamma, Z(s)) \quad (18)$$

where $X(s)$and $Z(s)$are exumbrella profile coordinates as a function of profile length s, and Γ is angle of the 3D point from the $\overrightarrow{X_J}$axis. The area vector $\overrightarrow{A_J}$ has magnitude given as:

$$|\overrightarrow{A_J}| = X(s)\left(\frac{D}{2}\right) d\Gamma\, ds \left(\frac{D}{2}\right) \quad (19)$$

and,

$$\overrightarrow{A_J} = |\overrightarrow{A_J}|(-\sin\theta, 0, cos\theta) \quad (20)$$

where, $\theta = arcTan[X'(s), Z'(s)]$

In base coordinate system, the point and area vector are given by Eq.(21) and (22) as:

$$\overrightarrow{p_b} = R.\overrightarrow{p_J} \quad (21)$$

$$\overrightarrow{A_b} = R.\overrightarrow{A_J} \quad (22)$$

Incidence angle for the incremental area is given by Eq.(23) as:

$$i = \cos^{-1}\frac{\overrightarrow{A_b}.\vec{S}}{|\overrightarrow{A_b}.\vec{S}|} \quad (23)$$

where $\vec{S}$ is sunrays after refraction at air-water interface located in base co-ordinate system. We can obtain $\vec{S}$ if we know sun rays orientation in air, $\vec{S}_{air} = (l_a, m_a, n_a)$, by applying axis-angle rotation transformation along $\vec{S}_{air} \times \overrightarrow{Z_b}$ axis, which is perpendicular to plane of refraction, by angle $\theta_{air} - \theta_{water} = \cos^{-1} n_a - \sin^{-1}\left(\sin(\cos^{-1} n_a)\frac{n_{air}}{n_{water}}\right)$.

Depth of the point is given as:

$$z_b = \overrightarrow{p_b}.\overrightarrow{Z_b} \tag{24}$$

The total power calculated is given as:

$$P(d,T,D) = \int_0^l \int_0^{2\pi} X(s)\left(\frac{D}{2}\right)^2 \left[c_0\left(d - \left(\mathrm{z_b} + \frac{d\mathrm{z_b}}{2}\right)\right) - c_1\left(d - \left(\mathrm{z_b} + \frac{d\mathrm{z_b}}{2}\right)\right)T + c_2\left(d - \left(\mathrm{z_b} + \frac{d\mathrm{z_b}}{2}\right)\right)T^2\right]\left[\int_\lambda I_{p\lambda(sc)}\left(d - \left(\mathrm{z_b} + \frac{d\mathrm{z_b}}{2}\right)\right)\left(\frac{I_{p\lambda(as)}}{I_{p\lambda(sc)}}\right)d\lambda\right]\left(\frac{I_{p\theta}}{I_{p0}}\right)d\Gamma ds \tag{25}$$

With this model we can study the effect of inclination of sun rays and orientation of AJV on the total harvested power.

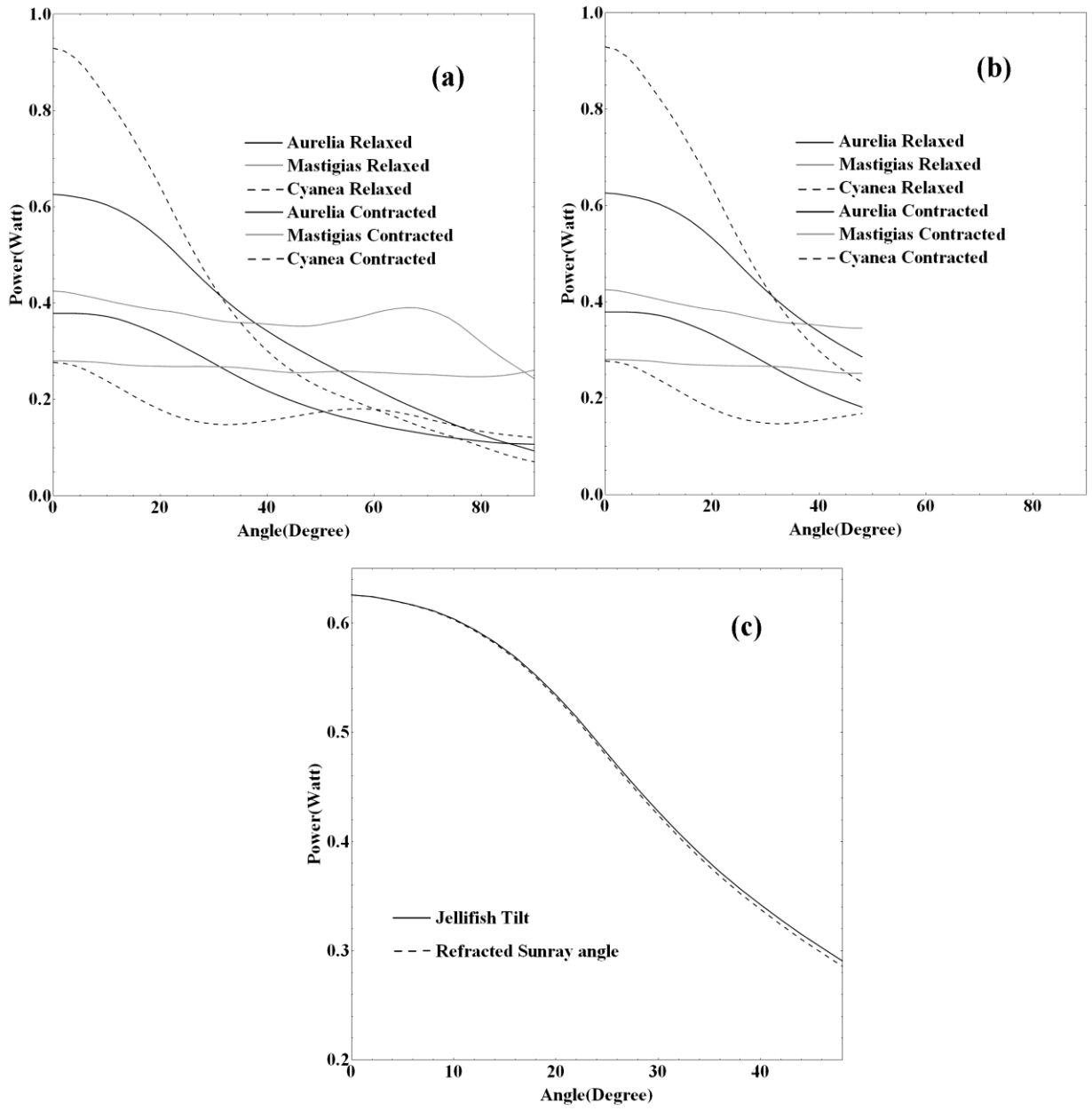

Figure 5-17. (a) Effect of AJV tilting along its axis on harvested power, (b) effect of refracted sun ray inclination on harvested power, and (c) comparison of effect of vehicle tilt and inclination of refracted sunrays for *Aurelia aurita* relaxed profile.

Figure 5-17 (a) and (b) illustrate the effect of vehicle tilt and inclination of refracted sunrays on the harvested power Figure 5-17 (c) compares both these effect for *Aurelia aurita*

relaxed condition. The trend is almost identical, with small difference related to change in depth of different point on AJV surface as it tilts on its axis. This effect is obviously absent in other case resulting in small difference. This difference may increase as the depth decreases, however for practical purposes we can consider it negligible. This result opens up opportunity to optimize the power harvested by tilting the vehicle axis such that it is always in the direction of refracted sunrays. Figure 5-18 shows that if refracted sunrays are striking at 20° angle, maximum power can be obtained by tilting the vehicle axis towards the refracted sunrays.

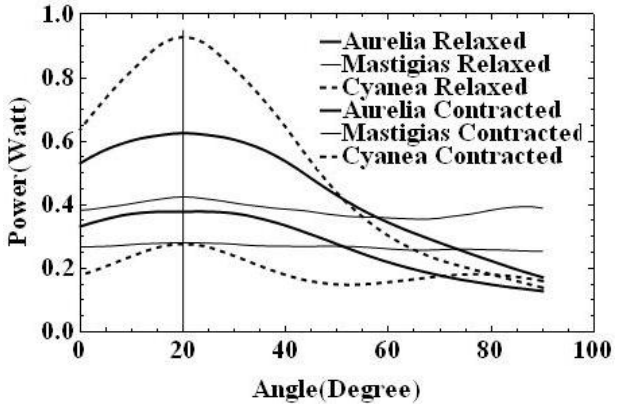

Figure 5-18. Optimizing the power harvested by orienting AJV axis towards the refracted sunrays.

5.8 Conclusion

In this study, we investigated the solar energy as a potential source for powering AJV. It was experimentally confirmed that salinity has no significant effect on the performance of solar cell but harvested power decreases with depth. The available power initially decreases with depth, mainly due to absorption and reflection of long wave radiation and solar spectrum shrinks and shifts towards short wavelength range around 400-600 nm range which is advantageous for amorphous silicon. Reduction in long wave radiation also results in increase in conversion efficiency with depth (~30-40% at depth 0.2m), before reaching the peak at 0.2m. Beyond this

depth, the efficiency shows a decreasing trend. Transmission of solar radiation decreases rapidly with depth and with increasing turbidity. The variation was found to be quadratic in turbidity and the coefficients of quadratic relation were linear function of depth. The performance of solar cells was found to be severely affected by the angle of incidence of the sun radiation. The variation can be represented by a bell-shaped curve. Higher refractive index of water was advantageous for undersea solar energy harvesting as the apparent zenith angle of sun is lower than that in the air. This helps to reduce the variation in incidence angle over the entire day. However, the reduction in radiation intensity in water is much sharper in comparison to that in air which overcomes this advantage.

An analytical model was developed to estimate the power harvested from AJV using spectral response of single crystal silicon cell with depth and applying a scaling factor to obtain the amorphous silicon cell response. Incident radiation was modified by using transmissibility information with depth and turbidity. Total power was estimated by integrating the areal power density over incidence angle and diameter. The model suggested monotonic reduction in harvested power with increase in fineness ratio (aspect ratio) of AJV.

It was found that in relaxed state, *Cyanea capillata* harvests the maximum power followed by *Aurelia aurita* and *Mastigias* sp., for same bell diameter. However, *Cyanea capillata* harvests the least power in contracted state due to increased inclination angle over the majority of its bell area. *Aurelia aurita* harvests the maximum power in contracted state. Comparison of average power harvested suggests that *Cyanea capillata* would be able to harvest the maximum average power for continuous operation. The parametric study suggested that variation in power harvested is a parabolic function of AJV bell diameter. For a diameter of 2m with turbidity of 1ntu and depth of 1m, we can expect power in excess of 85W, 55W and 125W respectively from

AJV mimicking *Aurelia aurita*, *Mastigias* sp. and *Cyanea capillata* profile respectively in relaxed condition. These are promising values for developing a surveillance vehicle that can be deployed in ocean. AJV can also charge their on-board batteries by staying at the surface for their intermittent propulsive needs. With increase in turbidity form 1 to 7, a quadratic decrement was observed that causes reduction in power harvested by more than 60%. With depth, power harvested increases slightly due to increased efficiency and after that shows a monotonous decreasing trend. At 5m depth, the power available was reduced by 75%.

A generalized model enabled power harvesting estimates in any field condition. It also suggests the advantage of tilting of the vehicle to face refracted sunrays. *Cyanea capillata* suffers the most if the refracted sunrays and AJV axis are not aligned. *Mastigias* sp. is least affected, giving almost constant power output at all inclinations. *Aurelia aurita* shows intermediate behavior. Thus, *Mastigias* sp. has the optimum shape for AJV required to achieve effective lateral motion. We expect this work to provide guideline for developing not only AJV but also other form of AUVs.

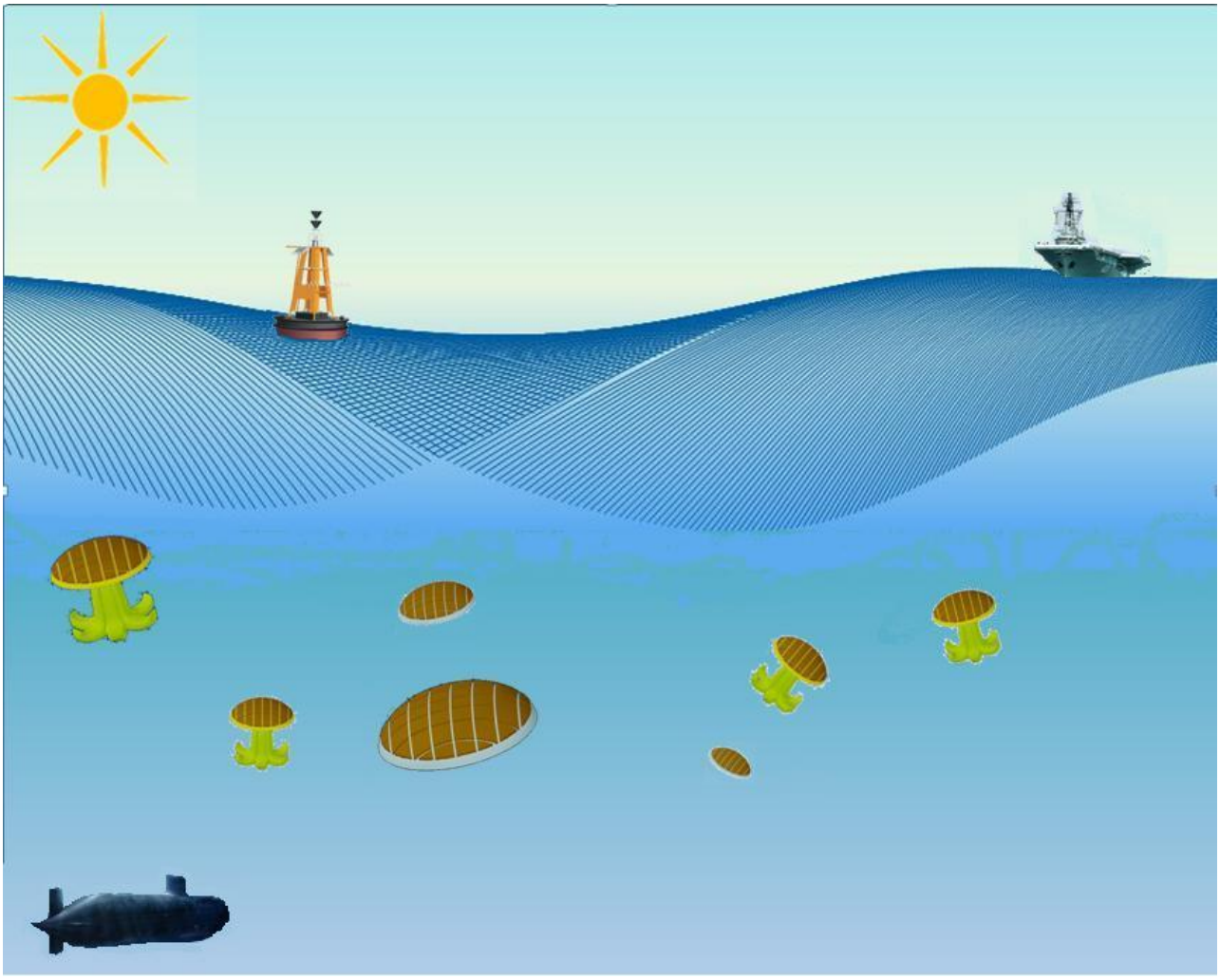

Cover Page Picture of "Autonomous Jellyfish Vehicles" (AJV). Credit: Joshi, Costello, and Priya.

Multi-physics model of a thermo-magnetic energy harvester

Harvesting small thermal gradients effectively to generate electricity still remains a challenge. Ujihara et al. (Ujihara,2007) have recently proposed a thermo-magnetic energy harvester that incorporates combination of hard and soft magnet on vibrating beam structure and two opposing heat transfer surfaces. This design has many advantages and could present an optimum solution to harvest energy in the low temperature gradient conditions. In this paper, we describe a multi-physics numerical model for this harvester configuration that incorporates all the relevant parameters including heat transfer, magnetic force, beam vibration, contact surface and piezoelectricity. The model was used to simulate the complete transient behavior of the system. Results show the evolution of magnetic force, changes in internal temperature of soft magnet (Gadolinium (Gd)), thermal contact conductance, contact pressure and heat transfer over complete cycle. Variation of vibration frequency with contact stiffness and gap distance was also modeled. Limit cycle behavior and its bifurcations were illustrated as a function of device parameters. Model was extended to include piezoelectric energy harvesting mechanism and using piezoelectric bimorph as spring material a maximum power of 318μW was predicted across 100$k\Omega$ external load.

TERMS USED

w_m	:	lateral position of top of the midpoint of the fixed-fixed beam
th	:	Gadolinium thickness
T, T_0, T_l, T_{Nd}, T_s	:	Temperature; temperatures of Gadolinium surface facing Nd magnet, Gadolinium surface facing heat sink, Neodynium and heat

		sink respectively
α	:	Gadolinium diffusivity
t	:	time
g, δ	:	nominal gap between two bounding surfaces, base offset
dd	:	Distance between Nd and T_0 surface ($g + \delta - th - w_m$)
x, z	:	coordinates in longitudinal and transverse direction (Coordinate system is fixed in Neodymium magnet bottom surface, $+z$ axis pointing downwards towards Gadolinium magnet
$\dot{q}$	:	heat flux
$h_{hot}, h_{cold}, h_c, h_g$	:	total thermal conductance at hot surface, total thermal conductance at cold surface, contact conductance and gap conductance respectively
k, k_g, k_1, k_2, k_s	:	conductivity of Gadolinium, interstitial fluid, surface 1, surface 2 and effective conductivity of contacting surfaces respectively
Y	:	actual gap distance
M_{hot}, M_{cold}	:	temperature jump at hot and cold surface respectively
P	:	contact pressure
H_{sur}	:	surface hardness of softer of the two contacting materials
$\sigma, \sigma_1, \sigma_2$	:	eff. surface roughness($\sqrt{\sigma_1^2 + \sigma_2^2}$), surface roughness of surface 1, surface roughness of surface 2 respectively
m, m_1, m_2	:	eff. rms slope($\sqrt{m_1^2 + m_2^2}$), rms slope of surface 1, rms slope of surface 2 respectively

$\alpha_h, \alpha_c, \alpha_{h1}, \alpha_{h2}, \alpha_{c1}, \alpha_{c2}$	:	thermal accommodation parameter of at hot side, cold side, Thermal accommodation parameter of surface 1 and that of surface 2 for hot and cold side respectively
γ	:	ratio of sp. heat of the gas
Pr	:	Pradtl number at given temperature and pressure
β	:	gas parameter $\left(\frac{2\gamma}{(1+\gamma)Pr}\right)$,
Λ	:	mean free path of gas molecules at given temperature and pressure
$M_{gas}, M_{air}, M_{Gd}, M_{Nd}$	:	effective molecular weight for diatomic gas, molecular weights of air, Gadolinium and Neodymium, respectively
$\mu_{Gd}, \mu_{Nd}, \mu_{sink}$	:	ratios of molecular weights of air with those of Gadolinium, Neodymium and heat sink
B_r	:	remnant magnetization of Neodymium magnet
$Br_J[]$	:	Brillouin function
$B_{mag}(z)$	:	B-magnetic field of Neodynium as function of distance z from the surface
$2a, 2b, l_{Nd}$	:	length, width and thickness of Neodymium magnet
$M_0, M \text{ or } M(T,H)$	:	Self magnetization at $0\ K$ temperature, magnetization as function of temperature and applied external field
k_B	:	Boltzmann constant
csm	:	Contact stiffness multiplier
k_{spring}	:	Spring stiffness
b_{pzt}, h_{pzt}	:	Width and thickness of piezoelectric bimorph spring

C_p	:	Piezo bimorph capacitance
d_{31}	:	Piezoelectric strain coefficient
Y_{11p}^{E}	:	Young modulus of piezoelectric material in absence of electric field in 11 direction
ϵ_{33}^{S}	:	Electrical permittivity in 33 direction in absence of strain

5.9 Introduction

Role of Unmanned Aerial Vehicles (UAV) has increasingly become important for surveillance. UAV's are being designed and tested to be powered by solar cells in order to increase their flight time. However, in order to generate sufficient power for persistent flight using currently available solar modules, the vehicles will require quite large surface area which may not be practical. Decrease in efficiency of solar cells at elevated temperatures further contributes towards this problem. There is significant progress being made in the development of multi-junction solar cells which will provide much higher efficiencies. But currently available multi-junction cells are extremely expensive to be used in the flight application and it will require breakthroughs in materials and synthesis process to bring the cost down. For cost-effective silicon solar cells, one of the ways to maintain their peak efficiency will be by keeping the cell operating temperature constant. Thus, if we can design a practical device that can effectively remove heat from solar cell module and convert significant fraction of this thermal energy into useful electrical energy then it will help in designing solar powered UAV's. At the altitudes of ~60000 ft, ambient temperature is quite low ~-80^{o}C (considering 1.8 ^{o}C drop every 1000 ft) and thus large thermal gradients are possible. We take motivation from the work of Ujihara et. al. (Ujihara,2007) towards the design of the non-conventional thermal energy

harvester and focus in this paper on developing a complete multi-physics model for this type of system.

Figure 5-19 shows the schematic of the proposed thermo-magnetic energy harvester. In this configuration, Neodymium (Nd) hard magnet was mounted on the backside of the photovoltaic cell or the hot surface which was assumed to be always at higher temperature then the heat sink. Soft Gadolinium (Gd) magnetic material was mounted on the top surface of the Belleville-shaped spring which in the neutral state is always in contact with the heat sink or base. Gd is mounted at the center of the vibrating beam with springs attached on both side surfaces. In this analysis, the base temperature of the heat sink was taken to be $\sim 273\ K$ but this is a variable depending upon the Curie temperature of the soft magnetic material. Base level was designed to be higher than the spring support points to provide interference δ that ensures sufficient contact pressure for better heat transfer between the heat sink (also referred as cold-side) and Gd.

The operating mechanism of the harvester shown in Figure 5-19 is as follows. In the initial state, Gd is below the magnetic Curie temperature and is attracted towards the Nd through magnetic force of attraction. Thus, it travels towards the Nd surface and the two magnets make contact against each other under magnetic and inertial forces. At that instant, heat is transferred from the hot surface of Nd to cold surface of Gd. Due to the temperature rise, Gd loses its magnetism above its Curie temp (~292 K). After that, spring force of the spring pulls it away from Nd and presses it against the colder surface of the heat sink which is assumed to be maintained at $\sim 273\ K$. Next, heat transfer occurs again between the Gd surface and heat sink, and Gd cools below the Curie temperature regaining its spontaneous magnetization. After regaining magnetization, Gd is again attracted to the Nd and the magnetic attractive forces pull it

towards the hot surface. This cycle will continue as long as the temperature gradients are maintained between the hot-side and cold-side within certain limits.

In this paper, our goal is to model this continuous cycle. The only assumption is that temperature gradient between the hot and cold side is maintained such that colder side is below the Curie temperature of soft magnet and hot side is above the Curie temperature of soft magnet. Further, the temperature difference between hot and cold side is at least 10 K. There were no other assumptions made in the paper which makes this model applicable to many different scenarios. The contact surfaces also act as elastic members absorbing impact energy of Gd magnet and restoring Gd kinetic energy later. This helps make device size smaller. The spring is very essential component to create a vibrating system; it stores strain energy due to Gd displacement and provides restoring force required to overcome magnetic pull to bring Gd back to heat sink for restoring magnetization. For energy harvesting application also the strain energy of the spring is essential for conversion to useful electrical energy. The biasing or preloading of the spring by initial deflection δ is required to provide unidirectional restoring force in the direction opposing the unidirectional magnetic pull.

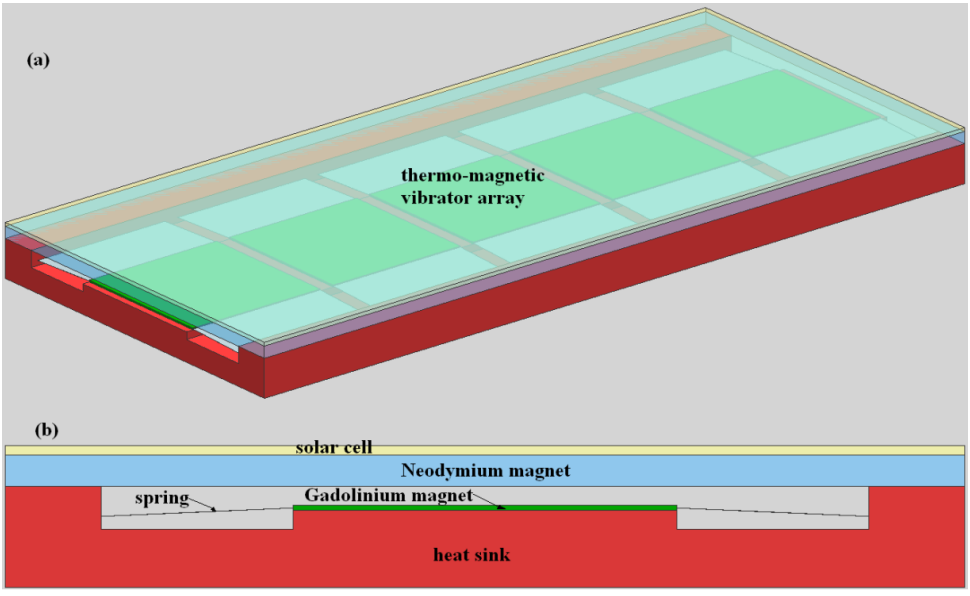

Figure 5-19. (a) Model of the thermo-magnetic harvester array that can be mounted on the back surface of solar cell module, and (b) side-view of the system.

5.10 Modeling

Modeling of the entire harvesting cycle can be divided into 3 distinct phases as follows: (i) Phase I – Gd or soft magnet is in contact with the cold surface (heat sink), (ii) Phase II – Gd magnet is in contact with the hot surface (Nd or hard magnet, heat source), and (iii) Phase III – Gd magnet is in motion. As discussed earlier, Phase I corresponds to the base configuration where Gd is in the rest state and with time cools down below its Curie temperature regaining its magnetization. Gd is pressed against cold surface and contact pressure and thermal contact conductance on cold side rises. T_l drops faster than T_0 and the temperature difference between T_0 and T_l increases correspondingly. Phase II corresponds to the state where Gd comes in contact with Nd and its temperature starts to rise above the Curie temperature losing its magnetization. Gd is pressed against hot surface and contact pressure and thermal contact conductance on hot side rises. T_0 rises faster than T_l and the temperature difference between T_0 and T_l increases correspondingly. Phase III corresponds to the state where Gd is heated up above its Curie temperature, has lost its magnetization, and is traveling towards the cold surface under the restoring spring force or Gd is cooled down sufficiently, has regained its magnetism and is traveling towards the hot surface under stronger magnetic pull. The temperature difference between T_0 and T_l decreases due to thermal diffusion. On either sides, thermal contact conductance is negligible and contact pressure is absent. Gd velocity is significant. In Phase I and Phase II the system is near its maximum displacement state, undergoes rapid retardation due to impact and rapid change in magnetic force is observed due to change in temperature of the Gd magnet. In this case, thermal contact conductance dominates heat transfer physics and contact

pressure dominates vibration physics. In Phase III, role of thermal contact conductance is negligible and temperature distribution changes only due to internal diffusion. Contact pressure is absent and thus the vibration is governed by magnetic pull and restoring spring force. Below we provide mathematical description of each of these phases.

5.10.1 Heat transfer model

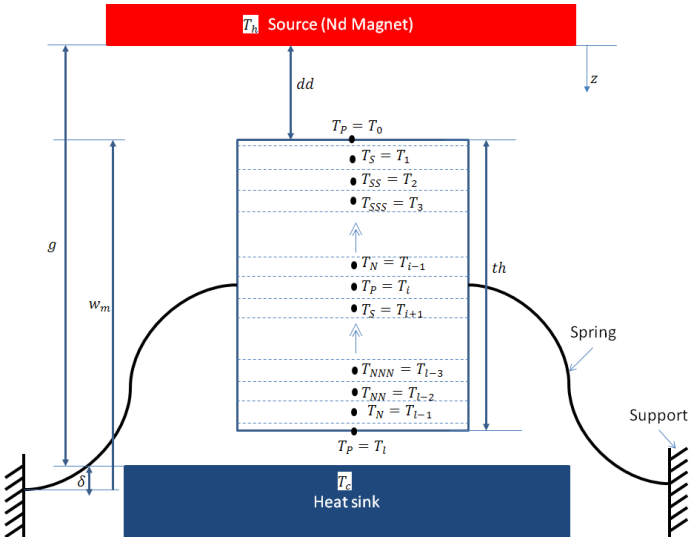

Figure 5-20. Schematic diagram of the proposed heat transfer model.

Figure 5-20 presents schematic of the modeling with emphasis on heat transfer discretization. The Nd magnet is maintained at higher temperature $T_h (> T_{GDcurie})$ and acts as heat source and heat sink is maintained at T_c $(< T_{GDcurie})$. Gd magnet is supported by springs on each side that are connected to side support. Since the purpose of heat transfer modeling is to compute temperature distribution in Gd and corresponding magnetic force, non-magnetic spring can be safely ignored for the heat transfer model. Any heat transfer with spring can be ignored because of its cross-sectional dimensions. Gd magnet is discretized into a number of finite volumes in the direction of heat transfer. The distance z is measured from Nd surface. The distance between Nd and Gd surfaces is dd and Gd thickness is th. Gd top and bottom surface

temperatures are T_0 and T_l. Here T_P represents node in question, T_N, T_{NN} and T_{NNN} are node 1, 2 and 3 nodes above T_P; and T_S, T_{SS} and T_{SSS} are node 1, 2 and 3 nodes below T_P.

Figure 5-20 can also be used to explain parameters for vibration modeling. As illustrated in the schematic, springs are rigidly connected to the support with zero displacement and zero slope. Heat sink surface is elevated by a small base offset δ compared to spring support to ensure spring restoring force is always in opposite direction to magnetic pull. Displacement was measured upwards from spring support location. Here w_m is the displacement of top of the Gd surface and g is the gap distance between hot and cold surfaces. Temperature rise in the Gd magnet can be modeled by one dimensional diffusion equation given as:

$$\frac{\partial \mathrm{T}}{\partial \mathrm{t}} = \alpha \frac{\partial^2 \mathrm{T}}{\partial \mathrm{z}^2}, \qquad z\epsilon[dd, dd + th] \tag{1}$$

where $dd =$ distance of top of the mid-point of the fixed-fixed beam from Nd magnet surface, $\alpha =$ thermal diffusivity of Gd, $t =$time, $z =$ distance from Nd surface, and $T =$temperature. At the hot and cold boundaries ($z = dd$ and $z = dd + th$ respectively), $\dot{q} = h\Delta T$, where h is thermal contact conductance and ΔT is temperature difference between contact surfaces. The other boundaries are assumed to have insulated ($\dot{q} = 0$) boundary condition.

A critical component of the modeling is accurate estimation of temperature distribution for reliable magnetic force calculation. Thus, in heat transfer modeling utmost importance was given to the estimation of thermal contact conductance modeling rather than selecting approximate values from literature. The thermal contact conductance can be divided in two parts: (i) contact conductance h_c, through solid-solid interface which is present only where two surfaces are in contact and (ii) gap conductance h_g, through interstitial fluid medium, which is

always present. Contact conductance causes conduction of heat through very small contact areas of the contacting surface that press against each other. It depends on various parameters such as thermal conductivities of contacting surface material k_1, k_2 (to increase surface thermal conductivity Gd was sputtered with gold particles), contact pressure P, surface roughness σ, average slope of the micro asperities of both surfaces m, hardness of the softer of the two materials H_{sur} (softer material yields easily and increases contact area, sputtering of soft material like gold on Gd surface offers larger contact area). Gap conductance is contributed by conduction of by interstitial fluid trapped between contacting surface. It depends on thermal conductivity of interstitial fluid, k_g, gap distance parameter Y (function of P, σ and H_{sur}) and temperature jump M_c or M_h(function of thermal accommodation factor α_c or α_h between surfaces, gas parameter β and mean free path of the molecules at given temperature and pressure Λ).

In Phase I and Phase II, all the thermal contact conductance mechanisms are present while in Phase III only gap conductance due to temperature jump effect is present. Though all the equations required for thermal contact conductance calculations are presented here, it is not intended to show the derivation of all the expressions. Interested readers may find it useful to refer to standard texts (Goodman,1980, Song,1987, Yüncü,2006).

Phase I:

In Phase I, the conductance can be given as:

$$h_{cold} = h_c + h_g \tag{2}$$

where h_c = contact conductance, h_g = gap conductance and is given as follows (Yüncü,2006):

$$h_g = \frac{k_g}{Y + M_c} \tag{3}$$

where $k_g =$ conductivity of interstitial fluid, $Y =$ gap distance parameter, $M_c =$ temperature jump at cold surface. The gap distance parameters can be derived as (Yüncü,2006):

$$Y = 1.184\sigma \left[\ln\left(3.132\frac{P}{H_{sur}}\right)\right]^{0.547} \tag{4}$$

where $P =$ pressure, $H_{sur} =$ hardness of softer material, and $\sigma =$ eff. rms surface roughness. The temperature jump at the cold surface can be written as (Yüncü,2006):

$$M_c = \alpha_c \beta \Lambda \tag{5}$$

where $\alpha_c =$ surface accommodation parameter between cold surface and corresponding Gd surface, $\beta = \frac{2\gamma}{1+\gamma} Pr$ gas parameter, $\Lambda =$mean free path of the molecules, $\gamma =$ratio of sp. heats of gas, and $Pr =$ Prandtl number. The surface accommodation parameters is given as (Song,1987):

$$\alpha_c = \frac{2 - \alpha_{c1}}{\alpha_{c1}} + \frac{2 - \alpha_{c2}}{\alpha_{c2}} \tag{6}$$

where α_{c1} and α_{c2} are surface accommodation parameter on Gd surface and the sink surface respectively. α_{c1} and α_{c2} in eq(7) and eq(8) can be thought of as the fraction of heat that can be transferred between the gas and the solid surface (Song,1987). (i.e. effective temperature difference for heat transfer between gas and solid surface is α_{c1} (or α_{c2}) times actual temperature difference)

$$\alpha_{c1} = \exp\left[-\frac{0.57(T_l - 273)}{273}\right]\frac{M_{gas}}{6.8 + M_{gas}} + \frac{2.4\mu_{Gd}}{(1+\mu_{Gd})^2}\left(1 - \exp\left[-\frac{0.57(T_l - 273)}{273}\right]\right) \quad (7)$$

$$\alpha_{c2} = \exp\left[-\frac{0.57(T_c - 273)}{273}\right]\frac{M_{gas}}{6.8 + M_{gas}} + \frac{2.4\mu_{c}}{(1+\mu_{c})^2}\left(1 - \exp\left[-\frac{0.57(T_c - 273)}{273}\right]\right) \quad (8)$$

where $M_{gas} = 1.4M_{air}, \mu_c = \frac{M_{air}}{M_{sink}}, \mu_{Gd} = \frac{M_{air}}{M_{Gd}},$ Here, $M_{air} = 28.966\frac{g}{mol}$, $M_{sink} = \frac{144.242g}{mol}, M_{Gd} = 157.25\frac{g}{mol}$ are molecular weight of air, heat sink (assumed same as Nd) and Gd respectively, $T_c =$ temperature of cold (sink) surface, $T_l =$ temperature of Gd surface in contact with heat sink. The contact conductance can then be written as (Yüncü,2006):

$$h_c = 1.25\frac{k_s\left(\frac{P}{H_{sur}}\right)^{0.95}}{\frac{\sigma}{m}} \quad (9)$$

where $k_s = \frac{2k_1k_2}{k_1+k_2} =$ harmonic mean of conductivities of mating surfaces, and $m =$ effective rms slope.

At hot surface, contact conductance is absent and only gap conductance needs to be taken into account. Thus, the separation distance $dd = g + \delta - th - w_m$, replaces gap distance parameter Y in calculation of gap conductance.

$$M_h = \alpha_h \beta \Lambda \tag{10}$$

$$\alpha_h = \frac{2-\alpha_{h1}}{\alpha_{h1}} + \frac{2-\alpha_{h2}}{\alpha_{h2}} \tag{11}$$

where α_{h1} and α_{h2} are surface accommodation parameter on Nd (hot) surface and the Gd surface respectively given as (Song,1987):

$$\alpha_{h1} = \exp\left[-\frac{0.57(T_h - 273)}{273}\right]\frac{M_{gas}}{6.8 + M_{gas}} + \frac{2.4\mu_h}{(1+\mu_h)^2}\left(1 - \exp\left[-\frac{0.57(T_h - 273)}{273}\right]\right) \tag{12}$$

$$\alpha_{h2} = \exp\left[-\frac{0.57(T_0 - 273)}{273}\right]\frac{M_{gas}}{6.8 + M_{gas}} + \frac{2.4\mu_{Gd}}{(1+\mu_{Gd})^2}\left(1 - \exp\left[-\frac{0.57(T_0 - 273)}{273}\right]\right) \tag{13}$$

$M_{gas} = 1.4M_{air},\ \mu_h = \frac{M_{air}}{M_{Nd}}, \mu_{Gd} = \frac{M_{air}}{M_{Gd}}.$ Here, $M_{air} = 28.966\ g/mol,\ M_{Nd} = 144.242 g/mol,$ $M_{Gd} = 157.25\ g/mol$ are molecular weight of air, Nd and Gd respectively, $T_h =$ temperature of Nd surface, and $T_0 =$ temperature of Gd surface in contact with Nd. The thermal conductance at hot surface is given as:

$$h_{hot} = \frac{k_g}{dd + M_h} \tag{14}$$

Phase II:

Thermal contact conduction estimation for Phase II also follows similar treatment as in Phase I.

In phase II, at cold surface, contact conductance is absent and only gap conductance is acting. Thus, the separation distance $g - th - dd$, replaces gap distance parameter Y in calculation of gap conductance.

$$h_{cold} = \frac{k_g}{g - th - dd + M_c} \tag{15}$$

At hot surface,

$$h_{hot} = h_c + h_g \tag{16}$$

$$h_g = \frac{k_g}{Y + M_h} \tag{17}$$

Phase III:

In Phase III, thermal contact conductance modeling is simplified due to absence of contact. Temperature jump being universal gas-solid interface phenomena is present and actual gap distance between two surfaces is used. On hot and cold sides the actual gap are dd and $g - th - dd$ respectively.

In Phase 3, none of the surfaces are in contact with other surfaces. Thus, only gap conductance contributes to thermal conductance.

$$h_{hot} = \frac{k_g}{dd + M_h} \tag{18}$$

$$h_{cold} = \frac{k_g}{g - th - dd + M_c} \tag{19}$$

We can solve the diffusion equation for the temperature distribution in Gd using finite volume approach, with second order central spatial discretization and implicit time marching scheme as described below:

$$\frac{\partial T_P}{\partial t} = \alpha \frac{\partial^2 T_P}{\partial z^2} \Rightarrow \frac{(T_P^{n+1} - T_P^n)}{\Delta t} = \alpha \frac{(T_S^{n+1} - 2T_P^{n+1} + T_N^{n+1})}{\Delta z^2} \tag{20}$$

$$T_P^{n+1} = T_P^n + \frac{\alpha \Delta t}{\Delta z^2}(T_S^{n+1} - 2T_P^{n+1} + T_N^{n+1}) \tag{21}$$

$$A_N T_N^{n+1} + A_P T_P^{n+1} + A_S T_S^{n+1} = S \tag{22}$$

Here subscripts P, S, N denote the finite volume for which the equation is written, and its north and south neighbors respectively. Superscript denotes the number of time step, Δt and Δz are time and space discretization respectively, $A_P = 1 + 2\frac{\alpha \Delta t}{\Delta z^2}, A_S = -\frac{\alpha \Delta t}{\Delta z^2}, A_N = -\frac{\alpha \Delta t}{\Delta z^2}$ are coefficients of the $T_P^{n+1}, T_S^{n+1}, T_N^{n+1}$ respectively, and $S = T_P^n$ is the source term in the equation.

At the hot boundary, (corresponding to $z = dd$), taking second order forward difference approximation,

$$\frac{\partial T_P}{\partial t} = \alpha \frac{\partial^2 T_P}{\partial z^2} \Rightarrow \frac{(T_P^{n+1} - T_P^n)}{\Delta t} = \alpha \frac{\left(-3\frac{\partial T_P^{n+1}}{\partial z} + 4\frac{\partial T_S^{n+1}}{\partial z} - \frac{\partial T_{SS}^{n+1}}{\partial z}\right)}{2\Delta z} \tag{23}$$

where subscripts SS and SSS correspond to second and third neighbor to south. Substituting $\frac{\partial T_S^{n+1}}{\partial z} = \frac{T_{SS} - T_P}{2\Delta z}, \frac{\partial T_{SS}^{n+1}}{\partial z} = \frac{T_{SSS}^{n+1} - T_S^{n+1}}{2\Delta z}$ and $\frac{\partial T_P^{n+1}}{\partial z} = -\frac{\dot{q}(dd)}{k} = -\frac{h_{hot}(T_h - T_P^{n+1})}{k}$, ($k$ is Gd conductivity), we get

$$T_P^{n+1} = T_P^n + \frac{\alpha \Delta t}{2\Delta z}\left(3\frac{h_{hot}(T_h - T_P^{n+1})}{k} + 4\frac{T_{SS}^{n+1} - T_P^{n+1}}{2\Delta z} - \frac{T_{SSS}^{n+1} - T_S^{n+1}}{2\Delta z}\right) \tag{24}$$

Simplifying, we can write,

$$A_P T_P^{n+1} + A_S T_S^{n+1} + A_{SS} T_{SS}^{n+1} + A_{SSS} T_{SSS}^{n+1} = S \tag{25}$$

Here, $A_P = 1 + \frac{\alpha \Delta t}{2\Delta z}\left(\frac{3h_{hot}}{k} + \frac{2}{\Delta z}\right)$, $A_S = -\frac{\alpha \Delta t}{4\Delta z^2}$, $A_{SS} = -\frac{\alpha \Delta t}{\Delta z^2}$ and $A_{SSS} = \frac{\alpha \Delta t}{4\Delta z^2}$ are coefficients of T_P^{n+1}, T_S^{n+1}, $T_{SS}^{n+1}$and T_{SSS}^{n+1} respectively and $S = T_P^n + \frac{\alpha \Delta t}{2\Delta z}\left(\frac{3h_{hot}T_h}{k}\right)$. Similarly, on the cold boundary $(z = dd + th)$, taking second order backward difference approximation,

$$\frac{\partial T_P}{\partial t} = \alpha \frac{\partial^2 T_P}{\partial z^2} \Rightarrow \frac{(T_P^{n+1} - T_P^n)}{\Delta t} = \alpha \frac{\left(3\frac{\partial T_P^{n+1}}{\partial z} - 4\frac{\partial T_N^{n+1}}{\partial z} + \frac{\partial T_{NN}^{n+1}}{\partial z}\right)}{2\Delta z} \tag{26}$$

Subscripts NN and NNN correspond to second and third neighbor to north. Substituting $\frac{\partial T_N^{n+1}}{\partial z} = \frac{T_P^{n+1} - T_{NN}^{n+1}}{2\Delta z}$, $\frac{\partial T_{NN}^{n+1}}{\partial z} = \frac{T_N^{n+1} - T_{NNN}^{n+1}}{2\Delta z}$ and $\frac{\partial T_P^{n+1}}{\partial z} = -\frac{\dot{q}(dd+th)}{k} = -\frac{h_{cold}(T_P^{n+1} - T_c)}{k} = \frac{h_{cold}(T_c - T_P^{n+1})}{k}$,

$$T_P^{n+1} = T_P^n + \frac{\alpha \Delta t}{2\Delta z}\left(3\frac{h_{cold}(T_c - T_P^{n+1})}{k} - 4\frac{T_P^{n+1} - T_{NN}^{n+1}}{2\Delta z} + \frac{T_N^{n+1} - T_{NNN}^{n+1}}{2\Delta z}\right) \tag{27}$$

Simplifying, we can write,

$$A_{NNN} T_{NNN}^{n+1} + A_{NN} T_{NN}^{n+1} + A_N T_N^{n+1} + A_P T_P^{n+1} = S \tag{28}$$

Here,$A_P = 1 + \frac{\alpha \Delta t}{2\Delta z}\left(\frac{3h_{cold}}{k} + \frac{2}{\Delta z}\right)$, $A_N = -\frac{\alpha \Delta t}{4\Delta z^2}$, $A_{NN} = -\frac{\alpha \Delta t}{\Delta z^2}$ and $A_{NNN} = \frac{\alpha \Delta t}{4\Delta z^2}$ are coefficients of T_P^{n+1}, T_N^{n+1}, $T_{NN}^{n+1}$and T_{NNN}^{n+1} respectively.$S = T_P^n + \frac{\alpha \Delta t}{2\Delta z}\left(\frac{3h_{cold}T_c}{k}\right)$. These equations were solved simultaneously to get the temperature distribution for each successive time step.

5.10.2 Magnetic model

NdFeB (Neodymium Iron Boron) or popularly known as Neodymium (Nd) magnet is a commercially available permanent magnet in various shape and size. It has remnant magnetism of $B_r = 1.32\ T$, and has relatively high Curie temperature $(593\ K)$ and can retain its magnetism within working range of solar module temperatures (hard magnet). We selected rectangular magnet of dimension 20 x 20 x 0.79375 $mm^3(1/32" \approx 0.79375\text{mm})$ for the analysis presented here.

Gadolinium (Gd) is a soft magnet with Curie temperature $of\ 292K$, and loses its magnetism if heated beyond it, making it very suitable for near room temperature application. A heat source slightly above and a heat sink slightly below this Curie temperature can make the cycling possible. We chose the size 20 x 20 x 0.25 mm^3 to provide matching cross –sectional area to Nd magnet. Nd magnet is of rectangular configuration, and its magnetic flux density can be expressed according to Equation (29) (Furlani,2001) as:

$$B_{mag(z)} = \frac{B_r}{\pi}\left[\tan^{-1}\left(\frac{(z+l_{Nd})\sqrt{a^2+b^2+(z+l_{Nd})^2}}{ab}\right) - \tan^{-1}\left(\frac{z\sqrt{a^2+b^2+z^2}}{ab}\right)\right] \quad (29)$$

Here, B_r is remnant magnetization of Nd magnet, and $2a, 2b$ and l_{Nd} are width, length and thickness of the magnet. Nd is magnetized in thickness direction, which corresponds to z-axis of the co-ordinate system, z is distance away from the magnet surface, and $B_{mag}(z)$ is the corresponding magnetic induction at location z. This induction subjects the Gd magnet to external field $H_{mag}(z) = B_{mag}(z)/\mu_0$, where μ_0 is magnetic permeability of vacuum.

Depending on the temperature distribution within the material Gd possesses a corresponding magnetization distribution. Estimating magnetization requires solving a transcendental equation given as (Ponomarev,1986):

$$\frac{M(T,H)}{M_0} = Br_{7/2}\left[\frac{\mu_s\left(H+\gamma M(T,H)\right)}{k_B T}\right] \tag{30}$$

Here, $M(T,H)$ is Gd magnetization corresponding to temperature T in external magnetic field H. M_0 is self-magnetization at reference temperature (0 K), Br_J is Brillouin function which depends on temperature and magnetization, $J = 7/2$ is spin parameter for Gd, μ_s is Bohr magnetron often measured experimentally, γ is effective field constant, and k_B is Boltzmann constant.

However, the applied external field is not very strong and thus the magnetization curve corresponding to the external field practically collapses onto self-magnetization curve as shown in Figure 5-21. In general, maximum self-magnetization is at 0K where material is in ordered state and all ferromagnetic domains are perfectly aligned. Magnetization decreases with increase in temperature as thermal vibration in the material increases disorder. The rate of magnetization drops off drastically as we approach Curie temperature for the material. Above Curie temperature, thermal vibrations overcome ferromagnetism completely and material behaves as paramagnetic. Under externally applied field paramagnetic material may still possess some magnetization due to induction as can be seen in Figure 5-21 for $H = 3.153e6\ A/m$ curve. Self magnetization curves are also available as a solution to transcendental equation involving Brillouin function. Darby (Darby,1967) has solved this transcendental equation and provided the results in tabular form which can be used in the form of look-up table. But linear interpolation

between magnetization curves results into much more accurate estimates and therefore we chose interpolation approach over self-magnetization curve.

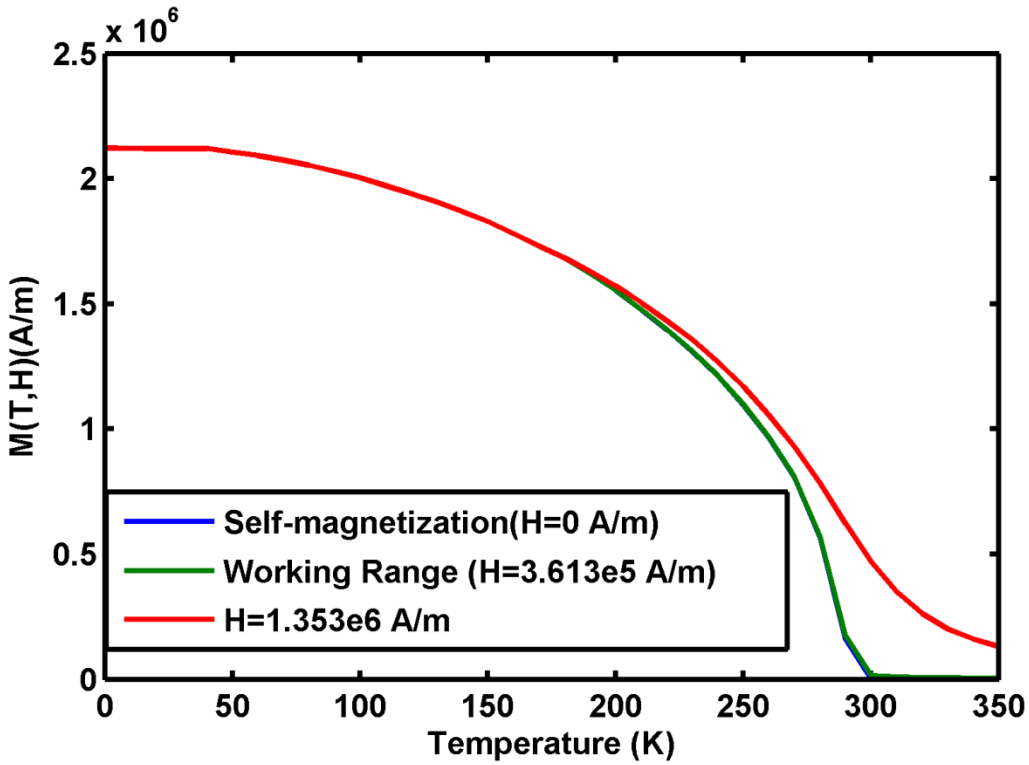

Figure 5-21. Gadolinium magnetization curve, using data from (Ponomarev,1986).

5.10.2.1 Demagnetization factor

Any magnetic material placed under external magnetic field induces magnetization in addition to any temperature dependent self-magnetization in it in the direction of the magnetic field. This magnetization in turn creates another magnetic field internally, called demagnetizing magnetic field that opposes the applied external field. This demagnetizing field reduces the internal magnetic field by a fraction called demagnetization factor. Demagnetization factor (D_z) is function of the magnet geometry. Analytical calculation of demagnetization factor is possible for a few simple geometries only, usually ellipsoid in shape. Aharoni (Aharoni,1998) has calculated the demagnetization factor for rectangular prism shaped magnets analytically. Akoun and Yonnet

(Akoun,1984) have developed finite element approach to calculate the force between two magnets that does take into account the shape effect. Equation (31) represents the demagnetization as a function of thickness, where $2a, 2b$ are length and width of the magnet and $2c = th$ is thickness of the magnet in the direction of magnetization (Aharoni,1998). Figure 5-22 illustrates the variation of demagnetization factor as a function of thickness for our configuration of Gd magnet($2a = 2b = 20mm$).

$$
\begin{aligned}
D_z\left(c = \frac{th}{2}\right) = \frac{1}{\pi}\Bigg[& \frac{a^3 + b^3 - 2c^3}{3abc} - \frac{(a^2+b^2)^{\frac{3}{2}} + (a^2+c^2)^{\frac{3}{2}} + (b^2+c^2)^{\frac{3}{2}}}{3abc} \\
& + \frac{c\left(\sqrt{a^2+c^2} + \sqrt{b^2+c^2}\right)}{ab} + \frac{(a^2+b^2-2c^2)\sqrt{a^2+b^2+c^2}}{3abc} \\
& + \frac{(b^2-c^2)\log\left(\frac{\sqrt{a^2+b^2+c^2}-a}{\sqrt{a^2+b^2+c^2}+a}\right)}{2bc} \\
& + \frac{(a^2-c^2)\log\left(\frac{\sqrt{a^2+b^2+c^2}-b}{\sqrt{a^2+b^2+c^2}+b}\right)}{2ac} \\
& + 2\tan^{-1}\left(\frac{ab}{c\sqrt{a^2+b^2+c^2}}\right) + \frac{b\log\left(\frac{\sqrt{a^2+b^2}+a}{\sqrt{a^2+b^2}-a}\right)}{2c} \\
& + \frac{a\log\left(\frac{\sqrt{a^2+b^2}+b}{\sqrt{a^2+b^2}-b}\right)}{2c} + \frac{c\log\left(\frac{\sqrt{a^2+c^2}+a}{\sqrt{a^2+c^2}-a}\right)}{2b} \\
& + \frac{c\log\left(\frac{\sqrt{b^2+c^2}+b}{\sqrt{b^2+c^2}-b}\right)}{2a}\Bigg]
\end{aligned}
\tag{31}
$$

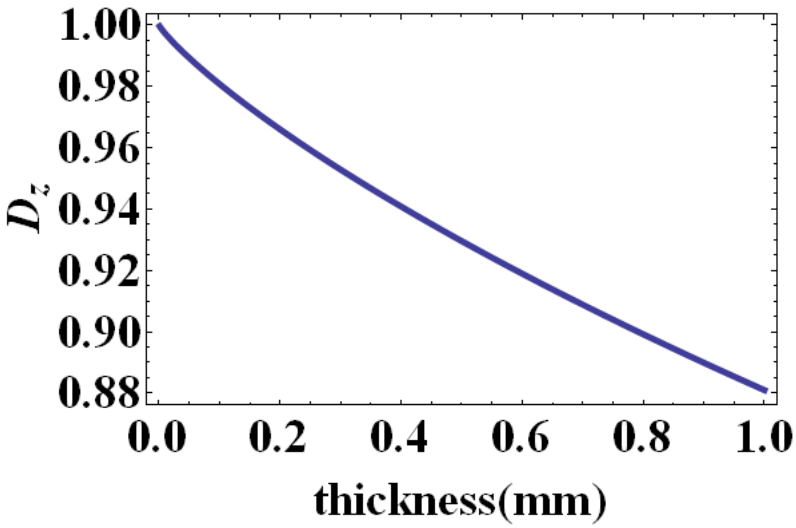

Figure 5-22. Demagnetization factor as function of thickness for rectangular prism shape magnet with 2cm x 2cm cross-sectional area.

It further establishes that internal magnetic field is much reduced compared to external field for Gd thickness $th = 0.25\,mm$ corresponding to demagnetization factor $of\ D_z = 0.9593$. Internal magnetic field generated due to applied external field was $(1 - D_z)H_{Mag} \approx 0.04H_{Mag}$.Thus effect of external field could be comfortably ignored as it is very weak and Gd magnetization can also be treated purely as function of temperature disregarding external magnetic field effect.

5.10.2.2 Magnetic force

In this system, the vibration is driven by the magnetic attraction force acting on Gd magnet, created by applied magnetic field $B_{ext} = B_{mag(z)}$ due to Nd magnet. Thus it is crucial to understand what parameters affect this force and how to derive it. It may be apparent from subsection 5.10.2 that remnant magnetization B_r of Nd magnet, its dimensions $2a, 2b, l_{Nd}$ and

distance z away from it determines external magnetic field at that location. It is also dependent on the volumetric and surface magnetic charge densities in Gd magnet, both of which are function of local magnetization and Gd magnet dimensions. Magnetization in turn is function of temperature as shown in Figure 5-21. Thus, after solving heat transfer model and getting temperature distribution in Gd magnet, magnetization distribution and magnetic force can be calculated. The magneto-static potential energy stored in the magnetic material is given by (Furlani,2001):

$$E_{mag} = \int_V M B_{ext} dV \tag{32}$$

Magneto-static force can be calculated as gradient of the potential,

$$F_{mag} = \nabla\left(E_{mag}\right) = \int_V \nabla(M B_{ext}) dV \tag{33}$$

Using vector calculus identity, we can write,

$$\begin{aligned} F_{mag} = \int_V M \nabla B_{mag} dV &= -\int_V (\nabla . \mathrm{M}) B_{mag} dV + \int_S \mathrm{M} B_{mag} dS \\ &= \int_V \rho_{mag} B_{mag} dV + \int_S \sigma_{mag} B_{mag} dS \end{aligned} \tag{34}$$

Here, $\rho_{mag} = -\nabla . M =$ volume (magnetic) charge density, $\sigma_{mag} = M =$ surface (magnetic) charge density. Thus, magnetic force is function of magnetization M and gradient of magnetization $\nabla . M$ that in turn are function of temperature and temperature gradient respectively. The force in z-direction, assuming temperature is uniform throughout cross-section can be determined as:

$$F_{mag}(z) = -A_{Gd}\int_{w_m}^{w_m+th}\frac{dM}{dz}B_{mag}(z)dz + A_{Gd}\left(M(w_m+th)B_{mag}(w_m+th) - M(w_m)B_{mag}(w_m)\right) \quad (35)$$

Numerically, $F_{mag}(z)$ force given by Eq (35) was solved for by finite volume discretization, calculating volumetric magnetic charge in each finite volume and summing them up. It may be noted that surface charge densities of different finite volume cancels with adjacent volume, thus only end surface magnetic charge densities need to be calculated.

Linear interpolation of the magnetization curve requires high number of division in z-direction to ensure smooth magnetization gradient and thus continuously varying force behavior. Too few divisions would result in unrealistic spikes in force history. Higher order interpolation could solve this issue, but was avoided as it predicts unreal negative magnetization near Curie temperature.

5.10.3 Vibration model

The vibration of Gd magnet attached to the leaf spring under the magnetic force can be given by,

$$\rho A\frac{\partial^2 w}{\partial t^2} + Y_1^E I_{22}\frac{\partial^4 w}{\partial x^2} = P_{ext}(x) \quad (36)$$

where $P_{ext}(x) = \begin{cases} 0, & 0 < x < x_s \\ \frac{F_{mag}(z)}{x_e - x_s}, & x_s \le x \le x_e \\ 0, & x_e < x < L \end{cases}$

is force distribution function, x =longitudinal location along beam length, x_s, x_e = start and end locations of Gd magnet respectively and L = total length of beam. The boundary conditions that the fixed-fixed beam is subjected to are:

$$w(0,t) = 0, \frac{\partial w(x,t)}{\partial x}|_{x=0} = 0 \tag{37}$$

$$w(L,t) = 0, \frac{\partial w(x,t)}{\partial x}|_{x=L} = 0 \tag{38}$$

and the initial conditions are $w(x,0) = w_0(x)$; $\dot{w}(x,0) = \dot{w}_0(x)$. Notice that linear force density $P_{ext}(x)$ is a square wave function having non-zero value over only Gd magnet and is obtained by dividing the total acting force with Gd length in longitudinal direction $(x_e - x_s)$. Assuming $w(x,t) = \sum_{i=1}^{2(n+1)} N_i(x) v_i(t)$, where $n =$ number of finite elements, $v_i(t) = i^{th}$ degree of freedom (DOF) (nodal displacement or nodal slope) as a function of time, and $N_i(x) =$ Shape function corresponding to i^{th} DOF, this Euler-Bernoulli beam equation, with addition of suitable damping, can be written in finite element form as following:

$$[M][\ddot{v}] + [C][\dot{v}] + [K][v] = [P_{ext}] \tag{39}$$

Here, $[C] =$ damping matrix obtained assuming uniform modal damping factor $\zeta = 0.05$ for all modes. For detailed derivation reader may refer to finite element books (Seshu,2006, Reddy,1984, Bathe,1996). To accommodate boundary conditions, since they are fixed value of zero displacement and zero slope at the supports, we only need to remove the equations corresponding to fixed DOFs (i.e. remove corresponding rows and columns from $[M], [C], [K]$ and corresponding rows from $[P_{ext}]$ matrices. In this case the first 2 and last 2 equations shall be dropped that shall also make the system of equations non-singular (i.e., matrices are invertible).

The addition of damping is necessary because in each cycle as the system is worked upon by magnetic force it accumulates work energy. If the same amount of energy is not

dissipated in the cycle, the vibration amplitude will keep increasing indefinitely and unrealistically. If the steady vibration is reached, which is represented by limit cycle on the phase plot, we can safely state that the energy accumulated by the system due to magnetic force equals the energy dissipated in damping. To compute $[C]$, we first need to find eigenvalue and eigenvector matrix of system $[K][EV] = [M][EV][\lambda]$, where $[EV]$ =eigenvector matrix and $[\lambda] =$ eigenvalue matrix (diagonal). Damping matrix is computed as $[C] = [EV]^T \left(2\zeta\sqrt{[\lambda]}\right)[EV]$. For better approximation, frequency dependent nonlinear damping can be considered based on experimentation (Sodano,2004).

We employed Newark average acceleration method for time integration of this equation. In this method, acceleration during the integration time step is assumed constant at average of previous and current time step $\left(\frac{1}{2}([\ddot{v}]_{n+1} + [\ddot{v}]_n)\right)$. Thus velocity and displacement can be found as:

$$[\dot{v}]_{n+1} = [\dot{v}]_n + \left(\frac{1}{2}([\ddot{v}]_{n+1} + [\ddot{v}]_n)\right)\Delta t \tag{40}$$

$$\begin{aligned}[v]_{n+1} &= [v]_n + [\dot{v}]_n \Delta t + \frac{1}{2}\left(\frac{1}{2}([\ddot{v}]_{n+1} + [\ddot{v}]_n)\right)(\Delta t)^2 \\ &= [v]_n + \left(\frac{1}{2}([\dot{v}]_{n+1} + [\dot{v}]_n)\right)\Delta t\end{aligned} \tag{41}$$

Simplifying Eq. (41), we can write,

$$[\dot{v}]_{n+1} = \frac{2}{\Delta t}([v]_{n+1} - [v]_n) - [\dot{v}]_n \tag{42}$$

$$[\ddot{v}]_{n+1} = \frac{4}{(\Delta t)^2}([v]_{n+1} - [v]_n) - \frac{4}{\Delta t}[\dot{v}]_n - [\ddot{v}]_n \tag{43}$$

Now equation of motion for current time step is,

$$[M][\ddot{v}]_{n+1} + [C][\dot{v}]_{n+1} + [K][v]_{n+1} = [P_{ext}]_{n+1} \tag{44}$$

Substituting Eq.(42) and Eq(.43) in Eq(44), and gathering terms of $[v]_{n+1}$ we can write,

$$[K_{iter}][v]_{n+1} = [F_{iter}] \tag{45}$$

where, $[K_{iter}] = \frac{4}{(\Delta t)^2}[M] + \frac{2}{\Delta t}[C] + [K]$ and $[F_{iter}] = [P_{ext}]_{n+1} + [M]\left(\frac{4}{(\Delta t)^2}[v]_n + \frac{4}{\Delta t}[\dot{v}]_n + [\ddot{v}]_n\right) + [C]\left(\frac{2}{\Delta t}[v]_n + [\dot{v}]_n\right)$.

Using Eq.(45) we can find displacement and subsequently velocity and acceleration for all the time steps. Please note that initial acceleration $[\ddot{v}]_0$ is evaluated from initial conditions of displacement $[v]_0$ and velocity $[\dot{v}]_0$ (obtained from $w_0(x)$ and $\dot{w}_0(x)$) as follows,

$$[\ddot{v}]_0 = [M]^{-1}([P_{ext}]_0 - [C][\dot{v}]_0 - [K][v]_0) \tag{46}$$

5.10.3.1 Modeling of contact

It can be noticed that in this system as Gd magnet travels under magnetic, spring and damping forces it gains momentum and it still would have that momentum as it reaches one of the heat transfer surface. Heat transfer surfaces are compliant but much stiffer than the spring. As Gd magnet impacts on one of the heat transfer surfaces (Nd magnet or heat sink) it encounters additional force that comes due to pressure between two impacting surfaces. It transfers its momentum to the heat transfer surface, which is stored as bending strain energy of the heat transfer surface till Gd magnet stops completely, then this stored strain energy is transferred back again to the Gd magnet to impart kinetic energy. The impact is assumed to be completely elastic. As stiffness of the heat transfer surface increases, time of impact becomes shorter, this reflects in increasing the frequency of vibration; however this effect tends to saturate as the contact stiffness

is increased further. The contact behavior is incorporated in the model by assigning a contact stiffness that is multiple of spring stiffness and applying force proportional to the interference. The applied force now gets modified as,

$$P_{ext}(x) = \begin{cases} 0, & 0 < x < x_s \\ \dfrac{F_{mag}(z) + csm\, k_{spring}(\delta - w_m)}{x_e - x_s}, & x_s \le x \le x_e \text{ and } w_m < \delta \\ \dfrac{F_{mag}(z)}{x_e - x_s}, & x_s \le x \le x_e \text{ and } \delta < w_m < g \\ \dfrac{F_{mag}(z) - csm\, k_{spring}\left(w_m - (g + \delta - th)\right)}{x_e - x_s}, & x_s \le x \le x_e \text{ and } g + \delta - th \\ 0, & x_e < x < L \end{cases} \quad (47)$$

5.10.4 Piezoelectric energy harvesting model

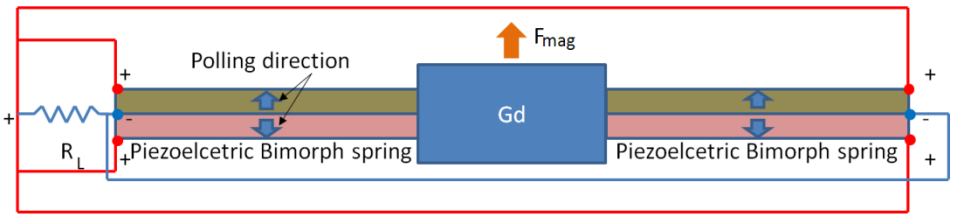

Figure 5-23. Circuit connection of piezoelectric bimorph springs

For energy harvester purpose, we can replace the spring with piezoelectric bimorphs as shown in Figure 5-23, which can harvest mechanical energy from the sustained vibration of system. We further assume parallel electrical configuration for bimorph. i.e., two halves of the springs are poled in opposite direction so that during bending when one half is in relative tension and the other is in relative compression, the generated surface charges have additive effect. All the surface terminals shown by (+) red dots are connected together to one end of the load resistance R_L, and all the negative/reference terminals connecting center of the bimorph spring

are connected together to the other end of R_L. The spring supports are not shown in the figure for simplicity, and magnetic force is shown acting on central Gd magnet. The dynamic system is now a coupled system between vibration equation and electrical charge equation as follows:

$$[M][\ddot{v}] + [C][\dot{v}] + [K][v] - [\Theta]V = [P_{ext}]$$
$$[\Theta]^T[v] + C_p V = q_e \tag{48}$$

where, $[\Theta]$ = control influence parameter = $d_{31}Y_{11p}^E \frac{b_{pzt}h_{pzt}}{2}\int_0^L \frac{\partial^2 N_i(x)}{\partial x^2}\psi(x)dx$, $\psi(x) =$

$\begin{cases} 0, & non\ piezo\ electric \\ 1, & piezo\ electric \end{cases}$,

$V =$ voltage generated, $C_p =$ piezoelectric capacitance = $4(x_s + L - x_e)b_{pzt}\epsilon_{33}^S/h_{pzt}$, $q_e =$electric charge. The system is also subjected to an additional (electric) boundary condition if a load resistance R_L is connected across output terminals. Since the voltage is generated by piezoelectric vibrations, i.e., energy of the system is reducing. Thus, the electrical boundary condition is given as:

$$V_i = -\dot{q}_e R_L \tag{49}$$

The voltage across piezo bimorph is $V = C_p^{-1}q_e$, which in terms of electric charge q_e is written as:

$$[M][\ddot{v}] + [C][\dot{v}] + [K][v] - [\Theta]C_p^{-1}q_e = [P_{ext}]$$
$$R_L\dot{q}_e + C_p^{-1}q_e - C_p^{-1}[\Theta]^T[v] = 0 \tag{50}$$

The coupled system can be solved iteratively, taking initial condition for charge as $q_{e0} = [\Theta]^T[v]_0$. Harvested electrical power can be calculated as $P_{elec} = \dot{q}_e^2 R_L$.

5.11 Results

Before discussing different effects governing the vibration, let's first understand the physics by just considering one complete vibration cycle after steady state vibration is achieved. Figure 5-24 illustrates the behavior of the system over one complete cycle in a steady state vibration. The simulation parameters are given in Table 5-2.

Table 5-2. Simulation parameter for the baseline thermo-magnetic beam vibration

Parameter	Value	Parameter	Value
Gap	2 mm	Prandtl number	0.713
Gd magnet dimension	20 x 20 x 0.25 mm^3	ratio of sp.heats γ	1.4
Spring dimension	2 (5 x 1 x 0.035 mm^3)	σ	0.12 μm
Nd magnet dimension	20 x 20 x 0.79375 mm^3	m	0.022
δ	0.4134 mm	H_{sur}	570 MPa
Density (Gd, spring)	(7900,7500) kg/m^3	B_r	1.32 T
E (Gd,Spring)	$(54.8,48.3)GPa$	dt	10^{-5}s
k (Nd, Gold, air)	$(71.6,318,0.0257)J/kgK$	Thermal divisions	2000
Mean free path	67 nm	Structural divisions	60

5.11.1 Simulation over one complete cycle

Figure 5-24 illustrates behavior of the system over one complete cycle in a steady state vibration. The entire cycle consists of 4 phases:

(i) Gd magnet has reached Nd magnet (hot surface) and is in contact with it, thermal contact conductance (h_{hot}) increases sharply on the contacting surface, heat flows into Gd magnet and it starts losing magnetization rapidly. Correspondingly magnetic force is decreasing and the

difference between T_0 and T_l increases rapidly. Gd magnet transfers its momentum to Nd magnet during a short time of impact and regains it back as it begins to travel back towards the heat sink. During impact, pressure between contacting surfaces varies as half-sinusoidal wave. To plot on the same graph as h_{hot} and h_{cold}, pressure was multiplied by 25.

(ii) Gd magnet loses its contact with Nd magnet and its thermal contact conductance h_{hot} drops sharply at the corresponding surface. The temperature inside the Gd magnet tends to equalize due to diffusion, trying to reach a uniform temperature. In the thermal diffusion process, part of the Gd magnet that was heated above Curie temperature cools down below Curie temperature and thus Gd magnet regains some of the magnetization back and magnetic force correspondingly increases during this phase of the cycle. Pressure on either surface is obviously zero. Thermal contact conductance on either surface is at relatively very low values.

(iii) Gd magnet comes in contact with heat sink. During impact, pressure rises on the corresponding surface in sinusoidal fashion, Gd transfer its momentum to heat sink surface and regains it back towards the later part of the impact. In Figure 5-24(b) to distinguish this pressure from that at the hot surface during phase 1, we assign a negative sign to it. Thermal contact conductance of the colder side increases rapidly, T_l drops rapidly and the difference between T_l and T_0 increases. Due to the temperature drop below Curie temperature, Gd magnetization and corresponding magnetic force increases rapidly.

(iv) Gd magnet loses contact with heat sink, its thermal contact conductance drops sharply at the corresponding surface. The temperature inside the Gd magnet tends to equalize due to diffusion, trying to reach a uniform temperature. In the thermal diffusion process, part of the Gd magnet that was cooled much below Curie temperature heats up to come in the vicinity of the Curie temperature and thus Gd magnet loses some of the magnetization and magnetic force

correspondingly decreases during this phase of the cycle. Pressure on either surface is zero. Thermal contact conductance on either surface is at relatively very low values.

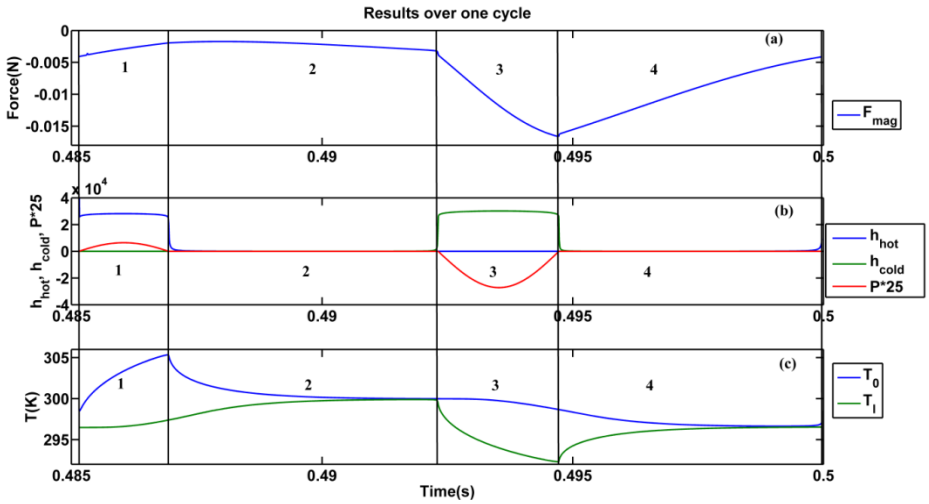

Figure 5-24. Results over one cycle (a) magnetic force (b) h_{hot}, h_{cold} and P*25 (c) T_0 and T_l against time (s)

5.11.2 Transient behavior and limit cycle

It can be stated that the system definitely has one uniform temperature in Gd corresponding to which the magnetic force equals the elastic restoring force of the spring. This point is the steady equilibrium point of the system. The system would have a natural tendency to reach this equilibrium which is its lowest energy state. Steady state vibration would require limit cycle behavior and the steady equilibrium point of system lies inside this limit cycle trajectory. For illustrative simulation, Figure 5-25 shows phase plot for the system and Figure 5-26 shows similar variables as in Figure 5-24 but with complete transient history. The system starts initially with a transient response, i.e., it starts from initial condition such that Gd magnet is touching heat sink surface, and is at temperature of the sink entirely. It sees very high magnetic force and hence accumulates much higher energy compared to what it loses in damping. The system is pushed comfortably beyond Nd magnet line and impact occurs. Spring accumulates strain energy

and is trying to bring back the system to heat sink against stronger magnetic force. Due to heat transfer, Gd magnet loses magnetization and magnetic force reduces and eases the return stroke for the spring. Thus the system does less work in direction opposite to magnetic force and accumulates energy. This additional energy causes Gd magnet to impact on heat sink traveling beyond heat sink line. The impact with heat sink reduces Gd magnet temperature, regains magnetism partially and begins its stroke towards Nd magnet under increased magnetic force again. In this way, the system keep accumulating energy but Gd magnet temperature is rising steadily until energy imparted by magnetic force integrated over the cycle is less than that lost into damping. At this point, the system starts losing more energy in damping than it accumulates due to magnetostatic attraction. It finally, approaches the limit cycle such that equilibrium point is avoided completely. If one complete cycle trajectory falls inside that of the previous cycle, the system is losing more energy with each cycle and can never reach limit cycle and shall spiral inwards to the steady equilibrium point. Also, the asymmetry in the limit cycle (Figure 5-25) suggests that impact is softer and shorter at hot surface compared to that at the cold side. This fact also reflects in thermal contact conductance values, $\max(h_{hot}) < \max(h_{cold})$ in Figure 5-26(c).

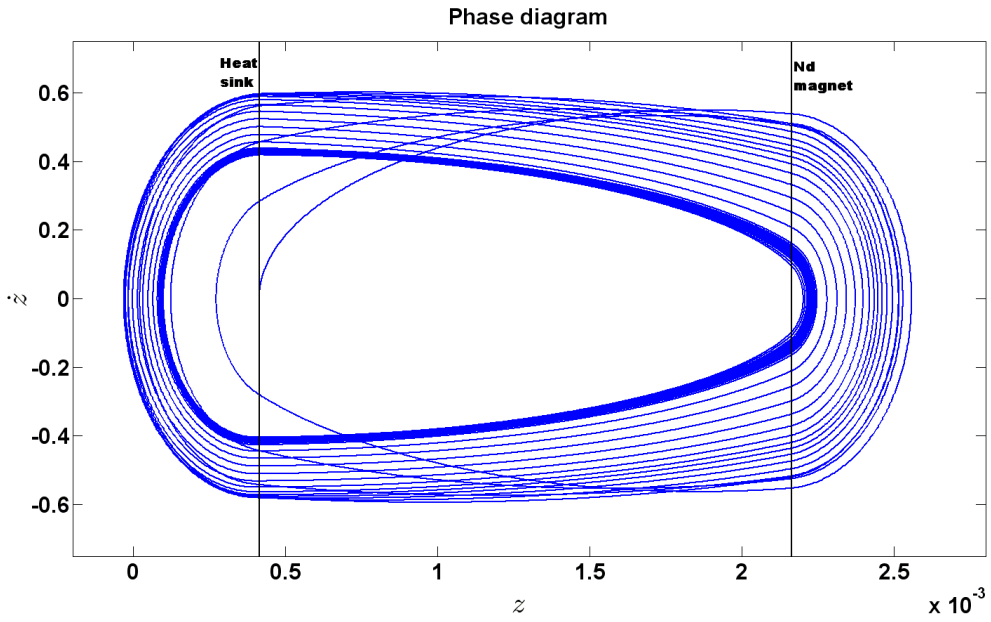

Figure 5-25. Phase diagram and limit cycle behavior of the vibration

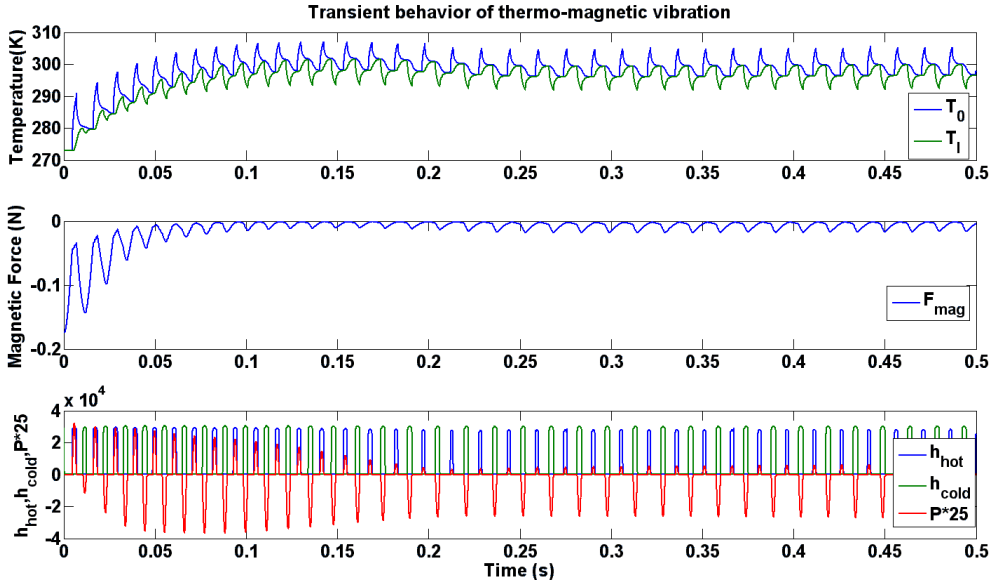

Figure 5-26. Transient response of thermo-magnetic beam vibration (a) temperature T_0 and T_l (b) magnetic force (c) thermal contact conduction on hot and cold side and Pressure*25

Figure 5-26(a) illustrates thermal response of the system, overall Gd temperature rises and overshoots beyond its steady state cycle values and then slowly decreases, magnetic force

(Figure 5-26(b)) correspondingly decreases first and then slowly tends to increase to reach its steady state vibration values. Figure 5-26(c) suggests that value of thermal contact conduction is not affected by this transient behavior much as main component of thermal contact conductance is gap conductance and contact conductance is relatively low because of small contact pressures. Contact pressure initially decreases on hot side and increases on the cold side, suggesting impact softening on the hot side and hardening on cold side and then the trend reverses before achieving values for steady state vibration.

5.11.3 Heat transfer

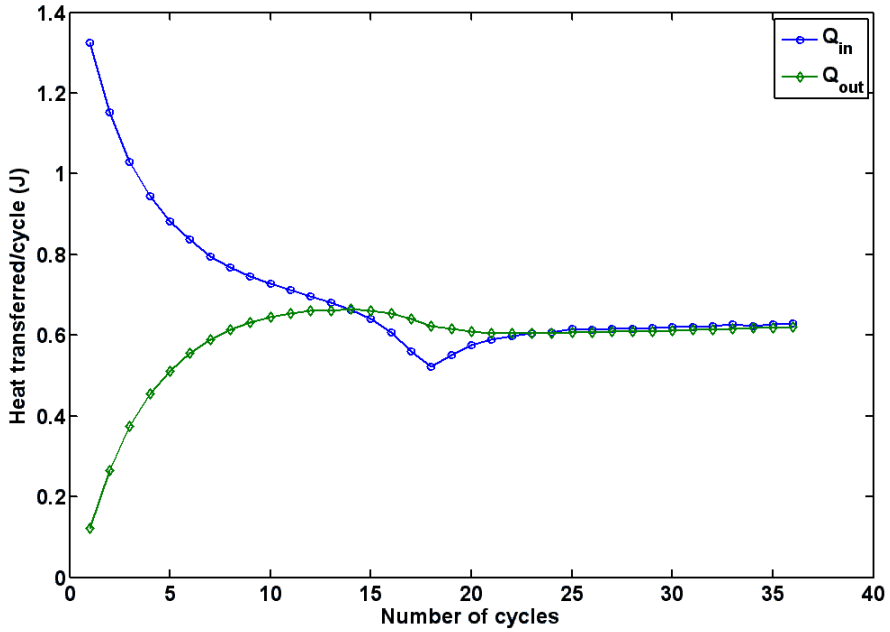

Figure 5-27. Heat transfer per cycle (Q_{in}= total heat inflow in Gd magnet during a cycle, Q_{out}= total heat outflow from Gd magnet during a cycle)

Figure 5-27 depicts the heat transfer from Nd magnet to the heat sink during each complete cycle. It can be calculated using equations (40) and (41) as:

$$Q_{in} = \int_{t'}^{t'+\tau} h_{hot} A_{Gd} (T_{hot} - T_0) dt \tag{40}$$

$$Q_{out} = \int_{t'}^{t'+\tau} h_{cold} A_{Gd} (T_l - T_{cold}) dt \tag{41}$$

$where\ t'$ is time at the beginning of a cycle (we chose the instance Gd leaves heat sink surface), τ is one cycle time, A_{Gd} is area of Gd magnet perpendicular to the direction of heat flow (length x width = $4ab$), Q_{in} and Q_{out} are heat inflow into Gd from Nd magnet and heat outflow from Gd to heat sink during one complete cycle. It can be observed that initially, the heat flowing into the Gd magnet is more compared to heat removed by the heat sink. Between cycles 14 to 22 the trend reverses. By 22nd cycle constancy of thermal behavior has almost been achieved.

5.11.4 Frequency of vibration

Frequency of vibrations depends on several factors: contact stiffness, spring stiffness, initial base deflection, gap distance, temperatures of source and sink relative to Curie temperature to name a few. Thus calculating it analytically is too complex due to multi-physics nature of the problem. Figure 5-28 illustrates variation in vibration frequency with change in gap distance and contact stiffness. For simplification, contact stiffness is considered to be in multiples of spring stiffness. We can deduce that as contact stiffness increases, frequency of vibration increases due to the two impact phases becoming shorter. Traveling time dominates in the cycle time and thus frequency of the oscillation tends to become constant in the limit as contact surfaces become increasingly rigid. When gap g is too small, the energy accumulation is high due to high magnetic force; also energy dissipation reduces due to shorter travel distance. The system vibration frequency increases rapidly due to higher energy dynamics, Gd magnet impacts each heat transfer surface with increasingly high momentum, vibration amplitude keeps increasing unrealistically, and

linear damping assumptions fail. To accurately predict the behavior in such instances, non-linear damping approximations should be used.

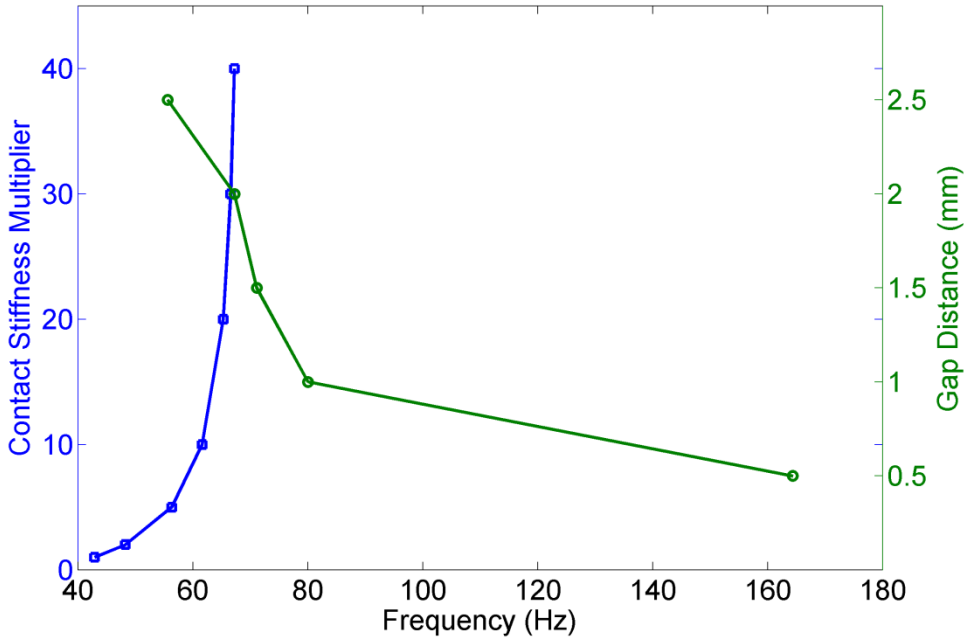

Figure 5-28. Variation in frequency with contact stiffness and gap distance.

5.11.5 Effect of source and sink temperatures

Depending on source and sink temperatures the system exhibits different dynamic behavior. Figure 5-29 (a-1 to d-1), depicts heat transfer per cycle, and Figure 5-29 (a-2 to d-2) depicts corresponding dynamic behavior of the system. As source temperature decreases limit cycle may start showing signs of instability in the limit cycle (Figure 5-29 (a)). In a range where system has sufficient temperature difference (Figure 5-29 (b-c)), the system exhibits stable limit cycle behavior and maintains steady state vibration. Increasing source temperature further makes it difficult for the Gd magnet to magnetize sufficiently in one cooling cycle, as average temperature has increased. This may cause system to fail to reach source surface due to insufficient magnetic pull. But it reaches cooling surface again and may regain sufficient

magnetization to reach source surface again. This causes more than one cooling pass per heating pass, or in other words causes cycle period to be multiple time original limit cycle period. This ultimately results in chaotic behavior as seen in (Figure 5-29 (d)). For ease of observation, only steady state limit cycle is plotted where applicable instead of complete transient phase plot in Figure 5-29 (a-2 to c-2). Figure 5-29 (d-2) shows a little bit more of transient behavior to be able to appreciate chaotic behavior. Figure 5-29 (d-1) shows corresponding heat transfer and it may be noted that heat Q_{in} is zero for certain number of cycles, before again achieving positive value; evidently the system fails to reach source surface for these cycles.

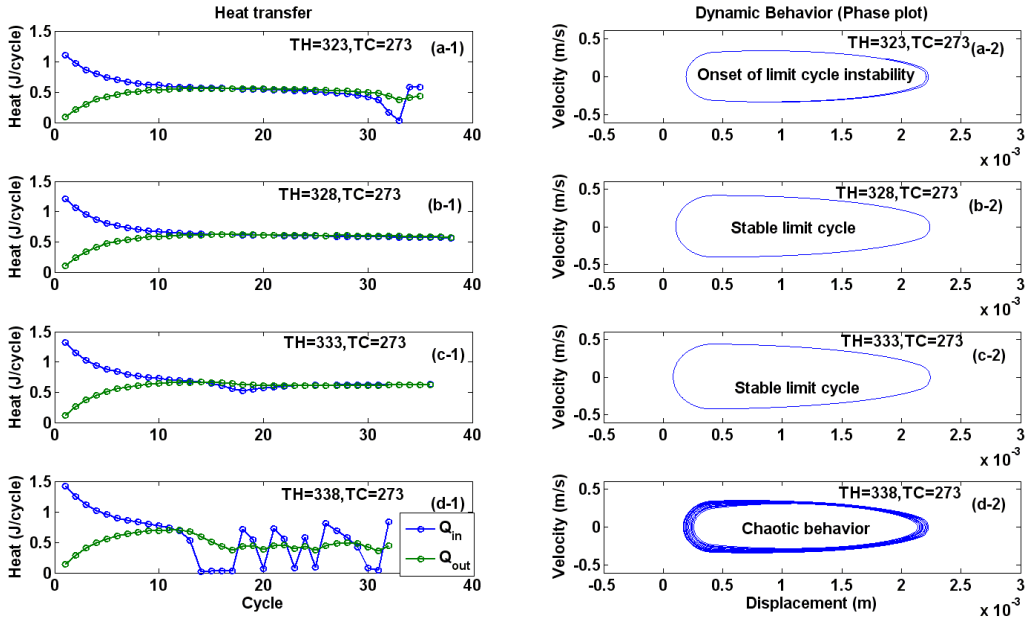

Figure 5-29. Effect of variation of source temperature (a-1, b-1, c-1, d-1) and heat transfer per cycle (a-2, b-2, c-2, d-2) dynamic behavior of the system

Similarly, we can study effect of variation of sink temperature on the system behavior as seen in Figure 5-30.

Lowering sink temperature makes the system reach limit cycle behavior faster Figure 5-30(a). Increasing sink temperature ultimately causes failure of reaching limit cycle behavior because of insufficient cooling and range of magnetic force narrows and the system ultimately goes into

stable spiral reaching an equilibrium point where magnetic force due to a uniform temperature in Gd magnet equals spring force Figure 5-30(c-d). This behavior can also be studied through heat transfer behavior. Figure 5-30(c-1, d-1) suggests that heat going into Gd is zero for several cycles towards end that causes the system to ultimately reach equilibrium point. Note that this equilibrium point may be different for different sink temperatures as is seen in Figure 5-30(c-2, d-2) that has different equilibrium points.

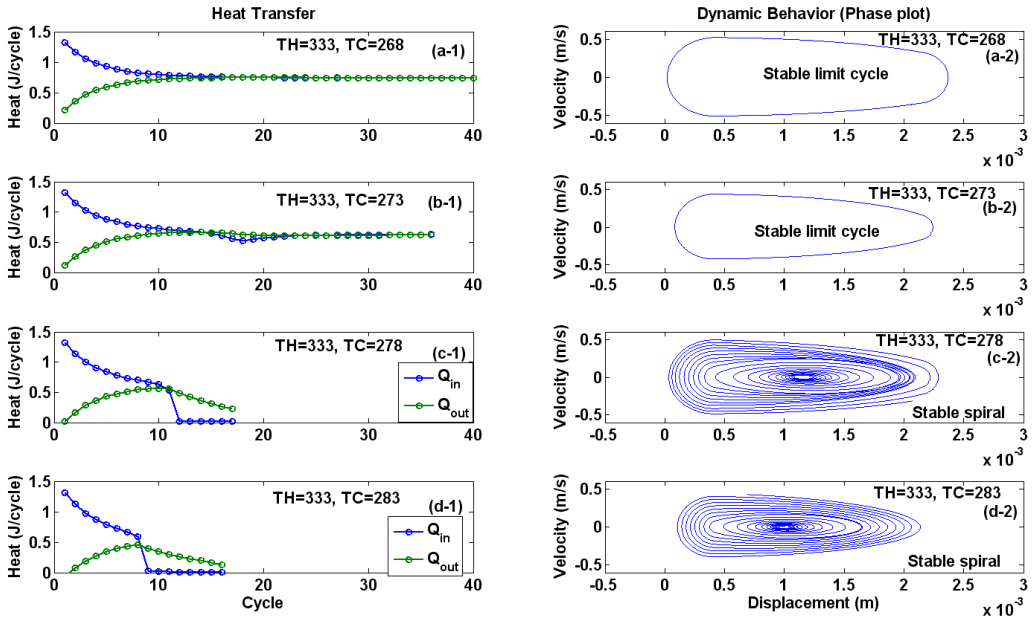

Figure 5-30. Effect of variation of sink temperature (a-1, b-1, c-1, d-1) Heat transfer per cycle (a-2, b-2, c-2, d-2) dynamic behavior of the system

5.11.6 Electrical power harvested as a function of load resistance

Prior researchers have developed models for energy harvesting using piezoelectric bimorph. Elvin and Elvin (Elvin,2009) have presented equivalent circuit approach and Ajitsaria et al. (Ajitsaria,2007) have validated this approach with experimental results. Youn and Becker (Youn,1991) have presented the finite element approach. Yu-His and Chien-Ching (Yu-Hsi,2009) have studied the vibration characteristics of series and parallel type bimorph

configuration using finite element approach. We selected Sonado et al.'s approach (Sodano,2004) because it fits with our modeling methodology. The properties for piezoelectric bimorph used in the modeling are presented in Table 5-3. These values were taken from Karami et al. (Karami,2011) corresponding to PZT-5H which are better for energy harvesting purpose.

As explained in modeling section, solving for electrical energy harvested requires solving a coupled system with an additional electrical boundary condition. Piezoelectric bimorph is assumed to behave linearly within working range of the model; any internal resistance in the piezoelectric bimorph is ignored compared to large load resistance R_L and power during the cycle was calculated as an average of instantaneous power throughout the simulation time. Effect of presence of magnetic field on the electrical charge was ignored. The additional parameters used to simulated power harvested are shown in Table 2. Electrical power harvested was determined as a function of load resistance. Maximum power was obtained when electrical impedance equals mechanical impedance. Figure 5-31 illustrates the variation of power with load resistance. The maximum power obtained was $P_{elec} = 318.17\mu W$ across $R_L = 100k\Omega$.

Table 5-3. Parameters for piezoelectric energy harvesting simulation (Karami,2011)

Parameter	Value
d_{31}	-3.2e-10 C/N
Y_{11p}	60.6 GPa
ϵ_{33}^{s}	3800 (relative)
ρ_p	$7800 kg/m^3$

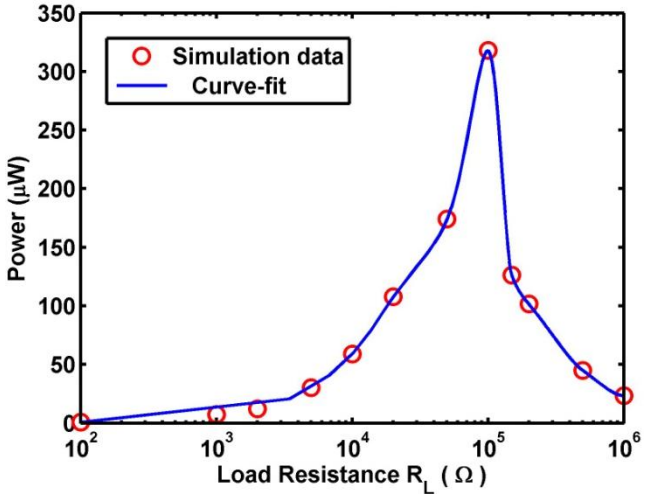

Figure 5-31. Harvested electrical power as a function of load resistance (R_L)

5.12 Conclusion

The multi-physics numerical model we developed here is capable of simulating a range of different scenario of the vibration behavior of the fixed-fixed beam in the thermo-magnetic energy harvester. It provides an opportunity to study interactions of different physics and effect of the device parameters on dynamic behavior of system. Since the magnetic force is unidirectional, restoring spring force should also be made unidirectional (but opposing magnetic pull) by intentionally adding a base offset. For sustained vibration indicated by a single limit cycle behavior constancy of thermal cycling must be achieved i.e., heat input to the system nearly equals heat rejected repeatedly cycle after cycle. Increasing source temperature much beyond Curie temperature may lead to insufficient cooling in one cycle, requiring multiple cooling pass per heating pass resulting in period doubling limit cycle bifurcation. Decreasing sink temperature too much causes insufficient demagnetization during heating, restoring spring has to work against stronger magnetic force and system may keep losing more energy each cycle resulting in stable spiral behavior.

Contact stiffness increases frequency of vibration by reducing impact duration with heat transfer surface, but tends to saturate as contact stiffness increases. Increase in gap distance reduces frequency of vibration. If the gap distance is too small, the magnetic force is strong even towards cold surface, this increases system energy and linear damping assumption fails to limit vibration amplitude to reasonable limit and results in modeling instability. If gap distance is too large, it has to travel farther and overcome stronger spring restoring force due to higher displacements, this may require multiple cooling passes to achieve strong enough magnetic force to reach hot surface. This multiple cooling pass per heating pass is indication of period doubling limit cycle bifurcation. Beyond a certain value, increase in gap could cause spring strain energy to be sufficiently high that magnetic force can't overcome it and Gd can no longer reach hot surface and the system will keep losing energy to achieve steady state equilibrium. The system exhibits different dynamic behavior, such as stable spiral, stable limit cycle, period doubling limit cycle bifurcation and ultimately chaos observable by variation in source and sink temperatures.

To achieve best performance of the system, it should be operated at source and sink temperature fairly equally apart from Gd Curie temperature that helps to achieve steady state vibrations at a gap distance and spring stiffness carefully adjusted such that total force on the Gd magnet over the cycle is symmetrical about zero to achieve energy balance faster. The thermo-magnetic energy harvester device modeled here shows a promising approach. It could transfer heat from solar module effectively and simultaneously convert part of the energy into useful electrical power that may be inspire a new generation of efficient and cost effective UAV designs. The device however is not restricted to UAV application but can harvest small thermal

gradients universally present around us: wall of pipe carrying hot water, radiators, electrical heat sinks, to name a few.

Acknowledgement:

This research is sponsored by AFOSR SBIR Phase I program . The authors would also like to acknowledge Office of Naval Research for partial support in the period after the Phase I through contract number N00014-08-1-0654.

Chapter 6. Bio-inspired buoyancy control for undersea vehicles

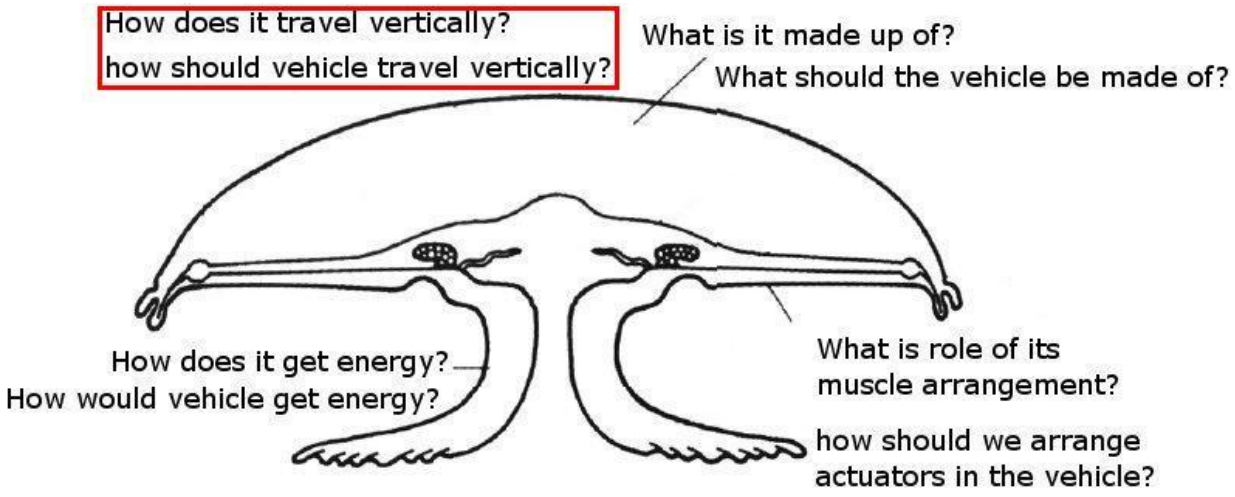

Figure 6-1. Research objective of chapter 6

Buoyancy control is almost universal in aquatic animals through different mechanisms: maintaining gas pressure in swim bladder, maintaining ion concentration in the bladder, reducing calcification of exoskeleton, increasing lipid content, and selective ion replacement. This buoyancy control provides them with a very energy efficient means of maintaining their vertical position in the water body. Most aquatic animals are homoiosmotic and maintain body fluid and ionic concentrations different than that of their surrounding environment. These animals for their very existence do have to maintain this concentration at the expense of some energy. We propose a bio-inspired buoyancy control chamber for undersea vehicle that employs electro-osmosis to achieve change in density in the buoyancy chamber. The model is developed from principles of electro-osmosis to be used in ocean water. The depth change is achieved depending on the local pycnocline, which is not modeled as part of this work.

6.1 Inspiration

Buoyancy control has been employed by marine animals almost universally in one or the other form to provide them with energy conservative means of maintaining their vertical

positions in water. Marine animals are known to employ various mechanisms to achieve positive or negative buoyancies according to requirement. Some species employ swim bladder and maintain equilibrium with surrounding by controlling gas pressure (usually Oxygen and Nitrogen) in the bladder, some species achieve it by, reduction in calcification of exoskeleton, or an increase in lipid content (Macdonald,1975). Some other pelagic marine invertebrates achieve it by ion replacement (Kahn,1978). Pelagic crustacean, the deep sea shrimp *Notostomus gibbosus* achieves it by changing the density of fluid content in its dorsal carapace, weighing about 43% of its body weight, by selectively replacing ions of higher or lower density. This mechanism allows it to achieve a lift of 17.7 mg/ml.(Sanders,1988). Some animals achieve buoyancy increasing or reducing water content by using osmotic regulation (Krogh,1965). These mechanisms employed by natural animals provide inspiration to achieve buoyancy control and thus controlled vertical motion in undersea vehicles in energy efficient way.

In many marine animals some form of electro-osmotic ion transfer is known to be employed as a mechanism to maintain the desired concentration of ions in the body fluid in ocean or freshwater environment. The animals that are in osmotic equilibrium with their surrounding fluid environment are called “poikilosmotic”. A large number of invertebrate animals fall in this class. Their body fluid concentration changes passively with concentration of surrounding fluid concentrations. The other and much broader class of animals that maintain concentration of body fluids different than surroundings is called “homoiosmotic”. The subclasses of homoiosmotic animals are “stenohaline” those can tolerate only a small range of concentration change from the outer fluid and “euryhaline” who can sustain a very different concentration of body fluid that the surroundings. Homoiosmotic has to employ some kind of constant ion transfer to achieve this at the expense of energy. Jellyfish does maintain

concentration of ions in mesoglea different than its surroundings as shown in Table 3-1 and the buoyancy mechanism that we shall discuss here is inspired by this phenomenon.

After a brief introduction to osmosis and osmosis potential, we will introduce electro-osmotic flow equations. We will apply these equations to design a buoyancy chamber (swim bladder) in ocean environment. We will discuss a little about ocean environment affecting pycnocline (plot of change in density with ocean depth) and what performance can be expected from this design.

6.2 Osmosis and electro-osmosis preliminary

The osmosis finds a very wide application in diverse fields. It is a very critical parameter of soil property affecting plant growth (Cochrane,2005) and is widely studied in plant-soil science and also in cell biology. In industry, it is used widely for gas separation (Lindbråthen,2009). In medical field, osmosis is used in hyperbaric oxygen therapy for rapid diffusion of oxygen in blood to achieve rapid recovery of patient, which may avoid amputation of limb in certain cases (Hills,1999, Babchin,2011). Principle of electro-osmosis is also used in corrosion prevention of underwater reinforced concrete structure (Hock,2005). In this process, the natural intrusion of water in the reinforced concrete structure due to hydrostatic pressure is reversed by applying electro-osmotic pulses such that the positive ions are repelled by the applied electric field and creating ion-density gradients that in turn create osmotic pressure gradient in direction opposite to hydrostatic pressure. In spite of such wide application, some misconception exists about the exact mechanism of osmosis and sign of osmotic pressure. Hammel (HAMMEL,1999) discusses quite a few of them in his review paper. Ben-Sasson (Ben-Sasson,2003) presents a microscopic model of the osmosis to explain the sign of the osmotic pressure. Müller (Müller,2005) provides a very detailed understanding of the osmosis

phenomena from thermodynamics point of view providing a complete understanding of the phenomena.

For illustration, considering only one solute we can write chemical potential of the solution as shown in Eq. (1)

$$\mu = \mu^* + RT\ ln\ x_1 = \mu^* + RT \ln(1 - x_2) \tag{1}$$

Where μ is the chemical potential of the solvent in the solution, μ^* is chemical potential of the pure solvent, x_1 and x_2 are mole fraction of the solvent and the solute respectively, R is universal gas constant and T is the temperature. The equation resembles that of ideal gas chemical potential equation. To calculate osmotic pressure created due to presence of solute, we can employ cyclic relation as shown in equation 3,

$$\left(\frac{\partial p}{\partial x_2}\right)_{\mu} = -\frac{\left(\frac{\partial \mu}{\partial x_2}\right)_{p,T}}{\left(\frac{\partial \mu}{\partial p}\right)_{x_2,T}} = -\frac{RT\frac{1}{1-x_2}(-1)}{\left(\frac{\partial G}{\partial p}\right)_{T}} = -\frac{RT\frac{1}{1-x_2}(-1)}{\bar{V}_1} \tag{2}$$

Here, p is pressure, G is Gibbs free energy $= U + pV - Ts$ (internal energy +pressure*volume + temperature*entropy), $\bar{V}_1$ is molar specific volume of the solvent. This increase in pressure with increase in solute concentration is termed as osmotic pressure. Thus, osmotic pressure is fundamentally related to thermodynamics of the solution. For dilute solutions, $1 - x_2 \approx 1$

$$\therefore \left(\frac{\partial p}{\partial x_2}\right)_{\mu} = \frac{RT}{\bar{V}_1}\frac{1}{1-x_2} \approx \frac{RT}{\bar{V}_1} \tag{3}$$

Total osmotic pressure can be obtained by integrating Eq.(3),

$$dp = \frac{RT}{\bar{V}_1}dx_2 \Rightarrow \Pi = RTx_2 = RT\frac{n_2}{n_1 + n_2} \tag{4}$$

Here, Π is osmotic pressure, n_1 and n_2 are moles of the solvent and solute respectively. By definition, $n_1\bar{V}_1 = V$ (total volume)

$$\Pi = RT\frac{n_2}{V} \tag{5}$$

If the solute dissociates into more than one component (e.g., in ionic solutions 1 mole NaCl gives 1 mole Na^+ and 1 mole Cl^-), van't Hopf factor is usually multiplied in the equation.

$$\Pi = iRT\frac{n_2}{V} = iNk_BT \tag{6}$$

Eq (6) is another popular equation for osmotic pressure, here, $i = 1 + \alpha(n-1)$, is van't Hopf factor, and is a function of dissociation factor α and number of component (ions) n created on dissociation of one solute atom, k_B is Boltzmann constant (a measure of kinetic energy of individual molecule at given temperature T), N is total number of solute molecule.

Ben-Sasson (Ben-Sasson,2003) explains that osmotic pressure just like hydraulic pressure arises due to aggregate momentum imparted to the semi-permeable membrane surface due to random thermodynamic motion of the molecules depending on the kinetic energy of the component at given temperature in unit time. If there is a pure solvent on one side and a solution on the other side, impact due to solvent molecules create hydraulic pressure and is equal on both sides of the membrane, whereas impact of solute atoms do not have any counterpart on pure solvent side and thus results in net pressure difference across membrane. This difference is called pressure jump.

The steady-state volume flux across the membrane can be given by,

$$J_v = -L_p(\Delta P - \sigma RT\Delta C) \tag{7}$$

Here, J_v is steady-state flux across membrane, L_p the hydraulic conductivity, ΔP the hydrostatic pressure difference, and σ the reflection coefficient. For ideal semipermeable

membrane $\sigma = 1$; for completely permeable membrane $\sigma = 0$.

It is interesting to note that if the membrane is leaking, then initially water would flow across due to osmosis towards high concentration solution, but due to leakage diffusion of the solute molecules across the membrane occurs and the osmotic pressure diminishes (A. Babchin,2011).

When the solution contains ions, on application of electric field, ion flow occurs and it also causes solvent flow due to viscous forces and osmosis. This special case of osmosis called electro-osmosis is very useful in many applications such as drying of capillary porous bodies, electro-osmotic loosening of soils, increasing strength of powder materials, extraction of an organic phase from natural headers to increase efficiency of petroleum header operation. Tikhomolova (Tikhomolova,1993) in his excellent work deals with various modeling aspects of electro-osmosis.

6.3 The buoyancy engine

We propose a buoyancy engine schematically presented by Figure 6-2to achieve change in buoyancy in the swim bladder by selective ion replacement. It consists of a closed volume of ocean water, with one side covered by semipermeable membrane (e.g., Nafion) that allows cations (+ve ions) to pass through but is impermeable to anions (-ve ions). Two electrodes – one inside the buoyancy chamber and one outside – are placed across semipermeable membrane and are connected to external power source that creates electric field across the membrane. Initially, swim bladder of our vehicle (also called buoyancy chamber) is in equilibrium with the open ocean and concentration of all the constituents are assumed to be the same. As we apply electric potential across electrodes parallel to semipermeable membrane such that cations start flowing into the buoyancy chamber, increasing density of the fluid inside. There will be chemical

reactions also at the electrodes accompanying along with this ion flow. Gas byproducts of the process are removed instantaneously and are assumed to have no effect on rest of the process dynamics. Detailed modeling considerations and assumptions are discussed in the following modeling section.

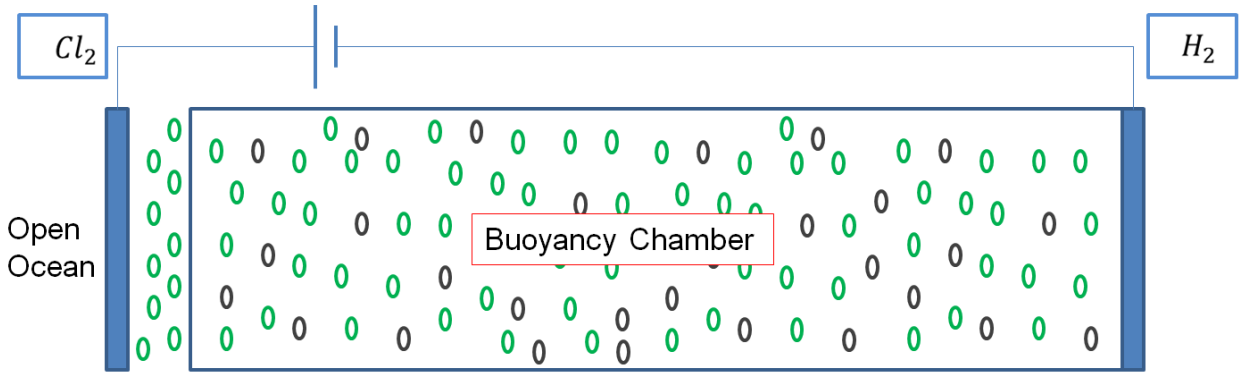

Figure 6-2. Schematic of the buoyancy engine

6.4 Ocean water contents

Ocean contains a variety of salts. The constituents of ocean water are given in Table 6-1 according to ASTM D-1141-98(2003). We shall consider only first 5 salts ($NaCl, MgCl_2, Na_2SO_4, CaCl_2, KCl$) that makes up for more than 99% of all salt content. Inclusion of all the salts wasn't possible for want of critical properties such as diffusivity, dissociation constant, van't hopf factor etc for simulation. We assume complete dissociation of the selected salts into their respective ionic components. After dissociation, total molar concentration, diffusion constant and valency are given in Table 6-2. Note that we have considered presence of H^+ and OH^- ions in water at pH 7, this was required to avoid numerical singularity.

Table 6-1. Chemical composition of substitute ocean water (ASTM D1141-98(2003))

Compound	Concentration, (g/L)	Molecular weight (g/mol)	mol/L	Compound	Concentration, (g/L)	Molecular weight (g/mol)	mol/L
NaCl	24.53	58.443	0.4197	**$SrCl_3$**	0.025	158.5	1.58E-4
$MgCl_2$	5.2	95.211	0.0546	**NaF**	0.003	41.988	7.14E-05
Na_2SO_4	4.09	142.042	0.0288	**$Ba(NO_3)_2$**	9.94E-5	261.337	3.8E-07
$CaCl_2$	1.16	110.98	0.0105	**$Mn(NO_2)_2$**	3.4E-5	146.949	2.31E-07
KCl	0.695	74.551	0.0093	**$Cu(NO_3)_2$**	3.08E-5	187.56	1.64E-07
$NaHCO_3$	0.201	84.007	2.39E-3	**$Zn(NO_3)_2$**	9.6E-6	189.4	5.07E-08
KBr	0.101	119	8.49E-4	**$Pb(NO_3)_2$**	6.6E-6	331.2	1.99E-08
H_3BO_3	0.027	61.833	4.37E-4	**$AgNO_3$**	4.9E-7	169.873	2.88E-09

Table 6-2. Important properties for selected ions

Ion	*Molecular weight (g/mol)*	*mol/L*	*Diffusion constant (10^{-10} m^2/s)*	*valency*	*Ion*	*Molecular weight (g/mol)*	*mol/L*	*Diffusion constant (10^{-10} m^2/s)*	*valency*
Na^+	22.9897	0.4773	11.3	+1	H^+	1.00794	1E-7	81.7	+1
Mg^{+2}	24.305	0.0546	5.94	+2	Cl^-	35.453	0.56	17.1	-1
Ca^{+2}	40.078	0.0105	6.73	+2	SO_4^{-2}	96.063	0.0288	8.9	-2
K^+	39.0983	0.0101	16.7	+1	OH^-	17.0073	1E-7	44.9	-1

6.5 The electro-chemical reaction

On the application of the electric field, the solution (ocean water) acts as electrolyte and the system acts as electro-chemical cell. At the positive and negative electrodes oxidation and reduction reactions would take place respectively. Normally, which reaction would take place is determined by half-cell potential comparing it with reference SHE (Standard Hydrogen Electrode). It is given by Eq (8),

$$E = E^0 + 2.303\frac{RT}{zF}\ln a(M^{z+}) \quad (8)$$

Here, R is gas constant, T is absolute temperature, z is number of electrons involved in the reaction, F is Faraday's constant $96485.34\ C/mol$. The activity of ion, $a(M^{z+})$, is defined by Eq.(9),

$$a(M^{z+}) = \gamma c(M^{z+}) \quad (9)$$

Here, $c(M^{z+})$ is the concentration of M^{z+} (mole/ liter) and $\gamma(M^{z+})$ is the activity coefficient of M^{z+}; When activity coefficient is low, such as 0.001M and lower, the activity may be replaced by concentration in mole/liter(Paunovic,2010). This justifies neglecting compounds with low concentration. The reactions that take place also follow this rule. Some of the possible half reactions are listed in Table 6-3.

Table 6-3. Possible half reaction potential

Half Reaction	Voltage Potential	Half Reaction	Voltage Potential
$Na^+ + e^- \rightarrow Na$	-2.71	$Cu^{2+} + 2e^- \rightarrow Cu$	0.34
$Ca^{2+} + 2e^- \rightarrow Ca$	-2.87	$2H_2O + 2e^- \rightarrow H_2(g) + 2OH^-$	-0.83
$Mg^{2+} + e^- \rightarrow Mg$	-2.37	$2Cl^- \rightarrow Cl_2 + 2e^-$	-1.36
$K^+ + e^- \rightarrow K$	-2.92	$Mn^{2+} + 2H_2O \rightarrow MnO_2 + 4H + 2e^-$	-1.28
$2H_2O + 2e^- \rightarrow H_2(g) + 2OH^-$	-0.83	$2H_20 \rightarrow O_2(g) + 4H^+ + 4e^-$	-1.23
$2H^+ + 2e^- \rightarrow H_2(g)$	0.00	$2H^+ + 2e^- \rightarrow H_2(g)$	0.00

The actual reaction taking place are as shown in Eq.(10) and Eq.(11)

$$Reduction: 2H_2O + 2e^- \rightarrow H_2(g) + 2OH^- \quad (10)$$

$$Oxidation: 2Cl^- \rightarrow Cl_2 + 2e^- \quad (11)$$

Minimum electromotive force for this reaction is (2.19V) for standard cell. Initially both at cathode and at anode ion concentrations are same, thus correction to standard half reaction

voltage cancels out. For other cases correction should be made by Eq (8). At 2.19 V this reaction is just at equilibrium. Any voltage above 2.19V is called over-potential and is responsible for rate of chemical reaction. For simulation purposes here, we shall assume 0.05V of over-potential applied. Due to this reaction, now there is now deficiency of cations in the buoyancy chamber and under electric field all the cations try to move towards the negative electrode. Cations usually are denser and thus faster moving ions, also because of their smaller size, they pass through Nafion pores easily which is typically of the order of 10nm.

6.6 Modeling strategy

There are different approaches to solving electro-osmosis equations. Usually, they are solved for flow through porous capillary(Tikhomolova,1993), voltage response of electro-active membrane (Sokalski,2003), flow of fluids through nano channels (Schuss,2001) etc. At this scale, a characteristic voltage potential possessed by any surface attracts either positive or negative end of solvent atom (assuming dielectric solvent like water). This causes charge adsorption into the surface, forms electrical double layer and makes the bulk fluid electrically charged. Interest for such researcher is to solve for electrical field close to electrical double layer. We however are solving at macro scale and Debye length, a characteristic measure of thickness of double layer is negligible O($10^{-11}m$). Thus we are neglecting this effect. Water is assumed incompressible and Nafion membrane is assumed rigid thus not permitting any water inflow. Thus density change is assumed to be caused only by change in ion densities in the buoyancy chamber.

We need to solve the following Nernst-Planck equations Eq(12) and Poisson equation Eq(13).

$$\frac{\partial c_i}{\partial t} = -\frac{\partial j_i}{\partial x} = D_i \frac{\partial c_i^2}{\partial x^2} + \frac{D_i z_i F c_i}{RT} \frac{\partial^2 \phi}{\partial x^2} - \frac{\partial (c_i v)}{\partial x} \quad (12)$$

$$\frac{\partial^2 \phi}{\partial x^2} = -\frac{\rho_E}{\epsilon} \quad (13)$$

here, c_i = concentration of ion $'i'$ in mol/m^3, j_i = flux of the ion $'i'$ in $mol/m^2 s$, D_i=self diffusion constant of ion $'i'$, z_i = valency of ion $'i'$, F =Faraday's constant 96485.34 C/mol, R = universal gas constant 8.3144621 $J/molK$, ϕ =voltage potential in V, v = mass averaged velocity≈ v_0 velocity of solvent m/s, ρ_E =electrical charge density C/m^3=$\sum_i z_i c_i F$, ϵ =electrical permittivity of medium,x = spatial dimension m and t =time s.

In Eq(12) first term on the right is diffusion term or equivalent to osmotic pressure term, the second term corresponds to electrostatic force, and third term is convection term. Since we assume incompressibility of water, $v_0 = 0$ for closed volume thus convection term can be neglected. Eq(12) for all the ions in questions need to be solved simultaneously, and as ions travel under electric field, the medium is no longer electrically neutral and electrical field is modified. Thus simultaneous solving of all Eq(12) and Eq (13) is required.

The equations were solve following approach suggested by Sokalski et. al. (Sokalski,2003). For ease of solving following dimensionless parameters were used.

$$\tilde{x} = \frac{x}{L}; \widetilde{c_i} = \frac{c_i}{c_{ref}}; \widetilde{D_i} = \frac{D_i}{D_{ref}}; \tau = \frac{t}{L^2/D_{ref}}; \widetilde{j_i} = \frac{j_i}{\frac{D_{ref} c_{ref}}{L}}; \tilde{\phi} = \frac{\phi F}{RT}; \tilde{E} = \frac{EF}{RTL}; \tilde{\epsilon} = \frac{\epsilon}{\epsilon_0} \quad (14)$$

Here, we chose L= length of buoyancy chamber (~distance between electrodes), $c_{ref} = c_{Na}; D_{ref} = D_{Na}; \epsilon_0$ =permittivity of vaccum= $8.85418E-12\ C^2/Nm^2$, $\tilde{\epsilon}$ =relative permittivity of ocean water= 85.

In this form, the flux at any cross-section is,

$$\widetilde{J_i} = -\widetilde{D_i}\left(\frac{\partial \widetilde{c_i}}{\partial \tilde{x}} - z_i \widetilde{c_i} E\right) \tag{14}$$

$$\frac{\partial \widetilde{c_i}}{\partial \tau} = -\frac{\partial \widetilde{J_i}}{\partial \tilde{x}} \tag{15}$$

We can also write current density equation,

$$\tilde{\imath}(x,t) = \sum_i \widetilde{J_i} + \tilde{\epsilon}\frac{\partial \tilde{E}}{\partial \tau} \tag{16}$$

Here, $\tilde{\epsilon}\frac{\partial \tilde{E}}{\partial \tau}$ corresponds to displacement current. Taking $\tilde{\imath}(x,t) = 0$, $\tilde{\epsilon}\frac{\partial \tilde{E}}{\partial \tau} = -\sum_i \widetilde{J_i}$ i.e., rate of change of electrical field resists further flux of ions.

The spatial discretization was done such that towards end the grid is finer and towards middle grid is coarser by following power law increase in steps. Ion concentration nodes were placed in the middle of the segment, while electric field and flux nodes were placed at segment boundaries. Time steps were taken as a power function. For N concentration nodes, there will be N+1 flux and electrical field nodes. If i denotes ion index and k denotes division, x_{fk} =distance between flux nodes k and $k+1$, x_{bk} = distance between concentration node k and $k+1$. For simplicity, '~' will be dropped in following equations.

$$j_{i1}^t = \begin{cases} -D_i\left(\dfrac{c_{i2}^t - c_{i1}^t}{x_{bk}(1)} - z_i c_{i1}^t E_1^t\right); & i \le 5 (+ve\ ions) \\ 0; & 6 \le i \le 8 \end{cases} \qquad k = 1 \tag{17}$$

$$j_{ik}^t = -D_i\left(\frac{c_{ik+1}^t - c_{ik}^t}{x_{bk}(k)} - \frac{z_i(c_{ik+1}^t + c_{ik}^t)}{2}E_k^t\right); \quad 2 \le k \le N \tag{18}$$

$$j_{iN}^t = \begin{cases} -D_i\left(\dfrac{c_{i1}^t - c_{iN}^t}{x_{bk}(N)} - \dfrac{z_i(c_{iN}^t + c_{i1}^t)}{2}E_N^t\right); & i = 8\ (OH^-\ ion) \\ 0; & i < 8 \end{cases} \qquad k = N+1 \tag{19}$$

As Eq(17) suggests, flux for only positive ions is present, semipermeable membrane is impermeable to –ve ions. Similarly at the other end, Eq(19) suggests that flux for all ions except

OH^- ion is zero, because it is wall, but at this electrode OH^- ion is produced due to chemical reaction thus has a flux.

From Eq$(17-19)$ we can write, Nernst-Planck equations as follows.

For $k=1$,

$$c_{i2}^t - c_{i2}^0 - \frac{D_i \Delta\tau}{x_{fk}(1)}\left[\left(\frac{c_{i3}^t - c_{i2}^t}{x_{bk}(2)} - \frac{z_i(c_{i3}^t + c_{i2}^t)}{2}E_2^t\right) - \left(\frac{c_{i2}^t - c_{i1}^t}{x_{bk}(1)} - z_i c_{i1}^t E_1^t\right)\right] = 0;\ i \le 5 \quad (20)$$

$$c_{i2}^t - c_{i2}^0 - \frac{D_i \Delta\tau}{x_{fk}(1)}\left[\left(\frac{c_{i3}^t - c_{i2}^t}{x_{bk}(2)} - \frac{z_i(c_{i3}^t + c_{i2}^t)}{2}E_2^t\right)\right] = 0; \qquad 6 \le i \le 8$$

For $2 \le k \le N-1$,

$$c_{ik}^t - c_{ik}^0 - \frac{D_i \Delta\tau}{x_{fk}(k-1)}\left[\left(\frac{c_{ik+1}^t - c_{ik}^t}{x_{bk}(k)} - \frac{z_i(c_{ik+1}^t + c_{ik}^t)}{2}E_k^t\right) - \left(\frac{c_{ik}^t - c_{ik-1}^t}{x_{bk}(k-1)} - \frac{z_i(c_{ik}^t + c_{ik-1}^t)}{2}E_{k-1}^t\right)\right] = 0; \quad (21)$$

For $k=N$,

$$c_{iN}^t - c_{iN}^0 - \frac{D_i \Delta\tau}{x_{fk}(N-1)}\left[\left(\frac{c_{i1}^t - c_{iN}^t}{x_{bk}(N)} - \frac{z_i(c_{iN}^t + c_{i1}^t)}{2}E_N^t\right) - \left(\frac{c_{iN}^t - c_{iN-1}^t}{x_{bk}(N-1)} - \frac{z_i(c_{iN}^t + c_{iN-1}^t)}{2}E_{N-1}^t\right)\right] = 0; \quad i = 8\ (OH^-\ ion) \quad (22)$$

$$c_{iN}^t - c_{iN}^0 - \frac{D_i \Delta\tau}{x_{fk}(N-1)}\left[-\left(\frac{c_{iN}^t - c_{iN-1}^t}{x_{bk}(N-1)} - \frac{z_i(c_{iN}^t + c_{iN-1}^t)}{2}E_{N-1}^t\right)\right] = 0; \quad i < 8$$

Similarly, we can write Poisson equation for electric field

For k=1,

$$\epsilon(E_1^t - E_1^0) - \Delta t\left[\frac{\sum_i z_i D_i(c_{i2}^t - c_{i1}^t)}{x_{bk}(1)} - E_1^t \sum_i z_i^2 D_i c_{i1}^t\right] = 0; i \le 5 \quad (23)$$

For $2 \le k \le N$,

$$\epsilon(E_k^t - E_K^0) - \Delta t \left[\frac{\sum_i z_i D_i (c_{ik+1}^t - c_{ik}^t)}{x_{bk}(k)} - E_k^t \sum_i \frac{z_i^2 D_i (c_{ik+1}^t + c_{ik}^t)}{2} \right] = 0 \quad (24)$$

For $k = N + 1$,

$$\epsilon(E_{N+1}^t - E_{N+1}^0) - \Delta t \left[\frac{z_8 D_8 (c_{81} - c_{8N})}{x_{bk}(N)} - E_N^t \frac{z_8^2 D_8 (c_{8N}^t + c_{81}^t)}{2} \right] = 0; \quad (25)$$

In Eq(20-25), superscript 't' represents current estimate of the variable, superscript '0' represents value of the variable at previous converged time step.

These equations can be written in form,

$$F(\bar{X}) = 0 \quad (26)$$

Where $\bar{X}$ = vector of all the variables E_{ik}, c_{ik}. However, as we can understand for the initial guess of the variable values the function $F(\bar{X}) \neq 0$, the residue can be reduced by taking Newton Raphson steps, where $F'(\bar{X})\bar{X} = -F(\bar{X})$, $F'(\bar{X})$ is Jacobian of the system. Continue Newton Raphson stepping till residue norm is below certain criterion. Solve for next time step, and so on.

6.7 Results

For cross sectional area $A = 0.01\ m^2, L_{ref} = 0.1m, \phi_{overpot} = 0.05V,\ ||err||_{L2} < 10^{-8}$ we obtain the following results through simulation.

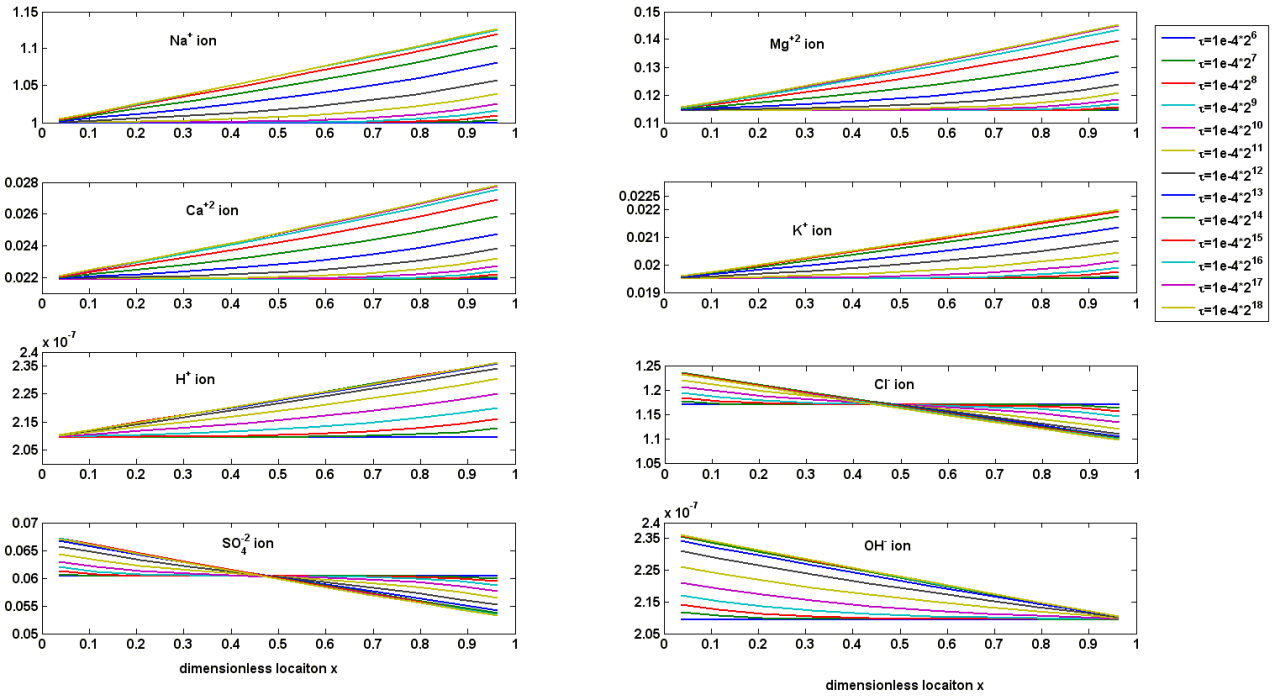

Figure 6-3. Variation in ion concentration distribution with time

Figure 6-3 shows variation in ion concentration distribution with respect to dimensionless time. We can note that all $+ve$ ions first show exponential increase in concentration near $\tilde{x} = 1$, the rate of change in concentration is initially increasing, but with time slows down and ultimately achieves steady state. In state state, the distribution of all positive ions is straight line with positive slope, and intercept at $\tilde{x} = 0$ is original concentration, i.e., concentration in open ocean water. For –ve ions, concentration decreases at $\tilde{x} = 1$ and increases at $\tilde{x} = 0$, with similar exponential trend and achieving a straight line distribution at steady state, however with negative slope. The original concentration is achieved not at $\tilde{x} = 0.5$ but a little earlier. This may have been necessitated by increased +ve ion densities.

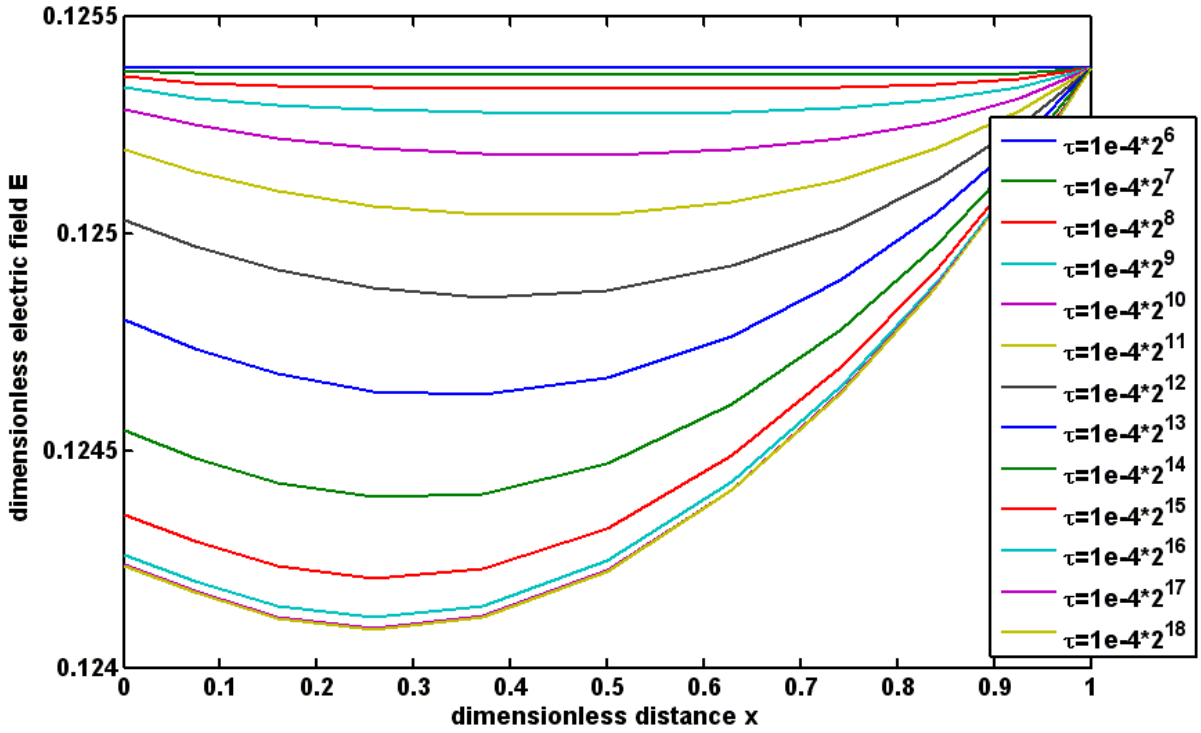

Figure 6-4. Variation in electric field with time

Figure 6-4 shows variation in electric field with respect to time. We can note that due to practically zero flux, electric field at $\tilde{x} = 1$ remains constant, while due to incoming flux of positive ions and redistribution of charges the electric field drops, the drop is in form of sag that starts in the middle but as time passes and drop increases shifts towards $\tilde{x} = 0$. The minimum electric field is $\approx 98.94\%$ of originally applied electric field.

Figure 6-5 shows increase in the density of the buoyancy chamber with respect to time, we can see an 'S' shape curve in semilog plot. The steady state however is achieved almost instantaneously as we can see $t \approx 1.16^8$s. We obtain density difference of $0.838277\ kg/m^3$, which is mere 0.0809% of the original density. However, this difference will cause the vehicle to sink to achieve new equilibrium depth where ocean density equals new density of the vehicle.

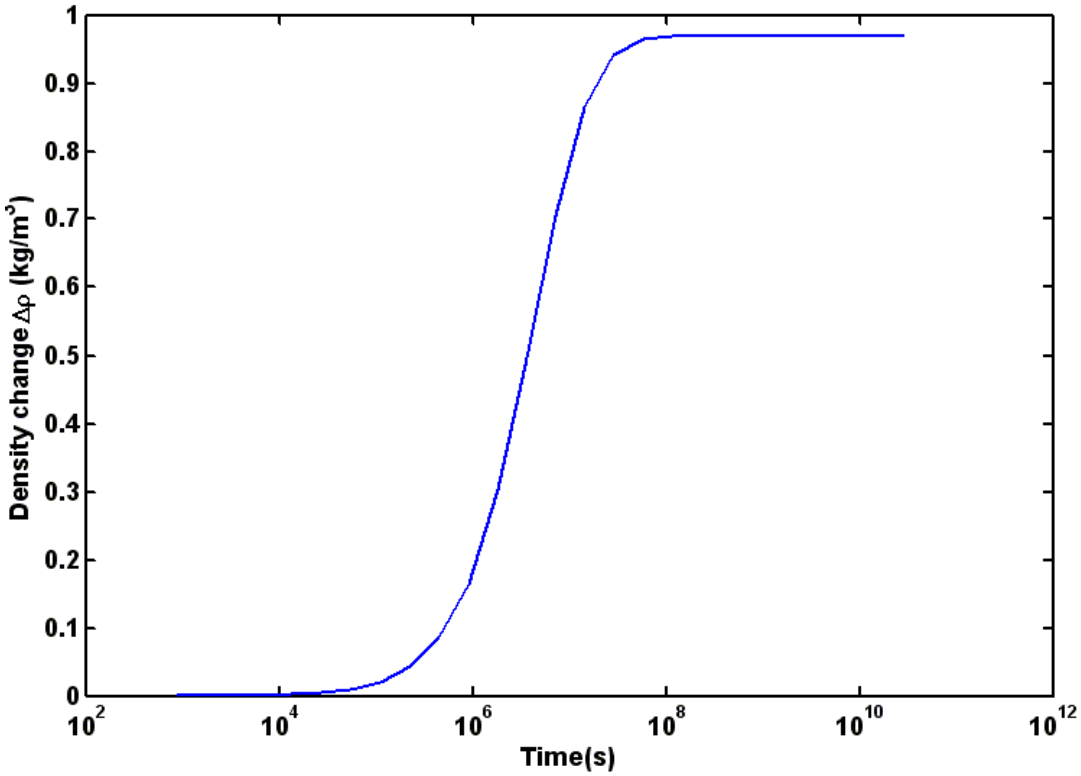

Figure 6-5. Increase in density with time

Typical density profile in a pycnocline is shown in Figure 6-6 and can be approximately given by parametric Eq(27).

$$\rho(z) = \rho_0(1 - \omega \tanh(\alpha z)) \tag{27}$$

Where, $\rho_0 = \frac{\rho_1+\rho_2}{2}, \omega = \frac{\rho_2-\rho_1}{2\rho_0}, \rho_1$ and ρ_2 are upper level and lower level densities respectively. z is depth parameter having origin at mid-pycnocline level, $h_1 =$ thickness of upper level, $h_2 =$ thickness of lower level. At surface $z = h_1$ and at lower boundary $z = -h_2$ are assumed to be constant boundaries. Detailed pycnocline profile estimation involves a lot more parameters such as, longitude, latitude, thermocline, halocline, season, ocean currents etc. and is beyond scope of this work. However taking an approximate $\frac{d\rho}{dz} = \frac{0.003\frac{kg}{m^3}}{m}$ would result in about 323.16 m dive. To achieve this steady state we produced 1.307E-5 mol of additional OH^- ion

(computed by difference in total concentration at steady state and original seawater concentration), using 1.2612 C charge at 0.05V overpotential. Thus energy spent is (2.19+0.05)* 1.2612=2.825 J.

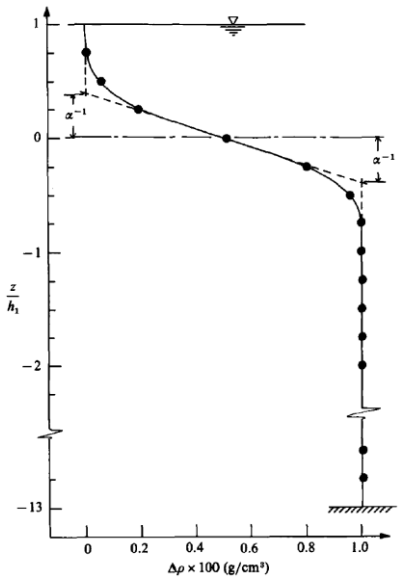

Figure 6-6. Typical density profile in a pycnocline (Kao,1985)

6.7.1 Grid independence study

To ensure that the results are reliable and not some numeric artifact of coarse grid, we carried out grid independence study. Figure 6-7 (a) and Figure 6-7 (b) illustrates that for grid divisions 10,20,40,80,160 results don't get affected. It takes more Newton Raphson iterations to get converged solution as we increase grid divisions.

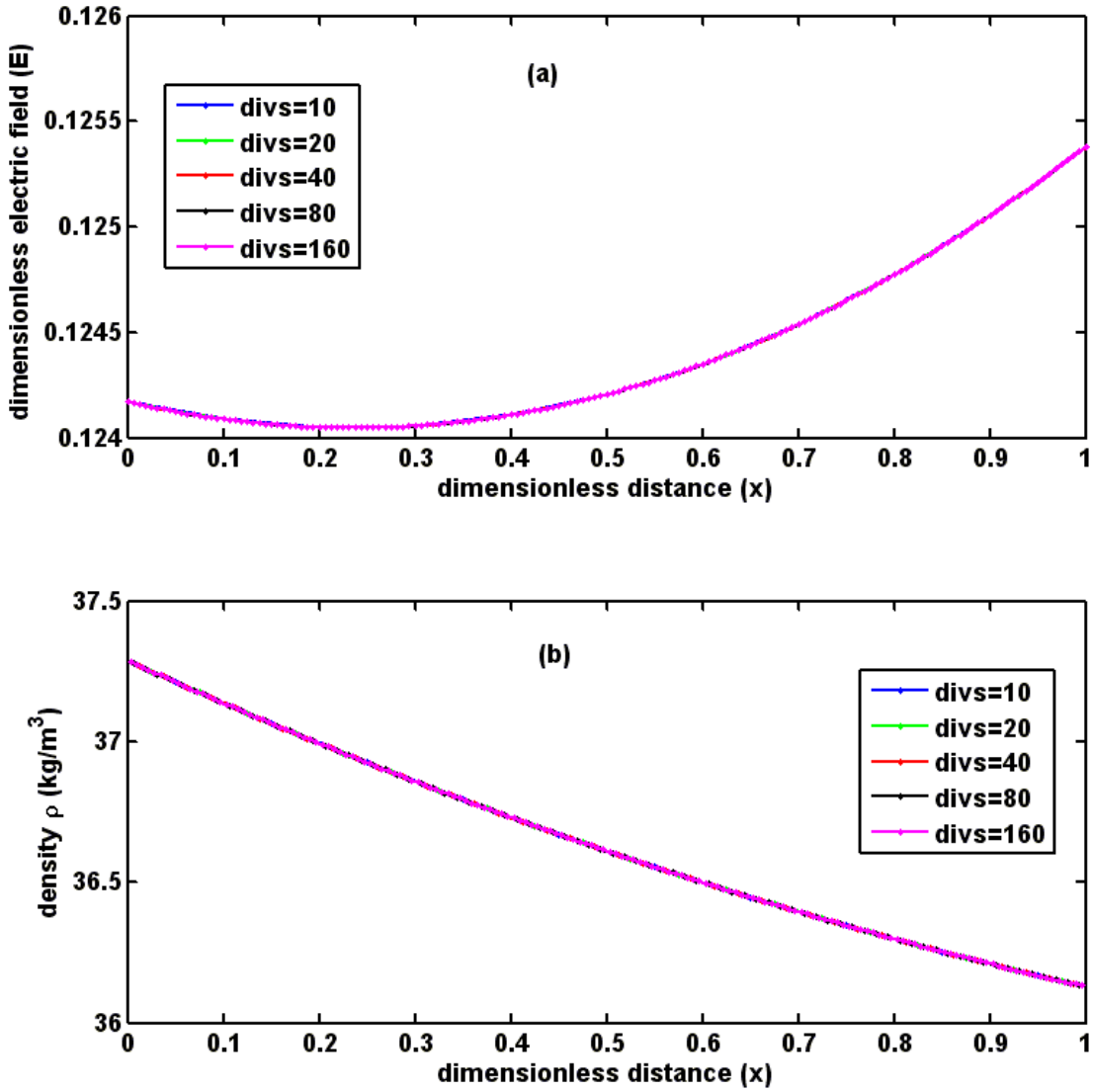

Figure 6-7. Grid independence study (a) dimensionless electrical field and (b) density vs dimensionless distance

6.7.2 Effect of increasing overpotential

As overpotential increases the sag seen in the electric field distribution increases too as illustrated in Figure 6-8. Density distribution however changes drastically as under higher overpotential positive and negative ions are more concentrated towards negative and positive electrodes respectively (Figure 6-9). The density change $\Delta\rho$ achieved at steady state can be fitted with cubic curve as depicted in Figure 6-10.

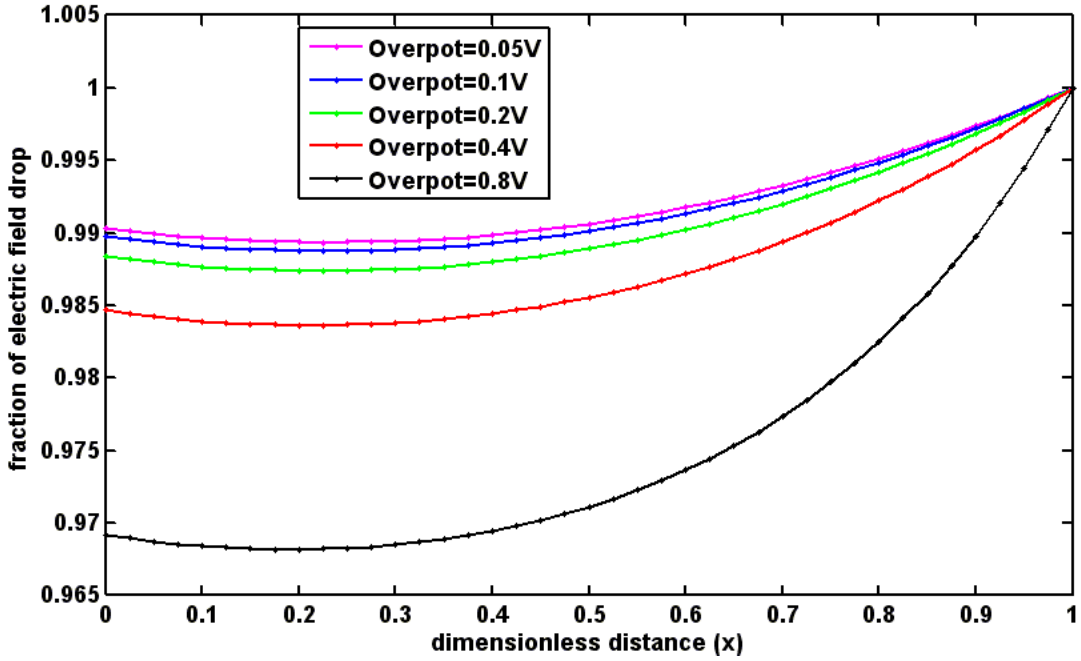

Figure 6-8. Effect of variation in overpotential on electric field distribution

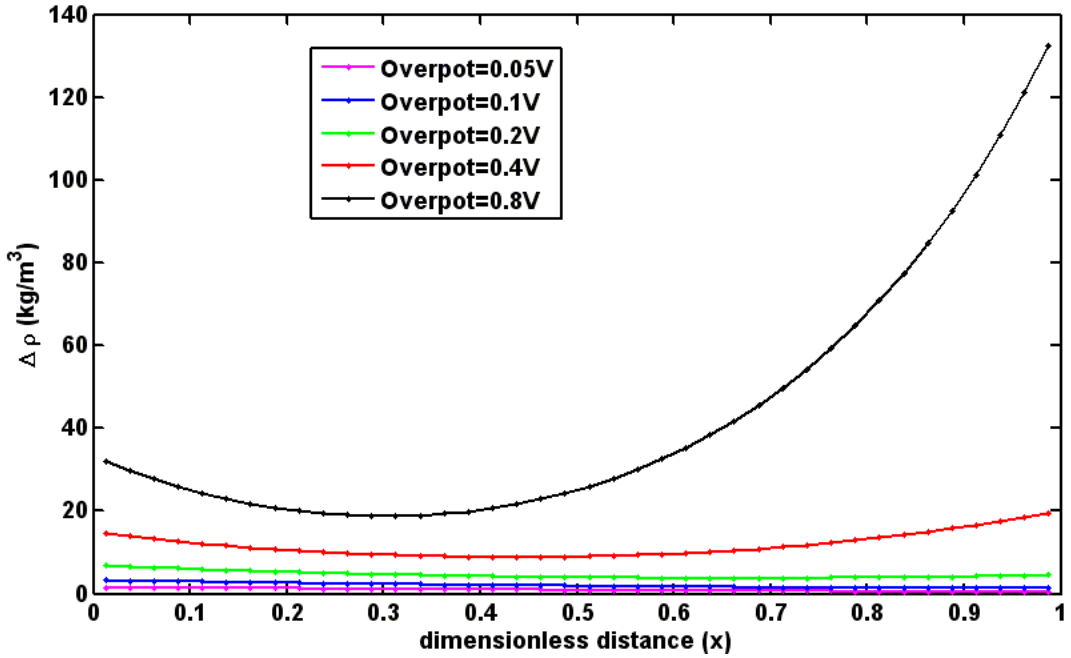

Figure 6-9. Effect of variation in overpotential on density distribution

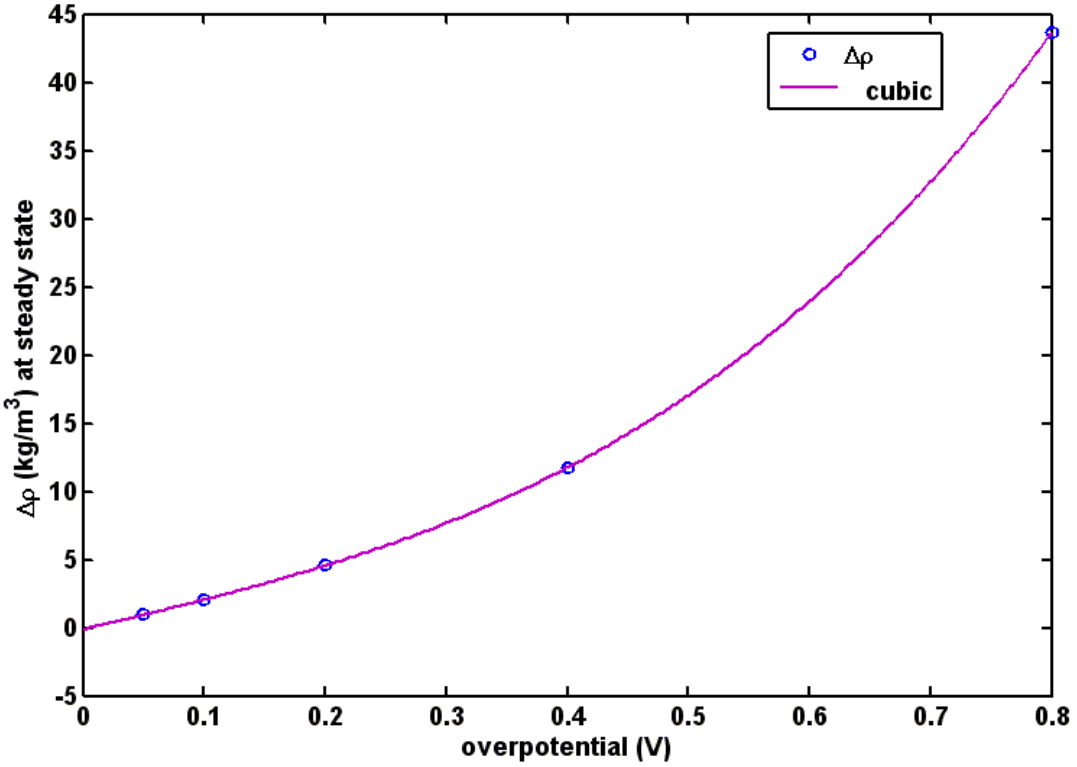

Figure 6-10. Variation in change in density at steady state as a function of overpotential

6.8 Conclusion

Marine animal almost universally use one or the other form buoyancy control mechanism to maintain their position and travel vertical in the water column. We have pioneered to design a bio-inspired buoyancy engine based on selective ion-replacement using electro-osmosis principles. We developed a bio-inspired buoyancy engine capable of changing ion concentration in the buoyancy chamber / swim bladder by a small amount with help of applied electric field. The Nernst-Planck-Poisson system of equations was solved using Newton Raphson algorithm and it was also demonstrated that the results are independent of the grid divisions. We illustrate that with increase in overpotential density change at steady state follows a cubic curve. With help of pycnocline, this small difference can result in significant change in equilibrium depth for the vehicle. We have ignored any other mass of the vehicle other than buoyancy chamber in the simulation. The effective change in density will be proportional to volume fraction of buoyancy

chamber compared to total vehicle volume. This bio-inspired buoyancy engine shows a great promise to vehicle travel with minimum energy requirement.

Acknowledgement

This research is sponsored by Office of Naval Research through contract number N00014-08-1-0654.

Chapter 7. Modeling of artificial *Aurelia aurita* bell deformation[5]

Recently, there has been significant interest in developing underwater vehicles inspired by jellyfish. One of these notable efforts includes the artificial *A.aurita* (Robojelly). The artificial *A.aurita* is able to swim with similar proficiency to the *Aurelia aurita* species of jellyfish even though its deformation profile does not completely match the natural animal. In order to overcome this problem, we provide a systematic finite element (FE) model to simulate the transient behavior of the artificial *A.aurita* vehicle utilizing Bio-Inspired Shape Memory Alloy Composite (BISMAC) actuators. The FE simulation model accurately captures the hyperelastic behavior of EcoFlex (Shore hardness-0010) room temperature vulcanizing (RTV) silicone by invoking three parameter Mooney-Rivlin model. Furthermore, the FE model incorporates experimental temperature transformation curves of SMA wires by introducing negative thermal coefficient of expansion and considers the effect of gravity and fluid buoyancy forces to accurately predict the transient deformation of the vehicle. The actual power cycle used to drive artificial *A. aurita* vehicle was used in the model. The overall profile error between FE model and the vehicle profile is mainly due to the difference in initial relaxed profiles.

[5] Reprinted with permission from Marine Technology Society: Joshi, K.B.; Villanueva, A.A; Colin, S.F.; and Priya,S. ," Modeling of artificial *Aurelia aurita* bell deformation", Marine Technology Society Journal, Vol.45 (4), pp.165-180, July/August,2011. http://dx.doi.org/10.4031/MTSJ.45.4.13

7.1 Introduction

Jellyfish have been in existence for millions of years and earliest known metazoans using muscles for swimming (Valentine,2004). They are found at various ocean depths and possess ability to survive under hostile ocean environment. They exhibit colonial behavior and have ability to maintain certain depth and certain distance from the ocean shore (Albert,2009). Jellyfish have relatively simple biological form and muscle architecture lacking advanced sensors and a complex neural network possessed by many oceanic creatures (Gladfelter,1972, Gladfelter,1973, Chapman,1974) but they are still able to survive and adapt in hostile environments. It maintains territorial existence by swimming on minimal energy intake. These abilities have created tremendous interest in the scientific community to discover their structure-property-performance relationships and apply the learning towards creating a jellyfish inspired swimming vehicle to perform various surveillance and monitoring tasks.

There have been various efforts in literature on developing jellyfish-inspired robots by using smart-material based actuators. Inspired by jetter class of jellyfish that swim by creating a jet of water by forcing it out of the bell, Villanueva et al. (Villanueva,2009) developed JETSUM . This prototype used shape memory alloy (SMA) wires and created an actuating stroke of bell segments attached to a passive neutrally buoyant bell structure. Yang (Yang,2007) used flappers with control surfaces made of ionomeric polymer metal composites (IPMC) to control directionality of the vehicle. Tadesse et al. (Tadesse,2010a) used polypyrrole –polyvinylidene difluoride (PPy-PVDF) composites to achieve bending actuation to create a jellyfish robot. Larger jellyfish typically use “rowing” locomotion (Colin,2002) and are characterized by formation of counter rotating starting and stopping vortex rings. Interaction of these vortex rings reduces energy lost in the wake and lends rowers their superior swimming efficiencies relative to

jetters (Colin,2002). Thus with regard to energy efficiency rowers provide a better platform for larger vehicles. Yeom et al. (Yeom,2009) proposed an entire jellyfish made from IPMC actuators with segments cut such that on contraction all the segments close to form a contracted bell shape. Recently, a significant breakthrough was made by Villanueva et al. (Villanueva,2010b) who proposed the high energy density Bio-Inspired Shape Memory Alloy Composite (BISMAC) actuator that opened the possibility of converting high force generation capability of SMA wires into high displacements. Using BISMAC, the design and implementation of biomimetic rowers became feasible.

In this study, we investigate the bell deformation of BISMAC-based jellyfish robots using Finite Element Model (FEM, conducted using ANSYS) and identify the correlation with the natural species. In order to do so the first major challenge was precise implementation of SMA in FEM due to their giant aspect ratio and hysteretic temperature transformation. We were able to successfully demonstrate the deformation of SMA using ANSYS by optimizing the meshing technique, identifying the variability in thermal coefficient of expansion, and separating the total deformation cycle into individual heating and cooling curves. Building upon this success, we implemented the SMA in BISMAC structure and investigated its mechanics to optimize the BISMAC configuration for mimicking the jellyfish profile. The FEM model provides the understanding of mechanism for bending strain amplification in BISMAC actuators and clearly delineates the effect of structural and thermal variables. Using the FEM results, we were able to identify the inaccuracies that can occur due to variability in prototyping of BISMAC. Further our results provide important insight towards the development of feedback controller based on resistance changes. Next, we introduce the design of bell geometry in FEM for artificial *Aurelia aurita* (later referred to as, *A. aurita* for convenience in this work) using

radial arrangement of BISMAC actuators. The objective was to develop the proper joint geometry that allows BISMAC's to provide maximum deformation. Next we describe the method for fabricating artificial *A. aurita* and experimental characterization. Lastly, using the FEM simulations we present a comparative analysis between the biological *A. aurita* (swimming profile) and artificial *A. aurita*.

7.2 BISMAC actuator[6]

The BISMAC actuator is a composite of an incompressible flexible metal strip and SMA wires separated by distance d and embedded in silicone rubber. Thermal transformation from martensite phase into austenite upon Joule heating induces the contraction of SMA wires which is resisted by the incompressible metal strip. This introduces a tensile force f in the SMA that opposes contraction and reduces the strain in SMA wire by a small amount.

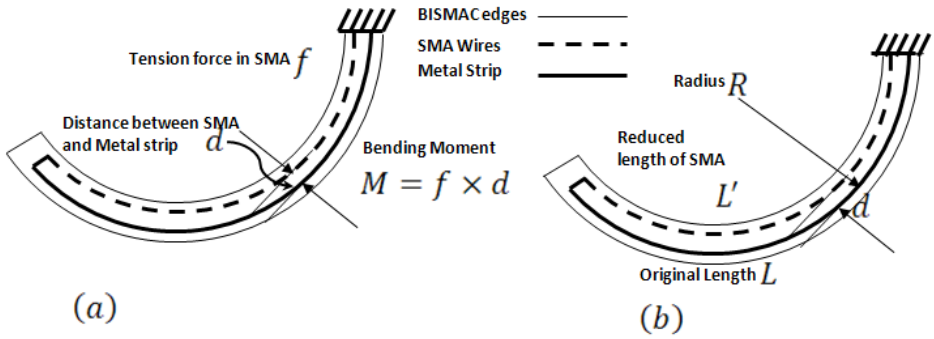

Figure 7-1. (a) Schematic of the force and moment in BISMAC, and (b) geometry of beam curvature.

Figure 7-1 helps in explaining the mechanics of BISMAC bending deformation. (Figure 7-1 (a)) Under Joule heating as SMA transforms from martensite to austenite phase and tends to contract but due to structure of the BISMAC the metal strip resists this contraction and induces

[6] Reprinted with permission from IOP Publishing: Colin, S.; Villanueva, A., Joshi, K., Tadesse, Y. and Priya,S., "Working principle of bio-inspired shape memory alloy composite actuators", Smart Materials and Structures, Vol.20(1), pp.012001, 2011, IOP publishing. doi:10.1088/0964-1726/20/1/012001

tensile force f in the SMA wire and compressive force f of the same magnitude in the metal strip. This force couple being distance d apart generates effective moment in the BISMAC actuator causing it to bend. Figure 7-1 (b) shows the deformed BISMAC geometry. The mechanics of BISMAC has been discussed in detail by Smith et al. (Smith,2011). By using constitutive relation for SMA, we can express the generated stress as:

$$\sigma - \sigma_0 = E_{SMA}(\epsilon - \epsilon_0) + \Omega(\zeta - \zeta_0) + \Theta(\mathrm{T} - \mathrm{T}_0) \quad (1)$$

where σ is the stress, ϵ is the strain, E_{SMA} is the effective Young's modulus of SMA, Ω is the transformation coefficient, ζ is the martensite fraction, Θ is the thermoelastic coefficient, and T is the temperature. Subscript zero denotes the initial state. Since transformation here is from fully martensite to fully austenite phase, $\zeta = 0$, and $\zeta_0 = 1$. Pure thermoelastic expansion is negligible and initial stress and strain states are zero. Using $E_{SMA} = E_{austenite}$, since SMA is completely in austenite phase, Eq.(1) transforms into:

$$\sigma = E_{austenite}\epsilon - \Omega \quad (2)$$

If there was no BISMAC structure to resist the SMA contraction, $\sigma = 0\ and\ \epsilon = -\epsilon_l$ transformation strain, providing:

$$\Omega = -E_{austenite}\epsilon_l \quad (3)$$

If there is a uniform tensile force applied onto the SMA wire while transformation takes place:

$$\sigma = E_{austenite}\epsilon + E_{austenite}\epsilon_l \quad (4)$$

Since SMA wires are thin with negligible bending stiffness it is safe to assume uniform distribution of axial stress. Thus, axial stress can be written as:

$$\sigma = \frac{f}{A_{SMA}} = \epsilon_f E_{austenite} \Rightarrow \epsilon_f = \epsilon + \epsilon_l \quad (5)$$

where f is the force generated by the SMA wire, A_{SMA} is the total area of SMA cross section, and ϵ_f is the force induced tensile strain. If SMA length after contraction is reduced from L to L', from kinematics consideration we can write:

$$\frac{L'}{L} = 1 + \epsilon = \frac{R - d}{R} \tag{6}$$

where R is the radius of curvature of the metal strip and d is the distance between SMA wire and the metal strip. Solving Eq.(5) and (6),

$$1 + \epsilon_f - \epsilon_l = 1 - \frac{d}{R} \tag{7}$$

$$R = \frac{d}{\epsilon_l - \epsilon_f} \tag{8}$$

Using Euler beam theory,

$$\frac{M}{I} = \frac{E}{R} \Rightarrow \frac{fd}{I} = \frac{E(\epsilon_l - \epsilon_f)}{d} \tag{9}$$

$$\frac{\epsilon_f E_{austenite} A_{SMA} d}{I} = \frac{E(\epsilon_l - \epsilon_f)}{d} \Rightarrow \epsilon_f = \frac{EI(\epsilon_l - \epsilon_f)}{E_{austenite} A_{SMA} d^2} \tag{10}$$

$$\epsilon_f = \frac{EI\epsilon_l}{E_{austenite} A_{SMA} d^2 + EI} \tag{11}$$

where EI is the total bending stiffness of the composite beam. For the particular configuration of the BISMAC used by Smith et al. (Smith,2011), Figure 7-2 (a) shows the relationship between radius of curvature for the BISMAC and the distance between SMA wires and flexible metal strip. Figure 7-2 (b) reveals that as the distance d decreases, the tensile force induced in SMA wires increases dramatically and attains a limiting value of 80g force for 100μ thick SMA wire (BioMetal Fiber, TOKI Corporation) beyond which high stresses causes austenite phase to transform into stress induced martensite resulting in loss of the transformation strain and thus loss of performance which is not accounted by Eqs. (1)-(11).

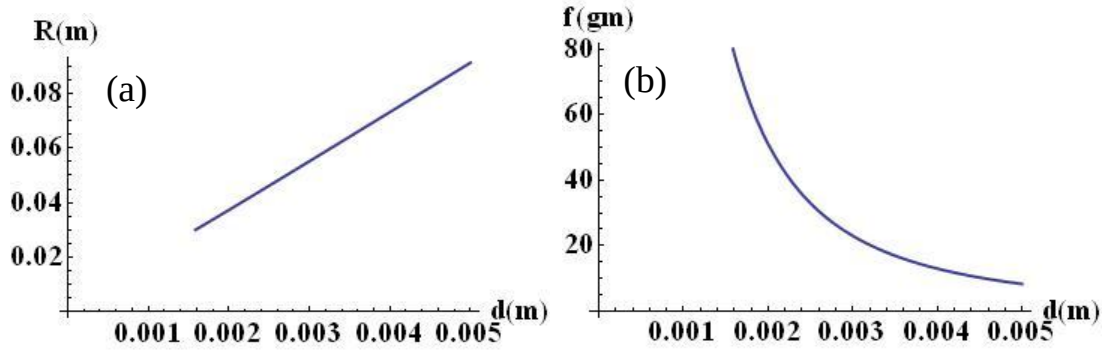

Figure 7-2. (a) Radius of curvature vs. distance d, and (b) tensile force in the SMA wires vs. distance d.

7.3 BISMAC customization and bell geometry

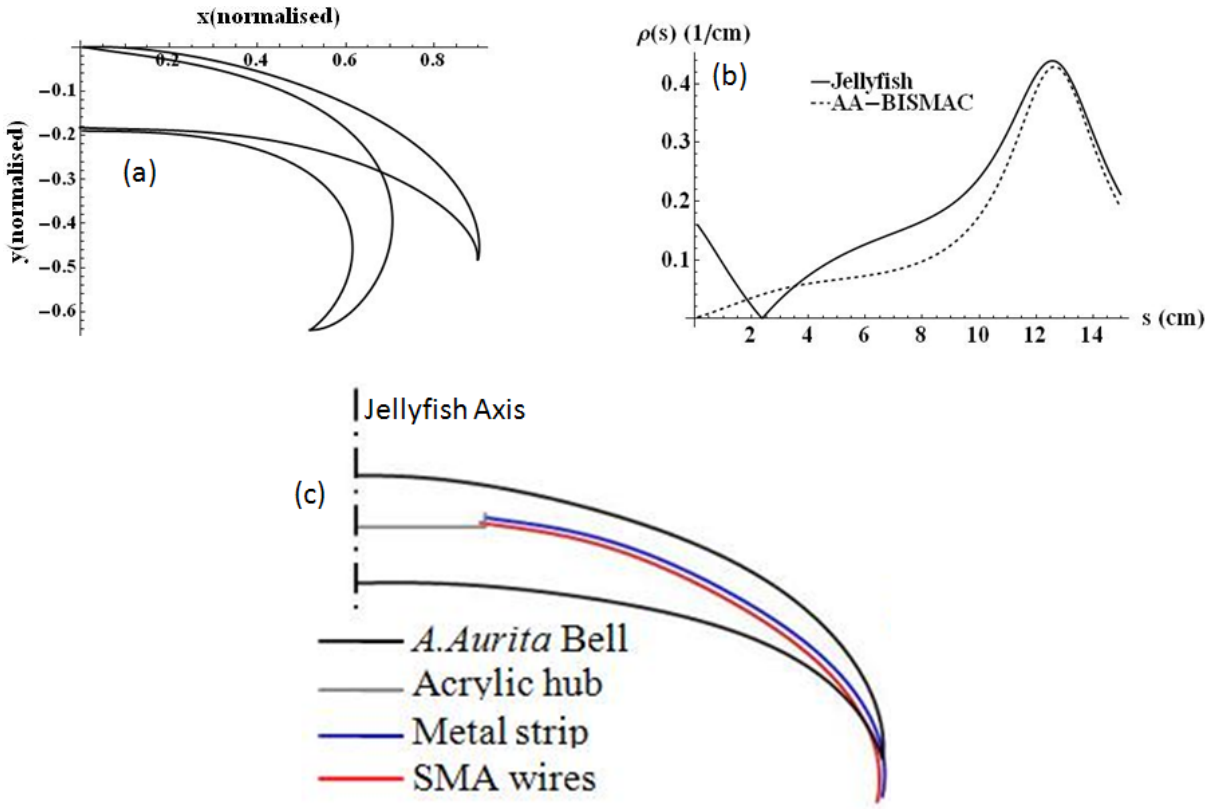

Figure 7-3. (a) *A.aurita* profile in relaxed and contracted condition, (b) curvature comparison of BISMAC muscle with *A. aurita* after customization, and (c) schematic of the BISMAC placment in the artificial *A. aurita*.

A. aurita curvature profiles in its relaxed and contracted state are shown in Figure 7-3(a)(Dabiri,2005b). Before any actuation, the bell is fully expanded and said to be in the relaxed position. Fully contracted state refers to the state corresponding to complete contraction of subumbrellar muscles and minimum bell volume. After actuation, the bell passively regains its original (relaxed) position. In earlier work (Villanueva,2010b), we have presented the methodology used to customize BISMAC configurations to mimic the natural *A. aurita* curvature profile. For a curved beam, we can write:

$$M = EI(s)\frac{d(\Delta\theta)}{ds} \tag{12}$$

where M is the moment, $EI(s)$ is the local bending stiffness at location s, $\Delta\theta(s) = \theta(s) - \theta_0(s)$ is the change in slope at location s, and s is location on curved profile length. Since the force generated by SMA wires is uniform; we ensure a constant moment M by maintaining the fixed distance between SMA wires and the metal strip. The bending stiffness was varied: (i) to match jellyfish exumbrella and subumbrella profiles in the relaxed state, and (ii) to manipulate the bending stiffness EI(s) such that upon SMA actuation, $\frac{d(\Delta\theta)}{ds}$ matches that of real *A. aurita* in order to ensure that we have a good match between natural and artificial vehicles in the contracted state. The resultant BISMAC achieved close similarity with *A. aurita* profile as illustrated in Figure 7-3 (b). The inflexion point in contracted *A.aurita* profile at ~2.5cm represents the fact that at the center bell thickens and profile becomes a little convex near the center and changes to concave at inflexion point. Towards the end of the profile, the BISMAC

shows reduction in curvature due to passive material at the tip end for protection from water. Similar reductions in contracted *A.aurita* curvature profile towards the bell margin lead to discovery of the passive flap in *A.aurita* near the bell margin. The passive flap was shown to improve the swimming performance of the artificial *A.aurita* significantly (Villanueva,2010a). Figure 7-3 (c) shows a schematic of artificial *A.aurita* consisting of 8 BISMAC's radially distributed around the bell which is made of soft silicone. Artificial *A.aurita* has shown bell deformation and kinematics as well as a swimming performance comparable to that of natural animal (Villanueva,2010a). Since most of the available engineering materials have lower compliance compared to that of natural animal, the artificial *A.aurita* design includes joint structures between BISMAC actuators to localize the material folding upon contraction. These joint structures modify the original axi-symmetric *A.aurita* bell shape and increases similarity to the *Cyanea capillata* bell shape. The joints are wedge-like cavities and are found on natural jellyfish. The joint structure is described by Smith et. al. (Smith,2010) and is copied from the *Polyorchis montereyensis*. Since the cross-sectional shape of the joints varies with bell height, we take the equation below to represent the profile at midbell. The joint structure can be described as a piecewise function representing two symmetric sides of a single function, mirrored about the y-axis.

$$y = \frac{\delta j(k - x)}{\delta k - jx} \tag{13}$$

This function has been formed to describe the joint shape across a 2-D plane with height, j, half-width, k, and curvature, δ as parameters. In this way the joint structure from a wide variety of species can be described with one basic equation by changing the constants. Artificial *A.aurita*'s joint structure was produced by using a program that could manipulate the constants in Mathematica. The values to match the shape of joints in *Polyorchis montereyensis* were found to

be height=2.15, half-width=3, and curvature=-2.75. The final shape was evolved by sweeping circular section at bell tip into the curve at mid-bell height joint section for a smooth blending.

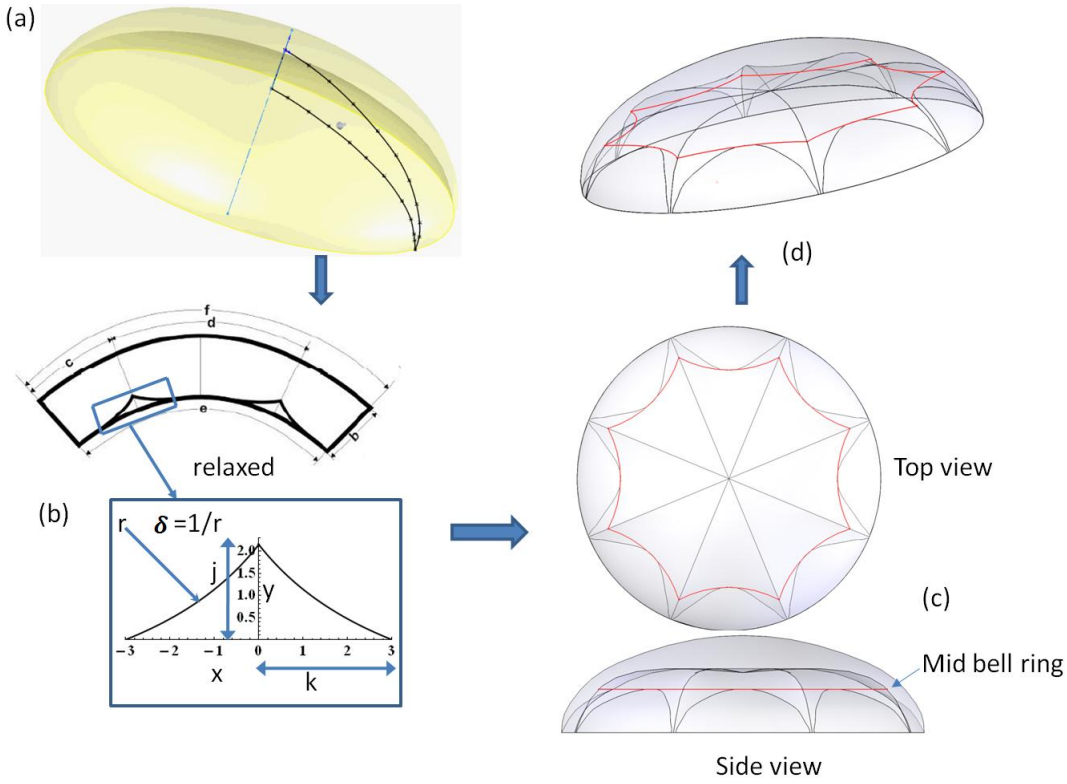

Figure 7-4. (a) Original axi-symmetric *A.aurita* bell, (b) schematic of joint geometry(Smith,2010), (c) top and side view showing location in bell for which joint calculations were made, and (d) final artificial *A.aurita* bell shape

Figure 7-4 shows the evolution of original axisymmetric *A. aurita* bell shape into the final bell design of artificial *A.aurita*. Figure 7-5 shows the details of the unigraphics model that was used in FE simulation.

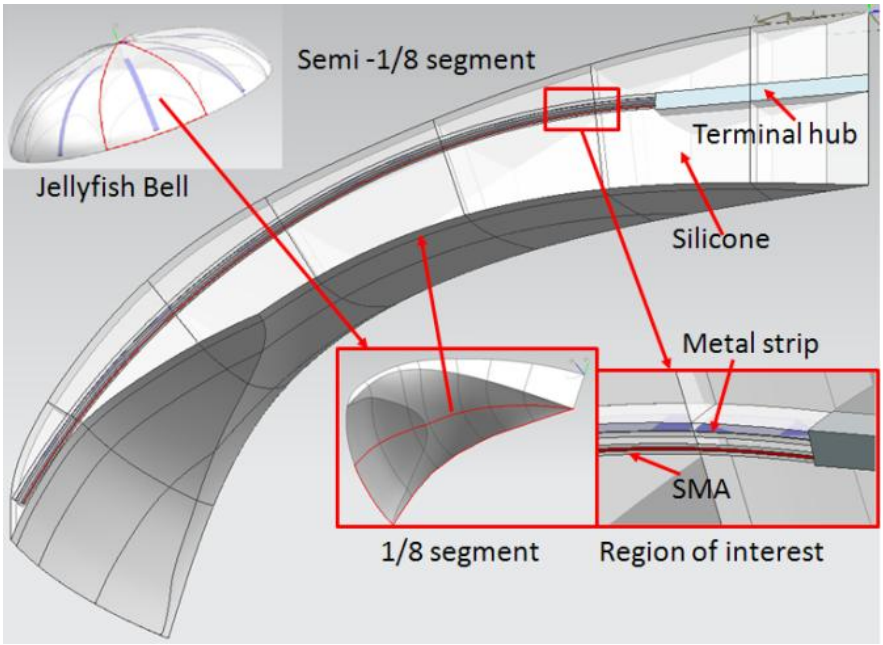

Figure 7-5. Unigraphics model of the artificial *A. aurita*

7.4 Experimental setup

Artificial *A.aurita* consists of a central mount that houses the electrical circuitry and clamps the BISMAC actuators together, see Figure 7-6. The radius of this hub was 25% of the bell diameter and covers a region where minimal deformation is expected to occur in both the natural and artificial *A.aurita*. Since the distance between the SMA wires and the metal strip is very crucial parameter in BISMAC design, the SMA wires and the metal strip are slide in position in small acrylic supports, designed to maintain this distance. The supports are then placed in the mold and silicone is poured in to settle (Villanueva,2010a). The actual vehicle has a small portion (3-4 mm) of metal strip and SMA wires protruding out of the bell geometry. This is neglected in this work for model simplification. The simplification is justified by negligible bending moment contribution from the protruded part towards the bell deformation. The

experimental data used for the deformation comparison was acquired by using the same artificial *A.aurita* and experimental setup as described in previous work (Villanueva,2010a). Artificial *A.aurita* was submerged underwater and clamped down by supports pressing on the top and bottom of the bell. The contacting area between supports and bell covered the region of the internal central mount. This region is meant to undergo negligible deformation since BISMAC actuators do not directly deform the bell at that location. The bell was contracted by heating the SMA wires using a rapid heating control algorithm (Villanueva,2010c). This controller uses SMA resistance feedback to monitor the bell state of deformation. It sends high current pulses for rapid contraction and low current to maintain deformation allowing fast contraction while minimizing power consumption. The controller was developed in LabView(National Instruments) and the measurements were made using a NI cDAQ 9172 with NI-9215 and NI-9263 analog input and output cards respectively. A NF HAS 4052 power amplifier was used to amplify the DAQ output and actuate the robot. The bell profile was recorded during the first actuation cycle. The deformation was captured using an IN250 high-speed camera from Fastec Imaging. The bell deformation was tracked by placing reflective beads along the profile and by processing the images manually using ImageJ (ImageJ). This process included an error on the order of +/- 1 cm.

Figure 7-6. Artificial *A.aurita* with uniform bell and flap, in the relaxed configuration

7.5 Finite element model setup and solution

7.5.1 Material properties

To ensure accuracy of the model in adequately representing the behavior of various materials, we determined the properties experimentally. There are three materials critical to the simulation: silicone matrix, flexible but incompressible metal strip and SMA wires (BioMetal Fiber).

7.5.1.1 Silicone rubber

Room temperature vulcanizing (RTV) silicone is a candidate material for bell mesoglea. In addition to forming the main jellyfish body, it is also responsible for maintaining the required distance between spring steel and the SMA wires. We have tested several silicone rubbers with different shore hardness to evaluate their mechanical properties. Ecoflex^{TM} (Smooth-On) with initial tensile Young's modulus of the order of 10580 Pa was selected to construct the Artificial *A.aurita* because it offered much less resistance to the BISMAC deflection. Figure 7-7(a) shows the tensile test, on a dog bone shaped sample with gauge length 7 mm and cross sectional area 2.45x2.8mm^2, for several cycles at room temperature at 1mm/sec displacement rate upto 20mm extension. to ensure silicone properties do not change with multiple loading cycles. Hysteresis is

evident in the figure and we used the average of the two curves to generate our model. Figure 7-7 (b) represents completely defined stress-strain behavior of silicone including compression test data carried out on 16 mm thick 25.4 mm diameter cylindrical specimen.

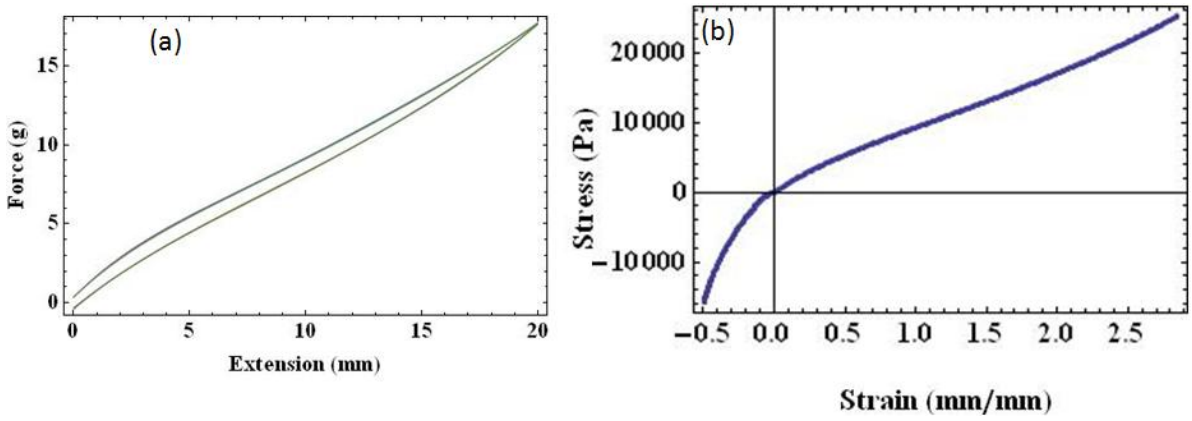

Figure 7-7 (a) Tensile test for several cycles showing hysteresis, and (b) stress-strain curve used to model Ecoflex™

We generated a three parameter Mooney-Rivlin model for silicone from test data using ANSYS's curve fitting tool. as more conventional two parameter Mooney-Rivlin model failed to provide a good fit to the experimental data. The Mooney-Rivlin model for Ecoflex™ is given by Eq. (14):

$$W = c_{10}(I_1 - 3) + c_{01}(I_2 - 3) + c_{11}(I_1 - 3)(I_2 - 3) + \frac{1}{d}(J - 1)^2 \qquad (14)$$

where W is the strain energy function, I_1, I_2, I_3 are the stretch invariants, J is the determinant of deformation gradient tensor and $c_{10} = 2307.1\ Pa$, $c_{01} = -223.76 Pa$, $c_{11} = 142.83\ Pa$, $d = 0\ Pa^{-1}$ (compressibility parameter). Silicone thermal conductivity was measured to be 0.22 W/mK. Silicone properties used in the FE model are tabulated in Table 7-1.

Table 7-1. Silicone properties used in the finite element model

Property	Value
Thermal Conductivity	0.22 W/mK
Elastic Modulus	Mooney-Rivlin model
Poisson's ratio	0.49
Density	982 kg/m^3
Specific heat	300 J/kgK

7.5.1.2 SMA wire

We selected 100 μm diameter BioMetal fibers due to their superior performance (Tadesse,2010b). The temperature transformation of the wires was measured experimentally as shown in Figure 7-8(a). Figure 7-8 (b) represents the stress-strain relationship as measured by tensile test to confirm the manufacturer's claims (Toki Corp) that the wires can easily take 400 MPa stress.

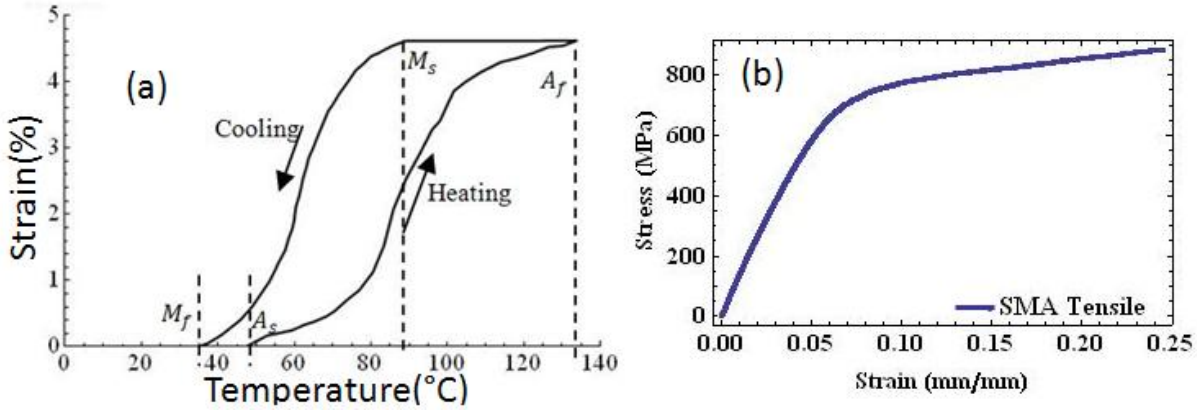

Figure 7-8. (a) BioMetal Fiber temperature transformation curve (A_s =Austenite start temperature, A_f =Austenite finish temperature, M_s =Martenite start temperature, M_f =Martenite finish temperature) and (b) Stress-strain relationship of martensite phase

Other properties that were used in the simulation are tabulated in Table 7-2. For temperatures other than transformation temperatures, the properties were interpolated according to martensite fraction in the SMA. Martensite fraction was calculated based on the temperature-strain curve.

Table 7-2. SMA properties used in the finite element model

Property	Martensite	Austenite
Thermal Conductivity	8 W/mK	18 W/mK
Elastic Modulus	28 MPa	75 MPa
Poisson's ratio	0.33	0.33
Density	6450 kg/m^3	6450 kg/m^3
Specific heat	837.36 J/kgK	837.36 J/kgK

In order to model the temperature transformation hysteresis of SMA wires we defined two separate material curves, one for the heating profile and other for the cooling profile. Accordingly, the elastic modulus **EX** and thermal conductivity **KXX** also followed two separate profiles as depicted in Figure 7-9(a) and (b). Figure 7-9 (c) shows the artificially defined negative thermal coefficient of expansion to achieve the transformation strains with increase in temperature during heating and cooling respectively.

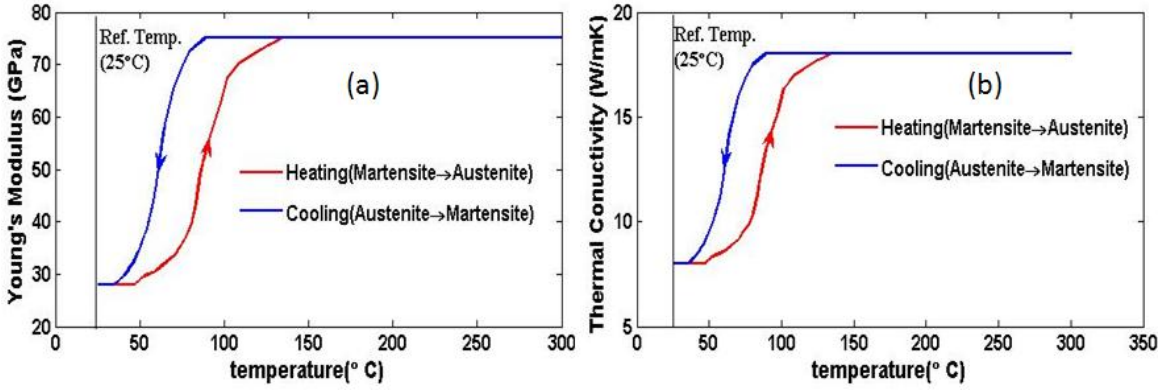

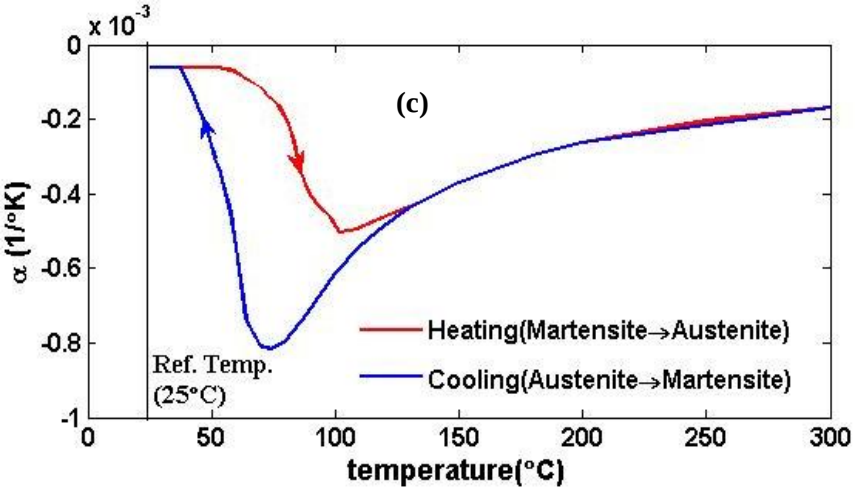

Figure 7-9. (a) Variation of SMA Young's modulus with temperature, (b)variation of SMA thermal conductivity with temperature, (c) variation of thermal coefficient of expansion with temperature

7.5.1.3 Metal strip

For choosing the metal strip, two criteria should be met: (i) incompressibility for BISMAC mechanics to work well, and (ii) flexibility (low bending stiffness) to obtain maximum deformation with a small actuation moment. We selected standard spring steel (low carbon steel) as the suitable metal strip material with properties tabulated in Table 7-3.

Table 7-3. Metal strip properties used in the finite element model

Property	Value
Thermal Conductivity	47 W/mK
Elastic Modulus	210 GPa
Poisson's ratio	0.3
Density	7860 kg/m^3
Specific heat	510 J/kgK

7.5.2 Transient heat transfer model

7.5.2.1 Meshing, boundary conditions and loads

We chose ANSYS as our simulation package. To simulate transient heat transfer, we built the model by meshing the SMA, metal strip and one element thick silicone layer around them with SOLID70 (8 node brick element). Rest of the silicone matrix was meshed with SOLID87 (10 node tetrahedrons) and SOLID90 (20 node brick elements) was used as transition element between SOLID70 and SOLID87 element meshes as shown in Figure 7-10(a). All these elements have TEMP degree of freedom.

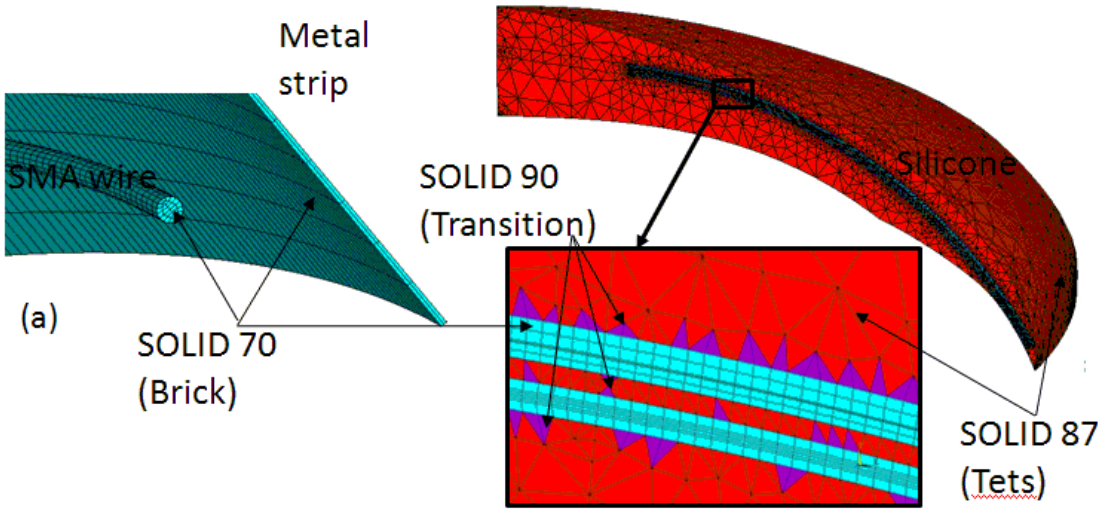

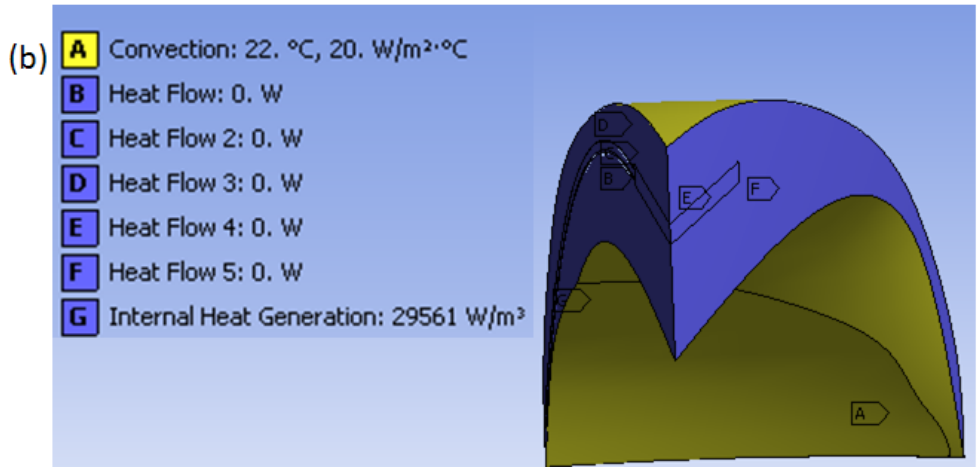

Figure 7-10. (a) Mesh detail for transient thermal model, and (b) boundary conditions.

We took advantage of the circular symmetry and modeled only $1/8^{th}$ of the bell segment with no loss of physics. To reduce the meshing efforts we chose to mesh only half of the $1/8^{th}$ segment of the bell, reflected the mesh about the plane of symmetry and finally merged the nodes to create the complete model. The boundary conditions are depicted in Figure 7-10 (b). Due to symmetry the circular symmetric sides (Figure 7-10 (b) violet colored faces) of the model does not have any temperature gradient, thus they are modeled as insulated boundaries. Exumbrella and subumbrella surfaces (Figure 7-10 (b) yellow colored faces) are in contact with surrounding water and conveys heat into the fluid and thus were modeled as convective boundaries. The heat transfer coefficient of both these surfaces were taken to be 20 $\mathrm{W/m^2K}$ (Baker,1972) and the ambient temperature was fixed at 25℃. The thermal loading resulting from electrical heating was applied using Villanueva et al.'s resistance feedback control algorithm (Villanueva,2010c) to reduce power requirement. The internal heating load was applied on the SMA wire as shown in Figure 7-11 which is consistently $1/8^{th}$ of total power consumed by the vehicle's eight segments. It consists of rapid heating pulses of high current followed by a constant current regime and finally reducing the magnitude to idling minimum current governed by need for resistance feedback measurement. The three initial spikes seen in the curve correspond to the high current impulse sent for rapid heating. Multiple pulses are usually needed during the initial actuation to rapidly reach temperatures close to A_f (Austenite finish). The material surrounding the SMA warms up and once SMA transformation is complete the low current input is enough to maintain deformation. Upon relaxation stroke, as current is reduced to minimal, just sufficient to meet resistance feedback requirement, SMA starts cooling down reaching close to M_f(Martensite finish) temperature at the end of the cycle.

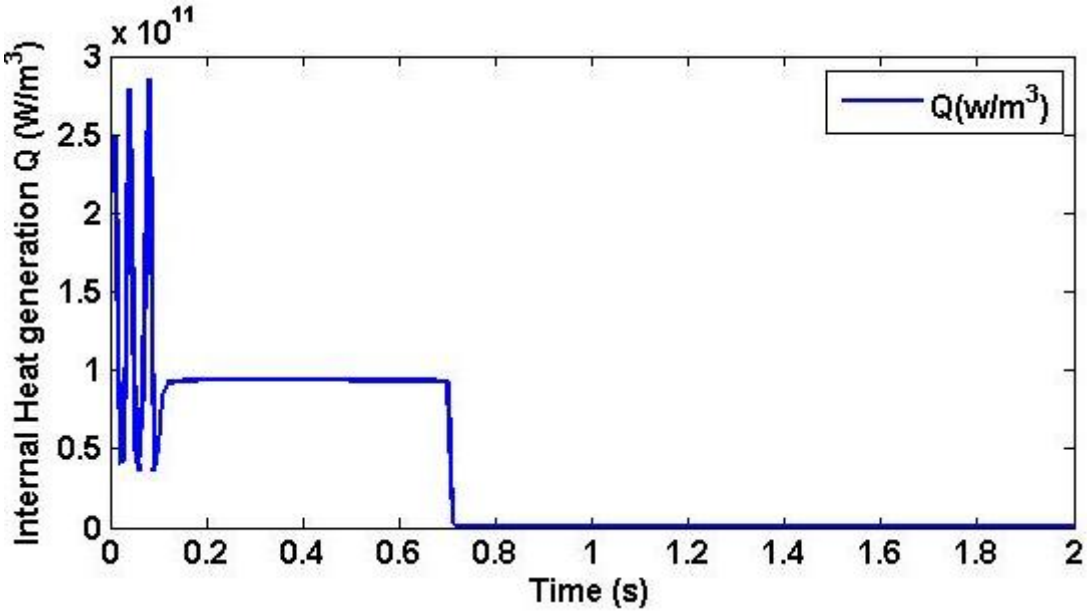

Figure 7-11. Variation of internal heating load on SMA wire with time.

7.5.2.2 Solution: transient thermal analysis

We first find the solution with SMA wires having material properties corresponding to heating curve. To capture initial sharp temperature rise accurately over the first 0.12sec, small time steps of 0.01sec were used to provide sufficient time resolution. The low current period from 0.12 sec to 0.70 sec was solved in 100 uniform time steps. After solving two more transient current time steps at 0.71 sec and 0.72 sec in one time step each, we switched the SMA wire material to the one with properties corresponding to cooling curve. Temperatures of SMA wires corresponding to t=0.72sec being far beyond A_f ensures properties of both the curves are same at this point. Finally, relaxation phase of *A. aurita* jellyfish vehicle from 0.72sec to 2.00 sec was solved in 200 uniform time steps.

7.5.3 Transient structural deformation model

7.5.3.1 Meshing, boundary conditions and loads

To simulate transient structural deformation, we reused the mesh from transient heat transfer model for rapid model building. SOLID70 (8 node brick element) of the SMA, metal strip and one element thick silicone layer around them were transformed into SOLID185 (8 node brick element) with structural degree of freedom UX, UY, UZ. Similarly, SOLID87 (10 node tetrahedrons) was transformed into SOLID187 (10 node tetrahedrons) elements and transition elements SOLID90 (20 node brick elements) were transformed into SOLID186 (20 node brick elements) as shown in Figure 7-12(a). Figure 7-12 (b) displays the displacement boundary condition for the model. The boundary condition was applied in cylindrical co-ordinate system defined using jellyfish vehicle central axis as the z-axis of the cylindrical co-ordinate system (CSYS=5). Both sides of $1/8^{th}$ segment being circular symmetric were constrained from moving in hoop direction (UY=0). The line on the axis of the vehicle was also constrained from moving in radial direction (UX=0). Also, to constrain any rigid body translation, we chose to constrain one node on rigid central hub lying on the axis of the vehicle from moving in axial direction (UZ=0).

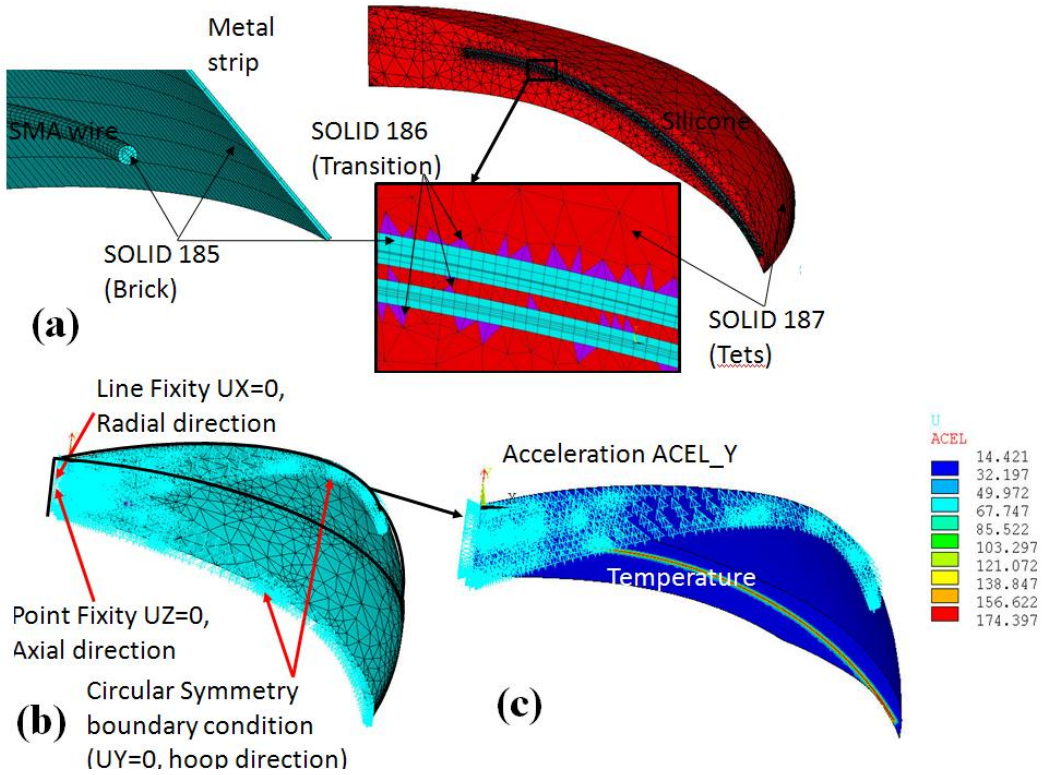

Figure 7-12. (a) Transient structural deformation model mesh, (b) displacement boundary conditions, and (c) temperature and acceleration boundary conditions.

We accounted for gravitation and buoyancy force of the water by applying inertial acceleration corresponding to reduced gravitation under buoyancy from Eq. (15):

$$ACEL\_Y = \left(\frac{\Sigma_{\mathrm{mat}=1}^{N} V_{mat}\rho_{mat} - \rho_{water}\Sigma_{\mathrm{mat}=1}^{N} V_{mat}}{\Sigma_{\mathrm{mat}=1}^{N} V_{mat}\rho_{mat}}\right) 9.81\ m/s^2 \tag{15}$$

where $ACEL\_Y$ is the inertial acceleration for the vehicle, mat is the material index, ρ is the density, and V is the volume. Earth's gravitation acceleration was taken to be 9.81 m/s^2. Temperatures were applied as body forces and were read from previously solved transient heat transfer model result. To account for the fluid drag we have introduced damping by

defining $BETAD = 0.03$. This creates a damping matrix $[C] = BETAD[K]$, where $[K]$=stiffness matrix of the FE model.

The overall FE system equation can be written as

$$[M]\ddot{\vec{U}} + [C]\dot{\vec{U}} + [K]\vec{U} = \vec{F} \quad (16)$$

Here, $[M]$, $[C]$ and $[K]$ are displacement dependent the mass matrix, the damping matrix and the stiffness matrix respectively, $\vec{U}$ is the displacement vector and $\vec{F}$ is effective force vector. The system defined by Eq. (16) is nonlinear due to variable $[M]$, $[C]$and $[K]$ matrices.

7.5.3.2 Solution: transient structural deformation analysis

As in transient heat transfer model, we start the modeling with SMA wires having properties corresponding to heating curve (martensite to austenite temperature transformation) for contraction phase of the cycle and during relaxation we use material corresponding to cooling curve (austenite to martensite temperature transformation). In simulation, this was achieved by defining two separate SMA material property curves corresponding to (martensite (M) to austenite (A) and austenite to martensite) and switching from material with $M \rightarrow A$ curve to material with $A \rightarrow M$ curve after completion of contraction phase. As SMA wire is well above austenite finish temperature A_f, for which both the material curves (cooling and heating) have identical properties there's no abrupt jump between these curves. We used the time intervals as used in transient heat transfer model.

7.6 Results and discussion

7.6.1 Transient heat transfer analysis

Figure 7-13 summarizes all major results of transient heat transfer analysis. Figure 7-13 (a) shows overall temperature distribution at the end of heating phase. It suggests that practical region of interest is concentrated near SMA wire, and for most part, it does not change along SMA wire length. Near the edge of the bell, however model predicts a little more temperature rise in the SMA wire compared to rest of the area due to very thin silicone layer as same amount of generated heat is absorbed by lesser silicone available. Since rate of heat conduction into silicone is higher compared to the rate of heat being convected away at the sub-umbrella surface, silicone temperature rises faster and temperature gradient between SMA wire and Silicone reduces, inhibiting heat conduction from SMA wire to sub-umbrella surface. Figure 7-13 (b) shows temperature history at a typical location at SMA center and in silicone 1 element away from SMA wire surface. It shows typical response of first order system to a given excitation. Initial high current pulses till t=0.12 sec result in fast temperature rise at SMA center which keep increasing at logarithmic rate from t=0.12 sec to t=0.70 sec. Temperature at SMA center decreases exponentially from t=0.70 sec to t=2.00 sec but fails to return to starting temperature of 25°C at the end of the cycle (T=45°C at t=2.00s) suggesting net heat accumulation in the model. It also suggests that we may be adding heat unnecessarily at higher rate during low current constant heating cycle as the temperature at the end of high current pulsed heating is well beyond austenite finish temperature A_f. This additional heating also aggravates heat accumulation problem that eventually results in partial loss of performance of the actuator as insufficient cooling results into incomplete transformation into martensite phase. Temperature in silicone 1 element away from SMA surface shows quite similar trend but has reduced temperature rise peaks during high current pulse cycle as low conductivity dampens out the sharp

peaks. Cooling cycle starts with significant temperature gradient between SMA center and the aforementioned silicone location but diminishes exponentially fast as is evident from Figure 7-13 (b). Figure 7-13 (c) compares temperature distribution near SMA length at typical location for key time points t=0.12 sec (end of high current pulse heating), t=0.70 sec (end of constant low current heating), and t=2.00 sec (end of cooling cycle).

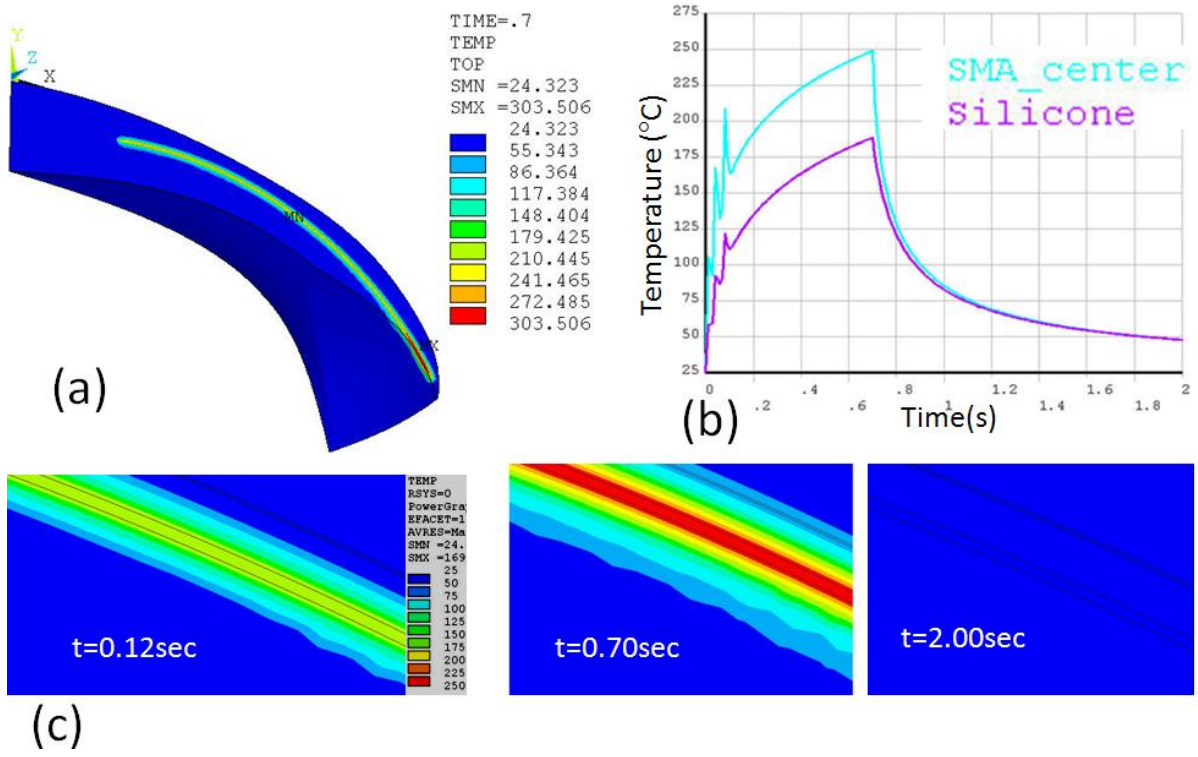

Figure 7-13. (a) Overall temperature distribution at t=0.70 sec, (b) temperature time history at SMA wire center and in Silicone 1 element away from SMA surface, and (c) typical temperature distribution along SMA wire length.

7.6.2 Transient structural deformation analysis

7.6.2.1 Overall bell deformation

Since, gravity and buoyancy forces are accounted for, in the two equilibrium positions (relaxed and contracted), where fluid pressure differential does not exist across subumbrella and exumbrella due to the FE model and the artificial *A.aurita* being held at the bell center; we can predict deformation at these positions accurately at this location without worrying about approximations involved in fluid drag. Figure 7-14(a) shows various views of FE simulation result for contracted state at t=0.12 sec. Original undeformed model is shown with only black edges superimposed on deformed model for comparison. Figure 7-14 (a.1) represents bottom view of the contracted artificial *A. aurita* bell model which qualitatively matches the contracted bell segments of *Cyanea capillata* species (Figure 7-14 (d)) and experimental artificial *A. aurita* contraction (Figure 7-14 (e)) that we have intended to model in our FE simulation. Note that due to manufacturing imperfections not all the bell segments deform the same amount (Figure 7-14 (e)). The comparison of contracted profile with that of *Cyanea capillata* is justified as our artificial *A.aurita* possess joint structure and radial muscles that were inspired by *Cyanea capillata* possessing similar radial muscle arrangement (Gladfelter,1973). Figure 7-14 (a.2) depicts isometric view of deformed model for better visualization. Figure 7-14 (a.3) shows cross-sectional view taken along BISMAC center line. Figure 7-14 (a.4) exhibits side view of the contracted FE model also matching well with natural *A. aurita* shown in Figure 7-14 (b) and experimental artificial *A. aurita* (Figure 7-14 (c)). It is evident that the bell curves inwards at the BISMAC locations radially and axially well and confirms that the joint design provided by Smith and Priya (Smith,2010) is effective in assisting the bell deformation at the BISMAC locations. This behavior was also confirmed in experimental *A. aurita* deformation (Figure 7-14 (c)).

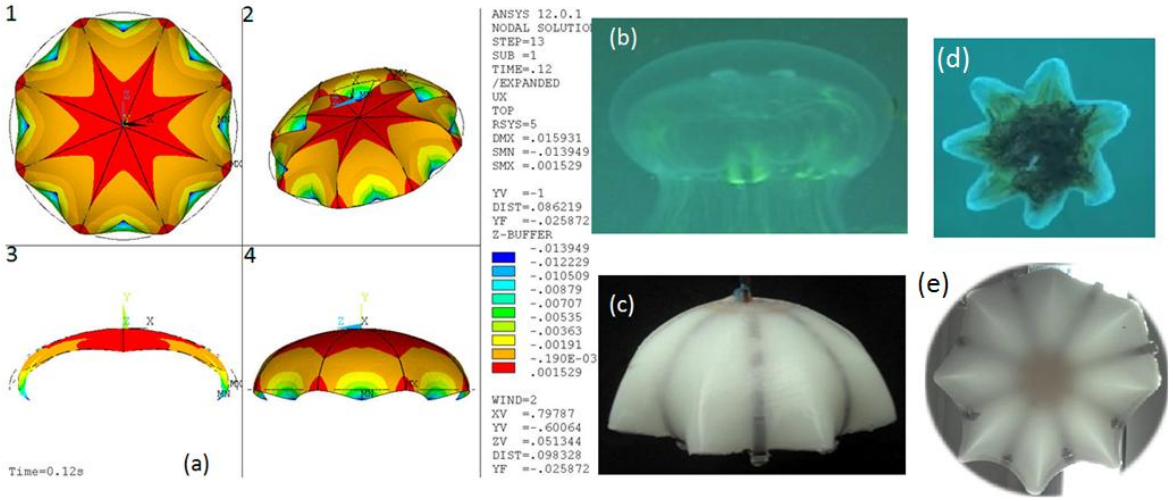

Figure 7-14. (a) Finite element result for artificial *A. aurita* bell contraction, (a.1)bottom view, (a.2) isometric view from bottom, (a.3) cross sectional view at BISMAC location, (a.4) side view (b) biological *A. aurita* contraction (c) artificial *A. aurita* experimental contraction (d) *Cyanea capillata* bell segment contraction bottom view (e) artificial *A. aurita* experimental contraction bottom view ((Villanueva,2011))

7.6.2.2 Comparison of deformation at the BISMAC location and at the joint location

Figure 7-15(a-f) reveal radial displacements in the bell at the BISMAC cross-section and in the joint cross-section respectively at the key time points (t=0.12s, t=0.70 s and t=2.0s); each group uses a common color legend for ease of comparison. It is obvious that the deformation is negligible near the centre of the jellyfish bell and maximum at the tip of the bell. At joint location the bell is practically undeformed.

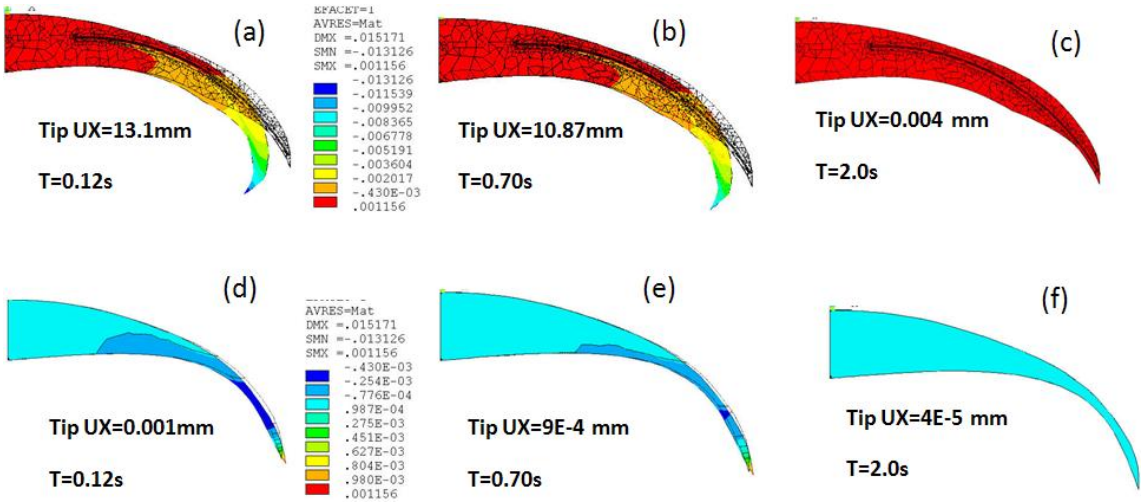

Figure 7-15 (a-c) Deformed artificial *A. aurita* bell at BISMAC location at different time t=0.12s,0.70s and 2.0s (d-f) deformed artificial *A. aurita* bell at joint location at different time t=0.12s,0.70s and 2.0s

Figure 7-16 (b) plots the time history of radial and axial tip displacement at BISMAC location which conforms to second order system response to step excitation. In fact, the high power pulse heating is done at much higher frequency than the bell is able to respond, thus inertia of the bell acts as low-pass filter for the pulsed heating excitation. But as discussed in transient heat transfer results, SMA goes through complete martensite to austenite transformation in this period, contracting due to phase transformation strain and achieves maximum deformation of $U_{radial} = 13.1mm$ and $U_{axial} = 7.87mm$ at t=0.12s. At the maximum deformation point, the inertial forces and elastic restoring forces are not in equilibrium. The bell has a slight overshoot above equilibrium position due to inertia. During moderate constant current excitation from t=0.12s to t=0.70s as temperature keeps rising, without any additional benefit to SMA transformation strain the structure relaxes under stored strain energy during rapid contraction and after a small oscillation around equilibrium condition finally settles to $U_{radial} = 10.87mm$ and $U_{axial} = 6.04mm$. During relaxation phase from t=0.70s to t=2.0s, SMA goes through austenite to martensite transition as temperature drops rapidly and returns to original configuration after little oscillations as is evident from Figure 7-16 (b) , Figure 7-15(a-b) and Figure 7-17 (a).

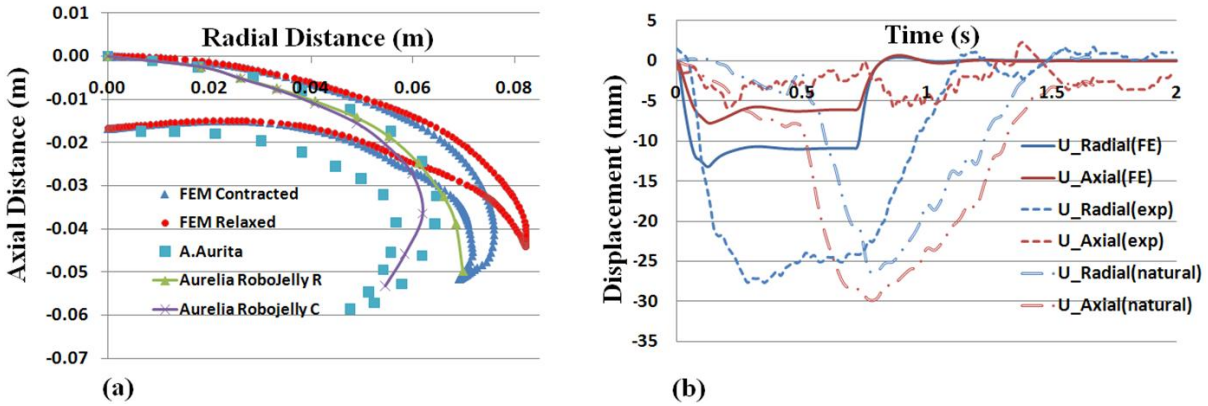

Figure 7-16. (a) Comparison of the FE results with artificial *A.aurita* bell deformation and natural *A. aurita* (b) time history of *A. aurita* tip displacement at BISMAC location

Figure 7-16 (a) compares the relaxed and contracted position of the simulated *A.aurita* bell with natural *A.aurita* and robotic *A.aurita*. The natural *A.aurita* with its muscle contracting in excess of 40% clearly achieves the highest deformation, not being fully matched by either artificial *A.aurita* or FE simulation. Experimental deformation on artificial jellyfish was measured through image processing thus only exumbrella points are available for comparison. Experimental model however has changed its form during manufacturing which was designed to match FE model in relaxed state. This results in apparent mismatch in FE prediction from the experimental deformation. Inspite of this mismatch, the overall deformations are comparable. Figure 7-16 (b) shows comparison of time response of the transient tip displacements between FE simulation and artificial and natural *A.aurita*. It should be noted that the natural *A.aurita* swims freely in water moving forward, while artificial (experimental) *A.aurita* and the model are held at the bell center and does not move it water. Also, for the particular cycle for which data is obtained has cycle time 1.7s instead of 2s. Natural *A.aurita* contracts and relaxes very smoothly and does not have any steady equilibrium position. Artificial *A.aurita* achieves about twice as much radial displacement as predicted by simulation, but follows similar trend of sharp rise (fall), overshooting above the equilibrium position beyond t=0.12s, relaxing to equilibrium

position during t=0.12s to t=0.70s due to stored strain energy in the bell during contraction cycle. In relaxation cycle, as SMA cools down and undergoes austenite to martensite transition, the bell returns back to its original location slightly overshooting beyond equilibrium position before returning back to relaxed configuration. FE simulation captures this entire physics perfectly. Artificial *A.aurita* returns to relaxed position slower than predicted by model, suggesting that heat gets conducted away from SMA more slowly than we predict. However, artificial *A.aurita* axial displacement being too small; gets affected by finite resolution of image processing and shows inconclusive trend. FE simulation predicts axial tip displacement time history similar to that of radial tip displacement but reduced in magnitude.

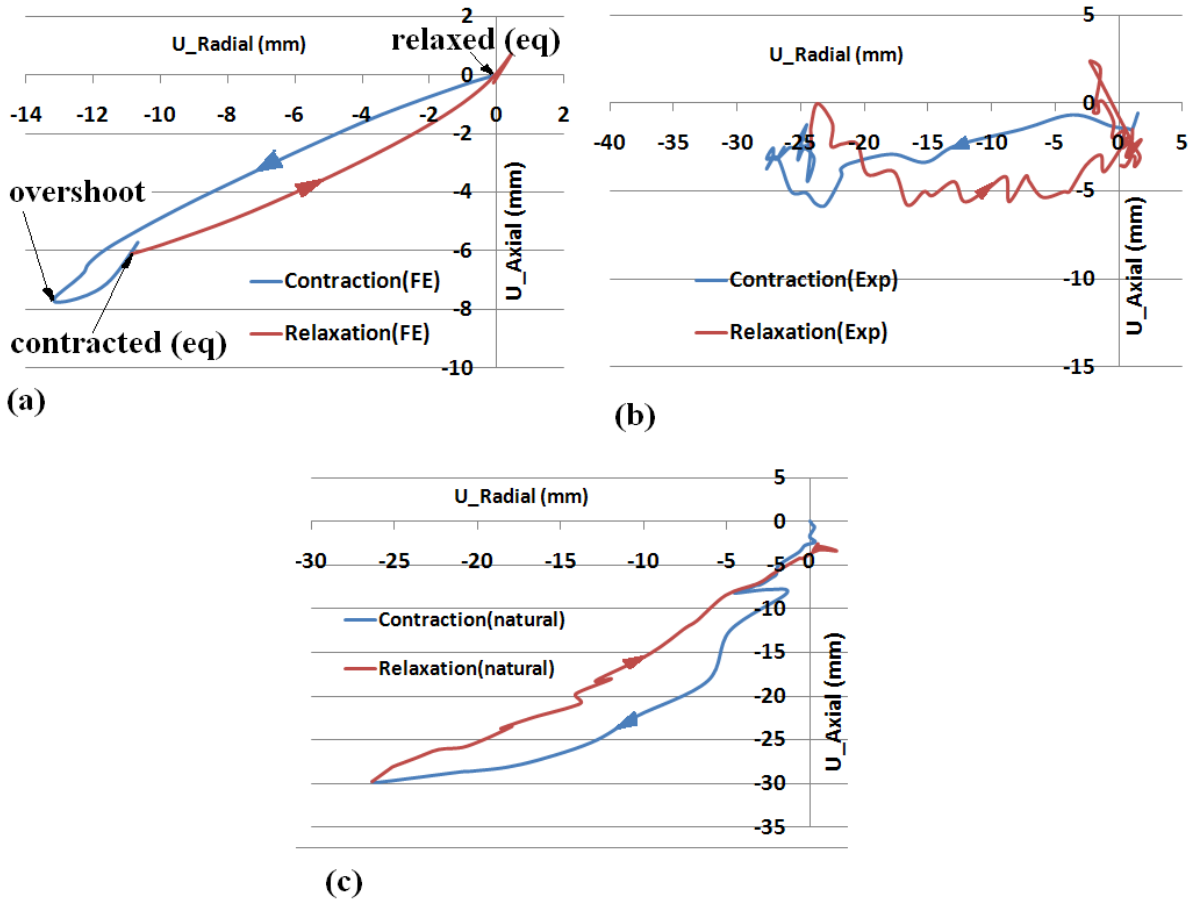

Figure 7-17. Trace of tip displacement at BISMAC location by (a) FE simulation and (b) artificial *A.aurita* experiment (c) natural *A.aurita*

Figure 7-17 (a) exhibits the trace of the bell tip at BISMAC location and suggests that bell-tip does not follow the same path while relaxing to its original configuration than it did during contraction. It also illustrates the overshoot around the equilibrium positions (relaxed and contracted). Tip displacement for the artificial *A. aurita* (Figure 7-17 (b)) shows different trace patterns during contraction and relaxation as predicted by the model. Since artificial *A. aurita* begins with different relaxation configuration, this is expected. Interaction with surrounding fluid would cause the tip displacement trace to change which are not accommodated in the model. Oscillations in the trace of the experimental results are partly due to tracking error. The magnitude of the oscillations is close to the predicted error from the tracking method. Figure 7-17 (c) represents trace of tip displacement of natural *A.aurita* scaled to the same bell diameter. Natural *A.aurita* is freely moving in water. The direction of contraction and relaxation is quite similar to the one predicted by the model (Figure 7-17 (a)), however relative location of the path during contraction and relaxation is reversed. We believe that this is caused by the fluid forces and the freely forward motion present in natural *A.aurita.*

For a more quantitative comparison, we calculated the curvature of the profiles by calculating radius of circle passing through 3 consecutive points.

$$R(P_2) = \frac{\sqrt{(x_1 - x_2)^2 + (y_1 - y_2)^2}\sqrt{(x_2 - x_3)^2 + (y_2 - y_3)^2}\sqrt{(x_3 - x_1)^2 + (y_3 - y_1)^2}}{2(x_2y_1 - x_1y_2 + x_3y_2 - x_2y_3 + x_1y_3 - x_3y_1)} \qquad (17)$$

$$\rho(P_2) = 1/R(P_2) \qquad (18)$$

where $R(P_2)$ is the radius at point $P_2(x_2, y_2)$, having previous point $P_1(x_1, y_1)$ and next $P_3(x_3, y_3)$. Except first and last point, radius and curvature of all points can be calculated by using Eq. (17) and (18). Equal interval of all the points is very essential for this method, thus additional or fewer points were generated from available FE nodes, experimental traces and *A. aurita* profile.

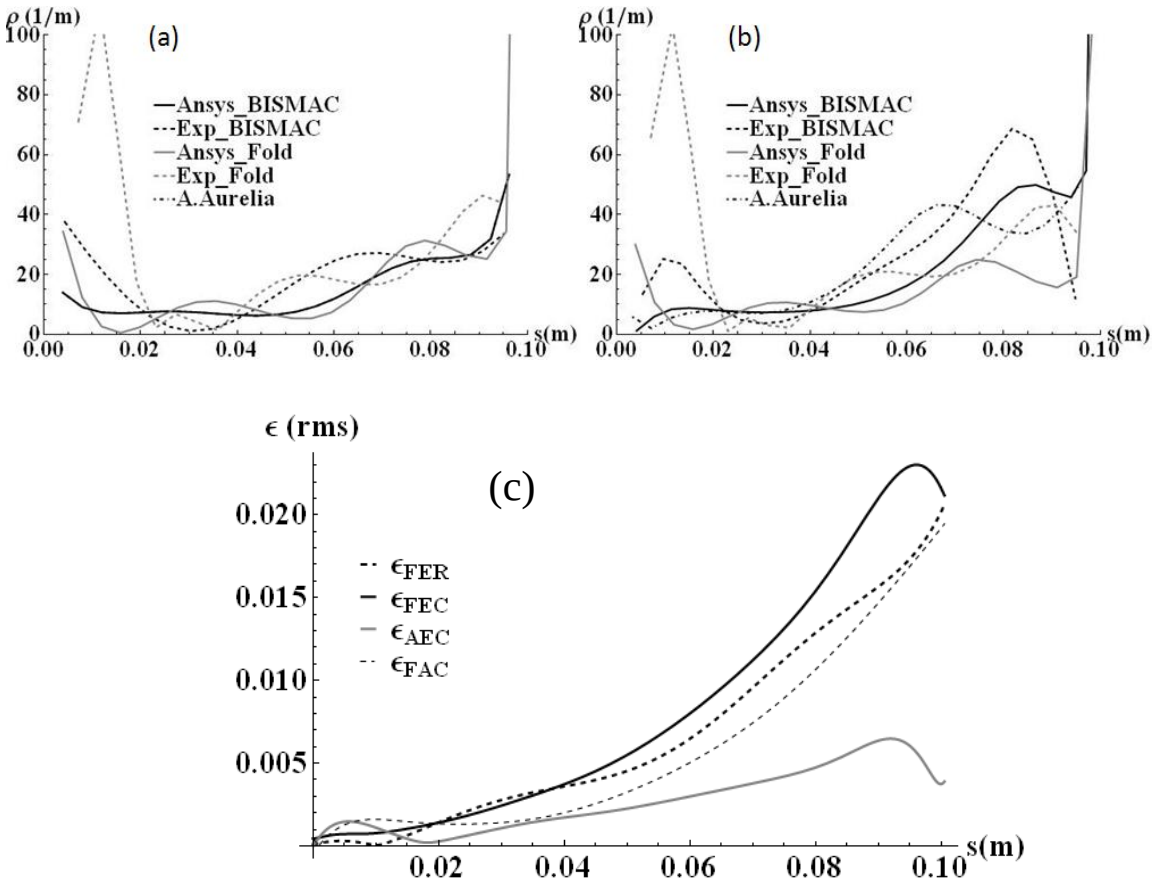

Figure 7-18. Curvature comparison At BISMAC and fold location between ANSYS,experiment and biological *A. aurita* (a) relaxed condition (b) contracted condition (c) profile errors at BISMAC location- FER:between FE and experiment relaxed profile, FEC:FE and experiment contracted profile, AEC: *A. aurita* and experimental contracted profile, FAC:FE and *A. aurita* contracted profile

Figure 7-18 (a) and (b) compares the curvature of the profile along the length of the curved exumbrella surface in relaxed and contracted condition between FE simulation, experimental and natural *A. aurita.* In relaxed condition, FE model curvature matches that of *A. aurita*. Experimentally as evident from Figure 7-16 (a) and Figure 7-18 (a) it does not match *A. aurita* profile in the relaxed state. Figure 7-18 (b) emphasizes that curvatures of FE model, experimental as well as natural animal, increases as the fish contracts. Artificial *A.aurita* does

not have the same relaxed state as the natural animal, but in contracted state it follows natural *A. aurita* exumbrella deformation. It outperforms the curvature of the natural *A. aurita* by achieving a maximum curvature of 67 m^{-1} at about 80% length. FE model and natural *A. aurita* achieve maximum curvature of 50 m^{-1} at 67% and 45 m^{-1} at 85% respectively and show sharp increase at the tip, suggesting dynamic overshoot of the passive flap that is hypothesized to help swimming performance. Figure 7-18(c) displays profile errors between various profiles and conditions.

$$\epsilon_{FER}(s) = \sqrt{\left(x_{FE_{BR}}(s) - x_{\mathrm{Exp}_{BR}}(s)\right)^2 + \left(y_{FE_{BR}}(s) - y_{\mathrm{Exp}_{BR}}(s)\right)^2} \tag{19}$$

The profile error ϵ_{FER}, is defined as the distance between corresponding points $(x(s), y(s))$(subscript BR corresponds to the BISMAC location and relaxed condition) of FE model and the artificial *A.aurita* vehicle relaxed profiles at location s. This was calculated by Eq. (19) and we observe that profile errors between the FE simulation and artificial *A.aurita* experiment in relaxed and contracted states, ϵ_{FER} and ϵ_{FEC}, have similar trends (Figure 7-18 (c)). This indicates that the difference between FE simulation and artificial *A.aurita* is mainly due to the initial difference in relaxed profiles. We hypothesize that if artificial *A.aurita* were re-designed to match the natual *A.aurita's* relaxed state, the simulation would match it more closely. The profile error does not increase beyond 5.8mm which corresponds to 22% of the initial profile error in relaxed configuration.

The model developed in this study gives better understanding of the temperature rise in the SMA wires and transient heat distribution in and around it during entire cycle. It reveals that in spite of complex geometry, heat distribution is practically uniform along SMA length and can be effectively captured by 1st order unsteady heat conduction equation. It explains degradation of performance of artificial *A.aurita*, over number of cycle due to heat accumulation resulting from insufficient cooling and suggests opportunity of making the bio-inspired *A. aurita* vehicle more

energy efficient by reducing oversupply of heat to SMA wire and effectively controlling SMA temperature. The model predicts transient deformation behavior of the artificial *A.aurita* qualitatively at BISMAC and fold locations, confirming effectiveness of the join design. It reveals that the transient tip displacement response can be modeled as a second order system, however due to mismatch in initial profile, predicts the radial tip displacement response ~44% of the experimental curve. The model captures these physical aspects of bell deformation accurately and is a useful tool to evaluate effectiveness of design changes on performance of the vehicle without building one.

7.7 Conclusion

We introduce a customization procedure for BISMAC actuators to be used as radial muscles in artificial *A.aurita* such that we can match the relaxed and contracted profiles of *A. aurita* at the BISMAC locations. By accurately modeling the hyperelastic behavior of EcoFlex (Shore 00-10) RTV silicone and using experimentally obtained temperature-strain transformation curves for SMA wires we provide a high fidelity model that captures most essential physics of artificial *A.aurita* deformation. The model suggests a unique approach to overcome ANSYS limitation in modeling SMA temperature transformation by using negative thermal coefficient of expansion and two separate material curves for heating and cooling. This approach is generic enough to be used in numerical modeling of the SMA temperature dependent transformation in any design. The transient heat transfer model provides better understanding of temperature rise in SMA wire and heat distribution around it during an entire contraction-relaxation cycle. This information is crucial in designing and evaluating SMA heating algorithm and cannot be obtained from the prototype directly. The model also reveals that in spite of the complex

geometry, the temperature distribution along the length of SMA wires is uniform and we could use a simple first order heat transfer model to study temperature distribution in and around SMA wires. It also exposes the reason for degradation of the performance of artificial *A.aurita* over a number of cycles due to heat accumulation and reveals an opportunity to make the artificial *A.aurita* more energy-efficient by reducing the amount of heat supplied above the austenite's finish temperature A_f that doesn't contribute toward bell deformation. Transient structural model accounts for the gravity and the buoyancy forces and thus in equilibrium conditions (Fully contracted and fully relaxed states), where fluid pressure differentials across subumbrella and exumbrella do not exist, we can predict the bell deformations fairly accurately. Transient structural analysis captures all essential behavior of artificial *A.aurita* at BISMAC and fold locations and confirms effectiveness of the joint design, though an exact match was not achieved due to initial profile mismatch. The model reveals that the transient tip displacement response can be modeled as a second order system, however due to initial profile mismatch; the model predicts the radial tip displacement response at ~44% of the experimental curve. Profile error analysis suggests that initial error in simulation and artificial *A.aurita* relaxed profiles is a major cause for the mismatch. The profile error increases by a small amount with an average of 0.00015m (0.58% of ϵ_{FER}) and reaches a maximum of 0.0058m (22% of ϵ_{FER}). The model captures these physical aspects of bell deformation physics accurately and is a useful tool to evaluate effectiveness of design changes on performance of the vehicle without the need for time-consuming physical construction. The modeling methodology is generic and could be used to model other bio-inspired robots using similar construction technique.

Chapter 8. Summary

This thesis has provided the physical understanding of jellyfish morphology, behavior and propulsion mechanism. It was shown through modeling and validation experimentation (conducted by collaborators) that jellyfish morphology and swimming mechanism can provide significant advantages in developing the high efficiency underwater vehicles. This thesis further provided the mathematical foundation for explaining the musculature arrangement and need for different types of muscles. Finite element models were developed to understand the effect of mechanical properties of mesoglea on the contraction – expansion cycle of the jellyfish. The modeling effort led to the prediction of mechanical characteristics that will be required in the biomimetic jellyfish vehicles to replicate the efficiency of natural counterpart. Modeling results were compared with natural animal and experimental prototype "Robojelly" over one complete swim cycle to validate the hypothesis. In addition, this thesis addressed two other important issues related to the deployment of artificial vehicles, namely, energy and buoyancy control. Novel concept is presented for the buoyancy control based upon the electromigration of ions through the ionic membrane. A very detailed analytical model was developed for the computation of the power from the amorphous silicon solar cells mounted on the exumbrella of aurelia, cyanea and mastigias species as a function of depth, turbidity and inclination. Major scientific contributions of this thesis are as follows.

8.1 Jellyfish morphology and kinematics

A detailed and complete analytical model of BISMAC actuator was developed employing the constitutive equations of the SMA that simulate the BISMAC deformation within operating range. The model was experimentally verified by Colin et al. (Smith,2011). The analytical model will provide the actuator designers an ability to customize the BISMAC parameters for optimal

deformation profile and force generation. In order to achieve biomimetic kinematics of the jellyfish bell, it is of utmost importance for the actuator to provide non-linear deformation profile with large flexural deformation and resemble the hysteretic cyclic response over a complete cycle. The results of the model show that modified SMA can meet most of the requirements for developing the artificial jellyfish vehicles. BISMAC design investigated in this thesis was able to convert the large force and small 4-8% transformation strain into high flexural deformation with acceptable bending moment.

An approach inspired by the curved beam theory was developed that illustrates the approach for implementing any flexural actuator for achieving jellyfish deformation profile by varying the bending stiffness of the curved beam. This analysis uses curved profile as a function of beam length and thus is not limited to small rotations and Cartesian coordinate system. A comparative analysis of two beam configuration was presented on the basis of curved profiles to reduce the effect of rigid body rotation. This approach opens up the new possibilities for development and optimization of flexible propulsors. As an illustration, it was shown that IPMC actuators can achieve biomimetic relaxation and contraction with much less strain requirement if fabricated with initial curved configuration that is mean value of relaxed and contracted curvature (Joshi,2011b).

An important observation was made on the basis of analytical model during the course of this thesis that reflected the importance of a passive region present at the tip of the bell on the kinematics of jellyfish. Villanueva et al. have experimentally demonstrated that by incorporating the flexible margin in the jellyfish vehicle prototype the proficiency can be increased by several fold and the thrust can be increased by more than 1000%. This observation predicted from the analytical model developed in this thesis is considered to be very significant and has already

generated great interest in the research community to conduct more experimentation on quantifying the dynamics and energetics of passive margin towards propulsion.

8.2 Fundamental understanding of muscle architecture

Jellyfish such as *Cyanea capillata* are characterized by the presence of three groups of muscles:

(i) coronal muscles (circular muscles),

(ii) coronal muscles with mesogleal fold in radial direction (segmented circular muscles), and

(iii) radial muscles (radial muscles)

In order to understand the role of these individual muscles and explain how they function collectively to provide efficient jellyfish bell contraction, a detailed finite model was developed. This analysis is highly desired to decide upon the placement of actuators in the artificial vehicles. There is not enough information available in literature to model the natural mesoglea and natural muscles are only one cell layer thick which poses extreme numerical challenges. Thus, innovative modeling approaches were developed by incorporating the proper geometry, functionality and form factor of the artificial actuators to simulate the natural muscles and their arrangement. These novel approaches further required modeling of the hyperelastic artificial mesoglea (EcoFlex0010 Silicone), metal strip and SMA wires with very high aspect ratios. Several novel strategies were adopted in the development of complete model: (i) modeling of the temperature – transformation behavior of SMA wires was achieved by artificially defining the negative thermal co-efficient of expansion, (ii) thermal conductivity and Young's modulus of SMA wire were computed as a linear function of martensite fraction and thus varied with temperature, (iii) hysteretic behavior of the SMA phase transformation was determined by using

two separate material curves – one for the heating phase (martensite to austenite) and another for the cooling phase (austenite to martensite). This novel approach circumvents the limitations of commercial finite element package such as ANSYS while ensuring the essential accuracy for understanding of the jellyfish propulsion.

Circular SMA muscles were found to not cause any appreciable bell deformation due to two reasons: (a) the closeness from the thick center of the bell offers high resistance to the contraction, and (b) muscle contraction is limited to 4-8%. However, they assist the overall deformation by compressing the central portion of the bell and increasing the buckling tendency of the bell. This makes further deformation of the bell easier.

Segmented circular muscles were found to result in bell deformation that is primarily in axial direction with a small radial deformation. The deformation breaks the axi-symmetry of the bell which helps the radial muscles. The trend of deformation obtained was quite non-intuitive. The bell deformation showed increasing trend from radial location 34-81% with maximum at 81%, and then decrease in axial deformation. When non-dimensionalized with actuator length, the optimum radial location for actuator placement was at 66%. Simultaneous actuations of all these muscles do have additive effect but it is quite non-linear. Center of the bell being thick is difficult to deform thus muscles closer to center see larger resistance and cannot achieve full contraction. The muscles too far from the center of the bell see much less resistance and can contract fully without problem, but have less leverage towards affecting the bell tip deformation. Also, with increasing distance from the center of the bell, the radius increases and effective length of SMA increases proportionately. Hence, even though actuator at 81% radial location achieves the most axial deformation it does so with increased length of SMA wire. The radial location at 66% was obtained as the most optimum location to incorporate the segmented

circumferential muscles. A single segmented circumferential muscle at 66% radial location can achieve 76% of axial bell deformation compared to having 5 muscle rings contracted simultaneously at 34.4%, 51.4%, 66%, 80.6% and 95.2%. Thus, this analysis revealed the optimal location for placement of segmented circumferential muscle for maximum effectiveness from energy efficiency standpoint.

Radial muscles impart non-axisymmetric deformation; mainly in radial and some axial direction at the cross-section of their location (BICMAC location) but at the fold location there is practically no bell deformation. Folds acts almost like a hinge between two bell segments.

Overall, the results from the analysis can be summarized as: (a) circumferential muscles mainly compresses central bell increasing its buckling tendency and eases task of segmented circumferential muscles; (b) segmented circumferential muscles impart mainly axial deformation to the bell and break axi-symmetry in deformed bell in turn helping the radial muscle contraction; (c) there is an optimum location at 66% radius for placement of segmented circumferential muscle that is most energy efficient to achieve axial bell deformation; (d) adding more segmented circumferential muscle does not have proportional justifiable advantages; (e) radial muscles impart mainly radial and some axial deformation to the bell at the location of placement; and (f) fold location acts as hinge between two bell segments and remains practically unaffected by contraction of radial muscles.

8.3 Optimization of the artificial *Aurelia aurita* prototype

After successful BISMAC model development and having understood the role of different muscle architecture, it was desirable to model an artificial jellyfish vehicle in order to validate the model and to enhance the confidence in the model's ability in capturing all the essential behavior of the prototype "robojelly". We used hybrid *Aurelia aurita* bell profile that

incorporated mesogleal folds suggested by Smith et. al. (Smith,2010) to facilitate the radial muscle. The model achieved very similar changes in curvature and captured all the qualitative behavior of robojelly deformation. Complete system level transient modeling of actual jellyfish vehicle presented here has been never attempted before. Having captured most essential physics, this modeling approach can be now easily used to perfect the design of the vehicle without having to go through the expensive trial and error prototype building. The model also provided insights into the system performance that are difficult to be obtained through the experimentation reveal opportunities for performance enhancement.

Measuring temperature of 100 micron diameter SMA wires in real time is practically impossible. The model can predict temperature and heat distribution in and around the SMA wires. The transient thermal model also revealed effectiveness of initial fast heating in achieving rapid phase transformation in SMA wires. It revealed that SMA wires were getting heated much beyond A_f (austenite finish temperature). This additional heating does not contribute to the bell deformation and is unwanted heat that needs to be removed during cooling phase. The model also suggested that there is insufficient cooling of SMA as it fails to achieve original temperature at the end of the cycle, which causes accumulation of heat, incomplete transformation into martensite and thus loss of performance with each cycle and ultimately burning of SMA wires (as noticed in the robojelly swimming). The model identified the cause of this behavior. As a corrective action resistive feedback algorithm was developed by Villanueva et. al. (Villanueva,2010a) that reduced the power consumption of robojelly from 90 watt to 18 watt. Model also captured the different paths followed by bell tip trace during contraction and relaxation.

Thus modeling of the robojelly not only proved as a useful design tool in predicting the bell deformation but it also provided useful insights into the design and performance of vehicle.

8.4 Model for underwater solar energy harvesting

To reduce the reliance on onboard battery, an investigation on solar energy as a potential source for powering AJV (Autonomous Jellyfish Vehicle) was conducted. It was experimentally confirmed that salinity has no significant effect on the performance of solar cell but harvested power decreases with depth. The available power initially decreases with depth, mainly due to absorption and reflection of long wave radiation and solar spectrum shrinks and shifts towards short wavelength range around 400-600 nm which is advantageous for amorphous silicon. Reduction in long wave radiation also results in increase in conversion efficiency with depth (~30-40% at depth 0.2m) before reaching the peak at 0.2m. Beyond this depth, the efficiency shows a decreasing trend. Transmission of solar radiation decreases rapidly with depth and increasing turbidity. The variation was found to be quadratic in turbidity and the coefficients of quadratic relation were linear function of depth. The performance of solar cells was found to be severely affected by the angle of incidence of the radiation. Higher refractive index of water was advantageous for undersea solar energy harvesting as the apparent zenith angle of sun is lower than that in the air. This helps in reducing the variation in incidence angle over the entire day. However, the reduction in radiation intensity in water is much sharper in comparison to that in air which overcomes this advantage.

An analytical model was developed to estimate the power harvested from AJV using spectral response of single crystal silicon cell with depth and applying a scaling factor to obtain the amorphous silicon cell response. Incident radiation was modified by using transmissibility

information with depth and turbidity. Total power was estimated by integrating the areal power density over incidence angle and diameter. The model suggested monotonic reduction in harvested power with increase in fineness ratio (aspect ratio) of AJV. It was found that in relaxed state, *Cyanea capillata* harvests the maximum power followed by *Aurelia aurita* and *Mastigias* sp., for same bell diameter. However, *Cyanea capillata* harvests the least power in contracted state due to increased inclination angle over the majority of its bell area. *Aurelia aurita* harvests the maximum power in contracted state. Comparison of average power harvested suggests that *Cyanea capillata* would be able to harvest the maximum average power for continuous operation. The parametric study suggested that variation in power harvested is a parabolic function of AJV bell diameter. For a diameter of 2m with turbidity of 1ntu and depth of 1m, we can expect power in excess of 85W, 55W and 125W respectively from AJV mimicking *Aurelia aurita, Mastigias* sp. and *Cyanea capillata* profile respectively in relaxed condition. These are promising values for developing a surveillance vehicle that can be deployed in ocean. AJV can also charge their on-board batteries by staying at the surface for their intermittent propulsive needs. With increase in turbidity form 1 to 7, a quadratic decrement was observed that causes reduction in power harvested by more than 60%. With depth, power harvested increases slightly due to increased efficiency and after that shows a monotonous decreasing trend. At 5m depth, the power available was reduced by 75%.

A generalized model enabled power harvesting estimates in any field condition. It also suggested the advantage of tilting of the vehicle to face refracted sunrays. *Cyanea capillata* suffers the most if the refracted sunrays and AJV axis are not aligned. *Mastigias* sp. is least affected, giving almost constant power output at all inclinations. *Aurelia aurita* shows intermediate behavior. Thus, *Mastigias* sp. has the optimum shape for AJV required to achieve

effective lateral motion. It is expected that this generalized model will provide guidelines for developing not only AJV but also other form of AUVs.

8.5 Multi-physics model of thermo-magnetic energy harvester

The multi-physics numerical model developed in this thesis is capable of simulating a range of different scenario of the vibration behavior of the fixed-fixed beam in the thermo-magnetic energy harvester. It provides an opportunity to study interactions of different physics and effect of the device parameters on the dynamic behavior of the system. Since the magnetic force is unidirectional, restoring spring force should also be made unidirectional (but opposing magnetic pull) by intentionally adding a base offset. For sustained vibration indicated by a single limit cycle behavior constancy of thermal cycling must be achieved i.e., heat input to the system nearly equals heat rejected repeatedly cycle after cycle. Increasing source temperature much beyond Curie temperature may lead to insufficient cooling in one cycle, requiring multiple cooling pass per heating pass resulting in period doubling limit cycle bifurcation. Decreasing sink temperature too much causes insufficient demagnetization during heating, restoring spring has to work against stronger magnetic force and system may keep losing more energy each cycle resulting in stable spiral behavior.

Contact stiffness increases frequency of vibration by reducing impact duration with heat transfer surface, but tends to saturate as contact stiffness increases. Increase in gap distance reduces frequency of vibration. If the gap distance is too small, the magnetic force is strong even towards cold surface, this increases system energy and linear damping assumption fails to limit vibration amplitude to reasonable limit and results in modeling instability. If gap distance is too large, it has to travel farther and overcome stronger spring restoring force due to higher

displacements, this may require multiple cooling passes to achieve strong enough magnetic force to reach hot surface. This multiple cooling pass per heating pass is indication of period doubling limit cycle bifurcation. Beyond a certain value, increase in gap could cause spring strain energy to be sufficiently high that magnetic force can't overcome it and Gd can no longer reach hot surface and the system will keep losing energy to achieve steady state equilibrium. The system exhibits different dynamic behavior, such as stable spiral, stable limit cycle, period doubling limit cycle bifurcation and ultimately chaos observable by variation in source and sink temperatures.

To achieve best performance of the system, it should be operated at source and sink temperature fairly equally apart from Gd Curie temperature that helps to achieve steady state vibrations at a gap distance and spring stiffness carefully adjusted such that total force on the Gd magnet over the cycle is symmetrical about zero to achieve energy balance faster. The thermo-magnetic energy harvester device modeled here shows a promising approach. It could transfer heat from solar module effectively and simultaneously convert part of the energy into useful electrical power that may be inspire a new generation of efficient and cost effective UAV designs. The device however is not restricted to UAV application but can harvest small thermal gradients universally present around us: wall of pipe carrying hot water, radiators, electrical heat sinks, to name a few.

8.6 Bio-inspired buoyancy engine

A novel buoyancy engine was developed based on another pelagic crustacean, the deep sea shrimp *Notostomus gibbosus* that achieves buoyancy control by selective ion replacement (Sanders,1988) in its dorsal carapace. The buoyancy engine was capable of changing the ion

concentration in the buoyancy chamber / swim bladder by a small amount with help of applied electric field to induce the flow of positive ions through semi-permeable membrane. The membrane allowed positive ions to pass through it but restricted the flow of negative ions across it. We considered 5 major salts present in ocean water ($NaCl, MgCl_2, CaCl_2, Na_2SO_4$ and KCl) that comprise 99.9% of all the salt content in the substitute ocean water. A system of Nernst-Planck equations for each participating ion and Poisson equation for electric field were solved simultaneously using Newton Raphson (NR) algorithm in their non-dimensionlized form. At steady state, negative ions readjust their concentrations such that they have higher concentration at the positive electrode and linearly drop towards negative electrode. Similarly positive ions readjust their concentrations such that maximum concentration is towards negative electrode and linearly drops off towards positive electrode. The semi-permeable membrane allows flow of only positive ions through it, thus the concentrations at the positive electrode (where semipermeable membrane is located) are the same as those in the surrounding open ocean water. This net inflow of positive ions created a small change in density of the buoyancy chamber. For a representative buoyancy chamber of 10cm side each, with overpotential of 0.05V, the change in density at steady state was 0.9695 kg/m^3 which was achieved in $1.16E-8\,s$. For a representative pycnocline value of $\frac{0.003\frac{kg}{m^3}}{m}$, this small difference can result in significant change, of 323.16m, in equilibrium depth of the vehicle. The limiting acceleration however would be slow according to $\frac{\Delta\rho}{\rho} g \left(\frac{m}{s^2}\right)$ or $9.18\left(\frac{mm}{s^2}\right)$ and as one sinks deep in ocean water the density increases thus $\Delta\rho$ reduces. This dive can be achieved with minimal energy of $2.825J$.With increase in over-potential steady state, density increases almost as cubic function, however, it takes longer to achieve steady state. This bio-inspired buoyancy engine shows a great promise for vehicle to travel with minimum energy requirement.

8.7 Mesoglea and collagen properties

Mesoglea forms the main body of jellyfish, is neutrally buoyant, highly flexible and hyperelastic. Collagen fibers made up of insoluble proteins form network throughout the mesoglea and impart elasticity to it. They store strain energy during muscle contraction that is later used to relax the bell since jellyfish lacks antagonistic muscles to achieve relaxation. A 3-parameter Mooney-Rivlin model (hyperelastic) was developed to represent the mesoglea property. This opens opportunity for a multi-scale modeling approach for mesoglea properties built with collagen fiber network from the fundamental collagen properties. Representing the mesoglea properties correctly also forms the basis of comparison for other artificial mesoglea properties that may be used in vehicle design. The choice of artificial mesoglea material Ecoflex0010 Silicone was based on similar hyperelastic behavior and near neutral buoyancy as that of natural species. An artificial mesoglea based on hydrogel that closely mimics the physical nature of mesoglea was modeled. This new material shows the promise of operating with less force and less power, thereby enhancing the vehicle energy efficiency.

Chapter 9. Future work

In future, elaborate multi-scale modeling of jellyfish mesoglea and in general of a composite made of complex network structures needs to be conducted. This might open doors to a whole new modeling in materiomics and help in developing new material models for hydrogel, protein and tissue modeling. Simulation of actual jellyfish with actual mesoglea properties can be very interesting study.

A prototype needs to be fabricated based on the buoyancy engine calculations to experimentally validate the model. Experimental validation for solar energy harvesting model and thermo-magnetic harvesters also needs to be conducted. Non-dimensionalization of thermo-magnetic harvester can be done to extend understanding of simulations to general physical rules of the system. A complete two way fluid-structure interaction code should be developed to complete the modeling of the jellyfish vehicle prototype. This code will serve as a useful tool in understanding of the scaling effect, turning mechanism, directional swimming, swimming in a school, swimming behavior in turbulence and in development of non-dimensional parameters governing the dynamics of fluid-structure interaction.

Appendix : Jellyfish Glossary

(Taken from :(Stachowitsch,1992))

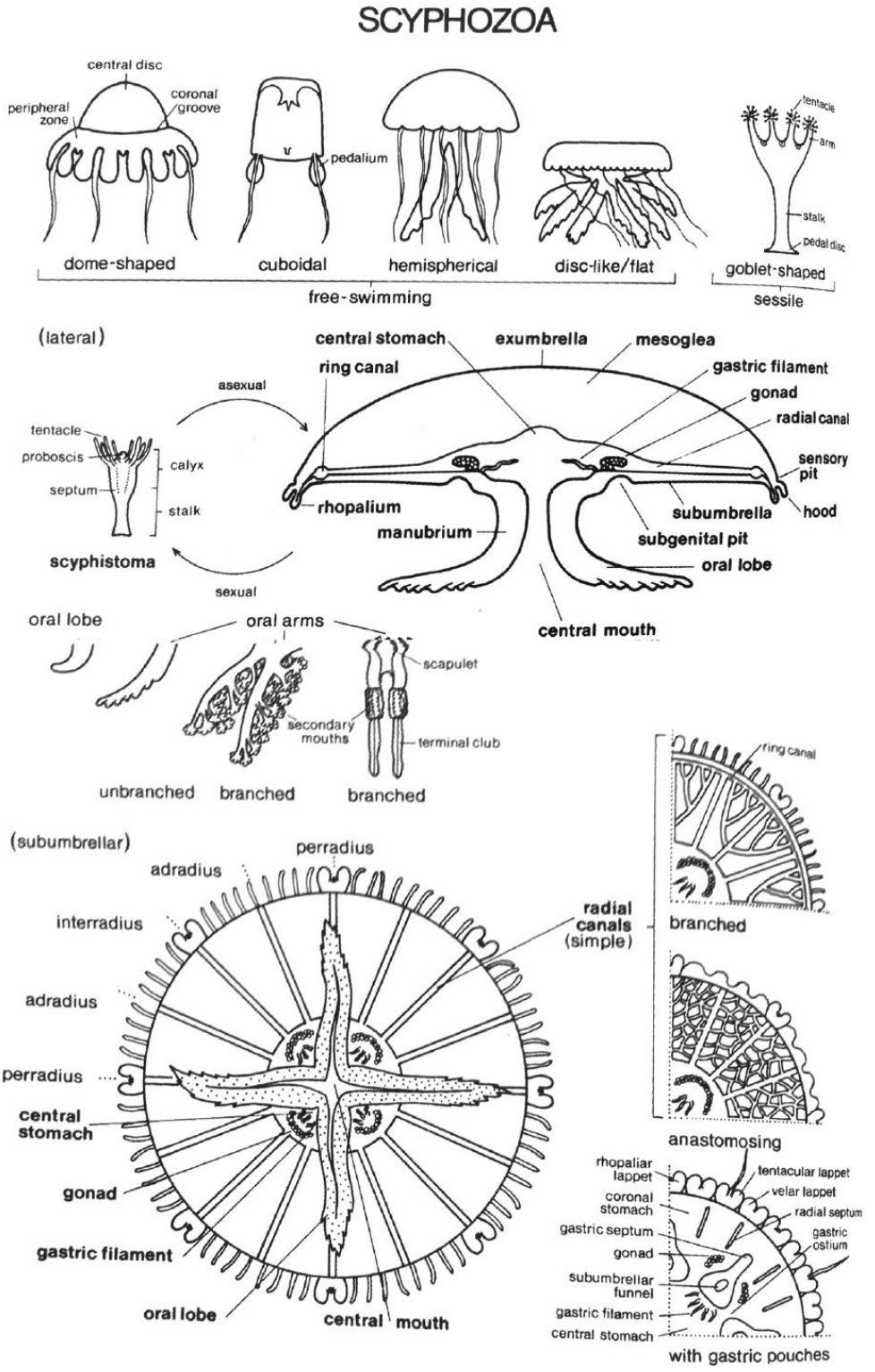

adhesive disc: pedal disc

adradius (adradial): One of eight radial axes halfway between each perradius and interradius; may correspond to projections (tentacles, rhopalia) of umbrellar margin.

anchor (colletocystophore): In sessile scyphozoan, well-developed, cushion-like rhopalioid containing mucus glands.

appendage: One of numerous small projections of oral arms; bears nematocysts and mucus cells, (elongate, filiform, vesicular) (See also terminal club)

arm: In sessile scyphozoan, one of eight upwardly directed, adradial extensions of umbrellar margin; tip of each arm bears numerous minute, capitate tentacles. If short, may also be referred to as lobe, (simple, bifurcated) (See also oral arm)

arm canal (brachial canal): Longitudinal gastrovascular canal within each oral arm; communicates with central stomach and opens to exterior via numerous suctorial mouths.

arm disc: Thick, disc-shaped, gelatinous projection of subumbrella. Mouth arms arise from lower side of arm disc.

bell: umbrella

branchial canal: Arm canal

bud: Lateral outgrowth of scyphistoma; develops asexually into new scyphistoma.

calyx: Upper and wider of two divisions of scyphistoma (calyx, stalk); typically divided by longitudinal septa.

cathammatum: septal node

central stomach (stomach): Undivided central part of gastrovascular system as distinguished from outer part which may be divided into gastric pouches or radial canals by septa. (See also coronal stomach)

ciliated groove: Longitudinal, ciliated furrow running along middle of inner surface of oral arm.

circular canal: ring canal

claustrum: In sessile scyphozoan or medusa, partition parallel to umbrellar margin; divides each gastric pouch into inner and outer pocket.

collenchyme: mesoglea

collectocystophore: anchor

coronal groove: Circular furrow extending around upper surface (exumbrella) of umbrella; clearly delimits marginal region from central region of bell.

coronal muscle: Circular band of muscle around periphery of umbrella; located in subumbrella and serves in swimming. (continuous, divided)

coronal sinus: coronal stomach

coronal stomach (coronary stomach, coronal sinus, gastrovascular sinus, ring sinus: Outer part of gastrovascular system as distinguished from central part (central stomach); may be divided by septa.

coronary stomach: coronal stomach

delta muscle (deltoid muscle): One in a series of radial muscle bands in subumbrella; spans from manubrium to circular coronal muscle or umbrellar margin and increases in width peripherally.

digitellus: gastric filament

ectoderm (epidermis): Outermost layer of body wall (ectoderm, mesoglea, endoderm) forming outer surface of exumbrella and subumbrella. Contains muscle, nerve, and gland cells as well as nematocysts.

Endoderm (gastrodermis): Flagellated innermost layer of body wall (ectoderm, mesoglea, endoderm). Lines manubrium and walls of gastrovascular system, forms gastric filaments, and gives rise to gonads.

ephyra: Young, free swimming medusa stage typically developing from attached scyphistoma and occasionally directly from planula. Umbrellar margin typically characterized by eight bifurcated arms (primary lappets), each with medial rhopalium.

epidermis: ectoderm

excretory pore: One in a series of small pores occasionally observed on subumbrellar surface at junction of radial canals with ring canal; radial canals open to exterior here.

exumbrella: Upper (aboral) convex surface of bell (umbrella), (smooth, warty) (See also subumbrella)

eye: complex photosensitive organ consisting of cellular lens, retina-like arrangement of sensory cells, and epidermis cover. (see also ocellus)

festoon Canal: Narrow, ring-shaped canal running around umbrellar margin and extending into each marginal lappet.

filament: gastric filament

frenulum: One of four perradial gelatinous folds supporting velarium and extending to subumbrellar surface.

gastric filament (filament, digitellus): One of numerous tentacle-like structures projecting into central stomach either from free inner edge of each septum or from stomach floor. (See also phacella)

gastric ostium: One of four openings in partitions separating central stomach from four gastric pouches. (See also septal ostium)

gastric pocket: gastric pouch

gastric pouch (gastric pocket): One of four pocket shaped extensions of central stomach; communicates with other gastric pouches via septal ostia, with central stomach via gastric ostia. (See also coronal stomach)

gastric septum: septum

gastrodermis: endoderm

gastrogenital membrane: Membrane separating central stomach from subgenital porticus. Consists of ectoderm, mesoglea, and endoderm.

gastrovascular cavity: central stomach

gastrovascular sinus: coronal stomach

genital sinus: Cavity between gonad and gastrogenital membrane.

gonad: Aggregation of male or female reproductive cells; located in septate scyphozoan along sides of septa, in those lacking septa in groups on stomach floor. (crescentic, horseshoe-shaped, oval, round, U-shaped, W-shaped)

gullet: manubrium hood: Small, hood-like extension of exumbrella over rhopalium; may bear outer and inner sensory pits basally on outer (exumbrellar) and inner (subumbrellar) sides.

hypostome: proboscis

interradius (interradial): One of four radial axes, 90° apart, lying between perradii; corresponds to position of septa and subumbrellar funnels as well as to projections of umbrellar margin (rhopalia, tentacles). (See also adradius).

lappet (marginal lappet): One in a series of lobe-like extensions around umbrellar margin; according to whether sensory structures (rhopalia) or tentacles are located between lappets one may distinguish rhopalial and tentacular lappets. (See also primary lappet, velar lappet).

lip: oral lip

lobe: arm, oral lobe

manubrium (gullet, pharynx): Median quadrangular projection of subumbrella bearing terminal mouth; leads to central stomach. If well-developed, one may distinguish fused basal section (oral tube) and distal, elongate lobes (oral arms).

marginal lappet: lappet

mesoglea (mesogloea, collenchyme, mesolamella): Middle layer of body wall between ectoderm and endoderm; typically thick, containing fibers and ameboid cells. Occasionally referred to as collenchyme because of presence of latter.

mesolamella: mesoglea

mouth: Four-cornered opening of central stomach at end of manubrium. May give rise to oral lobes or oral arms. (see also suctional mouth).

mouth arm: oral arm

nematocyst: Organelle within cnidocyte; consists of thick, double –walled capsule with coiled tubule and distal operculum. Nematocysts basically classified according to whether end of tubule is open (stomocnidae) or closed (astomocnidae), whether discharged tubule is regionated into dilated proximal butt and tubule proper (heteroneme) or of equal diameter throughout (haploneme), and according to armature of butt and tubule. (see also acrophore, amastigophore, anacrophore, anisorhiza, aspirotele, birhopaloid, desmoneme, eurytele, isorhiza, mastigophore, rhabdoid, rhopaloid, rhopaloneme, spirotele, stenotele.) .

nematocyst wart: One of numerous wart-like, nematocyst-bearing projections on upper surface (exumbrella) or manubrium of medusa.

nerve ring: Ring of nervous tissue around margin of umbrella; loops upward perradially to connect with rhopalia.

ocellus (pigment-spot ocellus, pigment-cup ocellus): Small, simple photosensitive organ consisting either of pigment spot or pigment cup; typically associated with basal section of rhopalium at umbrellar margin. (See also eye)

olfactory pit: sensor pit

oral arm (mouth arm): one of four or eight elongate lobes with frilled edges extending from manubrium; bears nematocysts and numerous suctorial mouths, (branched, unbranched, three-winged, two-winged)

oral disc: In polypoid stage (scyphistoma), flat oral surface with central, elevated mouth opening (proboscis) and marginal tentacles.

oral lip: Folded, fringed margin of suctorial mouth on oral arm.

oral lobe (perradial lobe): one of four short, lobelike projections at each corner of mouth or manubrium. (see also oral arm).

oral tube: manubrium

ostium: gastric ostium, septal ostium

pedal disc (adhesive disc): expanded, disc-shaped base sessile scyphistoma; contains gland cells and serves in attachment to substratum. May also produce podocysts in scyphistoma.

pedalium: gelatinous basal expansion of tentacle at margin of umbrella.

peduncle: stalk

peristome: oral disc

peristomial pit: on oral disc of scyphistoma, one a four shallow depressions associated with Insertion of each longitudinal muscle. (Sec also subgenital pit, subumbrellar funnel)

perradial lobe: oral lobe

perradius (perradial): One of four main radial axes, 90° apart; correspond in position to oral lobes, but typically also to other major structures such as gastric pouches, radial canals, and structures along umbrellar margin. (See also adradius, interradius).

phacella (phacellus): Row of gastric filaments, one along each side of free inner edge of septum.

pharynx: manubrium

planula: Ciliated larva; attaches to substratum and develops into tentacle-bearing, polypoid stage (scyphistoma). (hollow, solid)

podocyst (pedal cyst): At base of scyphistoma, chitinous cyst produced by pedal disc and containing ciliated larva.

primary lappet: In ephyra, one of eight bifurcated arms projecting from umbrellar margin; each has median rhopalium and develops into rhopalial lappet of adult.

proboscis: At center of oral disc of scyphistoma, cone-shaped projection bearing terminal mouth.

radial canal: In scyphozoan lacking gastric pouches, one in a series of narrow canals extending from central stomach to rim of umbrella or to ring canal if present; may be associated with so called excretory pore. Termed radial channel if larger in diameter, (anastomosed, branched, simple).

radial channel: radial canal

radial septum: septum

rhopalar canal: Small diverticulum of gastrovascular system extending in to rhopalium.

rhopalar lappet: rhopalial lappet

rhopalial lappet (rhopalar lappet): Pair of small, rudimentary lappets flanking rhopalium on umbrellar margin. (See also tentacular lappet, velar lappet)

rhopalioid: In sessile scyphozoan, short perradial and interradial projection (reduced tentacle) of exumbrellar margin between drawn-out adradial arm. (lobe-like, tentacle-like) (See also anchor)

rhopalium: Small, hollow, club-shaped sensory structure projecting from umbrella margin; flanked by rhopalial lappet and covered by hood. Contains statoliths distally.

ring canal: In scyphozoan with reduced gastric pouches, continuous circular tube around umbrellar margin; connected to central stomach via radial canals.

ring sinus: coronal stomach

scapulet (epaulette, shoulder ruffle): on proximal outer surface of oral arm, fringed outgrowth bearing numerous suctorial mouths.

scyphistoma: Tentacle-bearing polypoid stage developing after attachment of planula to substratum; consists of pedal disc, stalk, peristome, and calyx with tentacles. Gastrovascular cavity typically divided by four longitudinal septa. (See also strobila).

scyphomedusa: General term for medusa stage of scyphozoan. (See also scyphopolyp)

scyphopolyp: General term for polyp stage of scyphozoan. (see also scyphistoma, scy phomedusa, strobili)

secondary mouth: suctorial mouth

sensory pit (olfactory pit): Small sensory depression associated with base of rhopalium; according to position one may distinguish an outer (exumbrellar) and inner (subtimbrellai) sensory pit.

septal muscle: Longitudinal (oral-aboral axis) muscle band in septum.

septal node (cathammatum, cathammal plate): One of four small interradial areas of fusion between exumbrella and subumbrella; separates central stomach from coronal stomach and represents reduced gastric septum.

septal ostium: Circular opening in peripheral region of septum; permits gastric pouches to communicate with one another.

septum: Partition spanning between exumbrella and subumbrella. Typically refers to one of four interradial partitions dividing gastrovascular system into central stomach and four marginal gastric pouches; may bear opening (septal ostium) and be penetrated by subumbrellar funnel. May be termed gastric septum to differentiate from more numerous radial septa in outer part of gastrovascular system (coronal stomach).

shoulder ruffle: scapuiet

stalk (peduncle): In sessile scyphozoan, slender aboral division of body; attached to substratum by pedal disc. May also refer to stalk of scyphistoma.

statocyst: Term applied to mass of cells, each bearing statolith, at distal end of rhopalium.

statolith: Minute, solid, movable body within one of numerous cells at distal end of rhopalium.

stolon: Hollow tubelike projection from stalk or base of scyphistoma; gives rise asexually to new scyphistomae.

stomach: central stomach

strobila: Stage of sessile polypoid form (scyphistoma) in which series of young medusae (ephyrae) are being produced simultaneously (polydisc strobilation) or singly (monodisc strobilation) by transverse constriction(s).

subgenital ostium: subgenital porticus

subgenital pit: One of four shallow depressions on interradius of subumbrella. May fuse to form subgenital porticus. (See also subumbrellar funnel)

subgenital porticus: Cross-shaped cavity formed by fusion of four subgenital pits. Located on subumbrellar surface between central stomach and bases of oral arms (original mouth degenerates); four original openings (subgenital ostia) remain.

subumbrella: Lower (oral) concave surface of medusa body (umbrella).

subumbrellar funnel (peristomial pit): One of four deep, funnel-shaped pits in subumbrella; located on interradius and therefore projecting into septum dividing gastrovascular system. (See also subgenital pit)

subumbrellar sac: Sac-like enlargement of proximal section of gastric pouch; hangs down into subumbrellar cavity.

suctorial mouth (secondary mouth): On oral arm, one of numerous communications between longitudinal groove along inner surface of arm and internal arm canal. Opening lo exterior surrounded by oral lips.

tentacle: One in a series of elongate processes around umbrella margin, either on or between lappets or projecting from subumrellar surface. In sessile scyphyzoan, one of numerous minute, capitate tentacles at tip of each arm. (hollow, solid; capitate, filiform; single, clustered)

tentacular lappet: Pair of lappets flanking tentacle on umbrellar margin. (See also rhopalial lappet, velar lappet)

terminal club (terminal appendage): Long, club-shaped appendage hanging from each oral arm. (See also appendage)

umbrella (bell): Main body or bell of medusa; upper surface termed exumbrella, lower surface subumbrella. Typically with thick mesoglea and marginal lappets. (conical, cuboidal, disc-like/flattened, domeshaped, hemispherical, pyramidal,saucer-shaped)

velarium (velum): Horizontal fold projecting inwardly from umbrella margin; consists only of subumbrellar tissue and may be supported by four frenula.

velar lappet: In scyphomeduse lacking marginal tentacles, type of lappet on umbrellar margin between rhopalial lappets. (See also tentacular lappet)

velum: velarium

wart: nematocyst wart

References

[1] J. W. Valentine, *On the origin of phyla*. Chicago: University of Chicago Press, 2004.

[2] W. G. Gladfelter, "Structure and function of the locomotory system of Polyorchis montereyensis (Cnidaria, Hydrozoa)," *Helgol. Wiss. Meeresunters.*, vol. 23, p. 38, 1972.

[3] W. G. Gladfelter, "Structure and function of the locomotory system of the Scyphomedusa cyanea capillata," *Mar. Biol.*, vol. 14, p. 150, 1973.

[4] D. M. Chapman, "Cnidarian histology," in *Coelenterate Biology*, L. Muscatine and H. M. Lenhoff, Eds., ed New York: Academic Press, 1974, pp. 2-92.

[5] D. J. Albert, "Aurelia labiata (Scyphozoa) jellyfish in Roscoe Bay: Their spatial distribution varies with population size and their behaviour changes with water depth," *Journal of Sea Research*, vol. 61, pp. 140-143, 2009.

[6] V. A. Tucker, "The Energetic Cost of Moving About: Walking and running are extremely inefficient forms of locomotion. Much greater efficiency is achieved by birds, fish—and bicyclists," *American Scientist*, vol. 63, pp. 413-419, 1975.

[7] R. J. Larson, "Costs of transport for the scyphomedusa Stomolophus meleagris L. Agassiz," *Canadian Journal of Zoology*, vol. 65, pp. 2690-2695, 1987/11/01 1987.

[8] Oxforddictionaries.com. Oxford dictionary [Online]. Available: http://oxforddictionaries.com/definition/english/coelenterate

[9] M. Stachowitsch and S. Proidl, *The invertebrates : an illustrated glossary*. New York: Wiley-Liss, 1992.

[10] J. Williams, *Optical properties of the sea*. Annapolis, Md.: United States Naval Institute, 1970.

[11] A. G. Macdonald, *Physiological aspects of deep sea biology*. Cambridge [Eng.]; New York: Cambridge University Press, 1975.

[12] Wikipedia. Available: http://en.wikipedia.org/wiki/Tiburonia

[13] D. C. Webb, P. J. Simonetti, and C. P. Jones, "SLOCUM: An Underwater Glider Propelled by Environmental Energy," *IEEE Journal of Oceanic Engineeing*, vol. 26, pp. 447-452, 2001.

[14] G. Chapman, "Reflections on transparency," ed: Plenum Press, New York, 1976, pp. 491-498.

[15] Y. van Bergen, "OOZING OXYGEN: IT'S ALL IN THE GEL," *Journal of experimental Biology*, vol. 208, pp. i-i, 2005.

[16] T. Hirano and M. Ohashi, "Molecular processes in bioluminescence of the jellyfish Aequorea victoria - mechanisms for generating an excited molecule in chemi- and bioluminescent reactions," *Yuki Gosei Kagaku Kyokaishi/Journal of Synthetic Organic Chemistry*, vol. 54, pp. 596-606, 1996.

[17] B. Rigby and M. Hafey, "Thermal Properties of the Collagen of Jellyfish (Aurelia Coerulea) and their Relation to its Thermal Behaviour," *Australian Journal of Biological Sciences*, vol. 25, pp. 1361-1364, 1972.

[18] M. E. Demont and J. M. Gosline, "Mechanics of Jet Propulsion in the Hydromedusan Jellyfish, Polyorchis Pexicillatus: III. A Natural Resonating Bell; The Presence and Importance of a Resonant Phenomenon in the Locomotor Structure," *Journal of experimental Biology*, vol. 134, pp. 347-361, January 1, 1988 1988a.

[19] B. Akle, J. Najem, D. Leo, and J. Blottman, "Design and development of bio-inspired underwater jellyfish like robot using ionic polymer metal composite (IPMC) actuators," pp. 797624-797624, 2011.
[20] S. Guo, T. Fukuda, and K. Asaka, "A new type of fish-like underwater microrobot," *IEEE/ASME Trans. Mechatronics,* vol. 8, p. 136, 2003.
[21] S. Liwei, G. Shuxiang, and K. Asaka, "A novel jellyfish-like biomimetic microrobot," in *Complex Medical Engineering (CME), 2010 IEEE/ICME International Conference on*, 2010, pp. 277-281.
[22] J. Najem, B. Akle, S. A. Sarles, and D. J. Leo, "Design and Development of a Biomimetic Jellyfish Robot That Features Ionic Polymer Metal Composites Actuators," *ASME Conference Proceedings,* vol. 2011, pp. 691-698, 2011.
[23] G. Shuxiang, S. Liwei, Y. Xiufen, and L. Lingfei, "A New Jellyfish Type of Underwater Microrobot," in *Mechatronics and Automation, 2007. ICMA 2007. International Conference on*, 2007, pp. 509-514.
[24] Y. Tadesse, A. Villanueva, C. Haines, D. Novitski, R. Baughman, and S. Priya, "Hydrogen-fuel-powered bell segments of biomimetic jellyfish," *Smart Materials and Structures,* vol. 21, Apr 2012.
[25] Y. Xiu Fen, H. Ya Nan, G. Shu Xiang, and S. Yu Dong, "Driving mechanism of a new jellyfish-like microrobot," in *Mechatronics and Automation, 2008. ICMA 2008. IEEE International Conference on*, 2008, pp. 563-568.
[26] Y. Yang, X. Ye, and S. Guo, "A New Type of Jellyfish-Like Microrobot," in *IEEE International Conference on Integration Technology, 2007*, 2007, pp. 673-678.
[27] S.-W. Yeom and I.-K. Oh, "A biomimetic jellyfish robot based on ionic polymer metal composite actuators," *Smart Materials and Structures,* vol. 18, p. 085002, 2009.
[28] A. Villanueva, S. Bresser, S. Chung, Y. Tadesse, and S. Priya, "Jellyfish inspired underwater unmanned vehicle," *Proc. SPIE,* vol. 7287, p. 72871G, 2009.
[29] A. Villanueva, S. Priya, C. Anna, and C. Smith, "Robojelly bell kinematics and resistance feedback control," in *IEEE International Conference on Robotics and Biomimetics (ROBIO)*, 2010a, pp. 1124-1129.
[30] W.-S. Chu, K.-T. Lee, S.-H. Song, M.-W. Han, J.-Y. Lee, H.-S. Kim, M.-S. Kim, Y.-J. Park, K.-J. Cho, and S.-H. Ahn, "Review of biomimetic underwater robots using smart actuators," *International Journal of Precision Engineering and Manufacturing,* vol. 13, pp. 1281-1292, 2012.
[31] G. Chapman, "Studies of the Mesogloea of Coelenterates: I. Histology and Chemical Properties," *Quarterly Journal of Microscopical Science,* vol. s3-94, pp. 155-176, June 1, 1953 1953a.
[32] A. Krogh, *Osmotic regulation in aquatic animals*. New York: Dover Publications, 1965.
[33] G. Chapman, "Studies on the Mesogloea of Coelenterates: II. Physical Properties," *J. Exp. Biol.*, vol. 30, pp. 440-451, September 1, 1953 1953b.
[34] R. McN. Alexander, "Visco-Elastic Properties of the Mesogloea of Jellyfish," *Journal of experimental Biology,* vol. 41, pp. 363-369, June 1, 1964 1964.
[35] W. M. Megill, J. M. Gosline, and R. W. Blake, "The modulus of elasticity of the fibrillin-containing microfibrils from the mesoglea of the hydromedusa: polyorchis penicillatus," *J. Exp. Biol.*, vol. 208, p. 3819, 2005.

[36] M. E. Demont and J. M. Gosline, "Mechanics of Jet Propulsion in the Hydromedusan Jellyfish, Polyorchis Penicillatus: II. Energetics of the Jet Cycle," *Journal of experimental Biology,* vol. 134, pp. 333-345, January 1, 1988 1988b.

[37] X. Zhang, R. P. Boot-Handford, J. Huxley-Jones, L. N. Forse, A. P. Mould, D. L. Robertson, LiLi, M. Athiyal, and M. P. Sarras, Jr., "The Collagens of Hydra Provide Insight into the Evolution of Metazoan Extracellular Matrices," *J. Biol. Chem.,* vol. 282, pp. 6792-6802, March 2, 2007 2007.

[38] T. Nagai, T. Ogawa, T. Nakamura, T. Ito, H. Nakagawa, K. Fujiki, M. Nakao, and T. Yano, "Collagen of edible jellyfish exumbrella," *Journal of the Science of Food and Agriculture,* vol. 79, pp. 855-858, 1999.

[39] B. A. Roeder, K. Kokini, J. E. Sturgis, J. P. Robinson, and S. L. Voytik-Harbin, "Tensile Mechanical Properties of Three-Dimensional Type I Collagen Extracellular Matrices With Varied Microstructure," *Journal of Biomechanical Engineering,* vol. 124, pp. 214-222, 2002.

[40] M. P. E. Wenger, L. Bozec, M. A. Horton, and P. Mesquida, "Mechanical Properties of Collagen Fibrils," *Biophysical Journal,* vol. 93, pp. 1255-1263, 2007.

[41] G. A. Horridge, "The nerves and muscles of medusae. I. Conduction in the nervous system of Aurellia aurita Lamarck," *Journal of experimental Biology,* vol. 31, p. 594, 1954.

[42] G. A. Horridge, "The nerves and muscles of medusae. II. Geryonia proboscidalis Eschscholtz," *Journal of experimental Biology,* vol. 32, p. 555, 1955a.

[43] G. A. Horridge, "The nerves and muscles of medusae. IV. Inhibition in Aequorea forskalea," *Journal of experimental Biology,* vol. 32, p. 642, 1955b.

[44] G. A. Horridge, "The nerves and muscles of medusae. III. A decrease in the refractory period following repeated stimulation of the muscle of Rhizostoma pulmo," *Journal of experimental Biology,* vol. 32, p. 636, 1955c.

[45] G. A. Horridge, "The nerves and muscles of medusae. V. Double innervation in Scyphozoa," *Journal of experimental Biology,* vol. 33, p. 366, 1956.

[46] G. A. Horridge, "The Nerves and Muscles of Medusae," *Journal of experimental Biology,* vol. 36, p. 72, 1959.

[47] R. A. Satterlie, "Control of swimming in the hydrozoan jellyfish Aequorea victoria: subumbrellar organization and local inhibition," *Journal of experimental Biology,* vol. 211, pp. 3467-3477, November 1, 2008 2008.

[48] R. A. Satterlie, "Do jellyfish have central nervous systems?," *Journal of experimental Biology,* vol. 214, pp. 1215-1223, April 15, 2011 2011.

[49] L. Passano, "Behavioral control systems in medusae: A comparison between hydro-and scyphomedusae," *Publ. Seto Mar. Biol. Lab,* vol. 20, pp. 615-645, 1973.

[50] R. A. Satterlie, "Neuronal control of swimming in jellyfish: a comparative story," *Canadian Journal of Zoology,* vol. 80, pp. 1654-1669, 2002/10/01 2002.

[51] A. A. Villanueva, K. B. Joshi, J. B. Blottman, and S. Priya, "A bio-inspired shape memory alloy composite (BISMAC) actuator," *Smart Mater. Struct.,* vol. 19, p. 025013, 2010b.

[52] K. B. Joshi, A. Villanueva, C. F. Smith, and S. Priya, "Modeling of Artificial Aurelia aurita Bell Deformation," *Marine Technology Society Journal,* vol. 45, pp. 165-180, 2011a.

[53] V. B. Sundaresan, "Controlled fluid transport using ATP-powered protein pumps," *Smart Materials and Structures,* vol. 16, pp. S207-S213, 2007.
[54] D. L. Rudnick, R. E. Davis, C. C. Ericson, D. M. Frantoni, and M. J. Perry, "Underwater Gliders for Ocean Research," *Marine Technology Society Journal,* vol. 34, pp. 48-59, 2004.
[55] D. C. Webb, "SOFAR floats for POLYMODE," in *Proc.Oceans'77 Conf.*, Los Angeles, CA, 1977, pp. 44B-1-44B-5.
[56] R. E. Davis, D. C. Webb, L. A. Regier, and J. Dafour, "The autonomous lagrangian circulation explorer (ALACE)," *Journal of Atmoaspheric Oceanic Technology,* vol. 9, pp. 264-285, 1992.
[57] S. Wang, Xie, C., Wang, Y., Zhang, L., Jie, W., Hu S.J., "Harvesting of PEM fuel cell heat energy for a thermal engine in an underwater glider," *Journal of Power Sources,* vol. 169, pp. 338-346, 2007.
[58] L. Muscatine, L. R. McCloskey, and R. E. Marian, "Estimating the daily contribution of carbon from zooxanthellae to coral animal respiration," *Limnology and oceanography,* vol. 26, pp. 601-611, 1981.
[59] P. Kremer, et al, "Significance of photosynthetic endosymbionts to the carbon budget of the scyphomedusa Linuche unguiculata," *Limnology and Oceanography,* vol. 35, pp. 609-624, 1990.
[60] D. T. Welch, et al., "Oxygen and nutrient dynamics of the upside down jellyfish (Cassiopea sp) and it influence on benthic nutrient exchanges and primary production," *Hydrobiologia,* vol. 635, pp. 351-362, 2009.
[61] S. P. Colin and J. H. Costello, "Morphology, swimming performance and propulsive mode of six co-occurring hydromedusae," *J. Exp. Biol.*, vol. 205, p. 427, 2002.
[62] J. V. Dave, "Performance of a tilted solar cell under various atmospheric conditions," *Solar Energy,* vol. 21, pp. 263-271, 1978.
[63] M. C. Gonzalez and J. J. Carrol, "Solar cells efficiency variations with varying atmospheric conditions," *Solar Energy,* vol. 53, pp. 395-402, 1994.
[64] M. C. Stoddard and F. P. Incropera, "Distribution of solar radiation in natural waters under field conditions," *Solar Energy,* vol. 28, pp. 425-432, 1982.
[65] J. A. Muaddi and M. A. Jamal, "Spectral response and efficiency of a silicon solar cell below water surface," *Solar Energy,* vol. 49, pp. 29-33, 1992.
[66] J. Wang and J. Seyed-Yagoobi, "Effects of water turbidity and salt concentration levels on penetration of solar radiation under water," *Solar Energy,* vol. 52, pp. 429-438, 1994.
[67] R. Gottschalg, D. G. Infield, and M. J. Kearney, "Experimental study of variations of the solar spectrum of relevance to thin film solar cells," *Solar Energy Materials and Solar Cells,* vol. 79, pp. 527-537, 2003.
[68] J. Y. Chen and K. W. Sun, "Enhancement of the light conversion efficiency of silicon solar cells by using nanoimprint anti-reflection layer," *Solar Energy Materials and Solar Cells,* vol. 94, pp. 629-633, 2010.
[69] C. Strümpel, M. McCann, G. Beaucarne, V. Arkhipov, A. Slaoui, V. Svrcek, C. del Cañizo, and I. Tobias, "Modifying the solar spectrum to enhance silicon solar cell efficiency--An overview of available materials," *Solar Energy Materials and Solar Cells,* vol. 91, pp. 238-249, 2007.

[70] E. Custodio, L. Acosta, P. J. Sebastian, and J. Campos, "A better solar module performance obtained by employing an infrared water filter," *Solar Energy Materials and Solar Cells*, vol. 70, pp. 395-399, 2001.
[71] D. Yun, W. Feng, H. Wu, and K. Yoshino, "Efficient conjugated polymer-ZnSe and -PbSe nanocrystals hybrid photovoltaic cells through full solar spectrum utilization," *Solar Energy Materials and Solar Cells*, vol. 93, pp. 1208-1213, 2009.
[72] http://www.powerfilmsolar.com.
[73] http://www.apogeeinstruments.com.
[74] http://www.hamiltontechnology.com.
[75] http://www.advancedaquarist.com/issues/july2004/review.htm.
[76] Dabiri, Costello, and Colin, "Flow patterns generated by oblate medusan jellyfish : field measurements and laboratory analyses," *Journal of experimental Biology*, vol. 208, pp. 1257-1265, 2005a.
[77] M. Ujihara, G. P. Carman, and D. G. Lee, "Thermal energy harvesting device using ferromagnetic materials," *Applied Physics Letters*, vol. 91, pp. 093508-3, 2007.
[78] F. O. Goodman, "Thermal accommodation coefficients," *The Journal of Physical Chemistry*, vol. 84, pp. 1431-1445, 1980/06/01 1980.
[79] S. Song and M. M. Yovanovich, "Correlation of Thermal Accomodation Coefficient for Engineering Surfaces," presented at the National Heat Transfer Conference, Fairfield, NJ, 1987.
[80] H. Yüncü, "Thermal contact conductance of nominaly flat surfaces," *Heat and Mass Transfer*, vol. 43, pp. 1-5, 2006.
[81] E. P. Furlani, *Permanent magnet and electromechanical devices : materials, analysis, and applications*. San Diego, Calif.; London: Academic, 2001.
[82] B. K. Ponomarev, "Magnetic properties of gadolinium in the region of paraprocess," *Journal of Magnetism and Magnetic Materials*, vol. 61, pp. 129-138, 1986.
[83] M. I. Darby, "Tables of the Brillouin function and of the related function for the spontaneous magnetization," *British Journal of Applied Physics*, vol. 18, p. 1415, 1967.
[84] A. Aharoni, "Demagnetizing factors for rectangular ferromagnetic prisms," *Journal of Applied Physics*, vol. 83, pp. 3432-3434, 1998.
[85] G. Akoun and J. P. Yonnet, "3D analytical calculation of the forces exerted between two cuboidal magnets," *Magnetics, IEEE Transactions on*, vol. 20, pp. 1962-1964, 1984.
[86] P. Seshu, *Textbook of finite element analysis*. New Delhi: Prentice-Hall of India, 2006.
[87] J. N. Reddy, *An introduction to the finite element method*. Boston; Burr Ridge, IL; New York ... [etc.]: McGraw-Hill, 1984.
[88] K.-J. Bathe, *Finite element procedures*. Englewood Cliffs, N.J.: Prentice Hall, 1996.
[89] H. A. Sodano, G. Park, and D. J. Inman, "Estimation of Electric Charge Output for Piezoelectric Energy Harvesting," *Strain*, vol. 40, pp. 49-58, 2004.
[90] N. G. Elvin and A. A. Elvin, "A General Equivalent Circuit Model for Piezoelectric Generators," *Journal of Intelligent Material Systems and Structures*, vol. 20, pp. 3-9, January 1, 2009 2009.
[91] J. Ajitsaria, S. Y. Choe, D. Shen, and D. J. Kim, "Modeling and analysis of a bimorph piezoelectric cantilever beam for voltage generation," *Smart Materials and Structures*, vol. 16, p. 447, 2007.
[92] S.-K. Youn and E. B. Becker, "A coupled field beam theory for piezoelectric biomorphs," *Ferroelectrics*, vol. 119, pp. 41-52, 1991/07/01 1991.

[93] H. Yu-Hsi and M. Chien-Ching, "Experimental and numerical investigations of vibration characteristics for parallel-type and series-type triple-layered piezoceramic bimorphs," *Ultrasonics, Ferroelectrics and Frequency Control, IEEE Transactions on*, vol. 56, pp. 2598-2611, 2009.
[94] M. A. Karami, O. Bilgen, D. J. Inman, and M. I. Friswell, "Experimental and analytical parametric study of single-crystal unimorph beams for vibration energy harvesting," *Ultrasonics, Ferroelectrics and Frequency Control, IEEE Transactions on*, vol. 58, pp. 1508-1520, 2011.
[95] N. Kahn and E. Swift, "Positive Buoyancy Through Ionic Control in the Nonmotile Marine Dinoflagellate Pyrocystis noctiluca Murray ex Schuett," *Limnology and Oceanography*, vol. 23, pp. 649-658, 1978.
[96] N. K. Sanders and J. J. Childress, "Ion Replacement as a Buoyancy Mechanism in a Pelagic Deep-Sea Crustacean," *J. Exp. Biol.*, vol. 138, pp. 333-343, September 1, 1988 1988.
[97] T. A. Cochrane and T. T. Cochrane, "OSMOTIC POTENTIAL PROPERTIES OF SOLUTES COMMON IN THE SOIL-PLANT SOLUTION CONTINUUM," *Soil science*, vol. 170, pp. 433-444, 2005.
[98] A. Lindbråthen and M.-B. Hägg, "Membrane separation of chlorine gas," *Chemical Engineering and Processing: Process Intensification*, vol. 48, pp. 1-16, 2009.
[99] B. A. Hills, "A role for oxygen-induced osmosis in hyperbaric oxygen therapy," *Medical Hypotheses*, vol. 52, pp. 259-263, 1999.
[100] A. Babchin, E. Levich, Y. Melamed M.D, and G. Sivashinsky, "Osmotic phenomena in application for hyperbaric oxygen treatment," *Colloids and Surfaces B: Biointerfaces*, vol. 83, pp. 128-132, 2011.
[101] V. Hock, S. Morefield, M. McInerney, O. Marshall, C. Marsh, S. Cooper, P. Malone, and C. Weiss, "Control of water migration through concrete using electro-osmosis," *Materials Performance*, vol. 44, pp. 42-47, Jul 2005.
[102] H. T. HAMMEL, "Evolving ideas about osmosis and capillary fluid exchange," *The FASEB Journal*, vol. 13, pp. 213-231, February 1, 1999 1999.
[103] S. A. Ben-Sasson, "OSMOSIS: A MACROSCOPIC PHENOMENON, A MICROSCOPIC VIEW," *Advances in physiology education*, vol. 27, pp. 15-19, 2003.
[104] I. Müller. (2005). *Entropy and energy a universal competition*. Available: http://dx.doi.org/10.1007/3-540-32380-5
[105] A. Babchin, E. Levich, Y. Melamad, and G. Sivashinsky. (2011, October 15). *Normal and anomalous osmosis through a leaking membrane*. Available: http://www.hyperbaric-oxygen-info.com/osmosis-osmotic-pressure-hyperbaric-oxygen-treatment-p2.html
[106] K. P. Tikhomolova and T. J. Kemp, *Electro-osmosis*. New York: E. Horwood, 1993.
[107] M. Paunovic, M. Schlesinger, and D. D. Snyder, "Fundamental Considerations," in *Modern Electroplating*, ed: John Wiley & Sons, Inc., 2010, pp. 1-32.
[108] T. Sokalski, P. Lingenfelter, and A. Lewenstam, "Numerical Solution of the Coupled Nernst−Planck and Poisson Equations for Liquid Junction and Ion Selective Membrane Potentials," *The Journal of Physical Chemistry B*, vol. 107, pp. 2443-2452, 2003/03/01 2003.
[109] Z. Schuss, "Derivation of Poisson and Nernst-Planck equations in a bath and channel from a molecular model," *Physical review. E, Statistical physics, plasmas, fluids, and related interdisciplinary topics*, vol. 64, 2001.

[110] T. W. Kao, F.-S. Pan, and D. Renouard, "Internal solitons on the pycnocline: generation, propagation, and shoaling and breaking over a slope," *Journal of Fluid Mechanics*, vol. 159, pp. 19-53, 1985.
[111] Y. Tadesse, J. Brennan, C. Smith, T. E. Long, and S. Priya, "Synthesis and characterization of polypyrrole composite actuator for jellyfish unmanned undersea vehicle," San Diego, CA, USA, 2010a, pp. 764222-11.
[112] C. Smith, A. Villanueva, K. Joshi, Y. Tadesse, and S. Priya, "Working principle of bio-inspired shape memory alloy composite actuators," *Smart Materials and Structures*, vol. 20, p. 012001, 2011.
[113] J. P. Dabiri, S. P. Colin, and J. H. Costello, "Flow patterns generated by oblate medusan jellyfish: field measurements and laboratory analyses," *J. Exp. Biol.*, vol. 208, p. 1257, 2005b.
[114] C. F. Smith and S. Priya, "Bio-inspired unmanned undersea vehicle," in *Behavior and Mechanics of Multifunctional Materials and Composites 2010, March 8, 2010 - March 11, 2010*, San Diego, CA, United states, 2010, pp. The Society of Photo-Optical Instrumentation Engineers (SPIE); American Society of Mechanical Engineers.
[115] A. Villanueva and S. Priya, "BISMAC control using SMA resistance feedback," in *SPIE NDE Conference*, San Diego, CA, USA, 2010c, pp. 76421Z-12.
[116] National Instruments. (June 20, 2011). *LabView*. Available: http://www.ni.com/labview/
[117] ImageJ. *Image Processing and Analysis in Java*. Available: http://rsbweb.nih.gov/ij/
[118] Y. Tadesse, N. Thayer, and S. Priya, "Tailoring the Response Time of Shape Memory Alloy Wires through Active Cooling and Pre-stress," *Journal of Intelligent Material Systems and Structures*, vol. 21, pp. 19-40, January 1, 2010 2010b.
[119] Toki Corp. (January 7, 2011). *Biometal Fiber*. Available: http://www.toki.co.jp/biometal/english/qanda.php
[120] E. Baker, "Liquid cooling of microelectronic devices by free and forced convection," *Microelectronics Reliability*, vol. 11, pp. 213-222, 1972.
[121] A. Villanueva, C. Smith, and S. Priya, "A biomimetic robotic jellyfish (Robojelly) actuated by shape memory alloy composite actuators," *Bioinspiration & Biomimetics*, vol. 6, Sep 2011.
[122] K. B. Joshi, B. J. Akle, D. J. Leo, and S. Priya, "Modeling and optimization of IPMC actuator for autonomous jellyfish vehicle (AJV)," San Diego, California, USA, 2011b, pp. 79750Q-10.